DISS. ETH NO. 30270

THE HYDROLOGY OF HIGH MOUNTAIN ASIAN HEADWATER CATCHMENTS VIA MECHANISTIC MODELLING

A thesis submitted to attain the degree of

DOCTOR OF SCIENCES

(Dr. sc. ETH Zürich)

presented by

STEFAN FUGGER

Dipl.Ing., University of Natural Resources and Life Sciences, BOKU, Vienna

Born on *10.10.1988*

accepted on the recommendation of

Prof. Dr. Peter Molnar (examiner)
Prof. Dr. Francesca Pellicciotti (co-examiner)
Prof. Dr. Heini Wernli (co-examiner)
Prof. Dr. John Pomeroy (co-examiner)
Prof. Dr. Benjamin Brock (co-examiner)
Prof. Dr. Walter Immerzeel (co-examiner)

2024

Abstract

The headwater catchments of High Mountain Asia (HMA) provide freshwater to large populations from the semi-arid lowlands of Central Asia to the densely populated agricultural plains and metropoles of Southern and Eastern Asia. Climatic conditions vary greatly between HMA sub-regions, with contrasting seasonality and amounts of precipitation, controlled by the interactions of several large-scale circulation systems. Climate change is altering the boundary conditions under which these systems are operating, with cascading effects on all components of the energy and water balances: Seasonal snow accumulation and glacier masses are decreasing, and hydrological regimes are shifting gradually towards less snowmelt runoff and more rainfall runoff. Changes in the land surface energy budget and properties of the atmosphere are altering vegetation productivity and evaporative fluxes, with largely unknown consequences for runoff. Projections of future high-mountain hydrology are highly relevant to society, however, they are currently limited by our understanding of the multiple and entangled physical processes at play, and a lack of appropriate modelling tools for representing their spatial and temporal integration.

In this thesis, we apply a modelling framework that combines a state-of-the-art model of snow, glacier, and ecohydrology, Tethys-Chloris (T&C), with glaciological, hydrological, and meteorological in-situ observations and gridded data products, to investigate the hydrology of headwater catchments in HMA. For this purpose, we collected in-situ data in one seasonally dry, westerly controlled catchment in the Pamir mountains (Kyzylsu) with a winter/spring accumulation regime, one monsoonal, summer-accumulation catchment in the Nepalese Himalaya (Langtang), and one monsoonal catchment on the Southeastern Tibetan Plateau (24K) with an intense spring/summer accumulation regime. We implemented new components in the model, and updated existing ones: an energy-balance scheme for ice melting under supraglacial debris, a multi-layer snow pack and advanced schemes for precipitation partitioning and albedo. We use this modelling framework and new in-situ data to address three primary research gaps:

First, we aim to understand the energy-balance controls on glacier ablation at multiple sites in the Central and Eastern Himalaya. We conduct point scale simulations at seven automatic weather stations installed in glacier ablation zones. Constrained by local measurements, we use the simulations to understand the impact of monsoonal conditions on the surface energy balance, ice ablation, snow accumulation and melting, evaporation and sublimation. On debris-covered glaciers, variations in the radiative budget are offset by changes in turbulent heat fluxes, leading to minimal or no changes in the melting of ice beneath debris, between the pre-monsoon and

peak monsoon seasons. In contrast, clean-ice melt is directly and primarily influenced by variations in the radiative budget while turbulent fluxes remain small. Over thin debris however, turbulent fluxes act to enhance melting during the monsoon.

Second, applying the model in a distributed way to the three main study sites, we focus on the current partitioning of water fluxes and in particular on the role of evaporative fluxes, including all-surface evaporation, transpiration and sublimation. We use downscaled reanalysis data, bias-corrected against weather station data, as meteorological forcing for the model. Evaporative fluxes account for 28%, 19% and 13% of the water losses from Kyzylsu, Langtang and 24K, respectively. Sublimation and evapotranspiration are both most important in the water balance of Kyzylsu, with sublimation returning 15% of snowfalls to the atmosphere, and evapotranspiration corresponding to 76% of total rainfall, while the largest evapotranspiration flux occurs at the wettest site, 24K with 413 mm yr^{-1}. Compensatory effects in the runoff generation between evaporative fluxes and ice melt runoff under warmer conditions are indicated, which motivates further experimentation under altered meteorological forcings.

Third, we investigate the impact of future climate warming on energy and mass fluxes and the potential hydrological response of the three catchments. We re-run the simulations under experimental conditions, representative of mid-21st century temperature increase under the shared socio-economic pathways SSP2-4.5 (W4.5) and SSP5-8.5 (W8.5). Warming increases the annual amount of water transferred through the catchment, but compensations between ice melt and evapotranspiration result in only moderate or no changes in runoff, depending on the hydroclimatic context: Changes in the water yield range from -1% in 24K under W4.5 to +14% in Kyzylsu, under W8.5. While the runoff sensitivity is higher in Kyzylsu, the sensitivity of glacier mass balances is greater at the monsoonal sites: shifts from solid to liquid precipitation are most pronounced in 24K, where up to 76% of additional ice melt (+130%) under W8.5, can be attributed to losses of glacier-protecting monsoon-season snow cover. Increases in vegetation productivity together with the pronounced increases in evapotranspiration manifest in the lengthening of the growing season, ranging between +9 days in Langtang (+26% evapotranspiration, W4.5) and +31 days in 24K (+ 50% evapotranspiration, W8.5). Sublimation shows a relatively insensitive and mixed response across sites, with seasonally varying increases and decreases, determined by the local temperature and vapour regimes.

In this thesis, we use a physically-based model consistently, to investigate the hydrological functioning of headwater catchments across the spectrum of HMA climates, and assess their sensitivity to warming. Integrating in-situ observations and remote sensing, our modelling framework allows us to study in a fully distributed way energy and mass fluxes in mountain catchments. This is, to our knowledge, the first time that these methods are applied to glacierized catchments in HMA, in order to disentangle the processes of runoff generation. This thesis clarifies the role of the cryosphere and evaporative fluxes in these environments, and in particular, the roles of debris-covered glaciers, evapotranspiration, sublimation and runoff compensations under warming. The presented work improves the scientific basis for the modelling of mountain-water-fed river basins, which will aid the reduction of uncertainty in future water resources projections.

Zusammenfassung

Die Kopfeinzugsgebiete Hochasiens (HMA) versorgen, von den halbtrockenen Tiefländern Zentralasiens bis zu den dicht besiedelten landwirtschaftlichen Ebenen und Metropolen Süd- und Ostasiens, große Bevölkerungsteile mit Süßwasser. Beeinflusst durch die Wechselwirkungen mehrerer großskaliger Zirkulationssysteme unterscheiden sich die klimatischen Gegebenheiten zwischen den Teilregionen von HMA stark, etwa in der unterschiedlichen Saisonalität der Niederschlagsmengen. Der Klimawandel verändert die Randbedingungen, unter welchen diese Systeme arbeiten, mit Auswirkungen auf sämtliche Komponenten der Energie- und Wasserbilanzen: Schneeakkumulation und Gletschermassen nehmen ab, hydrologische Regime verschieben sich allmählich zu weniger Schneeschmelzabfluss und mehr Regenabfluss. Veränderungen im Energiehaushalt der Landoberfläche und in den Eigenschaften der Atmosphäre verändern die Produktivität der Vegetation sowie Verdunstungsmengen, mit weitgehend unbekannten Folgen für den Abfluss. Prognosen über die zukünftige Hochgebirgshydrologie sind gesellschaftlich von großer Bedeutung, jedoch derzeit begrenzt möglich; einerseits aufgrund unseres bisherigen Verständnisses der vielfältigen und verflochtenen physikalischen Prozesse, die in der Hochgebirgshydrologie eine Rolle spielen, andererseits durch den Mangel an geeigneten Modellierungswerkzeugen zur Darstellung ihrer räumlichen und zeitlichen Integration.

In dieser Dissertation verwenden wir ein Schnee-, Gletscher- und Ökohydrologisches Modell, Tethys-Chloris (T&C), welches dem Stand der Technik entspricht. In unserem Modellierungsansatz kombinieren wir dieses Modell mit glaziologischen, hydrologischen und meteorologischen In-situ-Beobachtungen, sowie Rasterdatenprodukten, um die Hydrologie von

Kopfeinzugsgebieten in HMA zu untersuchen. Zu diesem Zweck wurden in drei Einzugsgebieten in-situ Daten erhoben: in einem semi-ariden, kontinental beeinflussten Einzugsgebiet im Pamir-Gebirge (Kyzylsu) mit einem Winter/Frühjahrs-Akkumulationsregime der Kryosphäre; in einem monsunal-geprägten Einzugsgebiet im nepalesischen Himalaya (Langtang) mit einem Sommer-Akkumulationsregimeund einem monsunalen Einzugsgebiet auf dem südöstlichen tibetischen Plateau (24K) mit einem intensiven Frühjahr/Sommer-Akkumulationsregime. Wir haben bestehende Modellkomponenten weiterentwickelt und neue hinzugefügt: ein detailliertes Energiebilanzmodell für den Massenhaushalt von schuttbedeckten Gletschern, ein verbessertes Energiebilanzmodell der mehrschichtigen Schneedecke, eine verbesserte Niederschlagsaufteilung in Schnee und Regen und eine verbesserte Repräsentation von Albedo-Prozessen. Wir verwenden unser Modell zusammen mit den neu gesammelten In-situ-Daten, um drei wesentliche Forschungslücken zu schließen:

Zunächst konzentrieren wir uns auf die Energiebilanzprozesse, die während der Ablationsperiode auf der Oberfläche von sieben verschiedenen Gletschern im zentralen und östlichen Himalaya ablaufen. Wir führen punktuelle Simulationen an sieben automatischen Wetterstationen durch, die in der Ablationszone dieser Gletscher installiert sind. Mit Stationsdaten als Inputdaten, nutzen wir diese Simulationen, um die Auswirkungen monsunaler Wetterbedingungen auf die Energiebilanz der Oberfläche, die Eisablation, die Schneeakkumulation und -schmelze sowie die Verdunstung und Sublimation zu verstehen. Auf schuttbedeckten Gletschern werden die saisonalen Veränderungen im Strahlungshaushalt durch Veränderungen der turbulenten Wärmeströme ausgeglichen, was zu minimalen oder keinen Veränderungen der Eisablation unter Schutt zwischen dem Vormonsun- und der Hauptmonsunzeit führt. Im Gegensatz dazu wird die Schmelze von schuttfreien Gletschern direkt und in erster Linie durch Schwankungen im Strahlungshaushalt beeinflusst, was zu einem Netto-Anstieg der Schmelzenergie während des Monsuns führt. Über dünnem Schutt hingegen erhöhen die turbulenten Wärmeströme die Schmelzenergie während des Monsuns.

Zweitens wenden wir das Modell räumlich verteilt auf unsere drei Hauptuntersuchungsgebiete an und quantifizieren im derzeitigen Wasserhaushalt die Rolle der Gesamtverdunstung, einschließlich der Verdunstung über die gesamte Einzugsgebiets-Oberfläche, der Vegetationstranspiration sowie der Sublimation von Schnee und Eis. Als meteorologische Inputdaten für das Modell verwenden wir herunterskalierte Reanalysedaten, die mithilfe von Wetterstationsdaten korrigiert wurden. Die Simulationen zeigen, dass Verdunstungsflüsse 28% (Kyzylsu), 19% (Langtang) respektive 13% (24K) der Wasserverluste ausmachen. Sublimation und Evapotranspiration sind in der Wasserbilanz von Kyzylsu am wichtigsten, wobei Sublimation 15% der Schneefälle an die Atmosphäre zurückführt und Evapotranspiration 76% der Gesamtniederschlagsmenge ausmacht, während der größte Evapotranspirationsfluss vom feuchtesten Einzugsgebiet, 24K, mit 413 mm pro Jahr auftritt. Die Verdunstungsflüsse und der Eisschmelzabfluss unter wärmeren Bedingungen legen nahe, dass Kompensationen zwischen diesen beiden Komponenten der Abflussbildung stattfinden, was uns zu weiteren Experimenten unter veränderten meteorologischen Bedingungen motiviert.

Drittens untersuchen wir den Einfluss künftig erwarteter Klimaerwärmung auf die Energie- und Massenbilanzen, sowie die potenziellen hydrologischen Auswirkungen auf die drei Einzugsgebiete. Wir führen die Simulationen erneut unter experimentellen Bedingungen durch, die den Temperaturanstieg Mitte des 21. Jahrhunderts unter den *shared socio-economic pathways* SSP2-4.5 (W4.5) und SSP5-8.5 (W8.5) darstellen sollen. Die Erwärmung erhöht die jährliche Wassermenge, welche durch das Einzugsgebiet geleitet wird, aber Kompensationen zwischen Eisschmelze und Evapotranspiration führen je nach hydroklimatischem Kontext nur zu mäßigen oder gar keinen Veränderungen des Abflusses: Die Änderungen der Wasserspende reichen von -1% in 24K unter W4.5 bis +14% in Kyzylsu unter W8.5. Während die Abflußsensitivität in Kyzylsu höher ist, ist die Sensitivität der Gletschermassenbilanzen an den monsunalen Einzugsgebieten größer: Verschiebungen von festem zu flüssigem Niederschlag sind in 24K am stärksten ausgeprägt, wo bis zu 76% der zusätzlichen Eisschmelze (+130%, W8.5) auf Verluste der gletscher-schützenden Schneedecke in der Monsunzeit zurückgeführt werden können. Die Sublimation zeigt eine relativ unempfindliche und örtlich gemischte Reaktion, mit jahreszeitlich unterschiedlichen Zu- und Abnahmen, die von den lokalen Temperatur- und atmosphärischen Wasserdampf-Regimen bestimmt werden. Die Zunahme der Vegetations-Nettoproduktivität (NPP) zusammen mit dem deutlichen Anstieg der Evapotranspiration zeigt sich auch in einer Verlängerung der Vegetationsperiode, welche zwischen +9 Tagen in Langtang (+26% Evapotranspiration, W4,5) und +31 Tagen in 24K (+ 50% Evapotranspiration, W8,5) liegt.

In dieser Dissertation verwenden wir ein physikalisch basiertes Modell, um die hydrologische Funktionsweise von Wassereinzugsgebieten über das klimatische Spektrum Hochasiens hinweg zu untersuchen und deren Sensitivität gegenüber der Klimaerwärmung zu bewerten. Durch die Einbindung von In-situ-Beobachtungen und Fernerkundungsdaten ermöglicht unser Modellierungsansatz die Untersuchung vollständig verteilter Energie- und Massenflüsse in Bergeinzugsgebieten. Unseres Wissens ist dies das erste Mal, dass diese Methoden auf vergletscherte Einzugsgebiete in HMA angewendet werden, um die Prozesse der Abflussbildung zu entschlüsseln. Die vorliegende Arbeit klärt die Rolle der Kryosphäre und der Verdunstung in diesen Gebieten, insbesondere die Rollen von schuttbedeckten Gletschern, Evapotranspiration, Sublimation sowie jener von Abflusskompensationen unter Klimaerwärmung. Die vorgestellte Arbeit trägt zu einer Erneuerung der wissenschaftlichen Grundlagen für die Modellierung von großskaligen Flusseinzugsgebieten bei, sowie zu der Reduktion der Unsicherheiten von künftigen Wasserressourcenprognosen.

Acknowledgements

I would like to express my deep gratitude to Dr. Francesca Pellicciotti as my main supervisor for trusting me with this PhD project, for inviting to work within a fantastic group, and for facilitating and supporting my work all along the way. I admire Francesca’s enthusiasm for this field of research, her determination, stamina, drive and success in opening doors for new research. Her ideas and clear-sighted guidance made my PhD an exciting journey and were fundamental to its success and I am grateful for the many things I learned from her as a professional and as a person.

I would also like to thank my “Doktorvater” Dr. Peter Molnar for his openness to support my PhD both institutionally and scientifically. Every single interaction with him was inspiring and indeed increased the scientific quality of my work.

My gratitude goes to Dr. Evan Miles for helping me establish the foundations of my PhD, for being a fountain of knowledge and ideas with respect to our research field, and for taking me to incredible places. Similarly, I would like to express my gratitude to Dr. Catriona Fyffe and Dr. Michael McCarthy for their tireless and uncompromising engagement and support at every stage of my work, from almost the first and until the last day of my PhD. Their vast and detailed knowledge on every aspect of mountain hydrology, their scientific rigor and creativity contributed fundamentally to the scope, depth and quality of my work and helped shape the academic I am now. This work would not have been possible without the contributions Dr. Thomas Shaw, whom I would like to thank for his stamina and lightning-fast responses during countless iterations over meteorological downscaling and paper editing, for inspiring discussions and sharing with me his in-depth knowledge about boundary layer meteorology and climate. Similarly, the contributions of Dr. Pascal Buri in terms of model setup, analysis and paper writing were crucial for my PhD, as well as his enormous effort of setting up the invaluable pluviometer stations in Kyzylsu and 24K.

My heartfelt thanks goes to my PhD brothers, Dr. Marin Kneib and (soon-to-be Dr.) Achille Jouberton, for being full of energy and drive for research in all its shapes and forms, for everything I learned from you, and for being true companions on the manifold and colorful adventures in the often uncharted lands of process-based modelling and fieldwork. I would like to thank all of HIMAL and Mountain Cryosphere and Hydrosphere group members, including Vinisha Varghese, Vicente Velasco Melo, Shaoting Ren, Adria Fontrodona, Haruki Hagiwara and Sarah Bonomelli for a truly collaborative spirit and for the fun at the office, in the mountains, pubs and bouldering gyms. Thank you also for being my friends and for being there when the PhD challenges became intense.

For countless exchanges on model details, developments and adjustments, for his scientific inputs during many interactions on analysis and paper writing, which were as substantial as brilliant, my many thanks go to the main developer of T&C, Simone Fatichi.

I had the opportunity to supervise and co-supervise master students, including Pascal Wyss, Gioele Piatti and Yuwei Liu. I would like to thank them for their curiosity, diligence, and great effort. They helped me reflect on my own work, perspectives and capabilities and were invaluable experiences for my academic growth.

I also had the chance of being part of an art-science tandem research project in the framework of "PolArts 2022" for which funding was offered by SPI and ProHelvetia. Special thanks go to my tandem Céline Ducret for stimulating interactions, shared time in the mountains and many sparks of inspiration, as well as to everyone involved from the HIMAL group.

My sincere thanks go to my colleagues at the research unit for Mountain Hydrology and Mass, but especially to our unit leader Dr. Manfred Stähli for hosting my work at WSL, supporting our fieldwork both technically and logistically, for always ensuring superb working conditions and for creating an open and friendly environment within the unit. I extend my thanks to the technical support, namely Stefan Boss for helping with several issues around our instruments and installations, sometimes on a short notice. I always enjoyed coming to WSL and having discussions during seminars, over lunch, coffee breaks and Rundis.

I want to express my great appreciation to Dr. Walter Immerzeel, Dr. Jakob Steiner and ICIMOD for their tireless efforts in equipping and maintaining the observation network in Langtang and curating data, and for being generous with respect to data sharing. I also enjoyed a lot discussing science with them and spending time learning from them in the field. I thank Patrick Wagnon for his interest and enthusiastic help with my first PhD paper and for sharing his datasets. I also owe my gratitude to Abdulhamid Kayumov from the Center for the Research on Glaciers in Tajikistan, for enabling and facilitating our fieldwork in Tajikistan, along with Khusrav Kabutov, Ardamehr Halimov, Hofiz Navruzshoev, Farrukh Homidov and others from the Research Center. I extend my thanks to Wei Yang, Zhao Chuanxi and Zhen Zhang from the Institute for Tibetan Plateau Research for enabling and facilitating fieldwork in Tibet and for sharing their datasets. Many thanks to Liu Qiao for a first-hand experience of Hailuogou glacier and for sharing his datasets.

Over the course of the PhD, I have benefited from funding from the European Research Council (ERC) under the European Union’s Horizon 2020 research and innovation program Grant Agreements No. 772751 (RAVEN, Rapid mass losses of debris-covered glaciers in High Mountain Asia). Further funding was provided by JSPS-SNSF (Japan Society for the Promotion of Science and Swiss National Science Foundation) Bilateral Programmes project (HOPE, High-elevation precipitation in High Mountain Asia; Grant 183633). Fieldwork support for Tajikistan was received from the Swiss Polar Institute Flagship Programme PAMIR, SPI-FLAG-2021-001. The project also received funding from the ESA and NRSCC Dragon 5 cooperation project “Cryosphere-hydrosphere interactions of the Asian water towers: using remote sensing to drive hyper-resolution ecohydrological modelling” (grant no. 59199).

I sincerely thank my PhD defence committee, including Dr. John Pomeroy, Dr. Ben Brock, Dr. Heini Wernli, Dr. Walter Immerzeel for their in-depth engagement with my research, for their constructive feedback, and for making that day an exciting and memorable experience.

I am indebted to Catriona Fyffe, Michael McCarthy and Inés Dussaillant for proofreading my thesis while helping me keep my composure during that last stretch of my PhD.

For their uncompromising support over many years of education, their enthusiasm about my work, travels and adventures, also for leaving room for failure, for being wonderful parents, I deeply thank my parents Maria and Gerhard.

For carrying me through rough tides with her love, for her patience, clear-sightedness, intelligence and humour, no words can express my gratitude to Luisa.

Table of Contents

1. Introduction

1.1. Motivation and problem statement

Importance of mountain water resources

Mountain watersheds collect, retain, transport and release water that determines downstream ecology, landforms, human settling, livelihoods and economic activity. Mountains provide proportionally around twice as much freshwater as the land surface area they occupy in mountain-water-fed river basins (Viviroli et al., 2003). Acting as topographic barriers, orographic lifting forces atmospheric moisture to condense and precipitate along mountain slopes. In the cold conditions prevalent in high mountain areas, this precipitation accumulates as snow packs and forms and nourishes glaciers, which act as storages and buffers for runoff production. The mountain cryosphere releases water during warm and dry periods, in this way attenuating the seasonality in discharge (Pritchard, 2019; Van Tiel et al., 2021). Mountain environments, including their geology and biogeochemistry, as well as the ecosystems and human societies they are home to, co-evolve with, and adapt to the interplay of climate and cryosphere. These places are extreme environments for the biosphere and are inhabited by generalist species adapted to cold and periodical dryness (Bosson et al., 2023). Typically settling where freshwater is available, which is nearby rivers and streams, around 40% of the global lowland population lives in mountain-water-fed river basins (Viviroli et al., 2020).

Mountain water resources under climate change

The mountain cryosphere is one of the most important and prominent indicators of climate change. Snow packs, ice volumes and permafrost storages have been observed to be in decline and are projected to decline further at accelerating rates with rising mean global temperatures (Zemp et al., 2019, Hock et al., 2019; Notarnicola, 2020; Hugonnet et al., 2021; Rounce et al., 2023). While the acceleration of snow and glacier mass losses is driven by demographically and economically growing societies emitting greenhouse gases at the global scale, the same growth increases downstream pressures on water resources at the regional scale (Immerzeel et al., 2020, Viviroli et al., 2020). At the same time, the importance of the global mountain water resources is growing with demographic evolution, with 25% of the global lowland population projected to be critically dependent on mountain water by the mid of the 21st century (Viviroli et al., 2020). Changes in the climatic drivers of mountain water storage and release patterns, initiate a cascade of effects from the headwaters to the deltas. The resulting deglaciation of mountain ranges has local to global impacts (Huss et al., 2017) that range from the occurrence and severity of natural hazards (Kirschbaum et al., 2020), freshwater supply and agriculture (Immerzeel et al., 2020, Viviroli et al., 2020), ecosystems and biodiversity (Bosson et al., 2023; Cauvy-Fraunié and Dangles, 2019), tourism (Steiger et al, 2022), and the rise of global ocean levels (Zemp et al., 2019, Edwards et al., 2021).

Climate and hydrology of High Mountain Asia

High Mountain Asia (HMA) is a vast mountain range extending from approximately 40°N and 70°E, to around 25°N and 100°E, featuring 14 summits higher than 8000 m a.s.l. and holding the largest snow and ice mass outside of the polar regions (Farinotti et al., 2019) and some of the most vulnerable water towers globally (Immerzeel et al., 2020). Waters originating from HMA supply major Asian river basins such as the Amu Darya, Indus, Ganges-Brahmaputra and Yangtze, and Yellow river, supplying freshwater to large populations and agricultural economies in Central Asia, China, Pakistan and India with mega-cities such as Karachi, Lahore, Delhi, Dhaka, and Beijing.

Two dominant climatic regimes, the South Asian monsoon system and the westerlies, interact in High Mountain Asia (Figure 4). The South Asian monsoon system, in turn, comprises the interacting East Asian and Indian summer monsoons (Bookhagen and Burbank, 2010). Acting as a topographic barrier, the Himalaya blocks and retains warm, moist air over India, intensifying the strength of monsoonal rainfall over the lowlands and causing orographic precipitation along the mountain slopes, while the Tibetan Plateau north of the Himalaya receives considerably less precipitation (Boos and Kuang, 2010).

The moist air masses carried far into the mountain range from the south and east by the monsoon create highly dynamic meteorological conditions with extensive cloud cover and high precipitation rates during a period of the year, when air temperatures also reach their annual maxima. These conditions create a complex pattern of accumulation and ablation of snowpacks and glaciers, cause rainfall to fill groundwater storages, speed up runoff generation and intensify discharge rates multiple times compared to the low-flow periods outside of the monsoon. During the winter months, the westerlies bring cold air masses and moisture from as far as the Mediterranean, where they interact with the mountainous terrain of the Pamir, Hindu Kush and Karakoram ranges, where the windward slopes experience intense precipitation due to orographic effects. These 'Western Disturbances' reach far across the Tibetan Plateau (Mölg et al., 2014) and Western Himalaya where they interact with the South Asian monsoon system (Bookhagen and Burbank 2010; Yao et al., 2012). The interactions of these circulation patterns cause approximately six-

fold east-west and ten-fold south-north gradients in precipitation across the South Asian lowlands and Himalaya, with considerable implications for the hydrological budget and the mass balance seasonality in each sub-region along these hydro-climatic gradients (Bookhagen and Burbank, 2006, 2010; Maussion et al., 2014; Huang et al., 2022).
HMA glaciers are a crucial and drought-resilient, albeit finite, source of water for large populations (Pritchard, 2019). A large proportion of glaciers in HMA carry supraglacial debris (Kraajenbrink et al., 2017), which modifies glacier melt rates in spatially heterogeneous and non-linear ways, thereby delaying and attenuating peak melt rates compared to debris-free glaciers (Fyffe et al., 2014). How large the snow and ice melt components in runoff are, depends on the hydro-geographic context of each basin (Kaser et al., 2010; Lutz et al., 2014, Khanal et al., 2021). Population density, irrigated agriculture and economic activity additionally determine the overall importance and vulnerability of these water towers (Viviroli et al., 2007; Lutz et al., 2016; Viriroli et al., 2020). As a result, some of the HMA-adjacent river basins, such as the Indus and Amu Darya, are among the most vulnerable high mountain basins in the world (Immerzeel et al., 2020).

Climate change impacts on water resources in High Mountain Asia

Climate change has substantially impacted the hydrology of High Mountain Asia, although its effects have varied across the region (Khanal et al., 2021, Nie et al., 2021, Yao et. al., 2022). Glacier mass balances have been observed to be near-stable or even slightly positive in the eastern and north-eastern parts of the region, namely the Pamir, Kunlun, Hindu Kush and Karakoram regions during the last decades (Hewitt et al., 2005; Gardelle et al., 2013; Shean et al., 2020). Particularly, the Karakoram region has shown balance and even positive glacier mass balances between the 2000s and 2020s (Farinotti et al., 2019). Recent evidence suggests, however, that glaciers might have entered a declining trajectory during the recent years, marking the potential end of the so-called ‘Karakoram anomaly’ (Hugonnet et al., 2021). Other HMA regions have experienced consistent mass losses over the last decades, increasingly negative towards the south-eastern portions of the region with the most negative mass balances on the Southeastern Tibetan Plateau (Shean et al., 2020, Miles et al., 2021, Yao et al., 2022).
The imbalance state of glaciers has direct impacts on hydrology downstream. In HMA glaciers have been studied through the lens of the 'peak water' concept (Huss and Hock, 2018), which considers the meltwater contribution from glaciers to river runoff and its past and future trajectories. When glaciers have consistently negative mass balances, they will initially release more ‘imbalance’ meltwater (or in other words, a ‘deglaciation discharge dividend’, Collins, 2008), until they reach a point (termed ‘peak water’) at which the remaining volume has decreased to

the degree that the glacial water yield will not increase further, but decrease again (Immerzeel et al., 2013). Many subregions are estimated to still be on the 'rising limb' in the total water yield, but will reach a peak in glacier-melt contribution during the 21st century (Huss and Hock, 2018) under a steady-state trajectory of most other processes of runoff generation. Future climate projections of the Coupled Model Intercomparison Project Phase 6 (CMIP6) suggest that total precipitation will increase over HMA due to intensified monsoons and westerlies in both summer and winter (Lalande et al, 2021). Winter precipitation increases in the Pamir, Karakoram and Hindu Kush regions indicate intensified westerlies, while summer increases over the Himalayas and Tibetan Plateau correspond to heightened monsoon-related precipitation. Across the entire HMA domain, the increase in precipitation is slightly higher in summer, and depending on the scenario, ranges from 9.1% to 25.6%, compared to 6.4% to 22.8% in winter, between the 1995-2014 and 2081-2100 periods (Lalande et al, 2021). Although the magnitudes of changes vary under different scenarios, they exhibit similar patterns (Lalande et al, 2021). However, there are notable uncertainties regarding these trends, largely lacking statistical significance (Lee et al., 2021). A few studies using hydrological models have gone beyond quantifying only glacier mass balance and melt and its past and future trajectories, by applying more sophisticated hydrological models. They established that, at the river basin-scale, such as the Ganges and Brahmaputra basins, the glacier melt component of river discharge is often only a few percent annually, while in the seasonally dry, western parts of the region, such as in the Indus and Amu-Darya river basins, it can be much higher (Lutz et. al, 2014, 2016; Immerzeel et al., 2013; Pohl et al., 2017; Nie et al., 2021). Khanal et al. (2021) found that annual water yield is not expected to be critically affected in many HMA catchments during the current century, but the different runoff contributions and therefore seasonality will change. As an example, future peaks in the glacial water yield are clearly distinguishable for Langtang headwater catchment in Nepal, but the catchment water yield might continue to rise for many decades and beyond the projected horizon, as a result of increasing precipitation, while runoff becomes less snowmelt- and more rainfall-dominated (Immerzeel et al., 2012). These examples show that hydrological studies, by carefully assessing individual water balance components under the inclusion of local observations, can provide a more nuanced picture of past and future hydrological regimes.

Problem statement

To robustly assess water yield and runoff seasonality in a river catchment, a thorough estimation of all the elements of the water balance at the appropriate scale is crucial. The simplicity of a generalised water balance equation (e.g. Oke, 2002):

$$P = Q + E + \Delta S \quad (1)$$

obscures much of the complexity encountered in real-world hydrologic systems. For example, precipitation (P) may be partitioned into solid and liquid shares; evaporative fluxes (E) may comprise not only evaporation, condensation and transpiration, but also sublimation and deposition; and storage changes (ΔS), may include the dynamics of groundwater bodies, surface water, surface interception, glaciers and snow packs. This is especially true across High Mountain Asia, where (i) the average annual precipitation inputs and relative melt water contributions range by least one order of magnitude or more across the region (Maussion et al., 2014; Lutz et al., 2014); (ii) glaciers and snow packs during the monsoon simultaneously accumulate and ablate across small spatial and temporal scales (Fujita and Ageta, 2000); (iii) highly dynamic meteorological conditions and gravitational mass redistribution cause complex distribution of snow cover and snow mass within small horizontal distances (Girona-Mata et al., 2019); (iv) debris layers controlling glacier melt cover around one third of glacier ablation zones (Kraajenbrink et al., 2017, McCarthy et al., 2022), complicating the observation and modelling of glacier mass balances (Pellicciotti et al., 2015), and (v) extreme spatial gradients of meteorological variables control the balance of energy and mass fluxes, further complicated by feedback loops causing additional warming at high elevations in some regions (Pepin et al., 2022; You et al., 2020).

These conditions are outside of the range of what most modelling frameworks have been designed for and calibrated to (Pomeroy et al., 2022). Widely used conceptual hydrological models today include at least a simplified module for glaciers, while hillslope and lowland hydrology remain their main strength. Glacio-hydrological models on the other hand typically have more complex implementations of glacier mass balance and glacier dynamics, while employing only simplified representations of other important land-surface and subsurface processes (van Tiel et al., 2020). Consequently, spatially distributed estimates of the magnitude and seasonality of certain terms of the water budget, such as evapotranspiration and snowpack sublimation remain unquantified in high elevation catchments in HMA. In this region, meteorological, glaciological and hydrological observations are scarce, thus more generally employable models, which do not require extensive calibration, are needed. Few models to-date provide consistently high levels of physical detail across the relevant land surface type, which is here deemed a prerequisite for robust hydrological simulations across space and time. For these reasons, our understanding of the water, carbon and energy budgets of headwater catchments in High Mountain Asia is fundamentally limited.

This thesis addresses this problem and improves our understanding of the hydrology of headwater catchments in HMA, by applying a model which allows for explicit, dynamic, spatially representative and robust calculations of water, carbon and energy fluxes. Specifically, it: (i) Presents new data to inform all stages of the modelling process with local observations; (ii) Implements new model components to improve the representation of glacierized high-elevation catchments; (iii) Analyses the mass and energy balances of glaciers in monsoonal climates, including the detailed modelling of debris-covered glaciers; (iv) quantifies all-surface evaporation, plant transpiration and sublimation including their role in the water balance and runoff generation; (v) Provides a better understanding about the role of the monsoon in HMA headwater hydrology and (vi) assesses the sensitivity of flux partitioning and runoff generation to climate warming.

1.2. Background and State of the Art

Observations indicate that headwater regions generate more runoff than lowland regions, proportional to the surface area they occupy, and considerably modify runoff seasonality due to the storage and buffering capacity of snow and ice (Viviroli et al., 2003). There is a need, therefore, in the hydrological modelling of mountain regions, to move beyond overly simplified representations of the mountain cryosphere and headwater hydrology in general. For High Mountain Asia, erroneous projections of glacier loss reported in IPCC's AR4 report in 2009 (Cogley et al., 2009), also known as "Himalaya Gate", highlighted considerable knowledge gaps around the state and future of the region's cryosphere (Bolch et al., 2012) resulting in the intensification of research efforts in the region and fueling the development of observation and modelling techniques.

1.2.1. Observations

Over the last decade, high-altitude weather stations and observational networks have been installed, re-established or expanded in the HMA region, e.g. in the Tien Shan, Pamir and Pamir Alai, the Himachal Pradesh in India, the Langtang Valley, the Everest region and the Hidden Valley in Nepal, and the Tibetan Plateau (Mölg et al., 2012; Wagnon et al., 2013; Shea et al, 2015; Azam et al., 2014; Yang et al., 2017; Hoelzle et al., 2017, Matthews et al., 2020; Steiner et al., 2021a). While the setup and maintenance of in-situ observations in high altitude environments involves considerable investments of time, financial and logistical resources, these datasets deliver invaluable, precise and local 'ground-truth' information on meteorological conditions, spatial gradients and energy balances, and are indispensable for developing, forcing and evaluating snow and glacier energy- and mass balance models (e.g. Mölg et al., 2012; Collier et al., 2014; Rounce et al., 2015; Steiner et al, 2021b; Stigter et al., 2021; Mandal et al., 2022; Miles et al., 2022), and glacio-hydrological models (Ragettli et al., 2015; Jouberton et al., 2022; Buri et al., 2023).

New remote sensing products, and especially high-resolution, multispectral imagery and advances in automatic photogrammetric processing have made large-scale studies possible to estimate snow cover dynamics (e.g. Tang et al., 2022), mapping of glacier and supraglacial debris cover outlines (Pfeffer et al., 2014; Scherler et al., 2018; Sakai et al. 2019; Herreid and Pellicciotti, 2020), ice volumes (Farinotti et al., 2019), surface lowering and geodetic mass balances of individual glaciers (Brun et al., 2017, Dussaillant et al., 2019, Shean et al., 2020, Hugonnet et al., 2021), glacier velocity and thickness (Dehecq et al., 2019, Millan et al., 2020), and in their combination, altitudinally resolved surface mass balances estimates (Miles et al., 2021), debris thicknesses and debris-supply-rates (McCarthy et al., 2022), as well as the mapping of vegetation and soil distribution and vegetation indices (Myneni et al., 2015; Myneni and Knyazkhin, 2018; Buchhorn et al., 2020; Poggio et al., 2021). These datasets have allowed for an unprecedented characterization of the distribution and state of the mountain cryosphere and land-cover from local to global scales, and delivered valuable input, calibration and evaluation data for hydrological and land surface modelling. However, even in times of remote sensing, the lack of in-situ glaciological, meteorological and hydrological datasets in regions like Central Asia continues to introduce large uncertainties regarding the past and future trajectories of hydrological changes, precisely where such information is most crucially needed (Barandun and Pohl, 2022). Motivated by the need to extend existing networks of high-elevation catchments and establish new ones in data-starved regions, systematic meteorological, glaciological and hydrological monitoring is integral in this thesis. The gathered data was used for model development, setup, forcing and testing (Figure 3).

1.2.2. Glacio-hydrological modelling

The goal of glacio-hydrological modelling is to gain insights into the hydrology of glacierized catchments and to predict future changes, by including all processes relevant in glacierized environments, while navigating the challenges posed by the complexity, data scarcity, and non-stationarity of these systems (van Tiel et al., 2020).

Today, a number of glacio-hydrological modelling approaches exist along the range between conceptual to process-based. More nuanced distinctions can be made with respect to the spatial discretization (semi-distributed vs. gridded), the predominant focus of the model (cryosphere vs. catchment hydrology), and the type of melt model applied (temperature-index vs. energy balance) (van Tiel et al., 2020). Model choices typically follow the study type and research questions asked, even though many models are designed for an application to specific spatial scales and grid resolutions. For water resources questions, e.g. on the topic of downstream water supply and its future evolution, and sub-basin to river-basin scale research, conceptual models are often applied, as for example in a recent study which estimated the future water yield of the upper Indus basin using SPHY (Lutz et al., 2016). In this study, the distributed model is applied at daily temporal and 1 km spatial resolution, and forced with temperature and precipitation data. It employs temperature index (TI) melt model with day-degree-factors (DDFs) for bare ice, debris-covered ice and snow separately, parameterizations for snow sublimation, evapotranspiration and vegetation dynamics, and a leaky-bucket-type representation of water routing including dynamic groundwater storage.

Models of intermediate complexity, on the other hand, are being applied at higher spatial resolutions of 100 to 250 m, such as TOPKAPI-ETH, but usually on smaller spatial scales (Pellicciotti et al., 2012; Ragettli et al., 2013, 2015, 2016; Ayala et al., 2019; Burger et al., 2019; Jouberton et al., 2022). TOPKAPI-ETH is forced with cloudiness, in addition to temperature and precipitation data and employs an enhanced temperature index melt model for glaciers and snow (Pellicciotti et al., 2005), features ice melt under distributed debris cover, a kinematic-wave implementation for routing, represents soil drainage and channel- and overland flow, and calculates actual evapotranspiration, based on the Priestly-Taylor equation, calibration of crop factors and soil moisture availability (Ragettli et al., 2015). These intermediate complexity models can help understanding the system behaviour, having relatively comprehensive treatment of snow, glacier and catchment processes. However, they still require extensive calibration of parameter sets which control semi-empirical functions representing lumped processes. Sophisticated calibration strategies have been developed to constrain parameters based on observations including snow cover, glacier mass balance and runoff, with the aim to reduce model error and equifinality issues (van Tiel et al., 2020). These strategies include multi-signal, multi-data and stepwise calibration, often combined with multi-objective calibration functions (e.g. Düthmann et al., 2015; Ragettli and Pellicciotti, 2012; Immerzeel et al., 2012; Ji et al., 2019; Meyer et al., 2019).

For investigative hydrological modelling, this thesis promotes the idea of reducing the need for extensive calibration and to replace parameterizations, wherever possible, with explicit and physically-based representations of processes. A likely reduction of error-compensation and an increase in transparency, realism and robustness of model outputs are the potential gains of such an approach.

1.2.3. Process- and energy-balance-based modelling

For research aiming at new process understanding about natural systems across spatial and temporal scales while understanding their internal dynamics, a certain level of complexity in model representation is needed. Newer-generation process-based (or physically-based) hydrological models employ coupled mass and energy balance schemes, to explicitly simulate the physical processes of interest, including their internal states and fluxes (Fatichi et al., 2016). If doing so consistently, the process-representation is sometimes referred to as 'mechanistic'. They rely on minimal parameter calibration and instead on literature values or measured data for parameter choices (Mimeau et al., 2019; Aubry-Wake et al., 2022; Buri et al., 2023). Process-based, hydrological models are typically applied at very high temporal (e.g. hourly) and spatial resolution (e.g. 100m). For estimating all terms of the energy balance, for precipitation and vapor flux partitioning, the models require additional variables to temperature and precipitation as model input data, such as distributed incoming short- and longwave radiation, relative humidity, wind speed and air pressure.

Many state variables and fluxes from this class of models can be directly evaluated with in-situ observations or remote sensing data sets, including surface temperature, soil moisture, evapotranspiration, vegetation state and density, snow cover and glacier mass balances, increasing the number of ways in which the model performance can be assessed, compared to the lower-complexity models discussed above. Regarded as potentially robust across a wide range of conditions, such models can serve as 'virtual laboratories' for hypothesis testing, model falsification and hydrological diagnosis, around topics such as catchment-internal hydrological dynamics, the coupled partitioning of energy and mass fluxes, biogeochemical processes and solute transport, under non-stationary climate and land-use change (Fatichi et al., 2016; Pomeroy et al., 2022).

One example of such a model is the cold-regions hydrological model (CRHM, Pomeroy et al., 2022) which is a modular platform for simulating hydrological processes pertaining to snow, vegetation, soil, subsurface flow, wetlands and permafrost in a semi-distributed and physics-based way. Forcing variables are typically given distributed in space based on elevation gradients. The model is capable of simulating complex terrain wind flow, blowing snow and blowing snow sublimation, canopy intercepted snowpack sublimation and the gravitational redistribution of snow. With a recently added energy-balance based glacier and firn module (Pradhananga et al.,

2022) and an enhanced-temperature-index method to model ice melt under debris (Carenzo et al., 2016), the model was applied to study the streamflow generation and streamflow variability in a glacierized research catchment in the Canadian Rockies, which showed remarkable evaluation performance for snow depth and runoff, without parameter-calibration (Aubry-Wake et al., 2022). Applied to the future and under a range of land-scape evolution scenarios, Aubry-Wake and Pomeroy (2023) forced the model with a combination of pseudo-global warming scenarios and WRF modelling. Compensatory effects between precipitation and ice melt along with seasonality shifts in the hydrograph due to shifted snowmelt timing and reductions in blowing snow transport and sublimation were observed for the future scenario. Streamflow was found to be most sensitive overall to temperature and precipitation as opposed to changes in ice cover and surface storage capacity, while increases in evapotranspiration due to environmentally limited vegetation growth were found only to be small (Aubry-Wake and Pomeroy, 2023).

Another such physically based model, the distributed Hydrological Soil Vegetation Model - Glacier Dynamics Model (DHSVM-GDM, Naz et al., 2014). It is forced with spatially distributed meteorology at an hourly time step including air temperature, precipitation, relative humidity, wind speed, longwave radiation, terrain-adjusted shortwave radiation, and simulates soil moisture, energy-balance based evaporative fluxes including snowpack sublimation, glacier mass balance, glacier dynamics and subglacial water storage (Mimeau et al., 2019). Sub-debris ice melt is simulated using a reduction factor. The snowpack is simulated with a two-layer energy-balance formulation and includes parameterizations of albedo decay and gravitational redistribution of snow. The model was applied to the highly glacierized Pheriche research catchment (Dudh Koshi) in Nepal (Mimeau et al., 2019). DHSVM-GDM was tested with different implementations of the snow and glacier components and in the best-performing setup, showed very good agreement with observed runoff, moderate agreement with snow cover and low agreement with glacier mass balance. Sublimation in this highly snow- and glacier dominated catchment was higher than evapotranspiration, but considerably lower in magnitude than the snowmelt and glacier melt contributions to outflow.

The fully-distributed ecohydrological Tethys-Chloris model (Fatichi et al., 2012a,b; 2021; Manoli et al., 2018; Botter et al., 2021; Fugger et al., 2022; Paschalis et al., 2022; 2024) resolves the coupled dynamics of energy, mass and vegetation physiology by using energy-balance and resistance analogy schemes for simulating the transfer of energy and water and carbon between the subsurface, land surface, vegetation and the atmosphere. The model is typically applied at hourly temporal resolution and hill-slope relevant spatial resolution. All forcing variables are provided either extrapolated from real or virtual station data using spatial gradients, which can be measured in the field, derived from gridded data products or taken from the literature, or as distributed input grids, such as downscaled reanalysis data (Chapter 3). Slope, aspect, and shadow effects are considered for adjusting incoming shortwave radiation to the local terrain and the shares of direct and diffuse shortwave radiation, as well as photosynthetically active radiation are computed as inputs to the hydrological and vegetation modules. The topography is further being considered for adjusting horizontal and vertical wind speeds to the terrain including the effects of wind shear, channelling, speed up or slow-down of air masses (Burlando et al., 2007). Topography information is also used for the gravitational redistribution of snow (avalanching) using SnowSlide (Bernhardt & Schultz, 2010). The dynamics of snow and ice packs, including accumulation and melt processes, ice melting under debris-cover, are simulated using numerical solutions of heat transfer functions to track changes in snow, debris, frozen soils and ice layers. The model simulates snow albedo decay, snowpack aging and snowpack sublimation including sublimation from the canopy-intercepted snow. Plant physiological processes are computed through detailed schemes of photosynthesis, respiration, stomatal resistances, and phenology via carbon cycling, including the simulation of different phenological stages, leaf area and reflectance properties. Buri et al. (2023) used Tethys-Chloris to model the upper Langtang basin in Nepal using, forced with automatic weather station data. In this pilot-study, without automatic tuning of model parameters, but manual adjustments of precipitation gradients, the model showed good performance for Leaf Area Index, glacier albedo, snow cover distribution, surface temperature, streamflow and glacier mass balance. Analysing one hydrological year, total evapotranspiration amounted to 20% of the precipitation input, whereby sublimation was found to be the dominant evaporative flux, amounting to the equivalent of 75% of the ice melt water generated in the catchment.

Tethys-Chloris (Figure 2) is the model that is also used for the bulk of this thesis. Further details about the model are given in Chapters 3-5. Model developments in the framework include the addition of supraglacial debris and the energy-balance-based computation of ice melt under debris, an updated precipitation partitioning scheme, an updated albedo scheme and the inclusion of new multi-layer snowpack model. These updates are summarised in Section 2.3.

1.2.4. Meteorological forcing

Meteorological observations suitable for forcing hydrological models are sparse in HMA and other remote mountain ranges (Thornton et al., 2021; Pritchard, 2021, Barandun & Pohl, 2022). In addition, spatial gradients in variables such as temperature, precipitation or wind speed vary greatly over short horizontal distances. A basic and common approach to describe the spatial distribution of these variables, albeit limited by the number and representativeness of available datasets, is the derivation of vertical and horizontal distributions based on station data, sometimes resolved seasonally, or in addition diurnally (Immerzeel et al., 2014; Ragettli et al., 2015; Buri et al. 2023). Since the linear assumptions often result in an over- or underestimation of snow accumulation and overly negative or positive glacier mass balances, other functional relationships (Ayala et al., 2016) or manual modifications of lapse rates at different elevations are sometimes used (Buri et al., 2023). In the absence of sufficient station data, spatial gradients have been derived from reanalysis data (Khadka et al., 2014), or calibrated against remotely sensed snow cover (Ragettli et al., 2015), while the main forcing dataset came from automatic weather stations located lower in the catchment. Observation-based, gridded precipitation datasets have been created (Yatagai et al., 2012) and used for glacio-hydrological modelling, after correcting for high-altitude precipitation biases (Lutz et al., 2016). More recent modelling studies in mountain areas have relied on model outputs from Regional Climate Models (RCMs) or General Circulation Models (GCMs) for past and future modelling, sometimes in combination with globally available re-analysis products such as ERA5 (Fiddes et al., 2022). ERA5 has also been used as a primary forcing for glacio-hydrological modelling (e.g. Azam et al., 2020) or to gap-fill, extend or complement station data (Jouberton et al., 2022; Buri et al., 2023). However, these datasets come at resolutions which do not resolve hillslope-scale meteorological variability, topographic effects on wind fields, precipitation and insolation, and are therefore inadequate to directly drive models of land surface processes (Fiddes et al., 2012).

Different methods have been developed to bridge this gap between the coarse resolution climate model outputs (10s of kilometres) and the hydrology-relevant hillslope-scale resolution (10s to 100s of metres), and can be categorised into physically based, dynamical methods and empirical-statistical methods. The value of high-resolution dynamical downscaling with models such as the Weather Research and Forecast Model (WRF) has been shown to improve air temperature estimates and local precipitation patterns (Bonekamp et al., 2018; Wang et al., 2021) and the downscaled data has been used to drive glacio-hydrological models (Collier et al., 2015; Engelhardt et al., 2017; Bonekamp et al., 2019). However, running such models at high resolution is computationally expensive and still affected by the biases inherent to the boundary forcing. Empirical-statistical downscaling methods are computationally more efficient, but usually require local observations. They typically combine some sort of interpolation algorithm with parameterizations relating small-scale heterogeneity, e.g. due to topographic variability, to the large-scale fields (Machguth et al., 2009; Fiddes et al., 2016).

Bias-correction methods involving local observations can be integrated into both dynamical or statistical-empirical downscaling schemes or applied in a subsequent step. Methods applied in the past included simple delta-change adjustment, multiple linear regression, stochastic methods or empirical quantile mapping (EQM) (Themessl et al., 2011). EQM is the preferable option when observed data does not conform to a common theoretical distribution, which is the case with time series subject to seasonality or a high degree of randomness, such as precipitation (Themessl et al., 2011).

For this thesis, an empirical-statistical method based on Machguth et al. (2009) was chosen to spatially downscale ERA5-Land and EQM was used to bias-correct the downscaled product using automatic weather station data from the study catchments. The resulting meteorological forcing product was then used for distributed catchment scale modelling.

1.3. Research Gaps and Research Questions

1.3.1. Research Gap 1

Making robust assessments of catchment hydrology in monsoon-dominated, highly glacierized regions, is a challenging task. The monsoon season is characterised by highly dynamic meteorological conditions, such as heavy cloud cover and precipitation. The seasons of glacier accumulation and melt in monsoonal regions coincide due to the contemporaneity of warm conditions and snowfalls at high elevation (Fujita and Ageta, 2000). Due to the harsh conditions on the ground during this period, data collection in the field usually takes place before and after the monsoon, while during the monsoon, researchers rely on automatic stations and data loggers. Since many typical glaciological and hydrological measurements, such as mass balance readings and discharge measurements require the presence of staff in the field, data often captures the before- and after-state, but not the dynamics during the core monsoon season. Similarly, the collection of remotely sensed optical data (e.g. ASTER, SPOT, Pleiades) is strongly impaired by cloud cover and useful imagery of the land surface state, such as imagery for generating repeat-DEMs or snow cover maps, is very sparse during this time of the year (e.g. Brun et al., 2017, Gardelle et al., 2013). As a result, melt-factors of temperature-index schemes for calculating snow-, ice-, and ice melt under debris, are sometimes transferred from other places, or recalibrated to annual or seasonal mass-balances and therefore static in time (Ayala et al., 2019; Burger et al., 2019; Ragettli et al., 2015). This is likely to mis-represent the dynamics of the meteorological controls on melting in the seasonal transition by integrating both wet and dry periods, ultimately resulting in erroneous estimates of melt rates and timings. Therefore, the melt regimes of glaciers, and especially debris-covered glaciers under monsoonal conditions, remain relatively unknown in the field of HMA hydrology. Energy-balance models are useful tools to understand the temporal dynamics of these mass fluxes including their controls (e.g. Brock et al., 2000a, 2010; Pellicciotti et al., 2008; Reid and Brock, 2010; Fyffe et al., 2021), as well as melt-water generation and sublimation at the glacier scale (Fyffe et al., 2014, Ayala et al., 2017). However, these models have typically been developed in well-accessible and well-instrumented places, and little is known about monsoonal controls on glacier energy and mass fluxes across the Himalayan arc. *Understanding the energy- and mass balances of Himalayan glaciers during the monsoon, but also their runoff contributing role* therefore remains a key research gap.

To address this research gap, we will use T&C to simulate the response of glaciers and catchments to monsoonal conditions. We will leverage the existing formulations of energy and mass fluxes of T&C, and extend them to debris-covered glaciers. First we will apply the model forced with the hourly data from seven on-glacier automatic weather stations, to study in detail the energy and mass exchanges of different types of glaciers under monsoon conditions, including clean-ice and debris-covered glaciers, located in different parts of the Central and Eastern Himalaya. We will then extend this modelling to the catchment scale at two out of the seven sites, to investigate the monsoon and year-round dynamics of the catchments' cryospheres in their water balances, and contrast the findings with those gained by modelling a third, westerly-dominated (non-monsoonal) catchment in Central Asia.

1.3.2. Research Gap 2

The variations of catchment runoff over a certain period of time, such as a hydrological year (hydrograph), can be explained by conceptualising the hydrologic system in terms of the major components of the alpine water balance, namely rainfall, evapotranspiration, snow-, glacier- and groundwater storages.

Large uncertainties in high-elevation snow accumulation have often been met by optimising precipitation correction factors in order to agree with remotely sensed snow cover or glacier mass balance observations (e.g. Finger et al., 2015; Ragettli et al., 2015; Jouberton et al., 2022), or by deriving snowmelt from remotely sensed snow cover dynamics (Singh and Bengtsson, 2005), without considering all the processes involved in accumulating and depleting a snowpack. Those include the partitioning of precipitation phase, typically done with single and static temperature thresholds (e.g. Immerzeel et al., 2012; Finger et al., 2015; Ragettli et al., 2015; Lutz et al., 2016;

Khanal et al., 2021; Jouberton et al., 2022), omitting the possibility of sleet events, and neglecting the impact of atmospheric humidity on the phase partitioning (Ding et al., 2014). Snow melt is calculated by linearly relating melt from a bulk snow storage to temperature using temperature index formulations (Hock, 2003) or additionally including shortwave radiation with a separate parameter (Pellicciotti et al., 2005).

The calculation of sublimation has usually been neglected in glacio-hydrological models, although it is known to remove considerable snow mass via the atmosphere from a limited number of observational and modelling studies in High Mountain Asia (Wagnon et al., 2003, 2013; Stigter et al., 2018; Buri et al., 2023).

Due to the cryospheric focus in glacio-hydrological research, dedicated observations targeting ET are lacking in high-elevation catchments. Actual ET has been estimated using potential ET calculated with standard equations and limited by soil moisture, with parameters calibrated or taken from the literature (e.g. Ragettli et al., 2015; Khanal et al., 2021), but over static land cover and vegetation without taking into account plant physiology. Furthermore, ET has often been limited to vegetated land, neglecting the role of evaporation from other surfaces, such as ET from supraglacial debris (Steiner et al., 2018). The simplified representation of evaporative fluxes is likely to result in error compensation during calibration, resulting e.g., in compensation of the mass lost from a catchment by evaporation by reduced snow- or glacier-melting. As a result of methodological and observational limitations*, the amount of ET and sublimation, the role of these evaporative fluxes in the water balance along with their limiting factors in glacierized headwaters are to date largely unknown*. It is necessary to *quantify these fluxes and their sensitivity, in order to close water balances for the right reasons*, especially when applying our models under scenarios representing future climates.

To address this research gap, we will conduct catchment-scale simulations of three study sites, representative for the monsoonal and non-monsoonal climatic regions in High Mountain Asia, and quantify the magnitude of evaporation, transpiration and sublimation, their seasonality, and relative role in the catchment water balance and runoff generation.

In order for these simulations to be as robust as possible, we will implement a regionally relevant and physically-oriented precipitation phase partitioning scheme based on moisture-sensitive thresholding with the wet bulb temperature, capable of simulating mixed-phase (sleet) precipitation (Ding et al., 2014), a new albedo scheme which accounts for sleet surface layers (Ding et al., 2017) and an updated snowpack, capable of realistic simulations of thick snow packs (Andreadis et al., 2009).

1.3.3. Research Gap 3

Global warming has profound impacts on the meltwater supply in High Mountain Asia (Kraajenbrink et al., 2021). These cryospheric changes are altering the seasonal water cycle in mountain basins, affecting water availability downstream with both positive and negative impacts, amidst increasing water demands (Pritchard et al. 2019; Viviroli et al., 2020, Immerzeel et al., 2020). Future projections of high-mountain hydrology are extremely valuable for economic planning, hazard mitigation and the generation of adaptation strategies, but are currently limited by our understanding of the processes at play and a lack of appropriate modelling tools for representing their spatial and temporal integration under shifting boundary conditions. As a prerequisite, it needs to be understood for a range of conditions, which elements of the high-mountain hydrological system are sensitive to climatic changes, and which are the ones that might respond in non-linear ways. Currently adopted models cannot be used for sensitivity studies in a robust way, since they are calibrated to past conditions and often lack dynamic schemes of e.g. snow and glacier mass balances, turbulent exchange of heat and mass, and vegetation growth. Transient, catchment-scale, ensemble simulations over many decades with models such as T&C are currently not feasible, due to their high computational demand, and are further limited by a lack of the full set of required meteorological variables for this kind of modelling from most GCM outputs. However, using mechanistic models for experimental simulations, in order to *investigate the sensitivity of hydrological processes to expected climatic changes* can be a first, valuable step in this direction.

To fill this research gap, we will contrast the simulations used to address Research Gap 2, of three HMA headwater catchments in the recent past, with experimental simulations representative of expected future warming conditions under two alternative pathways. We will explore the commonalities and differences in the response of water balance elements between the three distinct climates, with a focus on the role of precipitation amount and seasonality, snow and glacier mass balances, evaporative fluxes and the integrated runoff response.

The three research gaps can be summarised in the following research questions (RQs, illustrated in Figure 1):

RQ1: *How does the monsoon shape the glacier energy and mass balances, and their runoff contributing role in High Mountain Asian headwater catchments?*

RQ2: *How important are evaporative fluxes in monsoonal and westerly controlled catchments of HMA?*

RQ3: *How sensitive are the water balances of High Mountain Asian headwater catchments to warming in different climatic sub-regions?*

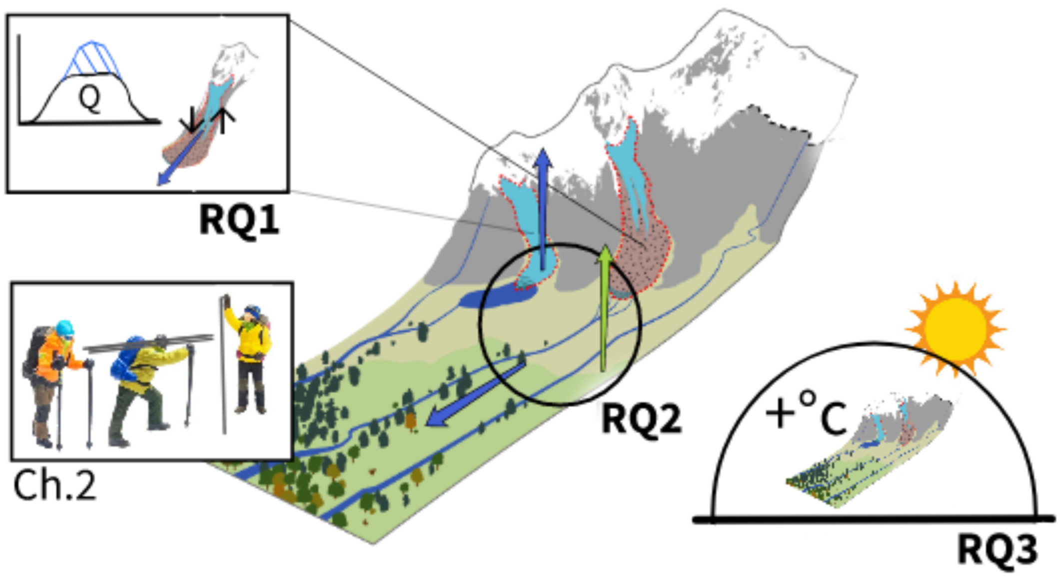

Figure 1: Illustration of Research Questions

1.4. Methodological Approach

The main method applied in this thesis is *investigative hydrological modelling*. Three main sources of information were used in this modelling framework:

- A fully distributed, mechanistic model of snow- glacier- and eco-hydrology, Tethys-Chloris (T&C; Fatichi et al., 2012a,b; 2021; Manoli et al., 2018; Botter et al., 2021; Paschalis et al., 2022; 2024), was chosen as the main research tool. In the framework of this thesis, T&C was enhanced in order to allow for a consistent level of detail in the representation of all land-surface and hydrological processes relevant in glacierized, high-mountain catchments (Figure 1, Section 2.3, Chapters 3-5).
- All meteorological input variables of the model namely, air temperature, relative humidity, precipitation, short- and longwave radiation, wind speed and air temperature, were measured with automatic weather stations in the field and used either for direct forcing of

the model or to inform the downscaling of a distributed forcing data set. Further in-situ data were collected for evaluating model-outputs namely runoff, snow depth and glacier melt.

- Gridded data products were required for the model set-up and forcing, calibration of specific parameters and model evaluation. These included data on meteorology and spatial data, including land cover and vegetation, soil types, snow cover and glacier mass balances. These data were based on remote sensing, large-scale modelling or a combination of the two, most of them openly available, were employed for the model setup, the adjustment of model parameters, the model forcing and the evaluation of model outputs.

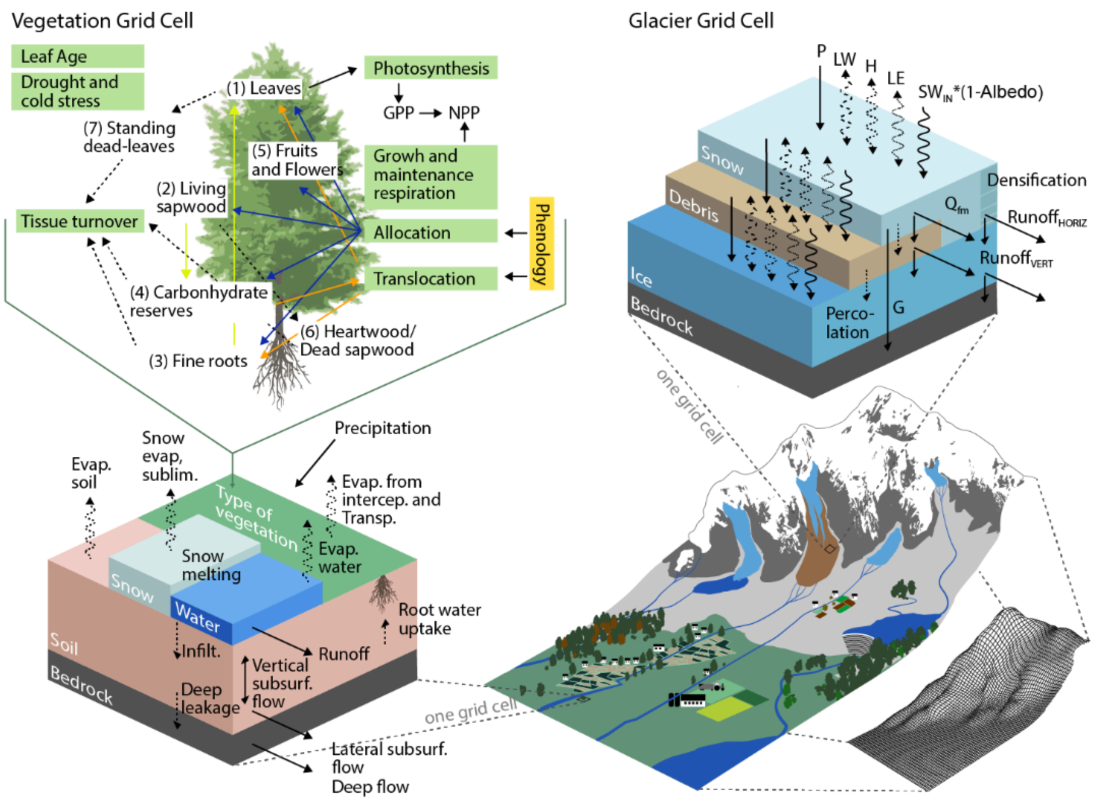

Figure 2: Illustration depicting essential components and processes in the Tethys-Chloris model. The fluxes involved in the energy balance calculation include SW (shortwave radiation), LW (longwave radiation), H (sensible heat flux), LE (latent heat flux), P (precipitation heat flux), Qfm (heat flux resulting from melting and refreezing), and G (ground heat flux).

The model was applied in three different ways (Figure 3):

- At the *point scale on* seven individual glaciers located in the Central and Eastern Himalaya, with the objective to understand the energy balance and mass fluxes experienced during one ablation season.
- In a *distributed way*, in order to reproduce all major elements of the high-elevation catchment water balance in three catchments over the time of a recent decade.
- The model was again applied in a distributed way, to conduct *numerical experiments* and test the sensitivity of catchment hydrology to temperature alterations representative of future warming.

The spatially distributed meteorological data used to force the model (i.e. air temperature, precipitation, relative humidity, incoming short- and longwave radiation, wind speed and air pressure) in Chapters 3 and 4 were generated as follows: we first applied an empirical-statistical downscaling following broadly Machguth et al. (2009), tailored to complex mountain terrain, of the globally available ERA5-Land reanalysis dataset (Muñoz-Sabater et al., 2021) for each specific variable to fit the model resolution. The remaining biases in the downscaled, higher resolution products were then further corrected with available in-situ observations from ground station data. The bias-correction strategy employed empirical quantile mapping for most variables as well as a specific treatment for precipitation to account for observed diurnal patterns and precipitation undercatch. All variables were spatially interpolated and adjusted according to elevation dependencies and topographic effects. Further details are given in Chapter 4.

Adopting a heuristic approach, this thesis proposes to gain new understanding from hydrological modelling by *avoiding extensive calibration of* integrated variables (e.g. snow duration, catchment runoff), i.e. by prioritising internal model consistency and physical understanding over empirical fitting to observed data. Parameter values were primarily sourced from literature or determined through expert judgement, with limited exceptions (Chapter 3 and 4).
Throughout this thesis, the term ‘evaluation’ is used when comparing model outputs against observations, instead of the more commonly used term ‘validation’, which already implies satisfactory performance. This usage of terminology is supported by the basis that natural systems, in contrast to the ‘model world’, are not closed nor observable without uncertainties, and therefore the outputs of numerical models are non-unique (Oreskes et al, 1994).

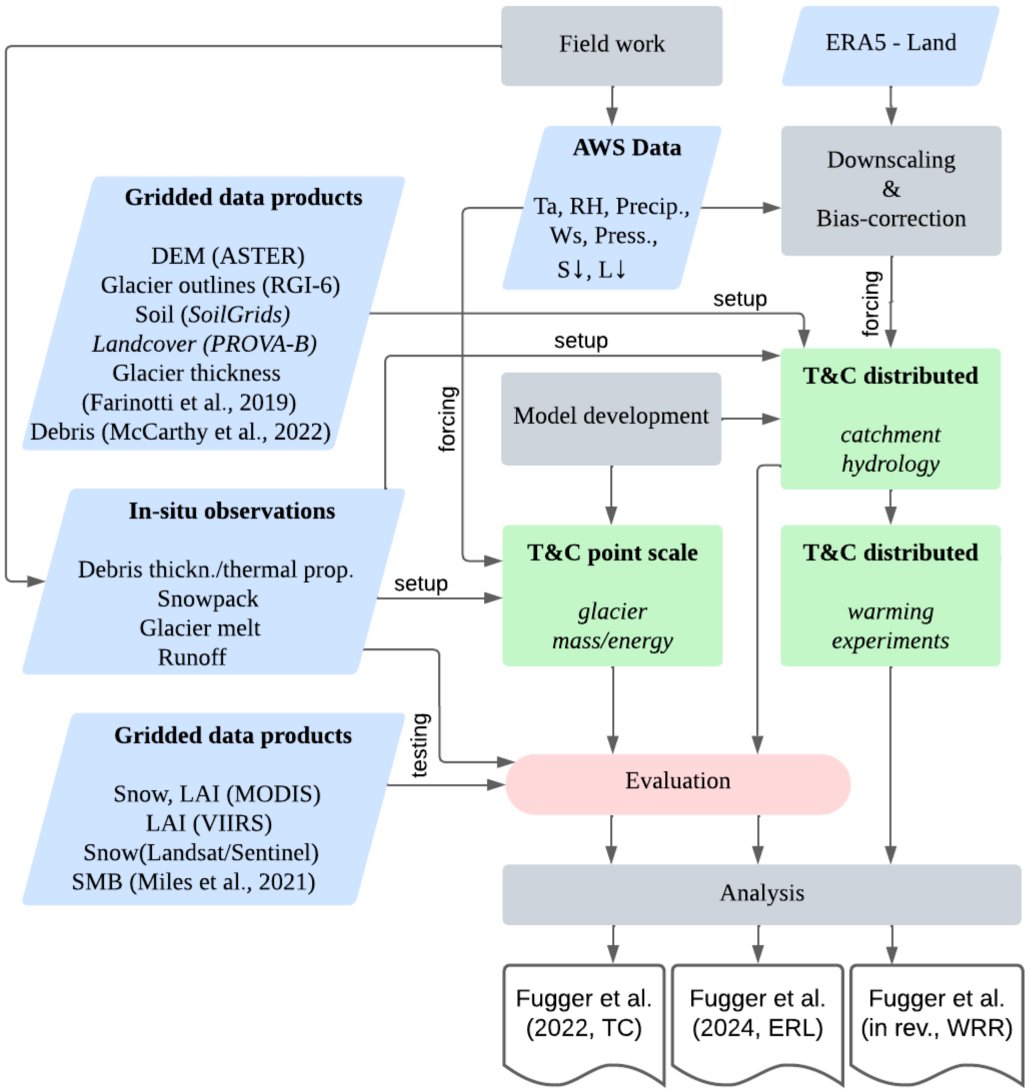

Figure 3: Flow chart of research methodology and thesis progression

1.5. Organization of the thesis

The thesis starts with an introductory chapter including a description of the state-of-the art in the modelling of high mountain headwaters, a summary of the research gaps and the research questions to be addressed. Chapter 2 describes the data collection approach, which was applied to three research basins in High Mountain Asia, in order to allow for well-informed modelling, as described in the subsequent chapters. Chapter 2 additionally summarises a number of advancements introduced for the purposes of this research into the model Tethys-Chloris, which was then applied to glaciers and catchments in the region. Chapters 3 and 4 consist of two peer-reviewed and open-access published journal articles (The Cryosphere and ERL), while Chapter 5 has been submitted to another open-access journal at the time of writing (Water Resources Research). In Chapter 3, the model was applied at the plot-scale to seven glaciers across the Central and Western Himalaya, to study the seasonal energy balance and mass fluxes of glaciers under monsoonal climate (RQ1). Chapter 4 addresses missing pieces in our understanding of headwater catchment hydrology under contrasting climates in three headwater catchments in HMA, through an assessment of the integrated catchment water balance and evaporative flux partitioning (RQ1, RQ2). Finally, Chapter 5 studies the sensitivities of the three catchments to climate warming, with a focus on runoff generation (RQ3). Chapter 6 provides a synthesis and summary of the results, concludes with some wider implications of the thesis to the field of study and society, and provides an outlook proposing avenues for further research.

2. Study sites, data collection and model developments

2.1. Study sites

Field work was carried out in three glacio-hydrological reference catchments, strategically situated in distinct sub-regions of High Mountain Asia (Figure 4). Each catchment contributes to a different major river basin, collectively covering a wide range of possible conditions within the hydro-climatic spectrum of High Mountain Asia. This diversity positions them as exemplary sites for in-depth studies on the hydrology of the region’s headwaters.

The catchments cover a similar elevation range and exhibit a similar set of land surface features, such as steep topography, a high share of glacier cover, a large portion of debris-covered glacier area and extensive vegetation cover. *Kyzylsu* is headwater catchment of the Amu Darya river basin, is located on the Northwestern slopes of the Pamir mountain range, where annual precipitation is low and mostly falls as snowfall during winter. Kyzylsu’s basecamp is accessible in one day from the Jirgatol town by truck. *Parlung 24K* (Yarlung Tsangpo - Brahmaputra river basin, Yang et al. 2017, Zhao et al., 2022) is not only located on the other side of the region, to the east, but is also on the other end of the climatic spectrum. Influenced by both the East Asian and the Indian Summer Monsoons, annual precipitation is 3.7 times higher and mostly arrives during the summer half-year. 24K is easily accessible by car from the nearby Bome town. Langtang (Ganges river basin; e.g. Immerzeel et al., 2012; Ragettli et al., 2015) in the Central

Himalaya is an intermediate case between the two in terms of the precipitation amounts, is situated in the longitudinal centre of the region, is more dominated by the ISM, and is relatively dry during the winter-half year. Langtang glacier is accessible on foot within 4 days from the town Syafru Besi (catchment outlet).
All three catchments are reference sites with a hydrometeorological station-network in place and where a similar set of variables are measured. Langtang and Parlung 24K have been studied in several previous publications, while Kyzylsu adds a new, under-represented climatic context for glacio-hydrological studies in the greater region.

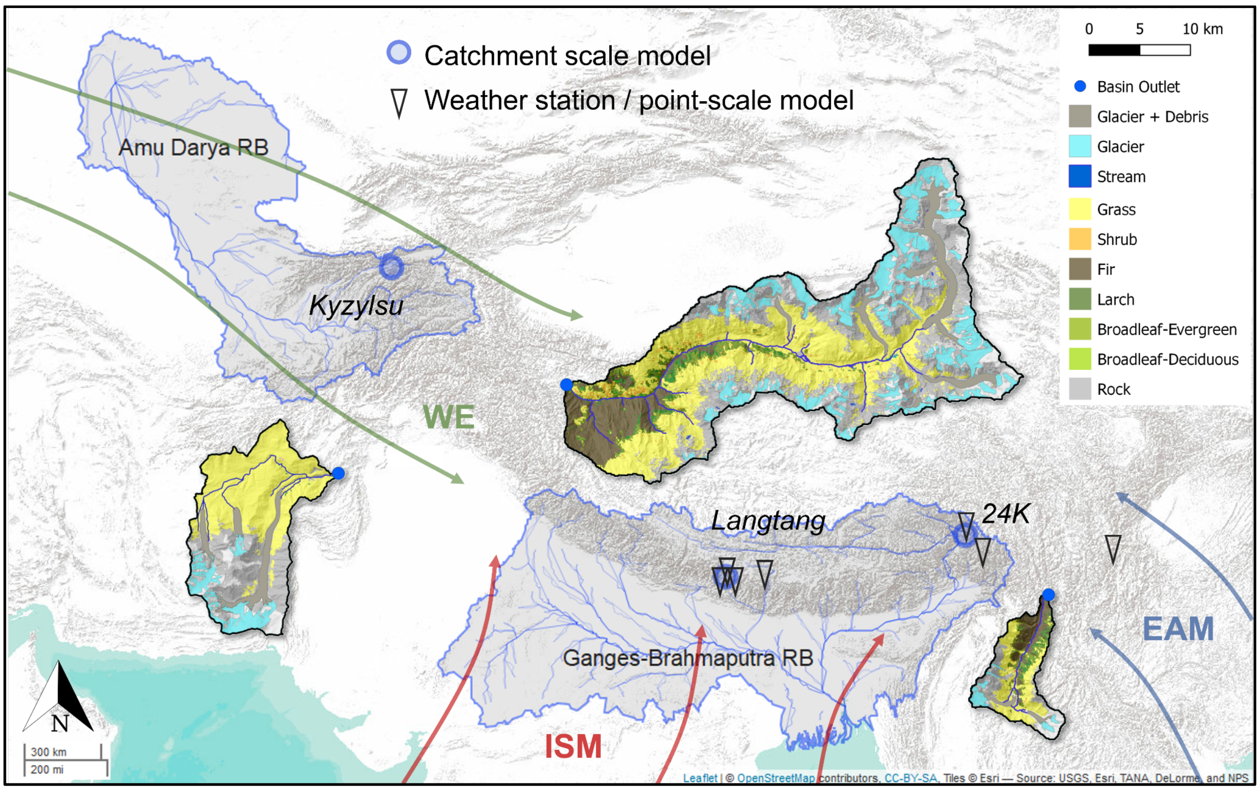

Figure 4. Overview of region, study sites, catchment maps as insets and major atmospheric circulation patterns as arrows. WE - westerlies; ISM - Indian Summer Monsoon, EAM - East Asian Monsoon;

2.2. Field work and data collection

A measurement programme was devised for the presented research, tailored towards data collection for physically based modelling of glacierized, high elevation catchments. The programme was applied to the three study catchments in a consistent way. The field measurements targeted meteorological, as well as glaciological and hydrological variables and were recorded in the form of time series, instantaneous measurements and spatial data. Glaciological measurements were primarily conducted on one target glacier in the valley (Figures 6-8). The data collection was designed to support all stages of the modelling process. Automatic weather station (AWS) data was collected for the bias correction, spatial distribution and evaluation of forcing data sets. Glaciological and hydrological station data, such as ablation stake measurements and stream discharge measurements, were recorded for the evaluation of model outputs. In Langtang and 24K, where monitoring networks already existed, they were complemented with additional stations and measurements in order to meet the requirements of the research project. Those were:

- One or several AWSs measuring the 'radiation balance', i.e. 4-way radiation (in- and outgoing short- and longwave radiation), along with air temperature, ground- or debris-temperature measurements, relative humidity, wind speed and wind-direction measurements at at least one height.
- Air temperature measurements in several locations, for deriving temperature lapse rates
- One or several pluviometer measurements of total precipitation
- Automatic measurements of snow depth and glacier ablation
- One or several stream gauges to measure pro-glacial runoff including sufficient rating curves
- Ablation or mass balance measurements targeting especially the ablation of debris-covered glaciers

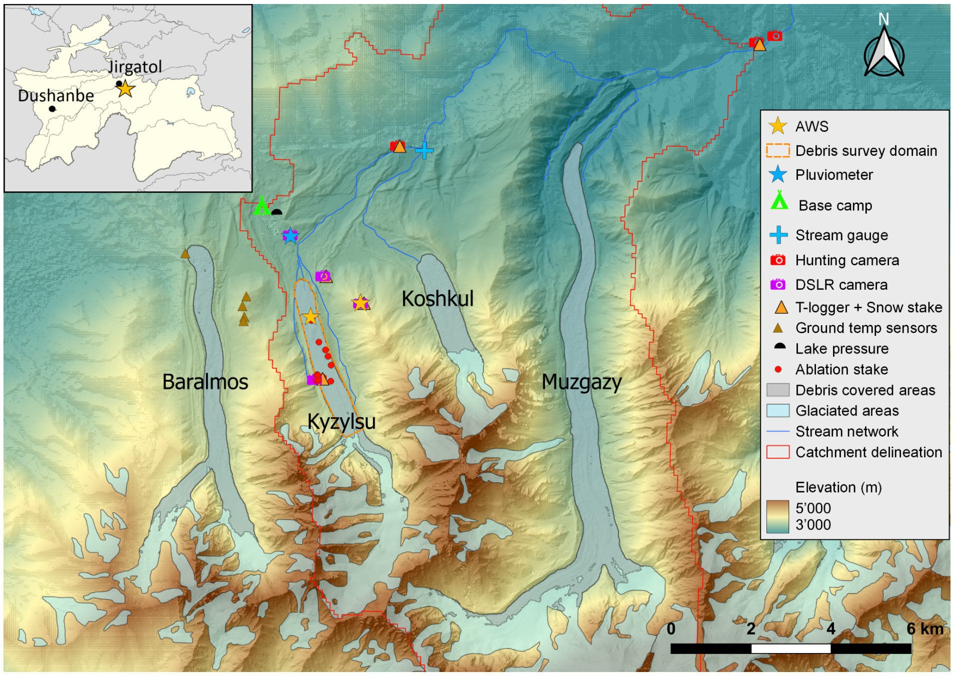

Figure 5: Map of Kyzylsu observation network as of Sep. 2023 (Map: Achille Jouberton)

The field visits took place between 2019 and 2023 in 24K (Southeastern Tibetan Plateau), Langtang (Central Himalaya) and Kyzylsu (Nortwestern Pamir) (Table 1). The sites were typically visited during late spring and early autumn, but were put on hold in the 2020 season, due to the global COVID pandemic. Field visits could be resumed in 2021 in Tajikistan, where establishing the initial measurement network required a continuation of field visits until 2023. Detailed field reports for each visit are available from the author on request.

Timing of field visits:

Langtang	May/June and October/November 2019
24K	June/July and October 2019
Kyzylsu	June/July and September/October 2021, 2022, 2023

Figure 6: A view on Kyzylsu glacier from the true-right side of the glacier (Foto: Jason Klimatsas, Sep. 2023)

Figure 7: Up-glacier view on a confluence of Langtang glacier from the true-right side of the glacier (Foto: Catriona Fyffe, Oct. 2019)

Figure 8 Down-glacier view on 24K glacier from the true-right side of the glacier; 23K glacier on the opposite side of the valley (Foto: Marin Kneib, Oct. 2019)

2.2.1. Meteorological observations

An on-glacier radiation-balance weather station was installed on both Langtang (2019 ablation season) and Kyzylsu glaciers (since July 2021, Figure 9), while one such station has been operated by a collaborator on 24K glacier since 2016. It was the first installation of such a station on Kyzylsu, but the second temporary one on Langtang glacier, and several other stations are currently, or were previously operated on glaciers in the Langtang catchment. In Kyzylsu, additionally, a weighing gauge pluviometer station measuring total precipitation was installed, while several weighing gauge pluviometers have been operated in the Langtang catchment since 2012. Measurements from a weighing gauge pluviometer station which was installed in the pro-glacial field of 24K have been available since spring 2021. While the pluviometers in Langtang were already equipped with Alter-type wind shields, one such shield was only added in Kyzylsu in September 2023 and the 24K pluviometer remained unshielded for the time being. Following Masuda et al. (2019), under-catch correction was applied to all measurements with parameters chosen accordingly for shielded/unshielded measurements, before used for bias-correction (Chapter 3).

Temperature loggers were installed on- and off-glacier in several locations at all sites, covering a large elevation range, in order to estimate temperature lapse rates. Station locations and details such as variables measured and station locations are provided in Chapters 3 and 4. A detailed overview about the large observation network installed in Langtang is given in Steiner et al. (2021a).

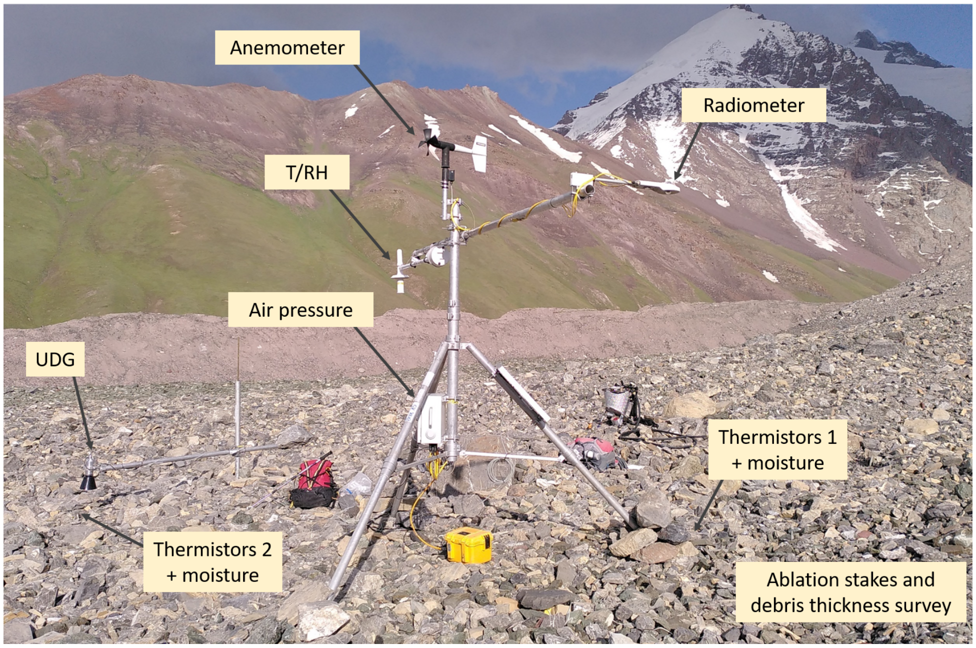

Figure 9: AWS including a ultrasonic depth gauge (UDG) mast installed on Kyzylsu glacier near the terminus (Foto: Stefan Fugger, July 2021)

2.2.2. Glaciological observations

Ablation stakes were inserted mainly in the debris covered zones of each target glacier (Figures 6-8), at the beginning of the ablation season and measured at the end of the ablation season at each site. In Kyzylsu, the stakes were maintained or re-drilled during the following seasons (Figure 10). Debris thickness measurements were systematically taken over large parts of the debris-covered ablation zones of all three focus glaciers. Ultrasonic depth gauges were installed on a mast and drilled into the ice at the AWS locations in Langtang and Kyzylsu, for the measurement of temporally resolved surface changes. An array of time lapse cameras was installed at each site, observing the sub-seasonal dynamics of the glacier surfaces and surrounding slopes (Kneib et al., 2022).

Figure 10: left: re-drilling of ablation stake in the debris-covered portion of Kyzylsu; right: debris thickness measurements (Fotos: Jason Klimatsas, Sep. 2023)

2.2.3. Runoff observations

Temporary and semi-permanent automatic stream discharge stations using pressure transducers were installed in all three catchments (Figure 11). Repeat measurements of discharges were conducted at all sites during the field campaigns, using mainly the salt- and dye-dilution methods (Figure 12). Transit times of meltwater to the glacier terminus and further downstream were measured using rhodamine and fluorescein additionally as tracers.

Figure 11: Pro-glacial stream gauge downstream of Kyzylsu glacier (Foto: Stefan Fugger, July 2021)

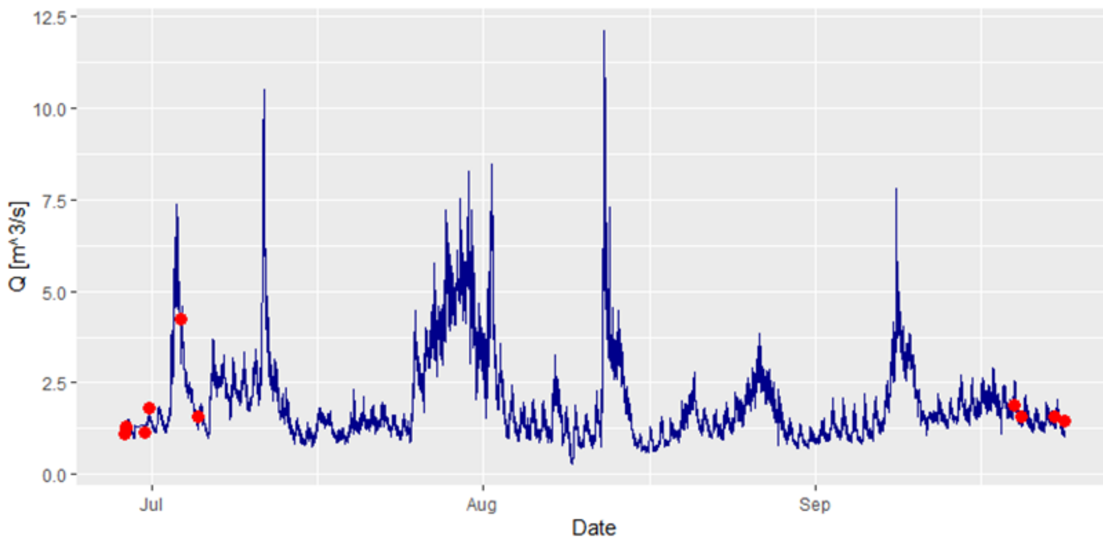

Figure 12: Hydrograph at pro-glacial stream-gauge downstream of Kyzylsu, with discharge gaugings indicated in red

2.3. Model development

With the aim of advancing physically based glacio-hydrological modelling in mind, a fully distributed, process-based model, Tethys-Chloris (T&C), representing the state-of-the-art in ecohydrological modelling, was adopted. At the time of adoption, the model had preliminary modules of glaciers and snowpacks included, but new components were successively included, in order to also be in line with the state-of-the-art in glacio-hydrological modelling. The data collected for the thesis was used for testing and evaluating new components, e.g. the energy balance scheme over debris-covered glaciers using on-glacier automatic weather stations. Methodological choices, testing and implementation of the new components were made by the author of the thesis, while the model developer, Dr. Simone Fatichi, performed the main technical implementation into the model.

2.3.1. Supraglacial debris energy balance

Depending on its thickness, supraglacial debris can have an insulating, as well as a melt-enhancing effect on the ablation of the ice underneath (Oestrem, 1959), while the properties of debris, such as thermal conductivity and surface roughness further modulate the melt energy arriving at the debris-ice interface (Nicholson and Benn, 2013). Clean-ice, ‘dirty ice’, and debris cover of varying thickness shape a spatially heterogeneous melt pattern and the glacier-wide melt rates integrate in complex ways to generate the total melt-water runoff (Fyffe et al., 2014, 2020). Turbulent energy fluxes (latent and sensible energy) are important components in the energy balance over debris-covered surfaces, which absorb a large portion of the solar radiation due to the low albedo of the debris. Drying of liquid water from the debris surface consumes part of this energy via latent heat, thereby reducing the energy conducted towards the ice (Steiner et al., 2018). To account for these processes in line with the general idea of T&C, which resolves the coupled energy, mass and carbon balances over all types of land surfaces represented, the debris energy balance model (DEB) of Reid and Brock (2010) was chosen and integrated into the energy-balance computation over ice packs in T&C. In this representation, supraglacial debris varies in space, can have any thickness above 1 cm and is discretized into a user-chosen number of thermal layers. Heat conduction through the debris is computed by iteratively closing the energy balance, resulting in an update of the surface temperature and the temperature of each layer. The turbulent energy fluxes are computed following the Monin-Obukhov similarity theory. The evaporation of liquid water from the debris was included by imposing an interception storage, simulating the drying of the debris surface (Chapter 3).

2.3.2. Precipitation partitioning using wet-bulb temperature

Besides the amount and timing of precipitation, accurate partitioning into liquid and solid precipitation shares is crucial when modelling mountain catchments, since all water balance elements are highly sensitive to the timing and amount of snow- and rainfall. This is especially true where temperatures hover around the freezing point during the time of intense precipitation (Higuchi et al., 1982) and where there are high fluctuations in atmospheric water content, which modulates the effective freezing point in the range of several degrees Celsius (Wang et al., 2019). Applied to large elevation ranges, a single and static air temperature threshold can result in unrealistic accumulation patterns, cascading into erroneous glacier mass balances, meltwater fluxes, rainfall runoff, groundwater recharge, and all the way to temporally shifted vegetation phenology and evapotranspiration rates. The more advanced simulation of mixed rain-snow (sleet) precipitation is possible by applying dual thresholds, so that partially liquid and partially solid precipitation is possible. Wet-bulb temperature has been shown to be a more reliable predictor of the actual freezing point than a fixed threshold of e.g. 2°C or a dual fixed threshold, since the atmospheric water content is implicit in this measure. A parameterization of phase partitioning based on the wet bulb temperature (T_w), relative humidity and surface elevation was developed and tested in Ding et al. (2014). The parameterization was based on a large dataset of daily manual precipitation phase classifications over 28 years at 824 observations station across China. The dataset was binned into classes of elevation and relative humidity and rain, snow and sleet events, before probability functions were derived for two wetbulb temperature thresholds (T_{min} and T_{max}), above/below which precipitation primarily fall as rain/snow, and between which mixed-phase precipitation was found. The two probability functions were derived as

$$P_1(T_w) = \frac{1}{1 - \exp\left(\frac{T_0 - T_0 + \Delta T}{\Delta S}\right)} \tag{2}$$

$$P_2(T_w) = \frac{1}{1 - \exp\left(\frac{T_0 - T_0 - \Delta T}{\Delta S}\right)} \tag{3}$$

whereby the parameters T_0, ΔT, and ΔS are dependent on relative humidity (RH) and surface elevation (Z)

$$T_0 = -5.87 - 0.1042 * Z + 0.0885 * Z^2 + 16.6 * RH\ , \tag{4}$$

$$\Delta T = 0.215 - 0.099 * RH + 1.018 * RH, \tag{5}$$

$$\Delta S = 2.374 - 1.634 * RH \tag{6}$$

The temperature thresholds were found as,

$$T_{min} = \begin{cases} T_0 - \Delta S * \ln\left[\exp\left(\frac{\Delta T}{\Delta S}\right) - 2 * \exp\left(-\frac{\Delta T}{\Delta S}\right)\right] & \frac{\Delta T}{\Delta S} > ln2 \\ T_0 & \frac{\Delta T}{\Delta S} \leq ln2 \end{cases}, \tag{7}$$

$$T_{max} = \begin{cases} 2 * T_0 - T_{min} & \frac{\Delta T}{\Delta S} > ln2 \\ T_0 & \frac{\Delta T}{\Delta S} \leq ln2 \end{cases}\ , \tag{8}$$

between the two thresholds, the precipitation type is snow if $T_w \leq T_{min}$, rain if $T_w \leq T_{max}$ and sleet if $T_{min} < T_w < T_{max}$ and fractions of either precipitation type involved are

$$F_{snow}(T_w) = P_1(T_w), \tag{9}$$

$$F_{sleet}(T_w) = P_2(T_w) - P_1(T_w), \tag{10}$$

$$F_{sleet}(T_w) = 1 - P_2(T_w) \tag{11}$$

For a more detailed description of the parameterization, see Ding et al. (2014). The parameterization proved robust in mountainous terrain and across different climates, which is why it was chosen to be implemented into T&C (Chapter 3).

2.3.3. Snow albedo scheme

Net shortwave radiation is usually the main energy input to the glacier surface energy balance (Klok and Oerlemans, 2004) and its magnitude is determined by the incoming shortwave radiation and the surface albedo. Inadequate representations of albedo can therefore lead to large biases in the snow and glacier mass balances (Naegeli and Huss et al., 2017). Early parameterizations were developed including only time- or temperature-dependent formulations. Brock et al. (2000b) however found snow albedo to be controlled by temperature-driven snow ageing, snowpack depth, cumulated melting, and the underlying surface, with albedo further modified by the presence of organic and inorganic deposits. Since all these factors vary greatly in complex mountain terrain, a spatially variable representation is indispensable for energy-balance modelling (Brock et al., 2000b). Albedo can also vary with the predominant precipitation type (rain, sleet, or snow) over short time scales (Ding et al., 2017). Ding et al. (2017) leveraged the detailed outputs of the physically based SNICAR albedo model (Flanner, 2007), in combination with existing parameterizations to develop a parameterization suited for glacio-hydrological modelling. This parameterization is based on cloud fraction, solar angle, solid fraction of precipitation, snow grain diameter, snow depth and the albedo of the underlying ground and performed very well against both the physical model and observations (Ding et al., 2017), and was therefore implemented into T&C (Chapter 3). In this parameterization, albedo is combined as

$$\alpha = \alpha_b + \Delta\alpha_c + \Delta\alpha_\beta, \tag{12}$$

where α_b is the “basic albedo”, which depends on new precipitation and snow aging, and is calculated following Baker et al. (1990) and Verseghy (1991) as

$$\alpha_b = \begin{cases} \alpha_{min} + (\alpha_{b,0} - \alpha_{min})\, e^{-\tau_f \frac{\Delta t}{86400}} & \mathit{if\ melting\ occurs} \\ \max\left(\alpha_{b,0} - \tau_a \frac{\Delta t}{86400}, \alpha_{min}\right) & \mathit{otherwise} \end{cases}, \tag{13}$$

where $\alpha_{b,0}$ is the basic albedo from the previous timestep, α_{min} is the minimum value of the glacier albedo, Δt is the timestep, and τ_f and τ_a are scaling factors. The cloud fraction effect is calculated following Petzold (1977) as

$$\alpha_c = 0.00449 + 0.097\, C^3, \tag{14}$$

where C is the cloud fraction, and the solar elevation effect is parameterized following Petzold (1977) as

$$\Delta\alpha_\beta = \begin{cases} -0.019 + 0.248\, e^{-\frac{\beta}{15.5}} & \beta \le 40° \\ 0 & \beta > 40° \end{cases}, \tag{15}$$

where β is the solar angle in degrees. A more detailed description of the albedo parameterization is found in Ding et al., (2017).

2.3.4. Updated snowpack model

Snowpack dynamics is one of the most important topics in the modelling of high-elevation catchments, since snow accumulation, ageing and melting have a profound control on glacier mass balance and the runoff seasonality. The simplest, and most efficient way to include an energy-balance based calculation of snowpack dynamics is by representing it with a single snow layer, for which the energy balance is resolved, since one set of state variables, including snowpack temperature and density are calculated. However, the assumption of an isothermal snowpack is only valid under melting conditions, while during warming and cooling, there will be a negative (warming) or positive (cooling) temperature gradient between the snow surface and the underlying ground, whereby the thermal conductivity of a snowpack determines how efficiently heat is transferred within the snow column (Marks et al., 1998). As soon as a snowpack exceeds a few centimetres in depth, a single-layer snowpack temperature will therefore fail to represent the thermodynamics of the snowpack over time, and result in biased estimations of melt- and sublimation-rates, and increasingly so with increasing snowpack depth (Essery et al., 1999). A two-layer snowpack, on the other hand, simulates the exchange of energy between the snowpack and the atmosphere at a thin surface layer and transfers energy through the underlying snowpack layer and further to the underlying ground (Marks et al., 1998). The snowpack scheme of T&C was updated to include a surface layer of user-adjustable thickness, inspired by the scheme proposed by Marks et al. (2001), while the heat-transfer within the underlying snowpack is computed over a variable number of snowpack layers. The skin-surface layer thickness was set to a default-value of 3 mm. The skin surface energy balance and the melting of the snowpack are solved in order to concurrently maintain the energy and mass balances. In this formulation, a single snowpack density and water content are used for the entire snow column, in order to reduce complexity and computational time. When the snowpack depth is smaller than twice the skin-layer depth, the model resorts back to a single-layer formulation of the heat profile.

3. Research Article: Understanding monsoon controls on the energy and mass balance of glaciers in the Central and Eastern Himalaya

published on 05 May, 2022 in *The Cryosphere*; authored by:

Stefan Fugger[1,2], Catriona L. Fyffe[3], Simone Fatichi[4], Evan Miles[1], Michael McCarthy[1,5], Thomas E. Shaw[1], Baohong Ding[6], Wei Yang[6], Patrick Wagnon[7], Walter Immerzeel[8], Qiao Liu[9], and Francesca Pellicciotti[1,3]

[1]Swiss Federal Institute for Forest, Snow and Landscape Research (WSL), Birmensdorf, Switzerland

[2]Institute of Environmental Engineering, ETH Zurich, Zurich, Switzerland

[3]Department of Geography and Environmental Sciences, Northumbria University, Newcastle, UK

[4]Department of Civil and Environmental Engineering, National University of Singapore, Singapore

[5]British Antarctic Survey, Cambridge, UK

[6]Institute of Tibetan Plateau Research, Chinese Academy of Sciences, Beijing, China

[7]Univ. Grenoble Alpes, CNRS, IRD, Grenoble-INP, IGE, Grenoble, France

[8]Faculty of Geosciences, Department of Physical Geography, Utrecht University, Utrecht, the Netherlands

[9]Institute of Mountain Hazards and Environment, Chinese Academy of Sciences, Chengdu, China

<u>Author contribution</u>

StF, FP and EM designed the study. StF carried out the analysis with the help of CLF, MM and SiF. StF interpreted the results, created the figures and wrote the paper with the help of CLF, EM, MM, TES and FP. SiF, PW, WI, and QL reviewed the paper. WY and BD facilitated field data collection and provided parameterisations for albedo and precipitation phase. WY, PW and WI also contributed datasets.

<u>Key findings</u>

- Radiation budget primarily controls the melt of clean ice glaciers, but turbulent fluxes also play an important role in modulating the melt energy on debris-covered glaciers.
- Debris-covered glacier melt rates stay almost constant through the different phases of the monsoon, while melt under thin debris increases pronouncedly
- Spring snow cover duration and intermittent, monsoonal snow accumulation are strong controls on the overall ablation.

Note: Separate section numbering in articles

Understanding monsoon controls on the energy and mass balance of glaciers in the Central and Eastern Himalaya

Authors: Stefan Fugger[1,2], Catriona L. Fyffe[3], Simone Fatichi[4], Evan Miles[1], Michael McCarthy[1,5], Thomas E. Shaw[1], Baohong Ding[6], Wei Yang[6], Patrick Wagnon[7], Walter Immerzeel[8], Qiao Liu[9], and Francesca Pellicciotti[1,3]

[1]Swiss Federal Institute for Forest, Snow and Landscape Research (WSL),Birmensdorf, Switzerland
[2]Institute of Environmental Engineering, ETH Zurich, 8093 Zurich, Switzerland
[3]Department of Geography and Environmental Sciences, Northumbria University, Newcastle, UK
[4]Department of Civil and Environmental Engineering, National University of Singapore, Singapore
[5]British Antarctic Survey, Cambridge, UK
[6]Institute of Tibetan Plateau Research, Chinese Academy of Sciences, Beijing, China
[7]Univ. Grenoble Alpes, CNRS, IRD, Grenoble-INP, IGE, 38000 Grenoble, France
[8]Faculty of Geosciences, Department of Physical Geography, Utrecht University, Utrecht, The Netherlands
[9]Institute of Mountain Hazards and Environment, Chinese Academy of Sciences, Chengdu, China

Correspondence: Stefan Fugger (stefan.fugger@wsl.ch)

Abstract. The Indian and East Asian Summer Monsoons shape the melt and accumulation patterns of glaciers in High Mountain Asia in complex ways due to the interaction of persistent cloud cover, large temperature ranges, high atmospheric water content and high precipitation rates. Glacier energy and mass balance modelling using in-situ measurements offer insights into the ways in which surface processes are shaped by climatic regimes. In this study, we use a full energy- and mass-balance model and seven on-glacier automatic weather station datasets from different parts of the Central and Eastern Himalaya to investigate how monsoon conditions influence the glacier surface energy and mass balance. In particular, we look at how debris-covered and debris-free glaciers respond differently to monsoonal conditions. The radiation budget primarily controls the melt of clean-ice glaciers, but turbulent fluxes play an important role in modulating the melt energy on debris-covered glaciers. The sensible heat flux decreases during core monsoon, but the latent heat flux cools the surface due to evaporation of liquid water. This interplay of radiative and turbulent fluxes causes debris-covered glacier melt rates to stay almost constant through the different phases of the monsoon. Ice melt under thin debris, on the other hand, is amplified by both the dark surface and the turbulent fluxes, which intensify melt during monsoon through surface heating and condensation. Pre-monsoon snow cover can considerably delay melt onset and have a strong impact on the seasonal mass balance. Intermittent monsoon snow cover lowers the melt rates at high elevation. This work is fundamental to the understanding of the present and future Himalayan cryosphere and water budget, while informing and motivating further glacier- and catchment-scale research using process-based models.

1 Introduction

High Mountain Asia (HMA) holds the largest ice volume outside the polar regions (Farinotti et al., 2019) and due to the large elevation range and vast geographic extent, HMA glaciers are highly diverse in character and hydro-climatic context (Yao et al., 2012). Several large-scale weather patterns interact with the region's topography (Bookhagen and Burbank, 2010), causing glaciers to contrast in terms of hypsometry (Scherler et al., 2011a) and accumulation and ablation seasonality (Maussion et al., 2014). The Indian Summer Monsoon dominates the Central Himalaya and the Southeastern Tibetan Plateau during summer, and gradually loses strength moving towards the Karakoram, Pamir and Kunlun ranges in the west, where the influence of Westerlies is particularly strong. A more continental regime, influenced by both monsoon and westerlies, controls the Central Tibetan Plateau (Yao et al., 2012; Mölg et al., 2014), while the East Asia Monsoon influences the eastern slopes of the Tibetan Plateau (Yao et al., 2012; Maussion et al., 2014). These major modes of atmospheric circulation control the surface processes and runoff regimes of glaciers (e.g. Kaser et al., 2010; Mölg et al., 2012, 2014) and lead to distinct responses of glaciers to climate change (Scherler et al., 2011b; Yao et al., 2012; Sakai and Fujita, 2017; Kraaijenbrink et al., 2017). Mass losses are high throughout most of HMA, and are particularly pronounced on the South-Eastern Tibetan Plateau, while glaciers exhibit a near-neutral mass balance regime throughout the Karakoram, Pamir and Kun Lun (Gardelle et al., 2012; Brun et al., 2017; Farinotti et al., 2020; Shean et al., 2020).

Accurate glacier mass balance modelling is essential to assess glacier meltwater contribution to mountain water resources, and to predict future glacier states and catchment runoff. Physically-based models of glacier energy and mass balance represent surface and subsurface energy fluxes using physical equations to calculate the energy available for melt, and the glacier runoff. Summer-accumulation glaciers in HMA experience simultaneous accumulation and ablation. Using an energy balance model, Fujita and Ageta (2000) found that the mass balances of this type of glacier is highly sensitive to climatic variability during the monsoon season, when warm air temperatures and high precipitation rates coincide. Using energy balance modelling for an interannual study at the Central Tibetan Zhadang glacier, Mölg et al. (2012) demonstrated that the timing of monsoon onset and the associated albedo variability can change melt rates considerably in subsequent years. At the same time, they observed a decoupling of the glacier mass balance from the Indian Summer Monsoon during the main monsoon season. Mölg et al. (2014) explain the mass balance variability of Zhadang Glacier as being controlled by both the Indian Summer Monsoon onset and mid-latitude Westerlies. Combining energy balance with weather forecast modelling, Bonekamp et al. (2019) identify the timing and quantity of snowfalls as the main source of differences in mass balance regimes between the Shimshal Valley in the Karakoram and the Langtang Valley in the Central Himalaya. Similarly, Zhu et al. (2018) attribute mass balance differences of three glaciers on the Tibetan Plateau mainly to different local rain/snow precipitation ratios and timing.

The presence of debris cover, a widespread characteristic of HMA glaciers, (e.g. Scherler et al., 2011b; Kraaijenbrink et al., 2017; Herreid and Pellicciotti, 2020), creates additional complexity to understanding and modelling the processes leading to (sub-debris) glacier melt. In recent years, much effort has gone into developing energy balance models for debris-covered glaciers (e.g. Nicholson and Benn, 2006; Reid and Brock, 2010; Lejeune et al., 2013; Fujita et al., 2014; Collier et al., 2014; Rounce et al., 2015; Evatt et al., 2015; Steiner et al., 2018). Yang et al. (2017) compare the energy balance of a debris-covered and a clean-ice glacier on the Southeastern Tibetan Plateau and finds the main differences, beside the differences in melt rates, is their climatic sensitivity and the important role of turbulent fluxes on debris-covered glaciers. Studies with observational data on two Indian glaciers showed that thick debris is a more important control on melt rates than elevation (Pratap et al., 2015; Shah et al., 2019) and also dampens and delays glacier melt in the diurnal cycle (Shrestha et al., 2020). Ablation is often expected to be higher on glaciers with debris around or below the critical thickness (site dependent, 1-5cm) (Nakawo and Rana, 1999) than at both clean-ice sites and at sites with thicker debris cover, as shown experimentally (Östrem, 1959; Reznichenko et al., 2010), and by means of modelling (e.g. Nakawo and Rana, 1999; Reid and Brock, 2010), with humidity being a determining factor for this enhancement (Evatt et al., 2015). Moisture in debris is an important factor under monsoonal conditions, controlling the debris' thermal properties and thus ablation (Sakai et al., 2004; Nicholson and Benn, 2006) and has been the focus of devoted modelling studies (Collier et al., 2014; Giese et al., 2020). Moreover, the representation of latent heat due to evaporation (Steiner et al., 2018; Giese et al., 2020) and atmospheric stability correction for turbulent fluxes were shown to be important to improve the simulation of sub-debris melt (Reid and Brock, 2010; Mölg et al., 2012). Previous studies explicitly dealing with the imprint of the monsoon on the surface thermal properties of glaciers remained limited to individual clean-ice glaciers in the Central Tibetan Plateau (Mölg et al., 2012, 2014).

Our main goal is to improve the understanding of monsoon controls on glaciers of various surface types in the Central and Eastern Himalaya. Applying the glacier energy and mass balance module of a land surface model suited to both debris-covered and clean-ice glaciers, and leveraging seven on-glacier automatic weather station (AWS) records from the region, we answer the following questions: 1) Which energy and mass fluxes dominate the seasonal mass balance of Himalayan glaciers? 2) How does debris cover modulate the energy balance in comparison to clean-ice surfaces? 3) How does the monsoon change the glacier surface energy balance? Answering these questions allows us to infer how these glaciers will respond to the possible future changes of the monsoons in the region. We apply the model at the point scale of individual AWSs, driven by high-quality in situ meteorological observations that guarantee accurate energy balance simulations, not affected by extrapolation of the meteorological forcing. By identifying the key surface processes of glaciers and their dynamics under monsoonal conditions, this study promotes their appropriate representation in models of glacier mass balance and the hydrology of glacierised catchments.

2 Study sites and data

In situ observations from seven on-glacier AWSs in different environments along the climatic gradient of the Himalaya were gathered and are used for forcing and evaluation of the model (Figure 1 and Table 1). Our seven study sites are located in the Central and Eastern Himalaya and cover a range of glacier types and local climates (Figure 1, 2 and Table 2).

The seven sites include both spring- (24K, Parlung No.4) and summer-accumulation glaciers (all others) as indicated by the proportion of monsoon precipitation to the annual precipitation (Figure S1). Langtang, Lirung and Yala are neighbouring glaciers found in the Langtang Valley (Figure 1). The Langtang Valley is strongly influenced by the Indian Summer Monsoon ($\sim$ June to October), during which more than 70% of the annual precipitation falls (Figure S1 and Table 2), while the period from November to May is a drier season (Immerzeel et al., 2012; Collier and Immerzeel, 2015). The Valley has been a site of extensive glaciological (e.g. Fujita et al., 1998; Stumm et al., 2020), meteorological (Immerzeel et al., 2014; Collier and Immerzeel, 2015; Heynen et al., 2016; Steiner and Pellicciotti, 2016; Bonekamp et al., 2019) and hydrological (e.g. Ragettli et al., 2015) investigations. On-glacier AWSs were installed during the ablation season on Lirung (2012-2015) and Langtang (2019) glaciers, and year-round on Yala (2012-ongoing) (Table 1). Both Lirung and Langtang are valley glaciers that have heavily debris-covered tongues, but the tongue of Lirung has disconnected from the accumulation zone (Figure 2). Yala is a considerably smaller clean-ice glacier, with most of its ice mass located at comparably high elevation. It is oriented to the southwest and has a gentle slope (Fujita et al., 1998) (Figure 2 and Table 2).

North Changri Nup Glacier (hereafter Changri Nup Glacier) is a debris-covered valley glacier located in the Everest region in Nepal (Figure 1). The southeast-oriented, avalanche-fed glacier discharges into the Koshi River system. The local climate is similar to that of the Langtang Valley, with 70-80% of precipitation falling during monsoon (Vincent et al., 2016) (Figure 2, S1 and Table 2).

24K and Parlung No.4 glaciers are located on the southeastern Tibetan Plateau, feeding water into the upper Parlung Tsangpo, a major tributary to the Yarlung Tsangpo - Brahmaputra River. The summer climate is characterized by monsoonal air masses reaching the Gangrigabu mountain range from the south through the Yarlung Tsangpo Grand Canyon. 24K Glacier is an avalanche fed valley glacier with a debris-covered tongue, located 24 km from the town of Bome (Yang et al., 2017). It is small in size, oriented to the northwest and surrounded by shrubland (Figure 1, 2 and Table 2). Parlung No.4 is a debris-free valley glacier, which is north-east oriented, considerably larger than 24K and located 130 km to the south-east from Bome (Yang et al., 2011) (Figure 1 and Table 2). Full automatic weather stations were installed in the ablation zones of both glaciers in 2016 and subsequent years (Table 1).

Hailuogou Glacier, the second-largest of our study sites (Figure 2) is located on the eastern slope of Mt. Gongga in the easternmost portion of the southeastern Tibetan Plateau (Figure 1). It is located at low elevation and large parts of its ablation zone are continuously covered with a thin layer of fine clasts and scattered with coarser clasts, leading to high annual ablation rates (Figure 2 and Table 2). The local climate influenced by the East Asia Monsoon with typically only 50 to 60% of the annual precipitation arriving during the monsoon period (Figure 1 and S1). The debris-covered tongue is connected to a steep and extensive accumulation zone via a large icefall, but avalanching is the primary mass supply mechanism through the icefall to the valley tongue (Liao et al., 2020), and a dynamic disconnect is expected to occur in the near future. Weather stations were installed at three nearby off-glacier locations and one on-glacier site during 2008, while precipitation was measured at the Alpine Ecosystem Observation and Experiment Station of Mt. Gongga, within $1.5\,km$ from the glacier terminus (Table 1).

We use the monthly averaged ERA5-Land reanalysis data (Muñoz Sabater, 2019) to evaluate the representativeness of the AWS records in terms of seasonal variability (Figures S2 to S8), and to provide an overview of the long term climatic patterns, e.g. the average monsoonal regime from June through to September (Figure S1). We thereby focus on the qualitative aspects, given that the absolute values from the reanalysis dataset are not representative for the AWS location at the glacier surfaces. A detailed description is given in the Supplementary Section S1.

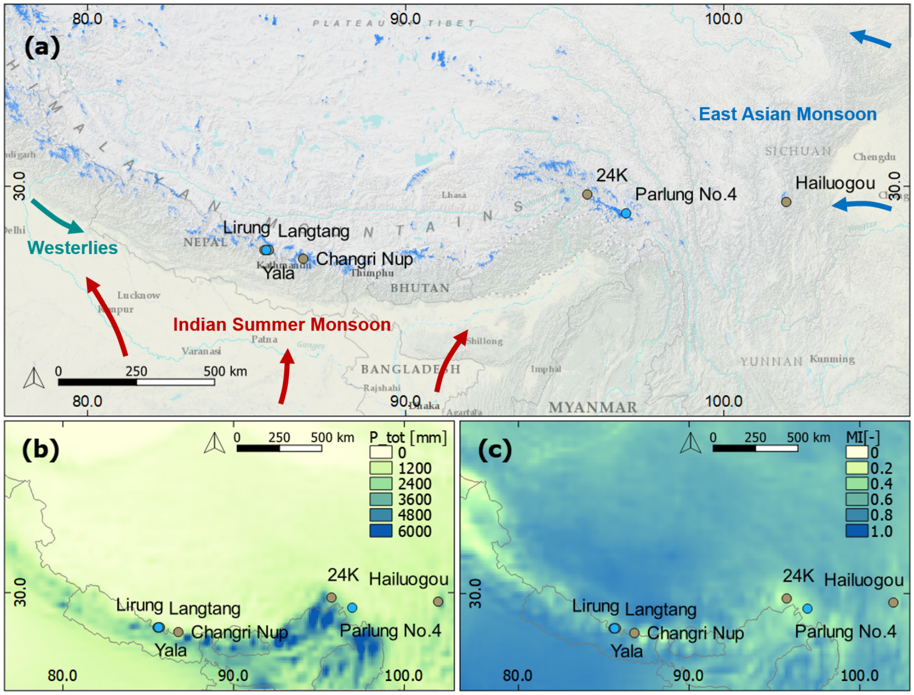

Figure 1. (a) shows the context of study sites with respect to large-scale weather patterns, topography and glacier distribution (blue, source: Randolph Glacier Inventory 6.0). Blue dots indicate clean-ice study glaciers and brown dots indicate debris-covered study glaciers. **(b)** displays the spatial pattern of average annual precipitation from ERA5-Land (1981-2019). **(c)** shows the monsoonal (June-September) portion of the ERA5-Land total annual precipitation (MI). Background map source: ESRI, U.S. National Park Service.

3 Methods

3.1 Tethys-Chloris energy balance model

We use the hydrological, snow and ice modules of the Tethys-Chloris (T&C) land surface model (Fatichi et al., 2012; Paschalis et al., 2018; Mastrotheodoros et al., 2020; Botter et al., 2020) to simulate the mass and energy balance of the seven study glaciers. The T&C model simulates, in a fully distributed manner, the energy and mass budgets of a large range of possible land surfaces, including vegetated land, bare ground, water, snow and ice. Here, we apply the model at the point scale of the AWS locations to simulate the energy fluxes of the underlying surface and subsurface, which can comprise snow, ice and supraglacial debris cover layers, according to the local and dynamic conditions. The melt and accumulation of ice and snow, and the ice melt under debris are also explicitly simulated. The surface energy balances for the three different possible surfaces are for snow,

$$R_n(T_{sno}) + Q_v(T_{sno}) + Q_{fm}(T_{sno}) + H(T_{sno}) + \lambda E(T_{sno}) + G(T_{sno}) - M(T_{sno}) = 0, \tag{1}$$

Table 1. Summary of available meteorological and ablation observations at each site, as well as each site's model period. Variables indicated with * were transferred from neighboring weather station. Variables with ** were reconstructed based on other variables measured at the same station.

	AWS Location				Variables measured			Model period	Reference
	Lat	Lon	Elevation [m.a.s.l.]	Debris thickness [cm]	AWS	Precipitation	Ablation	begin/ end	
Lirung	28.233	85.562	4076	30	$T, RH, W_s, W_d, SW_\downarrow, SW_\uparrow, LW_\uparrow, LW_\downarrow, P^*_{atm}$	Pluvio Kyanging (3857 m.asl, 2.7 km S of AWS) and Yala Basecamp (5090 m.asl, 4.7 km E of AWS) hourly, partly lapsed	SR50	2014-05-05/ 2014-10-24	Ragettli et al. (2015)
Langtang	28.237	85.699	4536	50	T, RH, $W_s, W_d, SW_\downarrow, SW_\uparrow, LW^{**}_\downarrow, LW_\uparrow, P_{atm}$	Pluvio Morimoto base camp 4919m.asl, 2.6km NW of AWS, hourly	SR50	2019-05-11/ 2019-10-30	unpublished
Yala	28.235	85.618	5350	-	$T, RH, W_s, W_d, SW_\downarrow, SW_\uparrow, LW_\uparrow, LW_\downarrow, P^*_{atm}$	Pluvio Yala base camp 5090 m.asl, 1km SW of AWS, hourly	SR50	2019-05-01/ 2019-10-31	ICIMOD (2021)
Changri Nup	27.993	86.780	5470	10	$T, RH, W_s, W_d, SW_\downarrow, SW_\uparrow, LW_\uparrow, LW_\downarrow, P^*_{atm}$	Pluvio at Pyramid meteorological station, 4993 m.asl, 4.9 km SE of AWS location, hourly	SR50	2016-05-01/ 2016-10-31/	Wagnon (2021)
24K	29.765	95.713	3900	20	$T, RH, W_s, W_d, SW_\downarrow, SW_\uparrow, LW_\uparrow, LW_\downarrow, P^*_{atm}$	On-glacier tipping bucket at AWS, hourly	stake	2016-06-01/ 2016-09-29	Yang et al. (2017)
Parlung No.4	29.247	96.930	4806	-	$T, RH, W_s, W_d, SW_\downarrow, SW_\uparrow, LW_\uparrow, LW_\downarrow, P^*_{atm}$	Pluvio, 4600m.asl, 7.9 km NE of AWS, hourly	stake	2016-05-01 2016-10-31	Yang et al. (2017)
Hailuogou	29.558	101.969	3550	1	$T, RH, W_s, W_d, SW_\downarrow, SW_\uparrow, LW_\uparrow, LW_\downarrow, P^*_{atm}$	Pluvio at GAEORS station, 3000m.asl, 1.5km from terminus, hourly	stake	2008-05-15 2008-10-31	Zhang et al. (2011)

Table 2. Characteristics of the study sites. Planimetric glacier and debris surface areas, mean elevation, slope and aspect were calculated using the updated Randolph Glacier Inventory 6.0 by Herreid and Pellicciotti (2020) and the USGS GTOPO30 digital elevation model. Slope (mean) and aspect (vectorial average) for the whole glacier. MI ('Monsoon-Index') is the mean June-September portion of the ERA5-Land total annual precipitation (1981-2019); For Lirung, where the ablation zone has dynamically disconnected from the accumulation zone, the glacier characteristics represent both zones together.

	Area [km^2]		**Elevation [$m.asl$]**			**Slope**	**Aspect**	**MI**
	Glacier	Debris	min	max	median	[°]	[°]	[-]
Lirung (LIR)	4.0	1.5	3990	6830	5010	27.6	151.2	0.74
Langtang (LAN)	37.0	17.8	4500	6620	5330	16.0	177.5	0.71
Yala (YAL)	1.4	-	5170	5660	5390	23.5	229.2	0.74
Changri Nup (CNU)	2.7	1.4	5270	6810	5510	15.9	189.4	0.76
24K (24K)	2.0	0.9	3910	5070	4290	18.3	302.6	0.46
Parlung No.4 (NO4)	11.0	-	4620	5950	5420	17.1	23.5	0.40
Hailuogou (HAI)	24.5	4.1	2980	7470	5340	27.0	104.3	0.56

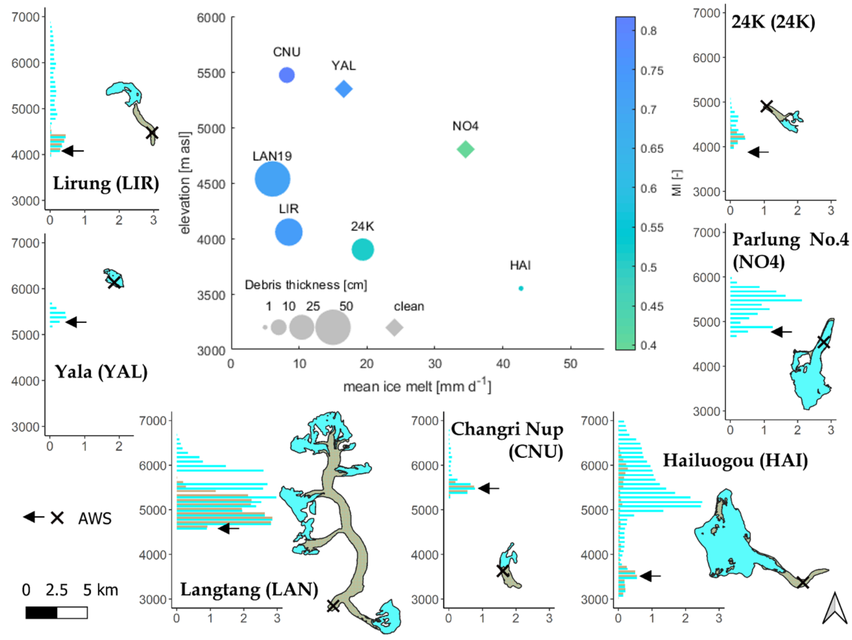

Figure 2. Characteristics of study sites, summarized (center) in terms of elevation, mean measured ice melt rate, measured debris thickness and JJAS contribution to the ERA5-Land total annual (1981-2019) precipitation (monsoon index; MI). For each site, we also show glacier (bars in aqua) and debris (bars in olive) hypsometry, with area on the x-axis [km^2] and altitude on the y-axis [$m.asl$], and glacier and supraglacial debris extents.

for debris cover,

$$R_n(T_{deb}) + Q_v(T_{deb}) + H(T_{deb}) + \lambda E(T_{deb}) + G(T_{deb}) = 0, \tag{2}$$

and for ice,

$$R_n(T_{ice}) + Q_v(T_{ice}) + H(T_{ice}) + \lambda E(T_{ice}) + G(T_{ice}) - M(T_{ice}) = 0, \tag{3}$$

where $R_n\,[W\,m^{-2}]$ is the net radiation absorbed by the snow/debris/ice surface, $Q_v\,[W\,m^{-2}]$ is the energy advected from precipitation, $Q_{fm}\,[W\,m^{-2}]$ is the energy gained or released by melting or refreezing the frozen or liquid water that is held inside the snow pack, $H\,[W\,m^{-2}]$ is the sensible energy flux and $\lambda E\,[W\,m^{-2}]$ the latent energy flux for any of the surfaces, and $G\,[W\,m^{-2}]$ is the conductive energy flux from the surface to the subsurface. In ice, the conduction of energy is represented in the model down to a depth of $2\,m$ after which it is assumed the ice pack is isothermal. Finally, $M\,[W\,m^{-2}]$ is the energy available for snow or ice melt. For debris on top of ice, and snow on top of debris or ice, the in-/outgoing fluxes towards/from the ice are adjusted according to the respective interface type. The sign convention is such that fluxes are positive when directed towards the surface. To close the energy balance, a prognostic temperature for the different surface types (T_{sno}, T_{deb}, T_{ice}) is estimated for each computational element. Iterative numerical methods are used to solve the non-linear energy budget equation until convergence for the ice and snow surface, and the heat diffusion equation for the debris surface, while concurrently computing the mass fluxes resulting from snow and ice melt and sublimation. In the case of snow, debris and ice surfaces, either of which is simulated to always fully cover a computational element, T_{sno}, T_{deb} or T_{ice} are equivalent to the element's overall surface temperature T_s. In the following, we use the surface type specific symbol for surface specific equations, while we use T_s for equations valid for all three surface types.

3.1.1 Radiative fluxes

R_n is calculated as the sum of incoming and outgoing shortwave and longwave fluxes as

$$R_n = SW_{\downarrow}(1-\alpha) + LW_{\downarrow} + LW_{\uparrow}, \tag{4}$$

where $SW_{\downarrow}\,[W\,m^{-2}]$ is the incoming shortwave radiation, $\alpha\,[-]$ is the surface albedo, $LW_{\downarrow}\,[W\,m^{-2}]$ and $LW_{\uparrow}\,[W\,m^{-2}]$ are the incoming atmospheric and outgoing longwave radiation components, respectively. In this study α is given as an input to the model based on the AWS observations. We prescribe α for all surface types as the daily cumulated albedo, which is the 24 hour sum of $SW_{\uparrow}$ divided by the sum of $SW_{\downarrow}$ centred over the time of observation (van den Broeke et al., 2004).

3.1.2 Incoming energy with precipitation

For calculating the incoming energy with precipitation, rain is assumed to fall at air temperature (T_a) when positive, with a lower boundary of 0 $°C$. Snow is assumed to fall at negative T_a with an upper boundary of 0 $°C$. Here, Q_v is the energy required to equalize the precipitation temperature with the surface temperature T_s and is therefore calculated as

$$Q_v = c_w\,P_{r,liq}\,\rho_w\,[max(T_a,0) - T_s] + c_i\,P_{r,sno}\,\rho_w\,[min(T_a,0) - T_s], \tag{5}$$

where $c_w = 4196\,[J\,kg^{-1}\,K^{-1}]$ is the specific heat of water, $c_i = 2093\,[J\,kg^{-1}\,K^{-1}]$ the specific heat of ice, $\rho_w = 1000\,[kg\,m^{-3}]$ is the density of water and $P_{r,liq}\,[mm]$, $P_{r,sno}\,[mm]$ are the rain- and snowfall intensities, respectively.

3.1.3 Phase changes in the snow pack

The snow pack has a water holding capacity Sp_{wc} described in section 3.2.2. The energy flux gained/released by melting/refreezing the frozen/liquid water that is held inside the snow pack is calculated as:

$$Q_{fm}(t) = \begin{cases} f_{sp}\frac{\lambda_f\,\rho_w\,Sp_{wc}(t-dt)}{1000\,dt}, & T_{sno}(t) < 0 \;\; and \;\; T_{sno}(t-dt) \geq 0 \\ -f_{sp}\frac{\lambda_f\,\rho_w\,Sp_{wc}(t-dt)}{1000\,dt}, & T_{sno}(t) \geq 0 \;\; and \;\; T_{sno}(t-dt) < 0 \end{cases} \tag{6}$$

where $f_{sp} = \frac{5}{SWE}\,[-]$ with $max(f_{sp}) = 1$ is the fraction of the snowpack water equivalent ($SWE\,[mm\,w.e.]$) involved in either melting or freezing. This choice was made in order to mimic refreezing in the upper portion of the snowpack, while the snowpack is otherwise represented as a single layer. $\lambda_f = 333700\,[J\,kg^{-1}]$ is the latent energy of melting and freezing of water, t stands for time, $dt\,[s]$ is the timestep, and the unit for T_{sno} is [$^{\circ}C$].

3.1.4 Turbulent energy fluxes

Over snow, debris and ice surfaces, the sensible energy flux is calculated as

$$H = \rho_a\, C_p\, \frac{(T_s - T_a)}{r_{ah}}, \tag{7}$$

where $T_s\,[℃]$ is the surface temperature (generalised term for $T_{sno}, T_{deb}, T_{ice}$), $C_p = 1005 + [(Ta + 23.15)^2]/3364\,[J\,kg^{-1}\,K^{-1}]$ is the specific heat of air at constant pressure, and $\rho_a\,[kg\,m^{-3}]$ is the density of air. The aerodynamic resistance $r_{ah}\,[s\,m^{-1}]$, is calculated using the simplified solution of the Monin-Obokhov similarity theory proposed by Mascart et al. (1995) and implemented in Noilhan and Mahfouf (1996), for details see also supplementary Section S3. The roughness lengths of heat ($z_{0h}\,[m]$) and water vapour ($z_{0w}\,[m]$) used in the calculation of the aerodynamic resistance are equal in the T&C model ($z_{0h} = z_{0w}$), and ($z_{0h} = z_{0w} = 0.1 z_{0m}$), with further details on these choices provided in the supplementary Section S3. The roughness length of momentum (z_{0m}) is set to 0.001 m for snow and ice surfaces (Brock et al., 2000), while we optimize it against the surface temperature for debris (see Section 3.3).
Correct estimates of the latent energy flux due to water phase changes at the surface are important to accurately model glacier melt, especially under moist conditions (Sakai et al., 2004). Phase changes between the water and gas phase and the resulting energy fluxes are considered over all surfaces. The latent energy is limited by the availability of water in the form of ice and snow, or in the case of a debris surface, by the amount of water intercepted (interception storage capacity is set to 2mm). The latent energy flux is estimated from:

$$\lambda E = \lambda_s\, \frac{\rho_a\,(q_{sat}(T_s) - q_a)}{r_{aw}}, \tag{8}$$

where λ_s is the latent energy of sublimation defined as $\lambda_s = \lambda + \lambda_f$, with $\lambda = 1000\,(2501.3 - 2.361\,T_a)\,[J\,kg^{-1}]$ as the latent energy of vaporisation. q_{sat} is the surface specific humidity at saturation at T_s, q_a is the specific humidity of air at the measurement height and r_{aw} the aerodynamic resistance to the vapour flux, which we assume equals r_{ah}.

3.1.5 Ground energy flux

The definition of the ground energy flux $G\,[W\,m^{-2}]$ differs based on the surface type. When there is snow, it is equal to the energy transferred from the snowpack to the underlying ice or debris surface. The snow-pack is represented as a single layer. In the assumption of a slowly changing process, G can be approximated with the temperature difference of the previous time step (t-1), which allows to solve for G outside the numerical iteration to find the snow surface temperature of the current time step:

$$G_{sno}(t) = k_{sno}\,\frac{T_{sno}(t-1) - T_{deb,ice}(t-1)}{d_{sno}} \tag{9}$$

where $k_{sno}\,[W\,K^{-1}\,m^{-1}]$ is the thermal conductivity of snow and $d_{sno}\,[m]$ is the snow depth. For ice, in the absence of snow and debris, it is the energy flux from the ice pack to the underlying surface or to the ice at a depth of $2\,m$:

$$G_{ice}(t) = k_{ice}\,\frac{T_{ice}(t-1) - T_{grd}(t-1)}{d_{ice}} \tag{10}$$

where $k_{ice}\,[W\,K^{-1}\,m^{-1}]$ is the thermal conductivity of ice, $T_{grd}\,[°C]$ is the temperature of the underlying ice, and $d_{ice}\,[m]$ is the relevant ice thickness. The icepack was is not discretized into sub-layers. For debris, which was discretised into eight layers at all debris-covered sites, G is the energy flux conducted into the debris layers. Its calculation is for a given time t and depth z

$$G(z,t) = -k_d\,\frac{\partial T_{deb}(z,t)}{\partial z_d}, \tag{11}$$

where $k_d[W\,K^{-1}\,m^{-1}]$ is the debris thermal conductivity (see section 3.3) and $T_{deb}(z,t)\,[°C]$ is the debris temperature at time t and depth z. $G(z,t)$ can be included in the heat diffusion equation as such:

$$cv_s\,\frac{\partial T_{deb}(z,t)}{\partial t} = \frac{\partial}{\partial z_d}\,(-G(z,t)), \tag{12}$$

where cv_d is the debris heat capacity. Under the assumption of homogeneous debris layers, $\kappa\,[m^2\,s^{-1}]$ as the debris heat diffusivity replaces the term $\frac{k_d}{cv_s}$ and equation (12) can be written as:

$$\frac{\partial T_{deb}(z,t)}{\partial t} = \kappa\frac{\partial^2 T_{deb}(z,t)}{\partial z^2}, \tag{13}$$

The heat diffusion equation (13) is solved using iterative numerical methods. This way, the debris temperature profile $T_{deb}(z,t)$ is solved together with $G(z,t)$ at any depth and time. The conductive energy flux at the base of the debris is used to heat the ice and to calculate ice melt once above the melting point.

Note, that G can also act in the opposite direction, i.e. when energy is conducted from the snowpack/debris/ice towards the surface. In our results, G sums up all types of conductive energy fluxes in the snow-debris-ice column. Part of the energy is used for heating the snow, ice or debris-ice surface layer until melt occurs (G, Table S3).

3.2 Mass balance in the T&C model

3.2.1 Precipitation partition

Precipitation is partitioned into solid Pr_{sno} and liquid Pr_{liq} precipitation, because of the differing impacts of snow and rain on the energy and mass balance. For this study, the precipitation partition method described by Ding et al. (2014) was implemented into the T&C model. This parameterisation has been developed specifically for High Mountain Asia based on a large dataset of rain, sleet and snow observations, and does not require recalibration. It determines the precipitation partition based on the wet-bulb temperature, station elevation and relative humidity and allows for sleet events, as a mixture between liquid and solid precipitation. Ding et al. (2014) found the wet-bulb (T_{wb}) to be a better predictor than T_a of the precipitation type. They also found that the temperature threshold between snow and rain increases at higher elevations, and that the probability of sleet is reduced in conditions of low relative humidity.

3.2.2 Water content of the snow, ice and debris layers

The water content of ice is approximated with a linear reservoir model. The liquid water outflow is proportional to the ice pack water content $Ip_{wc}\,[mm\,w.e.]$, which is initiated when Ip_{wc} exceeds a threshold capacity, prescribed as 1% of the ice water equivalent ($IWE\,[mm\,w.e.]$). The Ip_{wc} is the sum of ice melt and liquid precipitation, minus the water released from the ice pack. The water released is the sum of the ice pack excess water content plus the outflow from the linear reservoir, given as $I_{out} = Ip_{wc}/K_{ice}$, where K_{ice} is the reservoir constant which is proportional to the ice pack water equivalent. Unlike within snow packs, Q_{fm} is not accounted for within the ice pack, since water is presumed to be evacuated quickly from the ice due to runoff without refreezing.

The water content of the snow pack $Sp_{wc}\,[mm\,w.e.]$ is approximated using a bucket model, in which outflow of water from the snow pack occurs when the maximum holding capacity of the snow pack is exceeded. Following the method of Bélair et al. (2003), the maximum holding capacity of the snow pack is based on SWE, a holding capacity coefficient and the density of snow rho_{sno}. Snowmelt plus liquid precipitation, minus the water released from the snow pack gives the current Sp_{wc}. If T_{sno} is greater than $0\,°C$ then the snow pack water content is assumed to be liquid, whereas otherwise it is assumed frozen.

For supraglacial debris, both observations and methods for modelling its water content are lacking. We thus use a simplified scheme for moisture at the surface of the debris, in order to mimic the drying process of the debris surface: We assume debris to have a dynamic interception storage s_{In}, which can hold a maximum of $s_{In,max} = 2\,mm$ water at all debris-covered sites and can be refilled by snowmelt or liquid precipitation. The evaporative flux from the debris is limited by the state of this interception storage and LE can only result from evaporation if $s_{In} > 0$. The term $In\,[\%]$ (used in Section 4.5 and Figure 9b) is the percentage of time, during which this condition is met.

3.2.3 Snow and ice mass balance

The mass balance calculation of snow and ice is rather similar, so they will be described together here. Calculations are performed for snow if there is snow precipitation during a timestep or the modelled SWE at the surface is greater than zero. Net input of energy to the snow or ice pack will increase its temperature, and after the temperature has been raised to the melting point, additional energy inputs will result in melt. The change in the average temperature of the ice or snowpack dT is controlled using:

$$dT = \frac{M\,dt}{c_i\,\rho_w\,WE_b}1000, \tag{14}$$

Where dt is the time step $[h]$ and $WE_b\,[mm\,w.e.]$ is IWE or SWE before melting and limited to a maximum of $2000\,mm$, assumed to be the water equivalent mass exchanging energy with the surface. Energy inputs into an iso-thermal ice/snow pack result in melt $M\,[mm\,w.e.]$ as

$$M = \frac{M\,dt}{\lambda_f\,\rho_w}1000 \tag{15}$$

The water equivalent mass of the snow/ice pack after melting $WE(t)\,[mm\,w.e.]$ is updated conserving the mass balance following:

$$WE(t) = WE(t-dt) + Pr_{sno}(t) - E(t)\,dt - M(t), \tag{16}$$

Here $E = \lambda E/\lambda s\,[mm]$ is the sublimation from ice and snow. The snow density is assumed to be constant with depth and calculations are performed assuming one single snow pack layer. The snow density evolves over time using the method proposed by Verseghy (1991) and improved by Bélair et al. (2003). In this parameterisation the snow density increases exponentially over time due to gravitational settling and is updated when fresh snow is added to the snowpack. Two parameters are required in this scheme, ρ_{sno}^{M1} and $\rho_{sno}^{M2}\,[kg\,m^{-3}]$, which represent the maximum snow density under melting and freezing conditions, respectively. The depth of the ice pack can be increased through the formation of ice from the snow pack (ice accumulation), which is prescribed to occur if the snow density increases to greater than $500\,kg\,m^{-3}$ (a density associated with the firn to ice transition) and at a rate of $0.037\,mm\,h^{-1}$ (Cuffey and Paterson, 2010). The density of ice is assumed constant with depth and equal to $916.2\,kg\,m^{-3}$.

3.3 Debris parameters

A major challenge in physically based mass-balance modelling of debris-covered glaciers is the selection of appropriate debris properties. In addition to the debris thickness, which was measured at the AWS location, values are needed for the thermal conductivity k_d, the aerodynamic roughness lengths z_{0m}, z_{0h} and z_{0w} of the debris surface, the surface emissivity ϵ_d, the debris volumetric heat capacity cv_d and and the debris density ρ_d. While the latter three can be quantified using literature values, there is more uncertainty about k_d and the roughness lengths, which are highly variable quantities that are difficult to measure in the field. We thus choose to optimize them, since our primary requirement is an accurate representation of the energy and mass balance: (1) in a first step, we optimize k_d simulating only the conduction of energy through the debris during snow-free conditions, with the $LW_{\uparrow}$-derived surface temperature $T_{s,LW}$ as an input, the ice melt as the target variable and the Nash-Sutcliffe Efficieny $NSE\,[-]$ as performance metric. (2) Next, we run the whole energy balance model and optimize z_0m, and with it z_0h and z_0w, which are linked to z_0m via a fixed ratio (for details see Section S3). We use the AWS records for snow-free conditions, with all required meteorological inputs, and the optimal k_d from step (1), while comparing modelled T_s against $T_{s,LW}$, using NSE as performance metric. The resulting parameters are given in Table 3. All optimized values fall within the expected range based on prior energy-balance studies on debris-covered glaciers (Nicholson and Benn, 2006; Reid and Brock, 2010; Lejeune et al., 2013; Rounce et al., 2015; Collier et al., 2015; Evatt et al., 2015; Yang et al., 2017; Miles et al., 2017; Quincey et al., 2017; McCarthy, 2018; Rowan et al., 2020).

Table 3. Optimum debris parameters k_d and mean absolute error (MAE) from optimisation step 1 (modelled vs. measured melt). z_0m and Nash Sutcliffe Efficiency (NSE) from optimisation step 2 (modelled vs. measured surface temperature)

Glacier		**Lirung**	**Langtang**	**Changri Nup**	**24K**	**Hailuogou**
kd	$[W\,m^{-1}\,K^{-1}]$	1.09	1.65	1.77	1.45	0.72
MAE	$[mm\,i.e.d^{-1}]$	5.6	21.6	5.2	1.6	2.2
z0m	[m]	0.7	0.38	0.11	0.15	0.027
NSE	[-]	0.93	0.90	0.64	0.95	0.85

3.4 Uncertainty estimation

We calculate the uncertainty associated with all energy and mass balance components by performing 10^3 Monte Carlo simulations for each study site at the AWS location. We perturb three debris parameters (k_d,z_{0m},ϵ_d), debris thickness h_d, as well as six measured model input variables: air temperature T_a, the vapour pressure at reference height $ea[Pa]$, $SW_{\uparrow}$, $SW_{\downarrow}$, $LW_{\downarrow}$, the total precipitation before partition Pr, and the wind speed Ws. Measured outgoing shortwave radiation $SW_{\uparrow}$ was included into the Monte Carlo set, as it determines our input α, as discussed in Section 3.1.1. While the parameter uncertainty range was defined based on previously published values for debris (e.g. Yang et al., 2017; Rounce et al., 2015; Evatt et al., 2015; Reid and Brock, 2010; Nicholson and Benn, 2006; Rowan et al., 2020; Lejeune et al., 2013; Collier et al., 2015; Miles et al., 2017; Quincey et al., 2017; McCarthy, 2018), the debris thickness measurement uncertainty was given with a range of $1\,cm$ and the range for the meteorological inputs was set based on the respective sensor uncertainties (see Table 4). All uncertainties were equally distributed around the standard parameter values and observations. Uncertainties are given as one standard deviation of the error of the Monte Carlo runs against the standard run.

Table 4. Uncertainty ranges of parameters and input variables used for Monte Carlo runs. Where units are indicated with [-], the parameter or variable was perturbed by the fractional value shown.

Parameter/ Variable	Range	Parameter/ Variable	Range
$k_d\,[-]$	±0.1	$SW_{\downarrow}\,[-]$	±0.05
$z0\,[-]$	±0.1	$SW_{\uparrow}\,[-]$	±0.05
$\epsilon_d\,[-]$	±0.05	$LW_{\downarrow}\,[-]$	±0.1
$h_d\,[mm]$	±5	$Pr\,[-]$	±0.15
$Ta\,[℃]$	±0.2	$W_s\,[m/s]$	±0.3
$ea\,[-]$	±0.02		

3.5 Model evaluation

The model accurately reproduces the measured surface height change (ablation and accumulation) at both debris-covered and clean-ice glaciers (Figure 3). The maximum uncertainties associated with each model output ranges from $\pm4\%$ (Parlung No.4, Figure 3f) to $\pm15\%$ (Yala, Figure 3c). Where Ultrasonic Depth Gauge (UDG) records are available (Lirung, Langtang, Yala, Changri Nup), the deviations of the simulations from the observations stay within the uncertainty range (Figure 3a-d). We decided to not consider the UDG record from Changri Nup after a large August snowfall, as variables describing the surface state (e.g. α, $LW_{\uparrow}$) following this event indicate a discontinuous snow cover at the AWS location, while the UDG, which is some meters away from the AWS, shows continuous snow cover with depths of tens of centimeters. This discrepancy was also confirmed by observation of the site from October 2016. It was thus not possible to match the UDG record with the model for the late ablation period on Changri Nup, but the model closely reproduces observed surface height change for the pre-monsoon and early monsoon (Figure 3d), when AWS and UDG observations agree in terms of surface state. The deviation to measured melt stays within the uncertainty range at 24K, Parlung No.4 and Hailuogou (Figure 3e, f). For Parlung No.4 there are no stake measurements available before July 21 due to the long-lasting snow cover.

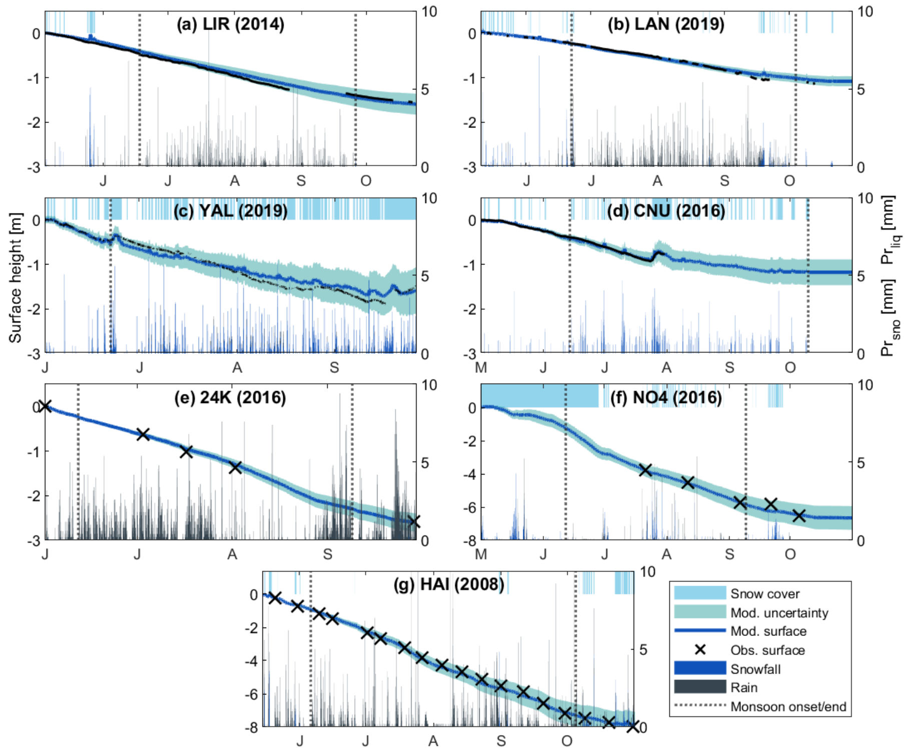

Figure 3. (a)-(g) Observed vs. modelled surface change at all study sites, precipitation phase and snow cover timing. Measured melt is either from ablation stakes (black crosses) or Ultrasonic Depth Gauges (black lines). Vertical dotted lines indicate monsoon onset and end.

4 Results

4.1 Modelled mass balance

The ablation season average melt rates vary considerably across sites: the highest value of $43.4\,mm\,d^{-1}$ is reached at the low-lying site with thin debris cover, Hailuogou, and the lowest value of $6\,mm\,d^{-1}$ is evident at Langtang, a site at moderate elevation but with the thickest debris cover out of all study sites (Figure 4). The largest average seasonal mass loss component at all sites is ice melt, with a minimum of 65.8% of the mass losses at Changri Nup (Figure 4c) and up to 95.4% at Hailuogou, (Figure 4g). This is followed by snowmelt, accounting for only 0.1% at 24K (Figure 4e) but as much as 33.1% at Yala (Figure 4c) of the seasonal mass losses. Sublimation from ice and snow represents a very small share of the seasonal mass losses, and ranges from 0.01% (Lirung, Figure 4a) to 1.2% (Changri Nup, Figure 4d). It mostly occurs under dry conditions during pre-monsoon at the highest sites (Changri Nup, Yala).

The timing of snow cover is an important control of both amounts and patterns of ice melt, as ice melt rates are close to zero during periods of snow cover. This becomes clear in Figure 4, where ice melt rates are low during weeks when

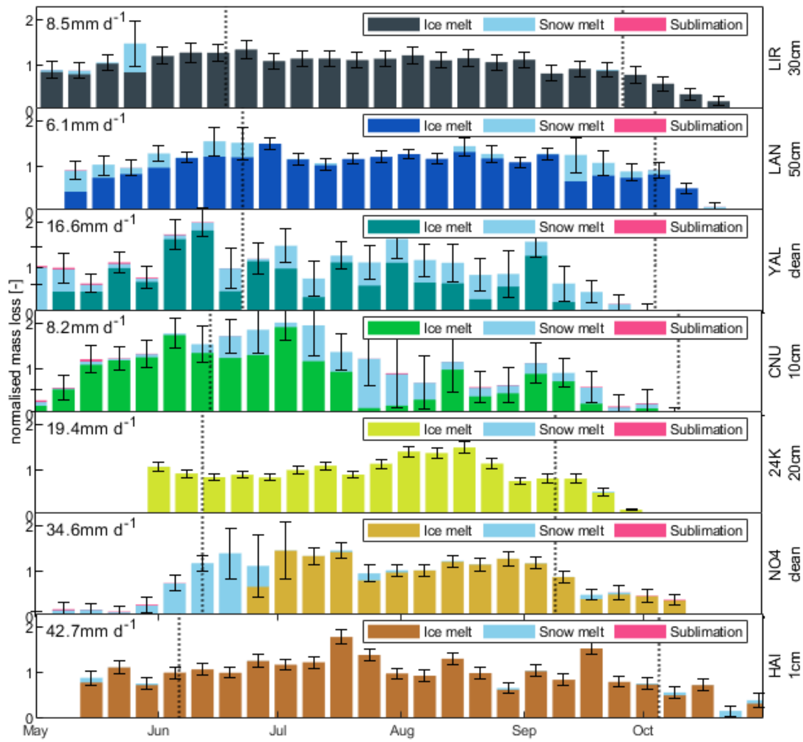

Figure 4. (a)-(g) Melt rates of ice and snow (stacked) as weekly averages at each site. Vertical dotted lines indicate monsoon onset and end. Error bars depict the uncertainty (standard deviation) of the estimates. Melt rates are normalized to the mean of the ice melt over the entire period (value in the upper left of each panel).

also snow melt takes place. A long lasting pre-monsoonal snowpack can delay the onset of ice melt considerably, e.g. at Parlung No.4, where ice melt is delayed until the end of June (Figures 3f and 4f). Similarly, intermittent snow cover protects the ice from melting at the two highest sites (Yala and Changri Nup) during the summer months (Figure 3c-d and 4c-d).

4.2 Modelled energy balance

The largest components in the energy balance are $LW_\uparrow$, $LW_\downarrow$ and $SW_\downarrow$ (Figure S9). The two longwave fluxes counteract and offset each other in large parts resulting in a moderate, melt-reducing LW_{net}, which reaches its highest values during the pre- and post-monsoon (Figure 5). $SW_\downarrow$ and its reflected counterpart $SW_\uparrow$ result in a net shortwave flux SW_{net}, which at all sites contributes the overall largest amount of energy available for melt M (Figure 5). M is additionally increased or reduced by the turbulent fluxes H and LE, while the energy advected to the glacier surface by precipitation (Qv) remains small ($< 2\,W\,m^{-2}$, Table S3). G links the snow/debris/ice surface to the subsurface, and is a result of all surface fluxes and the subsurface conditions. Before ice melt occurs, depending on season and site, a part dG of G between 0 and

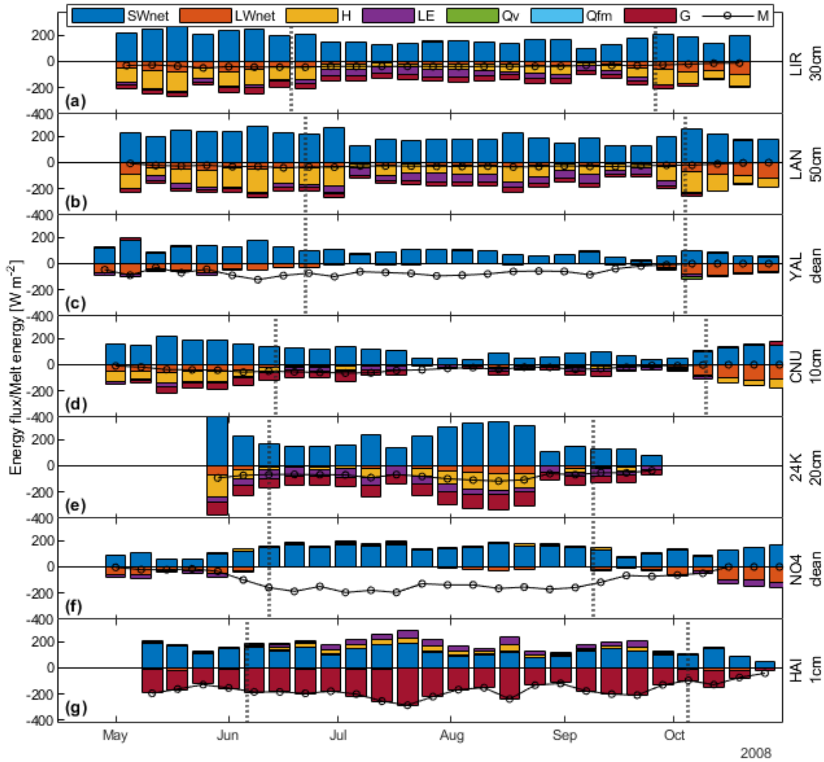

Figure 5. (a)-(g) Stacked energy fluxes weekly averages at each site, depicting the components SW_{net}, LW_{net}, H, LE, Q_v, Q_{fm}, G and M. Energy fluxes are negative fluxes when directed away from the surface and positive when directed towards the surface.

17.8 $W\,m^{-2}$, is invested into warming the debris or ice pack to the melting point (Table S3). dG tends to be larger during pre-monsoon and at the higher sites (Yala, Changri Nup), where air temperatures frequently fall below $0\,°C$.

4.3 Impact of debris cover

Debris cover modulates the energy balance in several ways: with the albedo of the snow-free debris surface ranging between 0.05 (24K) and 0.22 (Changri Nup), a much larger amount of $SW_{\downarrow}$ is absorbed by the surface than on clean ice glaciers, where the albedo typically ranges between 0.3 and 0.6. In contrast to clean-ice glaciers however, where the main flux re-emitting absorbed energy is $LW_{\uparrow}$ (Figure 5c and f), a large part of the debris-absorbed energy is also returned to the atmosphere by the turbulent fluxes H and LE (Figure 5a,b,d and e). As a result of this insulating effect of debris, the seasonal average melt rate of debris-covered 24K is considerably lower ($19.8\,mm\,d^{-1}$) than that of clean-ice Parlung No.4 ($34.4\,mm\,d^{-1}$), despite the latter site being 900 m lower in elevation than the former one (Figure 4e and f), and despite their geographical proximity (Figure 1). On Hailuogou, the site with very thin debris however, the turbulent fluxes act in the opposite direction, i.e. contributing energy for melt. Summed up, they can reach weekly averages of $150\,W\,m^{-2}$ (Figure 5g).

4.4 Impact of the monsoon

During monsoonal conditions, increased cloudiness results in $SW_{\downarrow}$ decreasing its melt contribution at all sites compared to pre-monsoonal conditions (Figure 6) with changes ranging between -41.8 (Hailuogou, pre-monsoon: 178.2; monsoon: 136.4) and -135 (Yala, pre-monsoon: 307.7; monsoon: 172.7) at the seven sites (all values in $W\,m^{-2}$, from Table S3). Note that we express fluxes in terms of the net energy absorbed by, or removed from the snow/debris/ice surface, (with positive and negative fluxes indicating energy absorbed and removed from surface, respectively). Reflected shortwave radiation $SW_{\uparrow}$, which removes energy from the surface, and which is controlled by the surface albedo, becomes less negative (Figure 6), by $+5.4$ (24K, pre: -18.5, mon: -13.8) and up to $+164.8$ (Parlung No.4, pre: -219.6, mon: -54.8) between sites. An exception to this is Changri Nup, where $SW_{\uparrow}$ becomes more negative by $-12.1\,W\,m^{-2}$ (pre: -60.6, mon: -72.7), as a consequence of the high albedo of ephemeral monsoonal snow cover (Figure 3e, Table S3). On the other hand, the melt contribution of $LW_{\downarrow}$ increases at all sites (Figure 6), by at least $+15.7$ (Hailuogou, pre: 314.6, mon: 330.3) and up to $+57.0$ (Yala, pre: 248.5, mon: 305.5) (Table S3). Its counterpart $LW_{\uparrow}$ further reduces melt, but to a lesser extent, by -1.0 (Changri Nup, pre: -318.7, mon: -319.7) to $-13.3\,W\,m^{-2}$ (Langtang, pre: -339.3, mon: -352.8) (Table S3). This balancing of the two LW components changes LW_{net} in the same direction at all sites over the diurnal cycle, with greater changes during the sunlit hours and smaller changes during the dawning and nighttime hours (Figure 7). As a result, LW_{net} plays only a minor role in cooling the glaciers at all sites during monsoon (Figure 5).

4.4.1 Impact of the monsoon on clean-ice sites

We observe opposite changes in M at the two clean-ice glaciers in the transition from pre-monsoon to monsoon: M becomes less negative (implying less melt) at Yala by $+10.2$ (pre: -74.8, mon: -64.6) and more negative at Parlung No.4 (implying more melt) by -130.4 (pre:-32.3, mon: -162.6) (all values in $W\,m^{-2}$, from Table S3). The difference in M is largely caused by the variability in SW_{net}, which almost entirely controls the melt of the clean-ice glaciers during monsoon. On Parlung No.4 the SW_{net} changes are dominated by variations in $SW_{\uparrow}$, whereas on Yala, $SW_{\downarrow}$ dominates. Hence, the bulk of changes in the diurnal melt cycle happen during the sunlit hours (Figure 7b, d). Both H and LE remain comparably small energy fluxes at the clean ice sites with highest averages of $LE = -17.6$ at Parlung No.4 and of $H = -13.7$ at Yala during the pre-monsoon (Table S3). At Parlung No.4, as much as 12.3 is added to the surface in the form of H during monsoon. Interestingly, LE changes from being a melt-reducing energy flux, emerging from sublimation during the pre-monsoon, to a small melt-contributing energy flux from condensation (< 4) at both clean-ice sites (Table S3).

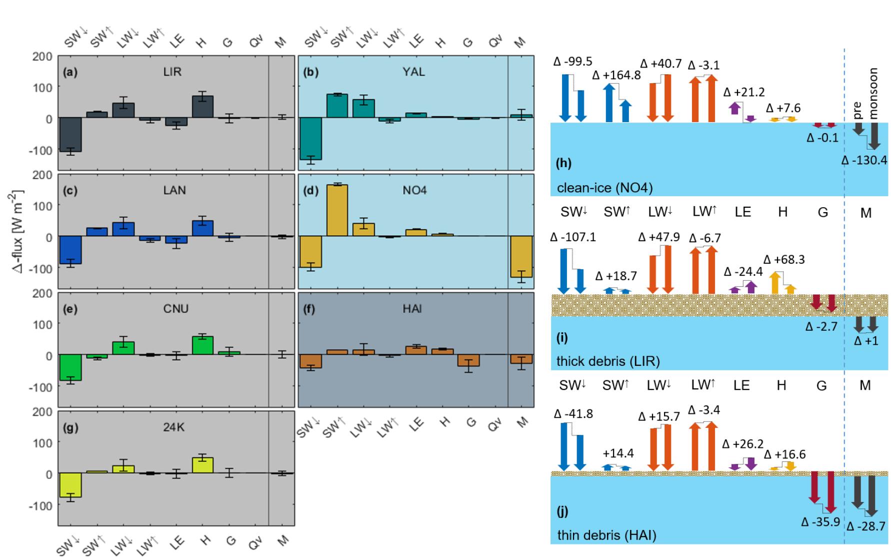

Figure 6. (a)-(g) Differences in energy balance components from pre-monsoon to monsoon at each site including their uncertainties (error bars). The direction of change is to be considered relative to the sign of the original flux (x-axis). Due to the sign convention mentioned in Section 4.3, the presented changes reflect whether the surface receives more energy (positive change) or less energy (negative change). Background indicates the surface type of the site: gray indicates thick debris cover, light blue indicates clean-ice sites, and grey-blue indicates thin debris. **(h)-(j)** Alternative depiction of the changes from (a)-(f), summarizing surface types; Example Δ-flux numbers in [W m-2] refer to (h) Parlung No.4, (i) Lirung and (j) Hailuogou; Numbers for the remaining glaciers can be looked up in Table S3.

4.4.2 Impact of the monsoon on glaciers with thick debris

Average M remains similar between the pre-monsoon and monsoon at the sites with thick debris cover, as the energy balance components adjust to monsoonal conditions: the changes in M, ranging between $+1.0$ (Lirung, pre: -37.5, mon: -36.5) and -2.1 (24K, pre: -79.5, mon: -81.6), stay below uncertainty levels (all values in $W\,m^{-2}$, Figure 6a, c, e, g and Table S3). Similar to the other surface types, LW_{net} reduces melt to a lesser degree during the monsoon (Section 4.4). There is a considerable reduction in the melt-contribution of SW_{net}, and the glacier-cooling H becomes less negative by 49.0 (24K, pre: -99.8, mon: -50.8) up to 68.3 (Lirung, pre: -116.7, mon: -48.4) (Table S3). The change in LE partly offsets the changes in H, with LE becoming more negative, from -2.1 (24K, pre: -50.6, mon: -52.7) to -24.4 (Lirung, pre: -16.0, mon: -40.4) (Figure 6a, c, e and g, and Table S3). Therefore, the changes in the average fluxes from the pre-monsoon to monsoon tend to balance each other out (reduced $SW_{\downarrow}$ and more negative LE are balanced by increased $LW_{\downarrow}$ and less negative H), so that overall melt rates remain similar. This balancing is also visible in the diurnal cycle of changes at Lirung, Changri Nup and 24K, where there is an increase in M during the night-time and morning hours, but a decrease in the afternoon hours (Figure 7 a, e, g). At Changri Nup (Figure 7e), the pattern is accompanied

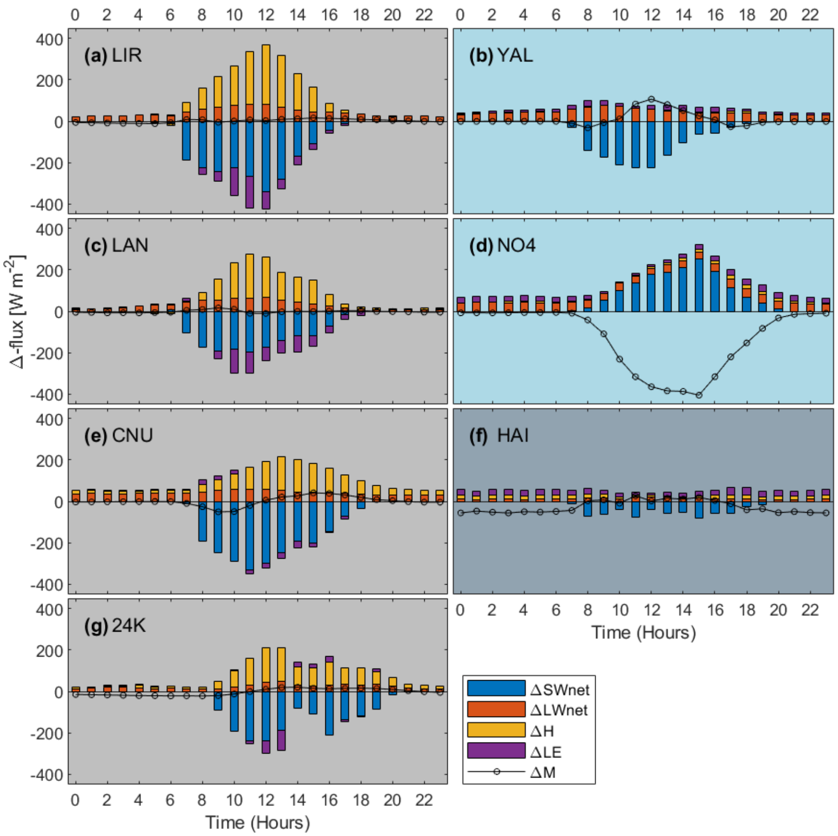

Figure 7. Energy flux differences in the diurnal cycle (stacked) between pre-monsoon and monsoon; The direction of change is to be considered relative to the sign of the orginial flux. Positive and negative sign corresponds to energy added or removed from the glacier, respectively; Grey background indicates debris-covered site, light blue indicates clean ice sites and gray-blue indicates 1cm debris site

by a lag of around four hours between the peak changes of the radiative and turbulent fluxes.

An interruption of the monsoon at 24K occurred in August 2016, possibly associated with an El Niño event (Kumar et al., 2006). During this interruption the energy balance returned to a pre-monsoonal regime (Figure 5e) due to clearer skies, more pronounced diurnal temperature amplitudes, low precipitation rates and lower relative humidity (Figure S6). This left a clear imprint in the diurnal cycle of changes (absence of heavy afternoon overcast in comparison to the other sites, Figure 7g) and resulted in higher melt rates during that period (Figure 4e).

4.4.3 Impact of the monsoon on a glacier with thin debris

In contrast to the glaciers with thick debris, during the monsoon, M becomes considerably more negative (more melt) at Hailuogou Glacier. Although SW_{net} contributes less energy for melt during the monsoon and LW_{net} remains overall small at this site (Figure 5), M became more negative by -28.7 (pre: -158.1, mon: -186.8) on average (all values in $W m^{-2}$, from Table S3), and mostly during the nights (Figure 7f). The increase in melt energy is mostly driven by the turbulent energy fluxes: H increases by 16.6 (pre: 9.1, mon: 25.7) and LE increases by 26.6 (pre: 5.4 mon: 31.6) (Figure 5 and Table S3), with higher increases during the nighttime than during the daytime (Figure 7f). While they act to reduce melt at the glaciers with thick debris cover, here the turbulent fluxes drive additional melt during the monsoon.

4.4.4 Sensitivity of seasonal flux changes to elevation and debris thickness

Our results are derived from simulations at one location (AWS) on each glacier. To understand how representative our results are of conditions across the glacier ablation zone at each site, and across the possible range of debris thicknesses in particular (Table S4), we conduct a sensitivity experiment to evaluate the transferability of our results across the glaciers' ablation areas (see detailed explanation in Supplementary Section S5). This experiment shows that even accounting for the range of conditions across each glacier ablation area, the pattern of pre-monsoon to monsoon difference in flux components, and importantly the equalizing effect on M, remain similar at the glacier scale at all sites with thick debris cover (Figure 8).

4.5 Controls on the turbulent fluxes

Our results show the importance of the turbulent fluxes in the energy balance of debris-covered glaciers, their varying role as melt-enhancing or melt-reducing fluxes depending on the debris thickness, and how the monsoon modulates them.

To assess the controls on the turbulent fluxes we regressed the modelled values of H and LE against climatic variables (see Supplementary Section S6). We find that H is largely controlled by the temperature gradient between surface and air (δ_T) on glaciers with thick debris: between 72 (Lirung, pre-monsoon) and 97% (24K, pre-monsoon) of the variability of H are explained by δ_T (Figure 9a), and δ_T decreases during monsoonal conditions by -0.05 (Langtang) to $-1.44\,°C m^{-1}$ (Changri Nup) (Table S1). It becomes clear that a smaller temperature gradient between surface and air during the monsoon weakens the melt-reducing effect of H. In contrast, Ws emerges as the most important control of H and LE at the glacier with thin debris, explaining up to 91 and 65% of the variability, respectively (Figure 9a). The mean magnitude of Ws increases at this site from 1.23 in pre-monsoon to $2.15 m s^{-1}$ in monsoon (Table S1). A cold surface in combination with a wind-enhanced turbulence and fast turnover of warm and moist air masses results in both H and LE becoming powerful drivers of melt on Hailuogou, the glacier with thin debris cover (Figure 5).

Across the sites with thick debris, vpd has somewhat more explanatory power than Ws in explaining LE (Figure 9a), but combined, their explanatory power does not exceed 52% (Lirung). An exception is the pre-monsoon at Changri Nup, where the combination of vpd and Ws explains 71% of the variability. Yet, LE increases consistently from pre-monsoon to monsoon together with an increase in the duration of moisture availability at the surface of those glaciers, with increases ranging between 22.3% at 24k and 63.1% at Changri Nup (Table S1). In fact, evaporation and its melt-reducing LE flux tend to be water-limited during the pre-monsoon, but energy-limited during the monsoon (Figure 9b). This implies that the availability of additional moisture drives the increase of LE from pre-monsoon to monsoon.

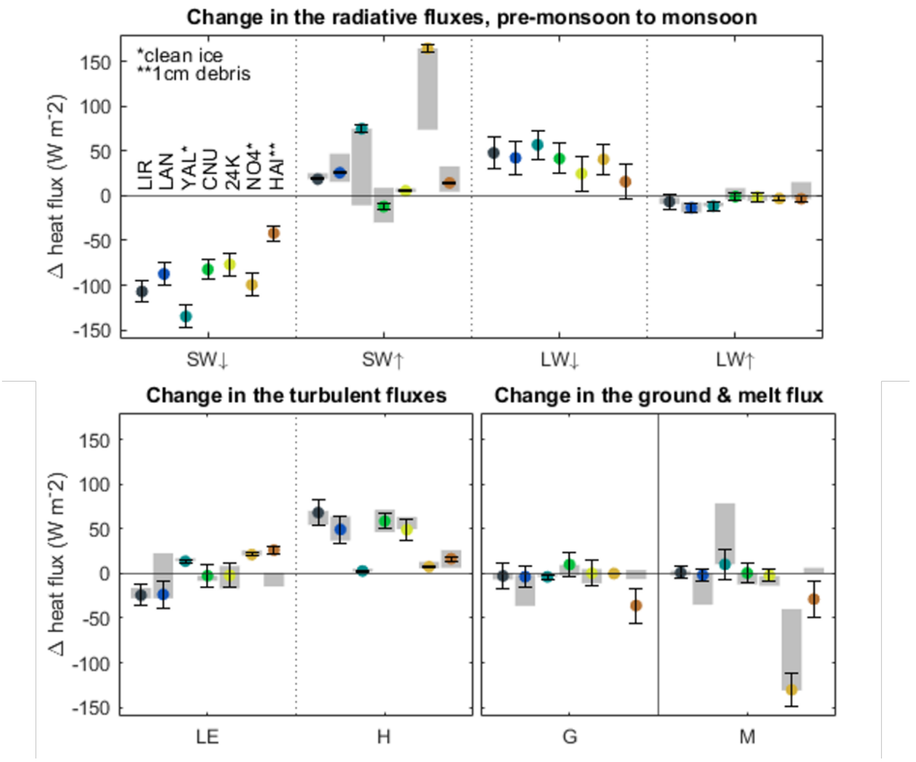

Figure 8. Changes in the individual fluxes when moving from premonsoon to monsoon. Color dots indicate 'standard' runs with AWS site specific conditions. Black bars indicate the uncertainty range on the standard runs. Grey indicates the sensitivity of flux changes (Δ-range) to elevation and debris thickness (debris-covered glaciers only). Ranges of elevation and debris thicknesses used here are given in Table S4. Positive and negative sign corresponds to energy added or removed from the glacier, respectively.

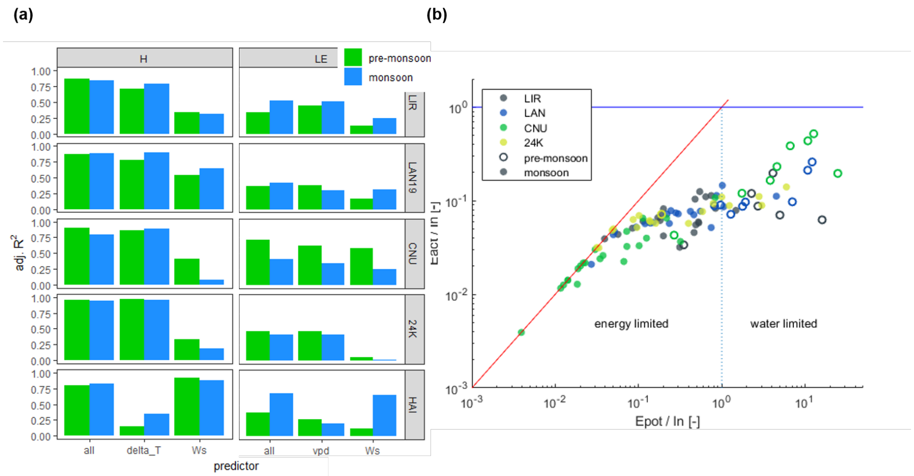

Figure 9. (a) left: Predictive power of temperature gradient between surface and air (δ_T) and wind speed (Ws) and their combination ('all') for determining H. **(a)** right: Predictive power of temperature gradient between surface and air (vpd) and wind speed (Ws) and their combination ('all') for determining LE. Details on the predictors and regression models used are given in Section S6. **(b)** Budyko-like diagram with the 5-day mean potential evaporation rate during snow-free conditions ($Epot$) relative to the mean available intercepted water (In) on the x-axis, and the actual evaporation rate during snow-free conditions ($Eact$) relative to In on the y-axis. Only debris-covered glaciers where LE is a glacier-cooling flux are shown.

5 Discussion

5.1 Which mass and energy fluxes determine the seasonal mass balance of glaciers in the Central and Eastern Himalaya?

We apply our model in a systematic way to seven glaciers in a variety of environments in the Central and Eastern Himalaya. We force the model with in-situ station data and constrain and evaluate it against observations of surface height change, lending great confidence to the energy flux components. Previous energy balance studies in the region were limited to two (Lejeune et al., 2013; Yang et al., 2017; Bonekamp et al., 2019) or three (Zhu et al., 2018) study sites, and partly relied on reanalysis products or atmospheric modelling for forcing (Zhu et al., 2018; Bonekamp et al., 2019), without the possibility to evaluate the model performance. At all our study sites, ice melt is the largest mass loss component during the ablation season, followed by snow melt, while sublimation plays only a small role early and late in the season (Section 4.1). Similar to several previous studies (Kayastha et al., 1999; Aizen et al., 2002; Yang et al., 2011; Sun et al., 2014), we find that the largest energy source for snow and ice melt is SW_{net} (Section 4.2). Thus, major controls on the energy and mass balance of all glaciers are the snowcover dynamics (Zhu et al., 2018) and the associated variations in albedo, which in turn are modulated by the timing of precipitation and the partition of precipitation into rain and snow (Ding et al., 2017; Bonekamp et al., 2019). For example, in the case of Parlung No.4, the onset of glacier melt was delayed until well after monsoon onset, until all snow had disappeared (Section 4.1). After snow has melted out, ephemeral snowcover from monsoonal precipitation increased surface albedo and raised $SW_{\uparrow}$, protecting the ice and suppressing melt rates throughout the summer (Fujita and Ageta, 2000) (Section 4.1). This was especially true at the highest sites (Yala, Changri Nup), highlighting the importance of observations of high-elevation surface condition for constraining seasonal glacier mass balance.

5.2 How does debris cover modulate the energy balance in comparison to clean-ice surfaces?

Previous energy balance studies on debris-covered glaciers were limited to one or two study sites (e.g. Lejeune et al., 2013; Collier et al., 2014; Rounce et al., 2015; Steiner et al., 2018). Applying the model at five sites with debris cover allows us to identify processes that are likely to be common for a large population of debris-covered glaciers in High Mountain Asia. At the four sites with thick debris, our work confirms that debris protects the ice by returning energy to the atmosphere in the form of turbulent fluxes H and LE in addition to $LW_{\uparrow}$ (Yang et al., 2017) and that the turbulent fluxes can be a major component in the energy balance during both dry and wet conditions (Steiner et al., 2018) (Section 4.3). We also find a melt-enhancing effect of thin debris (Östrem, 1959; Reznichenko et al., 2010; Reid and Brock, 2010) at Hailuogou Glacier (Section 4.4.3), and that the turbulent fluxes "work against" this glacier (Section 4.5). Our analysis extends beyond most prior representations however by including a water interception storage (Section 3.2.2), which is capable of mimicking the drying process of the debris (Steiner et al., 2018). Representing this process, which was often neglected in previous studies, allows for a more realistic estimation of LE, which is crucial in it's role as a glacier-cooling flux at the glaciers with thick debris, and as a control of potential melt enhancement of thin debris (Evatt et al., 2015). Uncertainty remains around the size of the interception storage - for this study it was fixed to 2mm - and investigations on the water interception and holding capacity of debris are needed in order to elucidate this process. It's representation however allows us to extend the short-period results of Steiner et al. (2018) to multiple sites and across distinct meteorological conditions, emphasizing the importance of turbulent fluxes for debris-covered glacier energy balance.

5.3 How does the monsoon change the glacier surface energy balance?

The ablation period occurs between April and November at all sites, and all sites are affected by the Indian and East Asian summer monsoons during this period (Figures S2 to S8). A long-term average of 65 to 85% of precipitation arrives during the summer months (June-September) at the Central Himalayan sites (Lirung, Lantang, Yala and Changri Nup, Figure S1 a-d and Table 2) in contrast to 40 to 56% at the eastern sites (24K, Parlung No.4 and Hailuogou, Figure S1 e-g and Table 2). $SW_{\downarrow}$ is reduced at all glacier surfaces due to the reflection and scattering by persistent, heavy clouds (Figure 10). Overcast conditions caused by monsoon also increase $LW_{\downarrow}$ at all sites (Figure 10). Our analysis shows that some effects of monsoon are common for all surface types, while the presence or absence of debris and its thickness control how the incoming energy is absorbed and transmitted to the ice (Figure 10). We therefore provide a synthesis of the changes based on surface types:

5.3.1 Glaciers with thick debris

Overcast cloud cover, increased air temperatures and additional moisture modify the energy balance of debris-covered glaciers, to result in a melt-equalizing effect between pre-monsoon and monsoon (Section 4.3): warm clouds emit additional amounts of energy towards the glacier in the form of $LW_{\downarrow}$ (Figure 10, Section 4.4). H reduces its cooling effect as a consequence of a smaller average temperature gradient between surface and air (Figure 10, Section 4.5). On the other hand, additional evaporative cooling in the form of LE takes place at the wet debris surface, balancing out the other, melt-enhancing changes (Figure 10, Section 4.3). Trade-offs between the first and second halves of the day are likely to play a role in this balancing: Melt-rates increase between the two seasons due to warmer conditions in the morning hours, but decrease as a result of a strong reduction in energy inputs and enhanced evaporative cooling due to moisture availability during the afternoon hours (Figure 7, Section 4.4.2). The debris surface shifts from a water-limited environment during pre-monsoon to an energy-limited process during monsoon (Section 4.5 and Figure 9). We account for the debris water content through the inclusion of a simple interception storage (Section 3.2.2). This allowed us to identify the importance of the glacier-cooling LE coming from the evaporation of liquid water from the debris.

5.3.2 Clean-ice glaciers

In contrast to debris-covered glaciers, when clean-ice glaciers are snow-free and the ice has been heated to the melting point, almost all net radiation goes into ice melt. (Section 4.4.1). Outside of the monsoon, LE removes some energy due to the sublimation of snow and ice. However, when entering the monsoon period, LE tends to switch sign (Figure 10), changing from sublimation/evaporation to condensation, which adds energy to the surface instead of removing it (Section 4.4.1). This behaviour has not been indicated for the drier conditions on the Tibetan Plateau (Mölg et al., 2012; Sun et al., 2014), but has previously been observed at Himalayan sites with a 'southern influence' (Azam et al., 2014; Yang et al., 2017). Similarly, a small H flux is added to the surface at both sites during monsoon. In contrast to the glaciers with thick debris, the energy balance of clean-ice glaciers is highly sensitive to elevation, as shown in our sensitivity experiment (Section S5)

5.3.3 Glacier with thin debris

At the site with thin debris, we observe a melt-enhancing effect during monsoon conditions. The dark debris surface absorbs almost 90% of $SW_{\downarrow}$ in the case of Hailuogou (Table S3), and with a short conduction length ($1\,cm$), the energy influx goes almost entirely to melt. As higher wind speeds enhance turbulence resulting in an increase in H (Section 4.5 and Table S1), warmer and more humid air increases LE inputs from condensation at the cold surface (Table S1 and Figure S8). While these increases in the turbulent fluxes are balanced with regards to M during the day by reductions in SW_{net}, both turbulent fluxes become important sources of additional melt energy during the night (Figure 7 and Section 4.4.3). This adds detailed insights to prior observations and modelling inferences that debris around or below the critical thickness causes higher melt rates than at both clean-ice sites and sites with thicker debris cover (Östrem, 1959; Nakawo

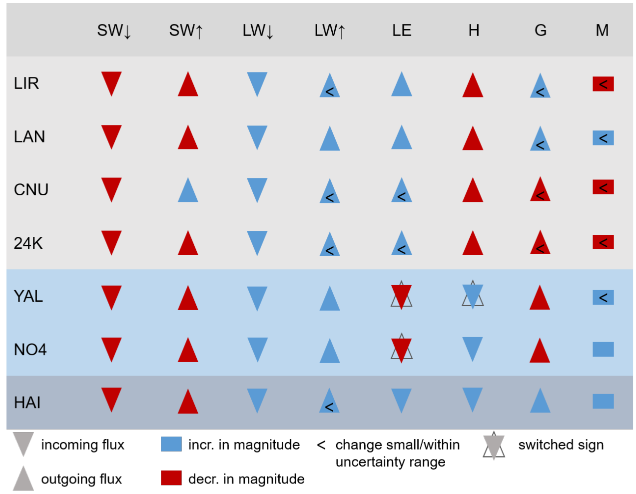

Figure 10. Symbolic representation of changes in energy balance components from pre-monsoon to monsoon. Triangles pointing down/up indicate a positive/negative flux with regards to our sign-convention, where positive/negative means a flux towards/away from the surface. Red/blue indicate an increasing/decreasing value of the flux when moving from pre-monsoon to monsoon. When signs switch, the underlying, empty triangles indicate the pre-monsoonal direction of the flux, while the overlying, colored ones indicate the monsoonal flux

and Rana, 1999; Reznichenko et al., 2010; Reid and Brock, 2010; Evatt et al., 2015; Fyffe et al., 2020). Artificially applying thick debris to Hailuogou, while acknowledging the limitations of this experiment (Section S5), results in the same change pattern as the one observed on the other debris-covered glaciers: Melt rates remain almost unchanged when going from pre-monsoon to monsoon (Section S5).

5.4 Implications for Himalayan glaciers in a changing climate

Monsoon-influenced, summer-accumulation glaciers (such as Langtang, Lirung, Yala, and Changri Nup) have been previously shown to be especially vulnerable to warming due to a decrease in accumulation and an enhancement of ablation due to reduced albedo (Fujita and Ageta, 2000), and our results confirm that SW_{net} is the key control on monsoon-period melt rates for clean-ice glaciers (Section 4.4.1). Our results also emphasize that the longevity of pre-monsoon snowcover into the monsoon period is a key control on melt rates (Section 4.1), supporting past findings that the strength and timing of the monsoon onset has a profound impact on small mountain glaciers (Mölg et al., 2014, 2012) through the phase change of precipitation in the transition to monsoon conditions (Fujita and Ageta, 2000; Ding et al., 2017; Zhu et al., 2018). Importantly, our insights into the differential response of glaciers with different surface types to the monsoon and its onset offers keys to interpret their future response under a changing climate:

All future climate scenarios agree on continued warming during the 21st century over High Mountain Asia (Masson-Delmotte, 2021), together with a strengthening of elevation dependent warming (Palazzi et al., 2017) and increases in moisture availability (Masson-Delmotte, 2021). An analysis on the ensemble estimates of regionally downscaled CMIP5 projections (CORDEX) for the Himalayas (Sanjay et al., 2017) shows that total summer precipitation is projected to increase for 2036-2065 (2066-2095) by 4.4% (10.5%) in the Central Himalaya and by 6.8% (10.4%) in the Eastern Himalaya under RCP4.5 scenarios, relative to 1976-2005. While there is broad model consensus on the increase in future precipitation, there is little consensus on the future variability, frequency and spatial distribution of precipitation across High Mountain Asia (Kadel et al., 2018; Sanjay et al., 2017). A slight shift towards an earlier monsoon onset of <5 days over the coming century together with an increasing shift towards a later retreat by 5 to 10 days (mid-century) and 10 to 15 days (end-century) might increase the length of the monsoon period, with stronger lengthening in the Eastern Himalaya (Moon and Ha, 2020).

The prospect of warmer temperatures together with increased precipitation would (1) cause a shift in the precipitation partition from snow to rain in the monsoon, resulting in snow cover shifting to higher elevations and increasing total melt; (2) potentially lead to an increase in early spring snowfall, which would delay the onset of ice melt; (3) increase the likelihood of ephemeral monsoonal snow cover but move it to higher elevations, thus leaving more of the lower ablation zones exposed; (4) increase the wet-bulb temperature together with humidity to result in a further reduction of the solid fraction of precipitation during monsoon. Overall it is likely that glacier ablation zones will be exposed for longer periods under future monsoon climate due to a net decrease of the snow covered duration, with a resulting increase in total ablation. A lengthening of the monsoon into autumn, on the other hand, (Moon and Ha, 2020) would somewhat offset warmer air temperatures with regards to the late-season melt for all glacier types.

The expected warmer and wetter monsoonal conditions, including increased cloudiness, will likely result in an overall increase of melt rates on clean-ice and glaciers with debris cover around or below the critical thickness. This is because (1) they are more directly controlled by net radiation (comprising both short- and long-wave fluxes), which is likely to increase in magnitude (Section 4.4.1); (2) the turbulent fluxes towards cold surfaces are also likely to increase in magnitude, and they tend to 'work against' these types of glaciers (4.4.1 and 4.4.3). Melt rates might increase to a lesser degree on debris-covered glaciers, since the turbulent fluxes 'work for' the glaciers with debris above the critical thickness, and the melt-equalising effect of debris under monsoon (Section 4.4.2) might remain in place. These components could sum up to have an overall protective effect on glaciers with thick debris, allowing them to potentially resist the projected changes in the monsoonal summer longer into the future. Previous studies hypothesised that the mass balance of debris-covered glaciers might be less sensitive to climate warming than clean-ice glaciers (e.g. Anderson and Mackintosh, 2012; Wijngaard et al., 2019; Mattson, 2000). Here we additionally suggest that this difference in sensitivity could even be stronger in the monsoonal environments of the Central and Eastern Himalaya. Similarly, we suggest that glaciers with debris under the critical thickness might be even more sensitive to future monsoons than clean-ice glaciers. New energy-balance modelling studies incorporating similar datasets and future projections might provide answers to these yet open questions.

5.5 Limitations

By applying an energy balance model to seven sites across the Central and Eastern Himalaya, we have identified monsoon effects on the ablation season energy and mass balance of glaciers, common for our studied debris-covered and clean-ice glaciers. A list of criteria used for choosing our modelling periods at each site is given in the Supplementary Material Section S2. Applying these criteria, we chose one summer season record for each site, for which all required variables were available at a high level of data quality. As a result of this selection process, our analysis remained limited to one summer season at each site. Our study has also highlighted knowledge gaps which require further study: First, the influence of spring and monsoonal snow cover (its timing and amount) on the seasonal glacier mass balance is currently difficult to discern due to the paucity of multi-annual data sets in High Mountain Asia. Second, the timing and quantity of post-monsoon and winter precipitation influence the annual mass balance, however, even fewer datasets exist for the winter half-year in HMA, preventing a year-round analysis of similar detail. Third, all our sites are located in glacier ablation areas, and surface and energy mass fluxes will change with elevation. While we have tested how representative our point-scale results are for the entire ablation area of the glaciers considered, the response of glacier accumulation areas to monsoon remains to be investigated. Meteorological data from accumulation areas are scarce, however, limiting our current understanding. Future work should establish new year-round and multi-year records, including datasets from accumulation areas, in order to extend some of our findings. Future work could also target the spatial distribution of forcing data and parameters necessary to run energy-balance models at the glacier-scale.

6 Conclusions

We model the energy and mass balance of seven glaciers in the Central and Eastern Himalaya at seven on-glacier weather stations. We find that:

1. At all sites, the largest mass loss component during the ablation season is ice melt, followed by snowmelt and sublimation, while the last only plays a role at our highest sites and outside of the core monsoon. We find that the seasonal energy and mass balance is strongly controlled by variations of absorbed shortwave radiation, a result of the prevalence of spring snow cover and the occurence of ephemeral monsoonal snow accumulation.

2. Debris cover above the critical thickness returns most of the energy it absorbs back to the atmosphere via longwave emission and turbulent heat fluxes. While H is primarily controlled by the temperature gradient between surface and air, LE is controlled by the availability of liquid water at the debris surface. When debris is around or under the critical thickness, the melt is more directly radiation-driven. In this case, however, melt is additionally increased by the turbulent fluxes H and LE, for which wind speed is the primary control. The cold surface favours condensation rather than evaporation as well as sensible heat exchange into the glacier surface.

3. The response of the glacier mass and energy balance to the monsoon depends on the surface type: melt-rates tend to increase compared to the pre-monsoon at the clean-ice glaciers and the glacier with thin debris cover (with

the exception of Yala), while they stay similar at the glaciers with thick debris cover. We attribute these differences to the role the turbulent fluxes play for each surface type. At the glaciers with thick debris cover, where the turbulent fluxes 'work for' the glacier, evaporation of the additionally available moisture (LE) provides extra cooling during the monsoon. The evaporation of liquid water is a moisture limited process during the pre-monsoon and turns into an energy-limited process during the monsoon. The monsoonal decrease in $SW_{\downarrow}$ is further offset by an increase in $LW_{\downarrow}$ and a decrease in cooling induced by H, with the result of unchanged available melt-energy M during monsoon. In a sensitivity experiment, we confirm that these results are representative of the entire ablation zones of the thickly debris-covered glaciers. At the clean-ice sites, in contrast, the melt is mostly radiation controlled throughout the ablation season and varies greatly over the elevation profile of the ablation zone. The turbulent fluxes play a subordinate role there, but can switch from melt-reducing to melt-enhancing in the seasonal transition into the monsoon. At the thin debris-covered site, on the other hand, the turbulent fluxes always 'work against' the glacier and intensify during the monsoon.

Given these findings, under projected future monsoonal conditions, namely warmer and possibly longer and wetter monsoons (Sanjay et al., 2017; Moon and Ha, 2020; Masson-Delmotte, 2021), the summer season mass balance of glaciers with thick debris-cover might react less sensitively than the one of clean-ice glaciers and glaciers with thin debris. We encourage future research to answer this still open question.

Code and data availability. All AWS datasets for the modelling periods considered in the analysis, together with ablation measurements, pre-processed forcing data, T&C model codes, outputs and scripts for analysing outputs are available under the following link: https://doi.org/10.5281/zenodo.6280986 . When previously published elsewhere, references and links to the full, original datasets are provided in the data repository.

Author contributions. SFu, FP and EM designed the study. SFu carried out the analysis with the help of CF, MM and SFa. SFu interpreted the results, created the figures and wrote the manuscript with the help of CF, EM, MM, TS and FP. SFa, PW, WI, and QL reviewed the manuscript. WY and BD facilitated field data collection and provided parameterisations for albedo and precipitation phase. WY, PW and WI also contributed data sets.

Competing interests. The authors declare that they have no conflict of interest.

Acknowledgements. This project has received funding from the European Research Council (ERC) under the European Union's Horizon 2020 research and innovation programme (grant agreement No 772751), RAVEN, "Rapid mass losses of debris-covered glaciers in High Mountain Asia". The National Natural Science Foundation of China (41961134035) financially supported the data collection on 24K and Parlung No.4 glaciers. We would like to thank our four anonymous reviewers, who's comments greatly helped to improve the manuscript. We would also like to thank Jakob Steiner and ICIMOD for hosting and contributing datasets. Our special thanks go to Marin Kneib for organizing the field campaigns, and the Langtang and 24K field teams for making the data collection possible.

References

Aizen, V., Aizen, E., and Nikitin, S.: Glacier regime on the northern slope of the Himalaya (Xixibangma glaciers), Quaternary International, 97, 27–39, 2002.

Anderson, B. and Mackintosh, A.: Controls on mass balance sensitivity of maritime glaciers in the Southern Alps, New Zealand: the role of debris cover, Journal of Geophysical Research: Earth Surface, 117, 2012.

Azam, M., Wagnon, P., Vincent, C., Ramanathan, A., Favier, V., Mandal, A., and Pottakkal, J.: Processes governing the mass balance of Chhota Shigri Glacier (western Himalaya, India) assessed by point-scale surface energy balance measurements, Cryosphere, 8, 2195–2217, 2014.

Bélair, S., Crevier, L.-P., Mailhot, J., Bilodeau, B., and Delage, Y.: Operational implementation of the ISBA land surface scheme in the Canadian regional weather forecast model. Part I: Warm season results, Journal of hydrometeorology, 4, 352–370, 2003.

Beljaars, A. C.: The parametrization of surface fluxes in large-scale models under free convection, Quarterly Journal of the Royal Meteorological Society, 121, 255–270, 1995.

Bonekamp, P. N., de Kok, R. J., Collier, E., and Immerzeel, W. W.: Contrasting meteorological drivers of the glacier mass balance between the Karakoram and central Himalaya, Frontiers in Earth Science, 7, 107, 2019.

Bookhagen, B. and Burbank, D. W.: Toward a complete Himalayan hydrological budget: Spatiotemporal distribution of snowmelt and rainfall and their impact on river discharge, Journal of Geophysical Research: Earth Surface, 115, 2010.

Botter, M., Zeeman, M., Burlando, P., and Fatichi, S.: Impacts of fertilization on grassland productivity and water quality across the European Alps: insights from a mechanistic model, Biogeosciences Discussions, pp. 1–35, 2020.

Brock, B. W., Willis, I. C., and Sharp, M. J.: Measurement and parameterization of albedo variations at Haut Glacier d'Arolla, Switzerland, Journal of Glaciology, 46, 675–688, 2000.

Brun, F., Berthier, E., Wagnon, P., Kääb, A., and Treichler, D.: A spatially resolved estimate of High Mountain Asia glacier mass balances from 2000 to 2016, Nature geoscience, 10, 668–673, 2017.

Brutsaert, W.: The surface roughness parameterization, Springer, 1982.

Collier, E. and Immerzeel, W. W.: High-resolution modeling of atmospheric dynamics in the Nepalese Himalaya, Journal of Geophysical Research: Atmospheres, 120, 9882–9896, 2015.

Collier, E., Nicholson, L., Brock, B., Maussion, F., Essery, R., and Bush, A.: Representing moisture fluxes and phase changes in glacier debris cover using a reservoir approach, The Cryosphere, 8, 1429–1444, 2014.

Collier, E., Maussion, F., Nicholson, L., Mölg, T., Immerzeel, W., and Bush, A.: Impact of debris cover on glacier ablation and atmosphere-glacier feedbacks in the Karakoram, 2015.

Cuffey, K. M. and Paterson, W. S. B.: The physics of glaciers, Academic Press, 2010.

Ding, B., Yang, K., Qin, J., Wang, L., Chen, Y., and He, X.: The dependence of precipitation types on surface elevation and meteorological conditions and its parameterization, Journal of hydrology, 513, 154–163, 2014.

Ding, B., Yang, K., Yang, W., He, X., Chen, Y., Guo, X., Wang, L., Wu, H., and Yao, T.: Development of a Water and Enthalpy Budget-based Glacier mass balance Model (WEB-GM) and its preliminary validation, Water Resources Research, 53, 3146–3178, 2017.

Evatt, G. W., Abrahams, I. D., Heil, M., Mayer, C., Kingslake, J., Mitchell, S. L., Fowler, A. C., and Clark, C. D.: Glacial melt under a porous debris layer, Journal of Glaciology, 61, 825–836, 2015.

Farinotti, D., Huss, M., Fürst, J. J., Landmann, J., Machguth, H., Maussion, F., and Pandit, A.: A consensus estimate for the ice thickness distribution of all glaciers on Earth, Nature Geoscience, 12, 168–173, 2019.

Farinotti, D., Immerzeel, W. W., de Kok, R. J., Quincey, D. J., and Dehecq, A.: Manifestations and mechanisms of the Karakoram glacier Anomaly, Nature Geoscience, 13, 8–16, 2020.

Fatichi, S.: The modeling of hydrological cycle and its interaction with vegetation in the framework of climate change, Ph.D. thesis, Technische Universität Braunschweig, 2010.

Fatichi, S., Ivanov, V. Y., and Caporali, E.: A mechanistic ecohydrological model to investigate complex interactions in cold and warm water-controlled environments: 1. Theoretical framework and plot-scale analysis, Journal of Advances in Modeling Earth Systems, 4, 2012.

Fujita, K Sakai, A. et al.: Modelling runoff from a Himalayan debris-covered glacier, Hydrol. Earth Syst. Sci, 18, 2679–2694, 2014.

Fujita, K. and Ageta, Y.: Effect of summer accumulation on glacier mass balance on the Tibetan Plateau revealed by mass-balance model, Journal of Glaciology, 46, 244–252, 2000.

Fujita, K., Takeuchi, N., and Seko, K.: Glaciological observations of Yala Glacier in Langtang Valley, Nepal Himalayas, 1994 and, Bulletin of Glacier Research, 16, 75–8, 1998.

Fyffe, C. L., Woodget, A. S., Kirkbride, M. P., Deline, P., Westoby, M. J., and Brock, B. W.: Processes at the margins of supraglacial debris cover: quantifying dirty ice ablation and debris redistribution, Earth Surface Processes and Landforms, 2020.

Gardelle, J., Berthier, E., and Arnaud, Y.: Slight mass gain of Karakoram glaciers in the early twenty-first century, Nature geoscience, 5, 322–325, 2012.

Giese, A., Boone, A., Wagnon, P., and Hawley, R.: Incorporating moisture content in surface energy balance modeling of a debris-covered glacier, The Cryosphere, 14, 1555–1577, 2020.

Herreid, S. and Pellicciotti, F.: The state of rock debris covering Earth's glaciers, Nature Geoscience, pp. 1–7, 2020.

Heynen, M., Miles, E., Ragettli, S., Buri, P., Immerzeel, W. W., and Pellicciotti, F.: Air temperature variability in a high-elevation Himalayan catchment, Annals of Glaciology, 57, 212–222, 2016.

ICIMOD: AWS Yala Glacier [Data set]. ICIMOD., 2021.

Immerzeel, W. W., Van Beek, L., Konz, M., Shrestha, A., and Bierkens, M.: Hydrological response to climate change in a glacierized catchment in the Himalayas, Climatic change, 110, 721–736, 2012.

Immerzeel, W. W., Kraaijenbrink, P. D., Shea, J., Shrestha, A. B., Pellicciotti, F., Bierkens, M. F., and de Jong, S. M.: High-resolution monitoring of Himalayan glacier dynamics using unmanned aerial vehicles, Remote Sensing of Environment, 150, 93–103, 2014.

Ivanov, V. Y., Bras, R. L., and Vivoni, E. R.: Vegetation-hydrology dynamics in complex terrain of semiarid areas: 1. A mechanistic approach to modeling dynamic feedbacks, Water Resources Research, 44, 2008.

Kadel, I., Yamazaki, T., Iwasaki, T., and Abdillah, M. R.: Projection of future monsoon precipitation over the central Himalayas by CMIP5 models under warming scenarios, Climate Research, 75, 1–21, 2018.

Kaser, G., Großhauser, M., and Marzeion, B.: Contribution potential of glaciers to water availability in different climate regimes, Proceedings of the National Academy of Sciences, 107, 20 223–20 227, 2010.

Kayastha, R. B., Ohata, T., and Ageta, Y.: Application of a mass-balance model to a Himalayan glacier, Journal of Glaciology, 45, 559–567, 1999.

Kraaijenbrink, P., Bierkens, M., Lutz, A., and Immerzeel, W.: Impact of a global temperature rise of 1.5 degrees Celsius on Asia's glaciers, Nature, 549, 257–260, 2017.

Kumar, K. K., Rajagopalan, B., Hoerling, M., Bates, G., and Cane, M.: Unraveling the mystery of Indian monsoon failure during El Niño, Science, 314, 115–119, 2006.

Lejeune, Y., Bertrand, J.-M., Wagnon, P., and Morin, S.: A physically based model of the year-round surface energy and mass balance of debris-covered glaciers, Journal of Glaciology, 59, 327–344, 2013.

Liao, H., Liu, Q., Zhong, Y., and Lu, X.: Landsat-based estimation of the glacier surface temperature of Hailuogou glacier, Southeastern Tibetan Plateau, between 1990 and 2018, Remote Sensing, 12, 2105, 2020.

Mascart, P., Noilhan, J., and Giordani, H.: A modified parameterization of flux-profile relationships in the surface layer using different roughness length values for heat and momentum, Boundary-Layer Meteorology, 72, 331–344, 1995.

Masson-Delmotte, V., P. Z. A. P. S. L. C. C. P. S. B. N. C. Y. C. L. G. M. I. G. M. H. K. L. E. L. J. B. R. M. T. K. M. T. W. O. Y. R. Y. B. Z.: IPCC, 2021: Climate Change 2021: The Physical Science Basis. Contribution of Working Group I to the Sixth Assessment Report of the Intergovernmental Panel on Climate Change, Cambridge University Press. In Press., 2021.

Mastrotheodoros, T., Pappas, C., Molnar, P., Burlando, P., Manoli, G., Parajka, J., Rigon, R., Szeles, B., Bottazzi, M., Hadjidoukas, P., et al.: More green and less blue water in the Alps during warmer summers, Nature Climate Change, 10, 155–161, 2020.

Mattson, L. E.: The influence of a debris cover on the mid-summer discharge of Dome Glacier, Canadian Rocky Mountains, IAHS PUBLICATION, pp. 25–34, 2000.

Maussion, F., Scherer, D., Mölg, T., Collier, E., Curio, J., and Finkelnburg, R.: Precipitation seasonality and variability over the Tibetan Plateau as resolved by the High Asia Reanalysis, Journal of Climate, 27, 1910–1927, 2014.

McCarthy, M. J.: Quantifying supraglacial debris thickness at local to regional scales, Ph.D. thesis, Scott Polar Research Institute and British Antarctic Survey, 2018.

Miles, E. S., Steiner, J. F., and Brun, F.: Highly variable aerodynamic roughness length (z0) for a hummocky debris-covered glacier, Journal of Geophysical Research: Atmospheres, 122, 8447–8466, 2017.

Mölg, T., Maussion, F., Yang, W., and Scherer, D.: The footprint of Asian monsoon dynamics in the mass and energy balance of a Tibetan glacier, The Cryosphere, 6, 1445, 2012.

Mölg, T., Maussion, F., and Scherer, D.: Mid-latitude westerlies as a driver of glacier variability in monsoonal High Asia, Nature Climate Change, 4, 68–73, 2014.

Monin, A. and Obukhov, A.: Main characteristics of turbulent mixing in atmosphericsurface boundary, Works Geophysical Institute, AS USSR, 24, 3–17, 1954.

Moon, S. and Ha, K.-J.: Future changes in monsoon duration and precipitation using CMIP6, npj Climate and Atmospheric Science, 3, 1–7, 2020.

Muñoz Sabater, J.: ERA5-Land monthly averaged data from 1981 to present .Copernicus Climate Change Service (C3S) Climate Data Store (CDS). (Accessed on 01-10-2020), 2019.

Nakawo, M. and Rana, B.: Estimate of ablation rate of glacier ice under a supraglacial debris layer, Geografiska Annaler: Series A, Physical Geography, 81, 695–701, 1999.

Nicholson, L. and Benn, D. I.: Calculating ice melt beneath a debris layer using meteorological data, Journal of Glaciology, 52, 463–470, 2006.

Noilhan, J. and Mahfouf, J.-F.: The ISBA land surface parameterisation scheme, Global and planetary Change, 13, 145–159, 1996.

Östrem, G.: Ice melting under a thin layer of moraine, and the existence of ice cores in moraine ridges, Geografiska Annaler, 41, 228–230, 1959.

Palazzi, E., Filippi, L., and von Hardenberg, J.: Insights into elevation-dependent warming in the Tibetan Plateau-Himalayas from CMIP5 model simulations, Climate Dynamics, 48, 3991–4008, 2017.

Paschalis, A., Fatichi, S., Pappas, C., and Or, D.: Covariation of vegetation and climate constrains present and future T/ET variability, Environmental Research Letters, 13, 104 012, 2018.

Pratap, B., Dobhal, D., Mehta, M., and Bhambri, R.: Influence of debris cover and altitude on glacier surface melting: a case study on Dokriani Glacier, central Himalaya, India, Annals of Glaciology, 56, 9–16, 2015.

Quincey, D., Smith, M., Rounce, D., Ross, A., King, O., and Watson, C.: Evaluating morphological estimates of the aerodynamic roughness of debris covered glacier ice, Earth Surface Processes and Landforms, 42, 2541–2553, 2017.

Ragettli, S., Pellicciotti, F., Immerzeel, W. W., Miles, E. S., Petersen, L., Heynen, M., Shea, J. M., Stumm, D., Joshi, S., and Shrestha, A.: Unraveling the hydrology of a Himalayan catchment through integration of high resolution in situ data and remote sensing with an advanced simulation model, Advances in Water Resources, 78, 94–111, 2015.

Reid, T. D. and Brock, B. W.: An energy-balance model for debris-covered glaciers including heat conduction through the debris layer, Journal of Glaciology, 56, 903–916, 2010.

Reznichenko, N., Davies, T., Shulmeister, J., and McSaveney, M.: Effects of debris on ice-surface melting rates: an experimental study, Journal of Glaciology, 56, 384–394, 2010.

Rounce, D., Quincey, D., and McKinney, D.: Debris-covered glacier energy balance model for Imja-Lhotse Shar Glacier in the Everest region of Nepal, 2015.

Rowan, A. V., Nicholson, L. I., Quincey, D. J., Gibson, M. J., Irvine-Fynn, T. D., Watson, C. S., Wagnon, P., Rounce, D. R., Thompson, S. S., Porter, P. R., et al.: Seasonally stable temperature gradients through supraglacial debris in the Everest region of Nepal, Central Himalaya, Journal of Glaciology, pp. 1–12, 2020.

Sakai, A. and Fujita, K.: Contrasting glacier responses to recent climate change in high-mountain Asia, Scientific reports, 7, 1–8, 2017.

Sakai, A., Fujita, K., and Kubota, J.: Evaporation and percolation effect on melting at debris-covered Lirung Glacier, Nepal Himalayas, 1996, Bulletin of glaciological research, 21, 9–16, 2004.

Sanjay, J., Krishnan, R., Shrestha, A. B., Rajbhandari, R., and Ren, G.-Y.: Downscaled climate change projections for the Hindu Kush Himalayan region using CORDEX South Asia regional climate models, Advances in Climate Change Research, 8, 185–198, 2017.

Scherler, D., Bookhagen, B., and Strecker, M. R.: Hillslope-glacier coupling: The interplay of topography and glacial dynamics in High Asia, Journal of Geophysical Research: Earth Surface, 116, 2011a.

Scherler, D., Bookhagen, B., and Strecker, M. R.: Spatially variable response of Himalayan glaciers to climate change affected by debris cover, Nature geoscience, 4, 156–159, 2011b.

Shah, S. S., Banerjee, A., Nainwal, H. C., and Shankar, R.: Estimation of the total sub-debris ablation from point-scale ablation data on a debris-covered glacier, Journal of Glaciology, 65, 759–769, 2019.

Shaw, T. E., Brock, B. W., Fyffe, C. L., Pellicciotti, F., Rutter, N., and Diotri, F.: Air temperature distribution and energy-balance modelling of a debris-covered glacier, Journal of Glaciology, 62, 185–198, 2016.

Shean, D., Bhushan, S., Montesano, P., Rounce, D., Arendt, A., and Osmanoglu, B.: A systematic, regional assessment of High Mountain Asia Glacier mass balance. Front, Earth Sci, 7, 363, 2020.

Shrestha, R., Kayastha, R., and Kayastha, R.: Effect of debris on seasonal ice melt (2016- 2018) on Ponkar Glacier, Manang, Nepal. Sciences in Cold and Arid Regions, 12 (5): 261- 271. DOI: 10.3724/SP. J. 1226.2020. 00261, Reeju Shrestha et al, pp. 0261–0271, 2020.

Steiner, J. F. and Pellicciotti, F.: Variability of air temperature over a debris-covered glacier in the Nepalese Himalaya, Annals of Glaciology, 57, 295–307, 2016.

Steiner, J. F., Litt, M., Stigter, E. E., Shea, J., Bierkens, M. F., and Immerzeel, W. W.: The importance of turbulent fluxes in the surface energy balance of a debris-covered glacier in the Himalayas, Frontiers in Earth Science, 6, 144, 2018.

Stumm, D., Joshi, S. P., Gurung, T. R., and Silwal, G.: Mass balances of Yala and Rikha Samba Glacier, Nepal from 2000 to 2017, Earth System Science Data Discussions, pp. 1–37, 2020.

Sun, W., Qin, X., Du, W., Liu, W., Liu, Y., Zhang, T., Xu, Y., Zhao, Q., Wu, J., and Ren, J.: Ablation modeling and surface energy budget in the ablation zone of Laohugou glacier No. 12, western Qilian mountains, China, Annals of glaciology, 55, 111–120, 2014.

van den Broeke, M., van As, D., Reijmer, C., and van de Wal, R.: Assessing and improving the quality of unattended radiation observations in Antarctica, Journal of Atmospheric and Oceanic Technology, 21, 1417–1431, 2004.

Verseghy, D. L.: CLASS—A Canadian land surface scheme for GCMs. I. Soil model, International Journal of Climatology, 11, 111–133, 1991.

Vincent, C., Wagnon, P., Shea, J., Immerzeel, W., Kraaijenbrink, P., Shrestha, D., Soruco, A., Arnaud, Y., Brun, F., Berthier, E., et al.: Reduced melt on debris-covered glaciers: investigations from Changri Nup Glacier, Nepal, 2016.

Viterbo, P. and Beljaars, A. C.: An improved land surface parameterization scheme in the ECMWF model and its validation, Journal of climate, 8, 2716–2748, 1995.

Wagnon, P.: IACS working group on debris-covered glaciers. AWS North Changri Nup Glacier [Data set]. Hosted on glacioclim.osug.fr., 2021.

Wijngaard, R. R., Steiner, J. F., Kraaijenbrink, P. D., Klug, C., Adhikari, S., Banerjee, A., Pellicciotti, F., Van Beek, L. P., Bierkens, M. F., Lutz, A. F., et al.: Modeling the Response of the Langtang Glacier and the Hintereisferner to a Changing Climate Since the Little Ice Age, Frontiers in Earth Science, 7, 143, 2019.

Yang, W., Guo, X., Yao, T., Yang, K., Zhao, L., Li, S., and Zhu, M.: Summertime surface energy budget and ablation modeling in the ablation zone of a maritime Tibetan glacier, Journal of Geophysical Research: Atmospheres, 116, 2011.

Yang, W., Yao, T., Zhu, M., and Wang, Y.: Comparison of the meteorology and surface energy fluxes of debris-free and debris-covered glaciers in the southeastern Tibetan Plateau, Journal of Glaciology, 63, 1090–1104, 2017.

Yao, T., Thompson, L., Yang, W., Yu, W., Gao, Y., Guo, X., Yang, X., Duan, K., Zhao, H., Xu, B., et al.: Different glacier status with atmospheric circulations in Tibetan Plateau and surroundings, Nature climate change, 2, 663–667, 2012.

Zhang, Y., Fujita, K., Liu, S., Liu, Q., and Nuimura, T.: Distribution of debris thickness and its effect on ice melt at Hailuogou glacier, southeastern Tibetan Plateau, using in situ surveys and ASTER imagery, Journal of Glaciology, 57, 1147–1157, 2011.

Zhu, M., Yao, T., Yang, W., Xu, B., Wu, G., and Wang, X.: Differences in mass balance behavior for three glaciers from different climatic regions on the Tibetan Plateau, Climate Dynamics, 50, 3457–3484, 2018.

Supplement. The supplement related to this article is available online at: https://doi.org/10.5194/jn-0-1-2024-supplement.

The Supplementary Material includes additional descriptions of data sets, extended figures, tables, methods and analysis, and is structured into these topics:

S1. Climatic and meteorological conditions

S2. Data selection and monsoon definition

S3. Aerodynamic resistance and aerodynamic roughness

S4. Extended results

S5. Sensitivity of seasonal flux changes to elevation and debris thickness

S6. Controls on turbulent fluxes

S1. Climatic and meteorological conditions

Average mean monthly 2 m air temperatures have a similar pattern at all study sites (Figure S1a), with a slow increase from January to a peak between July and August, just after peak monsoon, and a steeper decline from post-monsoon into winter. Incoming shortwave radiation (Figure S1b) shows a clear peak before monsoon onset at all sites. A smaller secondary peak is reached just after the monsoon in October at the Central Himalayan sites, but not at the Eastern Himalayan sites. Interruptions in monsoonal overcast conditions (break periods) seem to be more common at the eastern sites, leading to occasional secondary peaks in incoming shortwave radiation during monsoon. $LW_{\downarrow}$ follows a similar regime as Ta, with highest values reached during the core monsoon (Figure S1c). The yearly cycle of wind speeds (Figure S1d) varies considerably between sites. Common characteristics for most sites (except for Changri Nup) are that wind speeds are highest around December/January and that monsoonal wind speeds are generally higher than during the shoulder seasons. There is a clear difference in the seasonal evolution of precipitation between the Central (Lirung, Lantang, Yala, Changri Nup) and the Eastern Himalayan sites (24K, Parlung No.4, Hailuogou) (Figure S1e): relatively high mean monthly precipitation during the monsoon period is contrasted by comparably low precipitation outside of this period. The eastern sites have less pronounced monsoonal precipitation peaks, and more gradual changes in precipitation intensities over the annual cycle. The Parlung sites (24K and Parlung No.4) have two precipitation peaks: during spring and monsoon. Hailuogou exhibits the smoothest evolution over the annual cycle with a clear maximum in July. A simple monsoon index (MI) is calculated for each year including the study year as the ratio between monsoon precipitation and annual average precipitation (Figure S1e). This value tends to be higher in the Central Himalaya compared to the sites on the South-Eastern Tibetan Plateau.

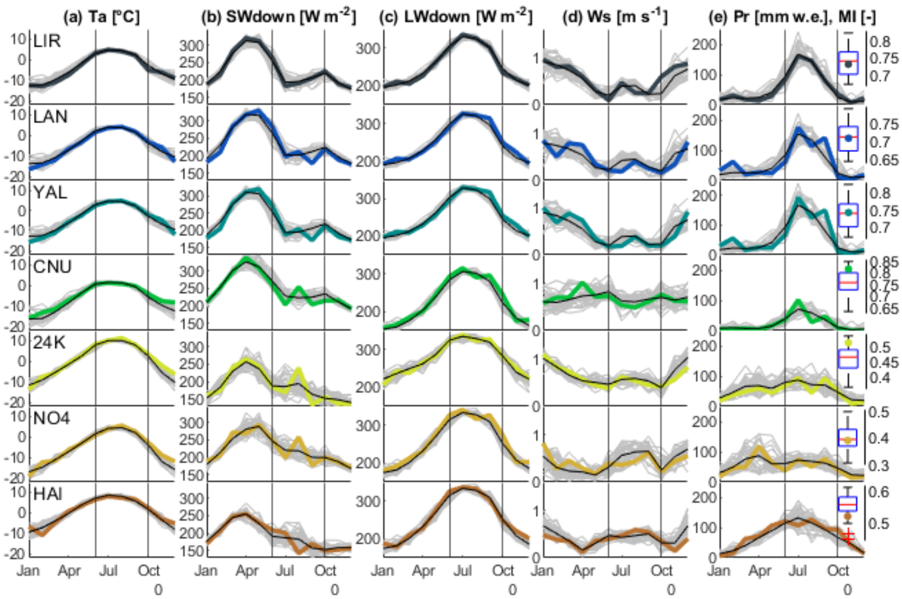

Figure S1. Monthly climatology derived from ERA5-Land for 1981-2019 (grey background lines), along with the monthly averages (black lines) and the study year at each glacier (colored lines). Plotted meteorological variables are **(a)** mean air temperature (Ta), **(b)** incoming shortwave radiation ($SW_{\downarrow}$), **(c)** incoming longwave radiation ($LW_{\downarrow}$), **(d)** wind speed (Ws) and **(e)** monthly precipitation sums (Pr). Black vertical lines indicate the average region-wide monsoon season. Boxplots show the monsoon index (MI) over ERA5-Land period as the fraction of monsoonal (June-September) to annual precipitation, with the colored dot indicating the value for the study year.

S2. Data selection and monsoon definition

The records and periods were chosen under considering the following criteria:

- Data availability
- Completeness of records (few or no data gaps)
- Availability of complete forcing data for modelling, including precipitation records
- Availability of ablation stake measurements or other recordings of surface lowering (e.g. Ultrasonic Depth Gauge)
- Highest quality and reliability of records (No unrealistic/erroneous/disagreeing records)
- Possibility to substitute from other stations when criteria 1.-4. were not met

At each site, we define the onset and recession date of monsoon based on visual inspection of the AWS records (Figures SS2 to SS8) following this procedure:

1. Inspect $SW \downarrow$ to identify a period with sustained cloud overcast and with few interruptions therein, lowering $SW \downarrow$
2. Inspect $LW \downarrow$ and compare the timing of constantly higher $LW \downarrow$ with the above
3. Identify the period of increased rainfall frequency and intensity
4. Inspect the relative humidity to see whether the timing of sustained humid conditions would agree with the above
5. Identify a plateau in average air temperature and dampening of the daily air temperature amplitude
6. Inspect wind speed to identify a regime change (mean and amplitude)

This was the general procedure followed, but the order was varied, when one or the other variable provided a clearer indication. We note, that in some cases, where heavy cloud cover and rainy conditions dominate the local weather from spring to autumn (e.g. Hailuogou, 24K) this distinction was less clear than in others, and some uncertainty remains around the exact monsoon onset and cessation dates at those study sites.

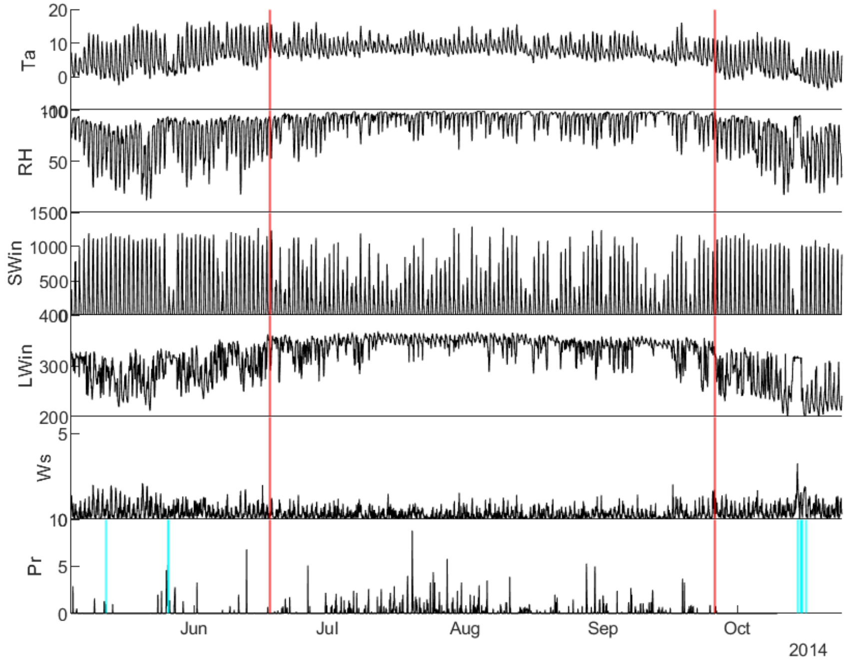

Figure S2. Meteoroligical observations on Lirung during the ablation season recorded by AWS; Red vertical lines indicate monsoon onset and end; cyan indicates time steps with snow cover at the AWS location, as determined from α (>0.5)

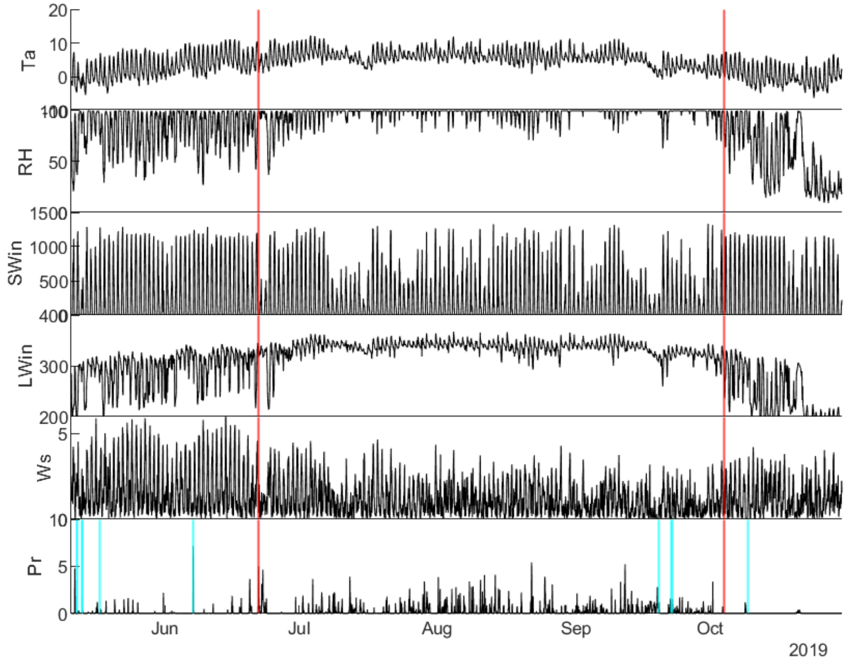

Figure S3. Meteoroligical observations on Langtang during the ablation season recorded by AWS; Red vertical lines indicate monsoon onset and end; cyan indicates time steps with snow cover at the AWS location, as determined from α (>0.5)

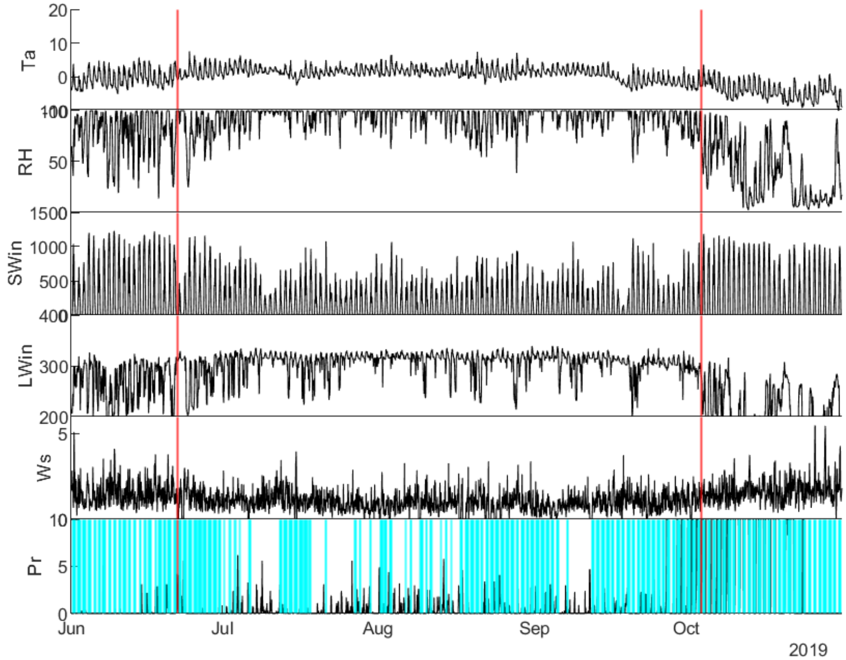

Figure S4. Meteoroligical observations on Yala during the ablation season recorded by AWS; Red vertical lines indicate monsoon onset and end; cyan indicates time steps with snow cover at the AWS location, as determined from α (>0.5)

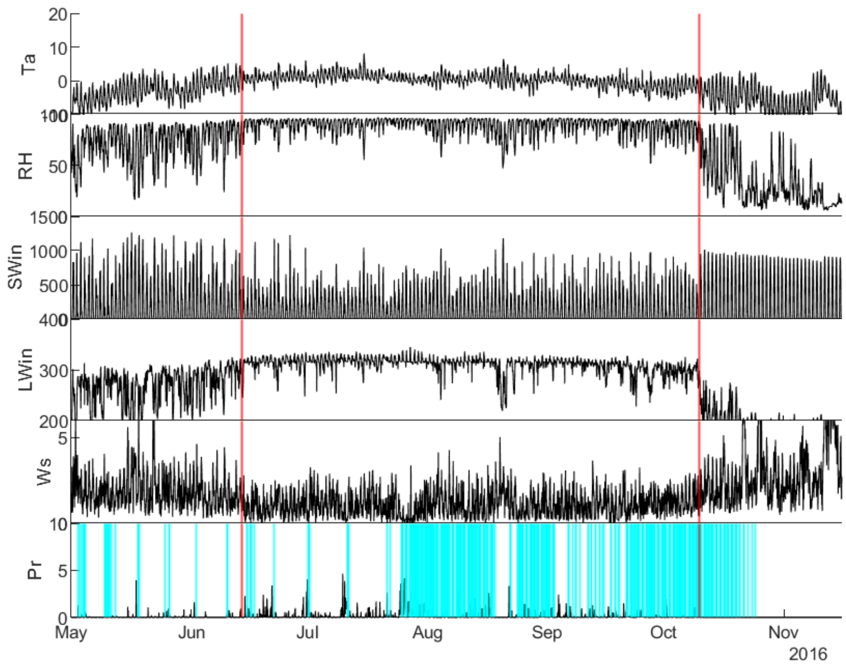

Figure S5. Meteoroligical observations on Changri Nup during the ablation season recorded by AWS; Red vertical lines indicate monsoon onset and end; cyan indicates time steps with snow cover at the AWS location, as determined from α (>0.5)

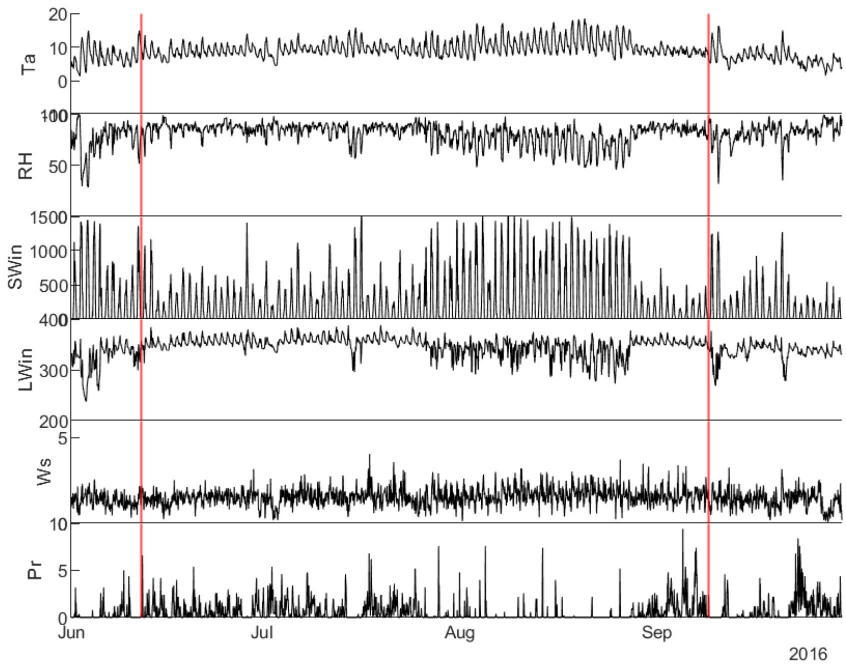

Figure S6. Meteoroligical observations on 24K during the ablation season recorded by AWS; Red vertical lines indicate monsoon onset and end; cyan indicates time steps with snow cover at the AWS location, as determined from α (>0.5)

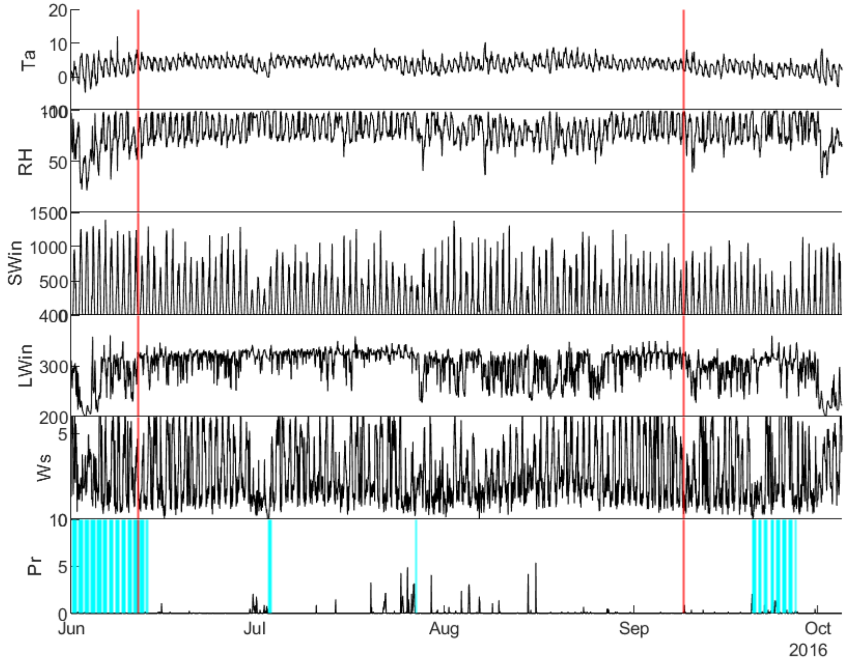

Figure S7. Meteoroligical observations on Parlung No.4 during the ablation season recorded by AWS; Red vertical lines indicate monsoon onset and end; cyan indicates time steps with snow cover at the AWS location, as determined from α (>0.5)

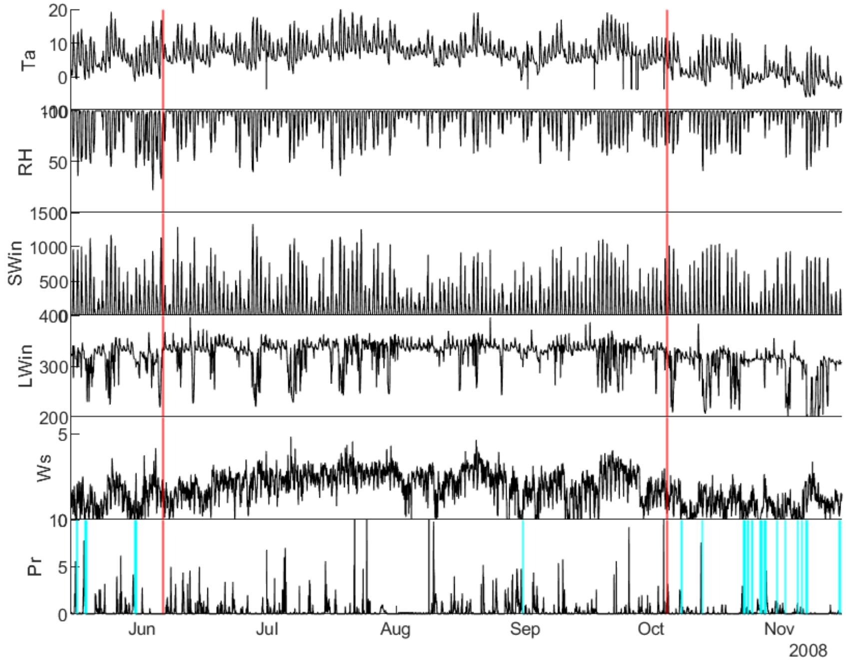

Figure S8. Meteoroligical observations on Hailuogou during the ablation season recorded by AWS; Red vertical lines indicate monsoon onset and end; cyan indicates time steps with snow cover at the AWS location, as determined from α (>0.5)

Table S1. Air temperature Ta, mean daily precipitation Pr_d, relative humidity RH, vapor pressure deficit vpd, mean cloud-cover fraction ccf, temperature gradient between surface and air δ_T, wind speed Ws and the percentage of time during which the debris is modelled to hold intercepted water In for each site and season, also indicating percent changes between the sub-seasons.

		Ta [°C]			Pr [$mm\,d^{-1}$]			Ws [$m\,s^{-1}$]			RH [$-$]			vpd [Pa]			δ_T [°$C\,m^{-1}$]			In [%]		
		pre	*mon*	*post*	*pre*	*mon*	*post*	*pre*	*mon*	*post*	*pre*	*mon*	*post*	*pre*	*mon*	*post*	*pre*	*mon*	*post*	*pre*	*mon*	*post*
LIR	mean	6.4	8.5	3.3	1.8	4.4	0.1	0.47	0.27	0.52	68.1	90.8	67.1	318.8	103.5	262.5	1.19	0.78	0.89	40.1	74.0	26.4
	Δ		*2.1*	*-5.2*		*2.6*	*-4.3*		*-0.19*	*0.24*		*22.6*	*-23.6*		*-215.3*	*159.1*		-0.40	0.10		33.9	-47.6
LAN	mean	3.1	5.7	0.5	2.2	5.9	0.3	1.79	1.10	1.27	80.7	96.9	56.3	152.1	28.7	282.3	1.02	0.97	0.95	38.8	75.3	9.5
	Δ		*2.6*	*-5.2*		*3.7*	*-5.6*		*-0.68*	*0.17*		*16.2*	*-40.6*		*-123.5*	*253.6*		-0.05	-0.02		36.5	-65.8
YAL	mean	-2.6	1.2	-4.1	2.0	17.0	345.2	1.74	1.00	1.68	69.8	93.0	39.4	156.1	47.1	278.4	-0.36	-0.96	-0.89	-	-	-
	Δ		*3.8*	*-5.3*		*15.1*	*328.2*		*-0.74*	*0.67*		*23.2*	*-53.6*		*-109.1*	*231.4*		-0.59	0.07		-	-
CNU	mean	-2.8	0.4	-4.7	0.5	3.1	0.0	1.88	1.09	2.48	71.2	89.2	39.3	147.4	68.1	270.5	1.69	0.25	0.89	16.2	79.3	5.3
	Δ		*3.1*	*-5.1*		*2.6*	*-3.1*		*-0.79*	*1.39*		*18.1*	*-50.0*		*-79.3*	*202.3*		-1.44	0.64		63.1	-74.0
24K	mean	7.3	9.8	6.9	6.5	13.8	18.3	1.33	1.56	1.35	73.1	80.6	81.2	279.3	238.0	189.2	1.86	0.73	0.18	56.8	79.1	84.3
	Δ		*2.5*	*-2.9*		*7.3*	*4.5*		*0.22*	*-0.21*		*7.4*	*0.7*		*-41.3*	*-48.8*		-1.13	-0.55		22.3	5.2
NO4	mean	0.9	4.1	0.4	2.4	1.7	0.7	2.96	2.67	3.23	65.7	81.3	73.1	230.8	153.9	173.9	-0.78	-2.01	-0.62	-	-	-
	Δ		*3.2*	*-3.7*		*-0.7*	*-1.0*		*-0.28*	*0.56*		*15.7*	*-8.3*		*-76.9*	*20.0*		-1.22	1.39		-	-
HAI	mean	6.1	7.8	-2.1	8.5	7.8	2.4	1.23	2.15	0.93	81.3	92.3	90.6	182.4	83.8	52.3	-2.08	-2.61	0.38	99.8	100.0	75.6
	Δ		*1.7*	*-9.9*		*-0.7*	*-5.4*		*0.91*	*-1.22*		*10.9*	*-1.6*		*-98.6*	*-31.5*		-0.53	2.99		0.2	-24.4

S3. Aerodynamic resistance and aerodynamic roughness

The aerodynamic resistance quantifies the ability of the surface boundary layer to resist or intensify turbulent transport of momentum, heat and water vapor. We calculate the aerodynamic resistances to heat flux r_{ah} and water vapor r_{aw} using the simplified solution of the Monin-Obukhov similarity theory, introduced by Mascart et al. (1995) and implemented into the ISBA landsurface model Noilhan and Mahfouf (1996). This parameterization of the full Monin-Obukhov similarity theory (Monin and Obukhov, 1954) is computationally less demanding, while providing concurring results (Fatichi, 2010). In T&C, the common assumption is of a single aerodynamic resistance (e.g. Viterbo and Beljaars, 1995; Ivanov et al., 2008), is used, such that $r_{ah} = r_{aw}$. To gain r_{ah}, in the simplified solution, a bulk transfer coefficient C_h can be expressed as:

$$C_h = 1\frac{r_{ah}}{W_s} = C_n F_h(R_{i_B}) \tag{17}$$

where the neutral transport coefficient C_n is:

$$C_n = \frac{k^2}{ln[(z_{atm} - d)/z_{0m}]^2} \tag{18}$$

and the empirical function of the bulk Richardson number R_{ib} is:

$$F_h(Ri_B) = \begin{cases} \left[1 - \frac{15Ri_B}{1+c_h\sqrt{|Ri_B|}}\right]\left[\frac{ln[(z_{atm}-d)/z_{om}]}{ln[(z_{atm}-d)/z_{0h}]}\right], & \text{if } Ri_B \leq 0 \\ \left[\frac{1}{1+15Ri_B\sqrt{1+5Ri_B}}\right]\left[\frac{ln[(z_{atm}-d)/z_{0m}]}{ln[(z_{atm}-d)/z_{0h}]}\right], & \text{if } Ri_B > 0 \end{cases} \tag{19}$$

wherein

$$c_h = 15c_h^* C_n[(z_{atm} - d]^{p_h}\left[\frac{\ln[(z_{atm} - d)/z_{0m}]}{\ln[(z_{atm} - d)/z_{0h}]}\right] \tag{20}$$

$$c_h^* = 3.2165 + 4.3431\mu + 0.5360\mu^2 - 0.0781\mu^3 \tag{21}$$

$$p_h = 0.5892 - 0.1571\mu + 0.0327\mu^2 - 0.0026\mu^3 \tag{22}$$

$$\mu = \ln(z_{0m}/z_{0h}) \tag{23}$$

To prevent a full inhibition of turbulent transport under wind-still conditions (r_{ah} would become infinite), when $Ws < 0.05\,m\,s^{-1}$, we calculate C_h following Beljaars (1995):

$$C_h = \frac{1}{r_{ah}} = 0.15\Big[\frac{g\nu}{0.5(T_s + T_a)Pr^2}\Big]^{1/3}(T_s - T_a)^{1/3} \tag{24}$$

where $\nu = 1.5110^{-5}[m^2 s^{-1}]$ and the Prandtl number $Pr = 0.71$.

As a consequence of the assumption explained above r_{ah} = r_{aw}), also the aerodynamic roughnesses of heat and water vapour are used as equal (z_{0w} = z_{0h}) and $z_{0h} = z_{0w} = 0.1 z_{0m}$. For the ratio r between the roughness lengths of water vapour, heat and momentum, $r = 0.1$ is a value based on (Brutsaert, 1982), often implemented in land surface models (e.g. Noilhan and Mahfouf, 1996), and is also used in TC. This ratio remains poorly constrained, not least due to the difficulties in measuring or deriving surface roughnesses (Miles et al., 2017; Quincey et al., 2017). Three values have been suggested in the literature: $r = 1$ (e.g. Reid and Brock, 2010), $r = 0.1$ (e.g. Giese et al., 2020) $r = 0.05$ (Steiner et al. 2018), who derived this value for Lirung from flux tower experiments. Since here, z_{0h}, z_{0w} and z_{0m} were effectively optimised together at the debris-covered glaciers, the turbulent fluxes remain insensitive to the choice of this ratio.

S4. Extended Results

Table S2. RMSE values for modelled vs. measured T_s at all sites. Measured T_s were derived from $LW_{\downarrow}$ and $LW_{\uparrow}$ measurements considering the entire modelling period at all sites

		Lirung	Langtang	Yala	Changri Nup	24K	Parlung No.4	Hailuogou
RMSE	[℃]	2.3	2.2	2.99	2.6	1.8	2.89	1.0

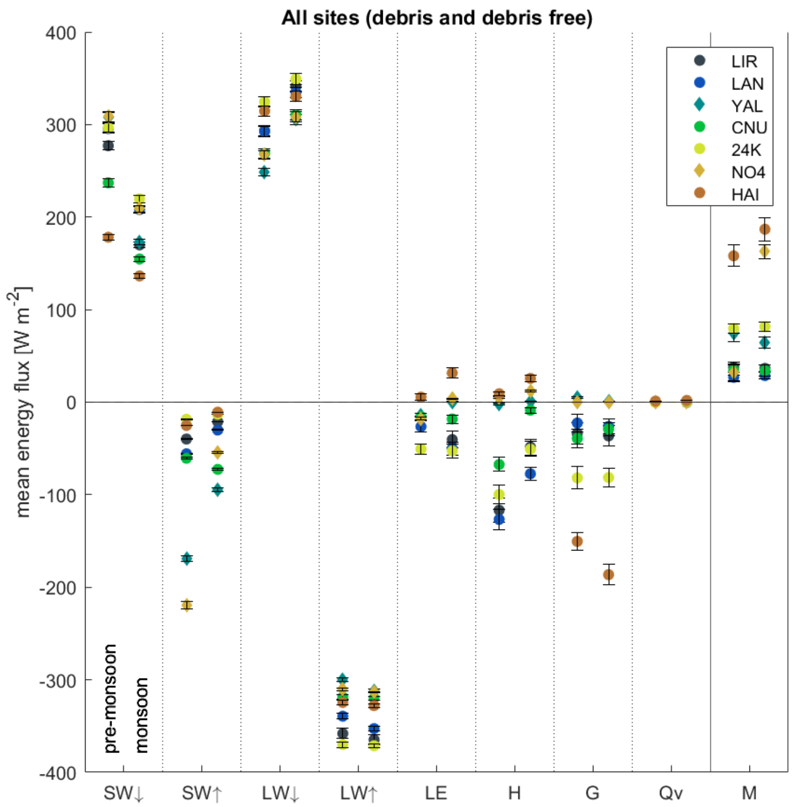

Figure S9. All energy balance components of all glaciers in comparison, split into pre-monsoon and monsoon; black bars indicate the uncertainty range;

Table S3. Mean energy balance components at each site and for pre-monsoon (pre), monsoon (mon), and post-monsoon (post) periods, as well as flux magnitude changes from pre-monsoon to monsoon, and monsoon to post-monsoon. All values are in $W\,m^{-2}$.

fluxes in W/m2		$SW_\downarrow$			$SW_\uparrow$			$LW_\downarrow$			$LW_\uparrow$			LE		
		pre	*mon*	*post*	*pre*	*mon*	*post*	*pre*	*mon*	*post*	*pre*	*mon*	*post*	*pre*	*mon*	*post*
LIR	mean	277.1	170.0	224.1	-39.8	-21.1	-41.3	293.3	341.2	264.0	-358.1	-364.8	-340.4	-16.0	-40.4	-1.9
	Δ		*-107.1*	*54.1*		*18.7*	*-20.2*		*47.9*	*-77.2*		*-6.7*	*24.4*		*-24.4*	*38.5*
LAN	mean	295.6	208.1	262.4	-55.9	-30.1	-48.6	292.3	334.7	238.6	-339.3	-352.8	-326.1	-26.4	-49.9	-5.8
	Δ		*-87.5*	*54.3*		*25.7*	*-18.4*		*42.3*	*-96.0*		*-13.5*	*26.7*		*-23.5*	*44.1*
YAL	mean	307.7	172.7	271.8	-169.4	-94.4	-195.0	248.5	305.5	212.3	-299.8	-311.6	-287.1	-13.7	0.1	-12.2
	Δ		*-135.0*	*99.1*		*75.0*	*-100.6*		*57.0*	*-93.2*		*-11.7*	*24.4*		*13.7*	*-12.3*
CNU	mean	237.1	154.7	258.1	-60.6	-72.7	-126.0	268.8	310.2	196.4	-318.7	-319.7	-300.4	-15.7	-18.1	-3.1
	Δ		*-82.4*	*103.4*		*-12.1*	*-53.3*		*41.5*	*-113.8*		*-1.0*	*19.3*		*-2.5*	*15.0*
24K	mean	296.6	219.7	140.9	-18.5	-13.0	-8.3	324.6	349.3	336.6	-369.9	-371.3	-351.0	-50.6	-52.7	-40.0
	Δ		*-76.9*	*-78.8*		*5.4*	*4.7*		*24.7*	*-12.7*		*-1.3*	*20.3*		*-2.1*	*12.7*
NO4	mean	308.5	209.1	197.3	-219.6	-54.8	-81.5	267.5	308.2	261.5	-310.3	-313.4	-310.5	-17.6	3.6	-18.5
	Δ		*-99.5*	*-11.8*		*164.8*	*-26.7*		*40.7*	*-46.7*		*-3.1*	*2.9*		*21.2*	*-22.1*
HAI	mean	178.2	136.4	105.8	-25.2	-10.8	-28.4	314.6	330.3	273.1	-324.5	-327.9	-309.1	5.4	31.6	-4.8
	Δ		*-41.8*	*-30.6*		*14.4*	*-17.6*		*15.7*	*-57.2*		*-3.4*	*18.8*		*26.2*	*-36.4*

fluxes in W/m2		H			G			dG			Qv			M		
		pre	*mon*	*post*	*pre*	*mon*	*post*	*pre*	*mon*	*post*	*pre*	*mon*	*post*	*pre*	*mon*	*post*
LIR	mean	-116.7	-48.4	-86.5	-33.7	-36.4	-18.7	5.6	0.0	16.6	0.0	0.0	0.0	-37.5	-36.5	-19.0
	Δ		*68.3*	*-38.0*		*-2.7*	*17.8*		*-5.6*	*16.6*		*0.0*	*0.0*		*1.0*	*-17.5*
LAN	mean	-126.7	-77.4	-111.4	-22.5	-26.2	-7.8	2.2	0.0	27.3	0.0	-0.3	0.0	-26.9	-28.7	-10.4
	Δ		*49.3*	*-34.1*		*-3.7*	*18.4*		*-2.2*	*27.3*		*-0.3*	*0.3*		*-1.8*	*-18.4*
YAL	mean	-2.3	0.5	1.4	4.7	0.9	0.0	4.7	0.9	0.0	0.0	-0.2	-4.1	-74.8	-64.6	-0.3
	Δ		*2.8*	*0.9*		*-3.8*	*-0.9*		*-3.8*	*-0.9*		*-0.2*	*-3.9*		*10.2*	*-64.3*
CNU	mean	-67.4	-8.7	-36.1	-39.2	-29.1	10.4	17.1	1.8	10.6	0.0	0.0	0.0	-34.6	-34.1	-0.2
	Δ		*58.7*	*-27.4*		*10.1*	*39.5*		*-15.3*	*8.9*		*0.0*	*0.0*		*0.5*	*-33.9*
24K	mean	-99.8	-50.8	-24.4	-81.8	-81.4	-53.1	0.3	0.0	0.0	-0.3	0.2	0.6	-79.5	-81.6	-53.7
	Δ		*49.0*	*26.4*		*0.4*	*28.4*		*-0.3*	*0.0*		*0.6*	*0.4*		*-2.1*	*-27.9*
NO4	mean	4.7	12.3	5.8	0.2	0.1	0.1	0.2	0.1	0.0	0.2	0.2	0.0	-32.3	-162.6	-54.1
	Δ		*7.6*	*-6.6*		*-0.1*	*-0.1*		*-0.1*	*-0.1*		*0.0*	*-0.2*		*-130.4*	*-108.5*
HAI	*mean*	9.1	25.7	-9.9	-150.4	-186.4	-16.5	1.8	0.5	17.6	1.2	1.9	0.1	-158.1	-186.8	-36.9
	Δ		*16.6*	*-35.5*		*-35.9*	*169.9*		*-1.4*	*17.2*		*0.7*	*-1.8*		*-28.7*	*-149.9*

S5. Sensitivity of seasonal flux changes to elevation and debris thickness

Assuming that the strongest changes in meteorological forcing with elevation would be the Ta, which in turns controls the precipitation partition and the albedo, we re-run the model varying Ta under applying a temperature lapse rate of $0.6\,℃/100m$ and, for the debris-covered sites, by varying also the debris thickness in the range 10-80 cm (for ranges and steps see Table S4). Using the station-measured, accumulated albedo is not appropriate during this experiment, due to changing snow conditions with varying elevation. We therefore include the parameterisation introduced by Ding et al. (2017) for modelling α. From the resulting range of EB flux outputs, we calculate the range of expected changes for the entire ablation zone when moving from pre-monsoon to monsoon (Δ-range). This allows us to place our results in the context of the changes that can be expected over the entire ablation zone, given its elevation span and debris thickness variability. Figure 8 shows that even accounting for the range of conditions across each glacier ablation area, the pattern of pre-monsoon to monsoon difference in flux components, and importantly M, remain similar for debris-covered sites: The Δ-range of M stays within the uncertainty range, with the exception of Langtang, where the unrealistic combination of relatively thin debris and low elevation causes high M Δ-range. This lends confidence to the results obtained at the individual AWS locations. Although we adjusted forcing data for elevation in this exercise, we could not represent the effects of variable debris thicknesses in modifying $2\,m$ meteorological variables (Steiner and Pellicciotti, 2016; Shaw et al., 2016). This comes with the assumption that surface-atmosphere interactions are negligible compared to the altitudinal patterns and temporal changes. While this might be acceptable at thicker debris sites, it is more questionable at Hailuogou, where the observations were taken above thin and cold debris. However, also at this site, the Δ-range ends up to be small (5 $W\,m^{-2}$) and close to zero when debris between 10 and $80\,cm$ thickness is applied artificially.

Table S4. Ranges of elevations and debris thicknesses used for the sensitivity runs, including the glacier terminus elevation (min), the AWS elevation (AWS) and the upper debris limit on debris-covered glaciers or to the approximated ELA elevation on clean-ice glaciers (max). We also show the range of debris thicknesses h_d modelled for debris-covered glacier sites. All combinations of elevations and debris thicknesses were used.

Glacier		Lirung	Langtang	Yala	Changri Nup	24K	Parlung No.4	Hailuogou
min	$[m.asl]$	3990	4500	5170	5270	3910	4620	2980
AWS	$[m.asl]$	4076	4557	5350	5471	3900	4800	3550
max	$[m.asl]$	4400	5600	5400	5600	4200	5400	3700
h_d $[cm]$	10, 20, 30, 40, 50, 60, 70, 80							

S6. Controls on turbulent fluxes

To understand which climatic variables of the boundary layer control the turbulent fluxes on debris-covered glaciers, regression models were fitted to the modelled values of the energy fluxes H and LE at the hourly timescale, and for pre-monsoon and monsoon separately. A summary figure is given in the main text (Figure 4.5). Values of $0\,W\,m^2$ were removed from LE, which appear at timesteps when no water is available at the debris surface. The predictive power of three variables and their combination was determined and evaluated with adjusted R^2: (i) The temperature gradient between surface and air $\delta_T\,[°C^{-1}]$:

$$\delta_T(t) = Ts(t) - Ta(t) \tag{25}$$

(ii) the vapour pressure deficit $vpd\,[Pa]$:

$$vpd(t) = esat(t) - e_a(t) \tag{26}$$

where $e_a\,[Pa]$ is the vapor pressure and $e_{sat}\,[Pa]$ is the saturated vapor pressure, and (iii) the wind speed Ws. Univariate quadratic regression models fitted for single predictors had the form:

$$y(t) = a + bx(t) + cx(t)^2 \tag{27}$$

and multivariate linear regression models fitted for multiple predictors had the form:

$$y(t) = a + bx_1(t) + bx_2(t) + bx_3(t) \tag{28}$$

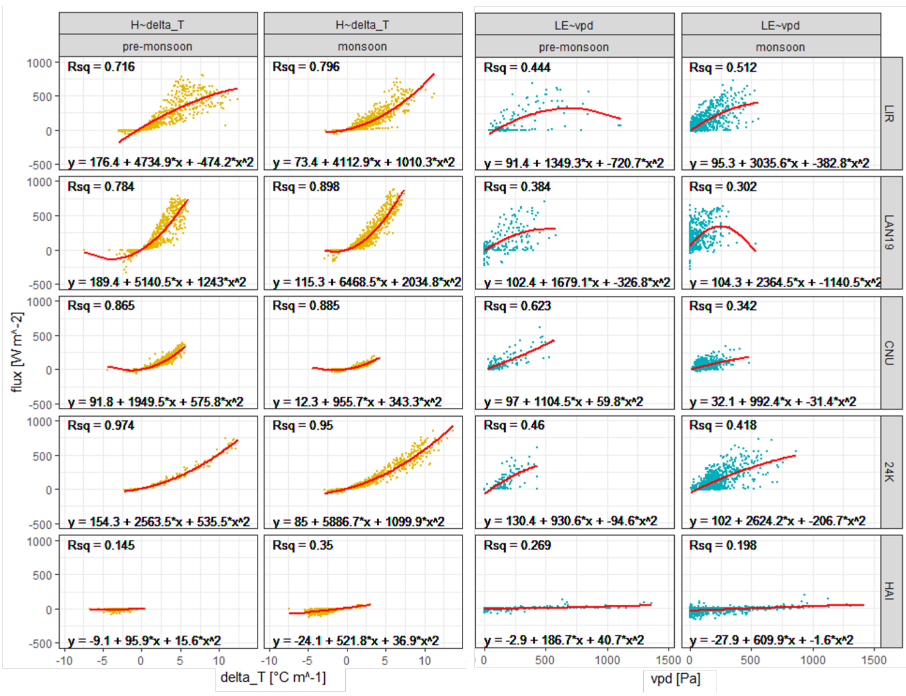

Figure S10. (a) Regression plots for temperature gradient between surface and air δ_T against H and vapor pressure deficit vpd against LE for the debris cover sites, seperately for pre-monsoon and monsoon. Fitted model (red line), adj.R^2 and model equation.

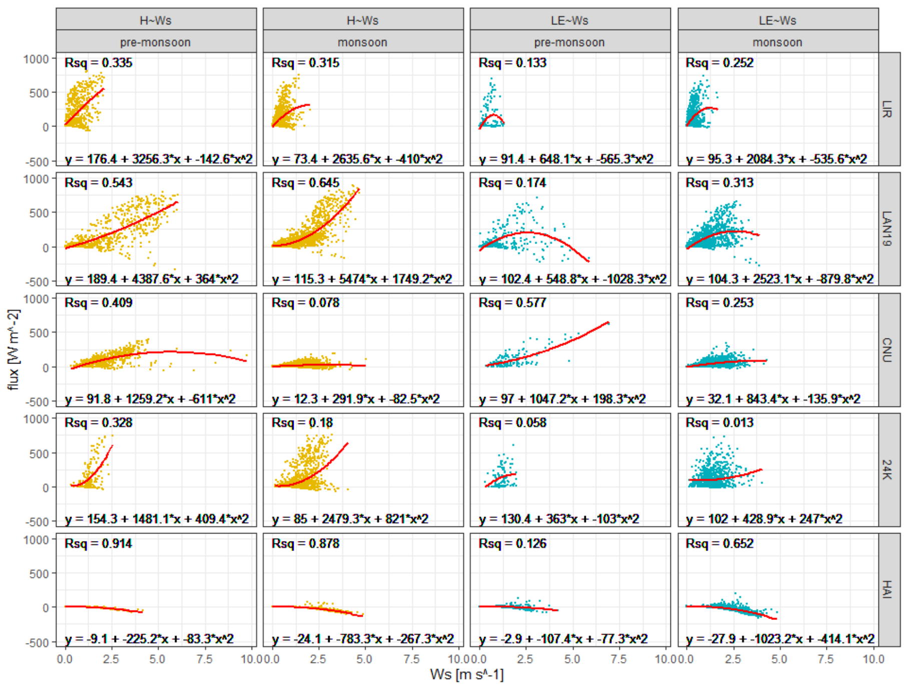

Figure S11. (a) Regression plots for wind speed Ws against H and LE for the debris cover sites, seperately for pre-monsoon and monsoon. Fitted model (red line), adj.R^2 and model equation.

4. Research Article: *Hydrological regimes and evaporative flux partitioning at the climatic ends of High Mountain Asia*

published on 2 February, 2024 in *Environmental Research Letters*, authored by

S. Fugger[1,2,3], T. E. Shaw[1,3], A. Jouberton[1,2], E. S. Miles[1], Pascal Buri[1], Michael James McCarthy[1,3], Catriona Fyffe[3], Simone Fatichi[4], Marin Kneib[1,5,6], Peter Molnar[2] and F. Pellicciotti[1,3]

[1]Swiss Federal Institute for Forest Snow and Landscape Research WSL, Zurcherstrasse 111, Birmensdorf, Zürich, 8903, Switzerland
[2]Institute of Environmental Engineering, ETH Zurich, Zurich, Switzerland
[3]Institute of Science and Technology Austria, Am Campus 1, Klosterneuburg, Lower Austria, 3400, Austria
[4]Department of Civil and Environmental Engineering, National University of Singapore, Singapore
[5]Institut des Géosciences de l'Environnement, Université Grenoble-Alpes, CNRS, IRD, Grenoble, France
[6]Department of Atmospheric and Cryospheric Sciences, University of Innsbruck, Innsbruck, Austria

<u>Author contribution</u>

StF, TES, SiF and FP designed the study. StF carried out the analysis with the help of AJ, ESM, PB, MM and PM. StF and TES interpreted the results, created the figures and wrote the paper with the help of AJ, ESM, MM, CF and FP. TES, AJ, ESM, PB, MM, CF, SiF, MK, PM and FP reviewed the paper. MK, ESM, AJ and SF organised field campaigns and data collection.

<u>Key findings</u>

- Water 'thoughput' determines the relative importance of both glacier melt and evaporative fluxes.
- Evaporative fluxes are large components in the water balance of all three catchments, but are most important in the westerly-controlled, seasonally dry catchment.
- Sublimation flux is largest in the westerly-controlled catchment, while evapotranspiration is largest in the wettest, monsoonal catchment.
- During warm and dry years, glacier melt partially compensated for the supply deficit.

Note: Separate section numbering in articles

Hydrological regimes and evaporative flux partitioning at the climatic ends of High Mountain Asia

S. Fugger[1,2,3], T. E. Shaw[1,3], A. Jouberton[1,2], E.S. Miles[1], P. Buri[1], M. McCarthy[1,3], C. Fyffe[3], S. Fatichi[4], M. Kneib[1,5,6], Peter Molnar[2], F. Pellicciotti[1,3]

1. *Swiss Federal Research Institute WSL, Birmensdorf, Switzerland*
2. *Institute of Environmental Engineering, ETH Zurich, Zurich, Switzerland*
3. *Institute of Science and Technology Austria, ISTA, Klosterneuburg, Austria*
4. *Department of Civil and Environmental Engineering, National University of Singapore, Singapore*
5. *Institut des Géosciences de l'Environnement, Université Grenoble-Alpes, CNRS, IRD, Grenoble, France*
6. *Department of Atmospheric and Cryospheric Sciences, University of Innsbruck, Innsbruck, Austria*

Corresponding Author: Stefan Fugger (stefan.fugger@ist.ac.at)

Abstract

High elevation headwater catchments are complex hydrological systems that seasonally buffer water and release it in the form of snow and ice melt, modulating downstream runoff regimes and water availability. In High Mountain Asia (HMA), where a wide range of climates from semi-arid to monsoonal exist, the importance of the cryospheric contributions to the water budget varies with the amount and seasonal distribution of precipitation. Losses due to evapotranspiration and sublimation are to date largely unquantified components of the water budget in such catchments, although they can be comparable in magnitude to glacier melt contributions to streamflow.
Here, we simulate the hydrology of three high elevation headwater catchments in distinct climates in HMA over 10 years using an ecohydrological model geared towards high-mountain areas including snow and glaciers, forced with reanalysis data.
Our results show that evapotranspiration and sublimation together are most important at the semi-arid site, Kyzylsu, on the northernmost slopes of the Pamir mountain range. Here, the evaporative loss amounts to 28% of the water throughput, which we define as the total water added to, or removed from the water balance within a year. In comparison, evaporative losses are 19% at the Central Himalayan site Langtang and 13% at the wettest site, 24K, on the Southeastern Tibetan Plateau. At the three sites, respectively, sublimation removes 15%, 13% and 6% of snowfall, while evapotranspiration removes the equivalent of 76%, 28% and 19% of rainfall. In absolute terms, and across a comparable elevation range, the highest ET flux is 413 mm yr^{-1} at 24K, while the highest sublimation flux is 91 mm yr^{-1} at Kyzylsu. During warm and dry years, glacier melt was found to only partially compensate for the annual supply deficit.

1. Introduction

The mountain cryosphere is on a downward trajectory globally, as indicated by widespread declines in seasonal snowpack and negative glacier mass balances (Mudryk et al., 2020; Hugonnet et al., 2021). However, the importance of snow and glaciers as runoff contributors differs from basin to basin (Immerzeel et al., 2020) and depends on the local hydro-geographical setting (Bookhagen and Burbank, 2010; Lutz et al., 2014). In monsoonal basins, such as the Ganges-Brahmaputra, concurrent melt, snowfall and rainfall amplify seasonal streamflow variability. In semi-arid basins, such as the Amu-Darya river basin, glacier melt sustains streamflow during the summer gap in precipitation inputs (Pohl et al., 2017; Unger-Shayesteh et al., 2013; Sorg et al.,2014; Pritchard et al., 2019).
A number of processes other than glacier melt shape the mountain water budget, including the amount and seasonality of precipitation, snow cover dynamics, plant transpiration, surface evaporation and sublimation, all of which are highly variable in mountain environments. High vapour pressure deficits and radiative energy inputs drive the latent (LE) and sensible (H) energy fluxes. Cloudy conditions and elevated humidity can reduce turbulent heat fluxes by up to 70%, due to a more stable boundary layer under such conditions, resulting in a lowering of the evaporative fluxes (Mandal et al., 2021).
Evaporative fluxes (E) are defined here to include all evaporation, transpiration and sublimation fluxes from the land surface (E = ET+S), while evapotranspiration (ET) and sublimation (S) are treated separately in this study.
Evapotranspiration (ET) represents a crucial mass loss from the hydrologic system, and is estimated to globally return around 60% of water inputs to the atmosphere over land (Seneviratne et al., 2010; Katul et al., 2012). However, despite its significance, ET has received limited attention in studies of high elevation catchments, which are extreme environments for vegetation. As an example, it remains elusive whether ET is a greater loss term in wet, monsoonal environments characterised by abundant water availability and energy limitations, or in semi-arid places with high energy inputs and potentially water limitations. ET is expected to increase with global warming due to greening and succession (e.g. Düthmann and Blöschl, 2018, Zhu et al., 2016; Yang et al., 2023), while sublimation is expected to decrease with reductions in snow cover and higher temperatures.
In HMA, where sublimation studies are still scarce, many questions remain around sublimation rates at high elevation, its sensitivity to monsoonal conditions, interannual variability and the importance of ground, canopy intercepted, and blowing snow sublimation at the catchment scale (Stigter et al., 2018; Mandal et al., 2021; Potocki et al., 2022; Buri et al., 2023). Neglecting sublimation as a mass sink leads to erroneous estimates of melt rates and streamflow when snow and glacier mass balances are calibrated (Stigter et al., 2018).
From the water balance perspective, ice melt and evaporative fluxes oppose one another in that ice melt generates runoff, whereas evaporative fluxes generally reduce runoff, while they are sensitive to similar meteorological variables. Modelling in the upper Langtang catchment has shown that the totals of ice melt and evaporative fluxes were comparable in magnitude during the 2018/19 hydrological year (Buri et al., 2023). However, it remains unknown under which conditions increased glacier melt would

also compensate for precipitation deficits and increased evaporative fluxes (van Tiel et al., 2021) at the seasonal scale in high-elevation catchments.

Serving as research tools, mechanistic models enable new process understanding and detailed quantification of flux partitioning and sensitivity to environmental changes (Poulin et al., 2011, Mastrotheodoros et al., 2018, Pomeroy et al., 2022). Previous applications of such models have highlighted counter-intuitive relationships of ET and water availability, such as an inverse correlation of ET with precipitation under drought conditions (Mastrotheodoros et al., 2020). Due to their physical basis, these models are regarded as robust across temperate, humid and sub-humid environments and under shifting boundary conditions, such as climate change and extreme events (Poulin et al., 2011; Fatichi et al., 2016, Pomeroy et al., 2022).

In this study, an ecohydrological model geared towards high mountain hydrological systems is applied to three glacierized headwater catchments in contrasting climates within HMA to constrain the hydrological fluxes at high elevations. After a thorough evaluation of the model, the partitioning of mass and energy fluxes, together with ecohydrological variables, are investigated to determine the main components of runoff generation. We hypothesise that:

(I) Sublimation is higher in semi-arid, high elevation catchments, where longer periods of cold and clear-sky conditions with high energy inputs occur.

(II) ET is higher in monsoonal catchments due to the prevalence of concurrent periods of liquid water abundance and high temperatures, along with intensive vegetation coverage.

(III) In warm and dry years, increased glacier melt fully compensates, or even overcompensates for precipitation deficits and enhanced evaporative losses.

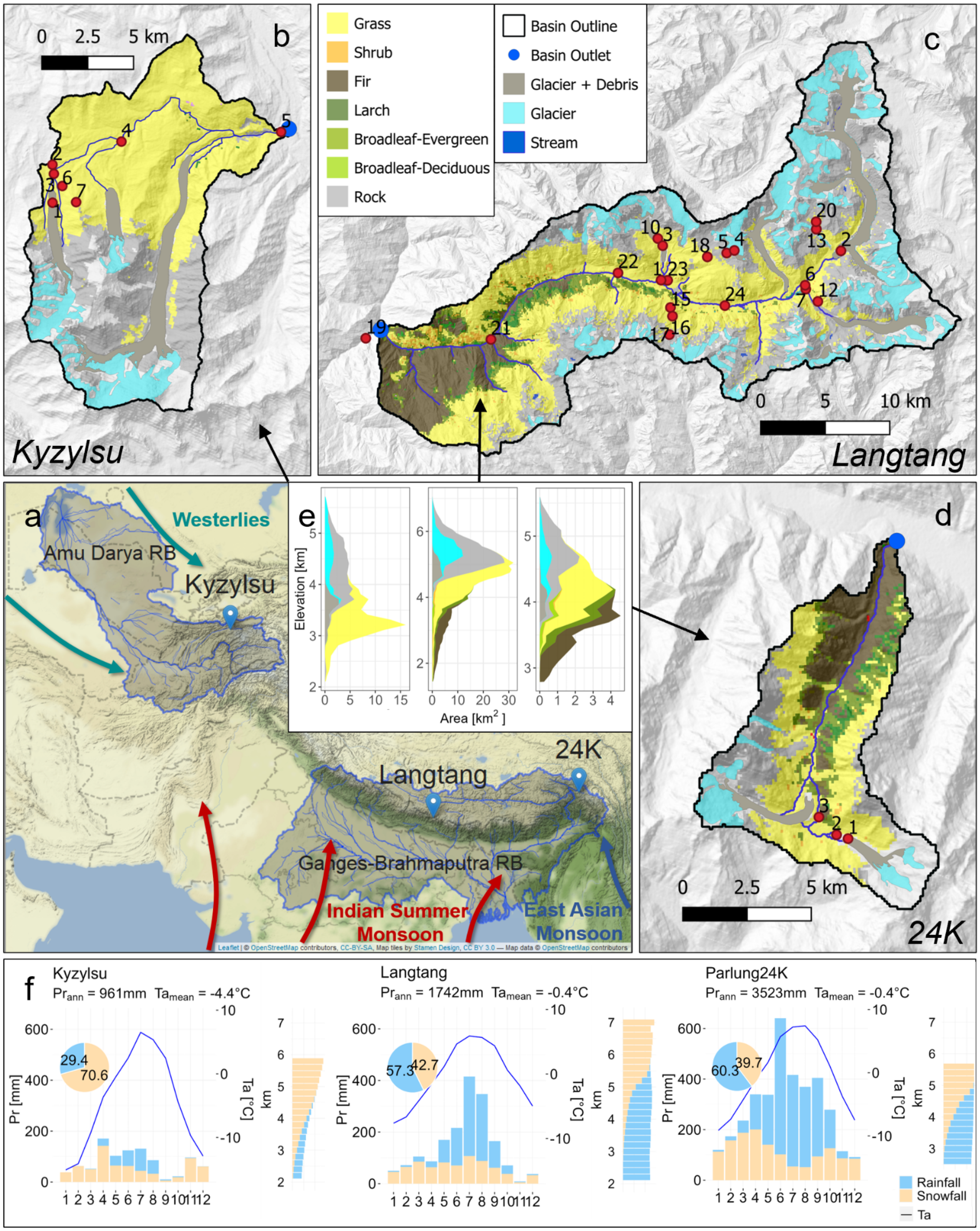

Figure 1: a) Map of the region with the location of the three study catchments indicated, along with b-d) detailed maps showing land cover and station locations and station identifiers. e) land cover hypsometry. f) average monthly meteorological conditions over the study period and hypsometry of precipitation partitioning.

2. Study sites

Three glacio-hydrological reference catchments are investigated, with the common features of steep topography, vegetation cover, substantial glacier coverage, abundance of supraglacial debris and large, but comparable elevation ranges (Figure 1a-e). Since they span the climatic spectrum of HMA, these catchments are ideally suited for a comparative perspective on the diversity of HMA headwater hydrology.
Kyzylsu (KYZ, 168 km^2) is located in the headwaters of the Amu Darya river basin, on the northernmost slopes of the Pamir mountain range in Tajikistan (Figure 1a,b). The local weather is controlled by a continental climate and has no direct influence from the Indian summer monsoon (Schienmann et al., 2008). Monitoring in this new reference catchment has only recently started (June 2021), and observations were geared towards glacio-hydrological modelling. The initial network is detailed in Supplementary Section 1. The region, with a mean glacier mass balance of -0.17 m w.e. yr^{-1} (Pamir and Pamir Alai regions, 2000-2016, Miles et al., 2021), has been regarded as part of the Pamir-Karakoram Anomaly (Hewitt et al., 2005; Farinotti et al., 2019; Barandun et al., 2021; Miles et al., 2021). Recent evidence however suggests that the region might be trending towards overall negative mass balances (Hugonnet et al., 2021).
Located in the Central Himalaya of Nepal and seasonally governed by the Indian Summer Monsoon (Figure 1a,c), *Langtang* (LAN, 586km^2) is a well-studied Ganges headwater catchment, where monitoring has taken place since the 1980s, and systematic meteorological and glaciological measurements have been made since 2012 (e.g. Higuchi, 1984; Fujita et al., 1997, 1998; Steiner et al., 2021). The region exhibits rapidly shrinking glaciers, with a mean mass balance of -0.43 m w.e. yr^{-1} (Everest region, 2000-2016, Miles et al., 2021).
Parlung 24k (24K, 64km^2), is a small Yarlung Tsangpo/Brahmaputra headwater basin on the Southeastern Tibetan Plateau (Figure 1a,d) that has been monitored since 2016 (Yang et al., 2017). Out of the three study sites, it has the wettest climate, with heavy precipitation occurring from March to September (Figure 1f), since it is affected by both the Indian and East Asian summer monsoons (Bookhagen and Burbank, 2010; Ding and Chan, 2005). Glacier mass balances in the region have been shown to be amongst the most negative in HMA, averaging around -0.68 m w.e. yr^{-1} (Nyainqentangla region, 2000-2016, Miles et al., 2021), which has been partly attributed to a shift in precipitation from snowfall to rain (Jouberton et al., 2022).

3. Methods

The model

To simulate the coupled dynamics of water, snow and glaciers, energy, vegetation physiology and carbon in the three catchments, the Tethys-Chloris model (T&C; Fatichi et al., 2012a,b; Manoli et al., 2018; Mastrotheodoros et al., 2019; Botter et al., 2021; Paschalis et al., 2022) (Figure S3), was applied to the period October 2010 to September 2022. The period October 2010 to September 2012 was considered a spin-up period and was not included into the analysis of model outputs. For each grid cell, the energy balance is solved for the surface temperature of any type of land cover, including vegetated and bare land, rock, surface water, snow, glaciers and supraglacial debris, and includes the computation of net radiation, sensible and latent heat, heat consumed by photosynthesis and heat exchange with the subsurface. The model also resolves infiltration and exfiltration, deep percolation, lateral surface and subsurface water flows, soil moisture dynamics in the unsaturated zone including root water uptake at different depths at the grid level. Glaciers are represented as a single-layered ice-pack including a retention capacity for water. Glacier outlines and debris covered areas were manually corrected, based on the Randolph glacier inventory (RGI-6) and the debris thicknesses product was prepared combining remote sensing data and in-situ observations (Supplementary Section 4). The snow-, ice and ice-under-debris mass balance models are described in detail in Fugger et al. (2022) and Fyffe et al. (2021). A more detailed description of T&C is provided in Fatichi et al., (2012a,b, Mastrotheodoros et al 2020), and a setup in the upper part of Langtang and additional model details are described in Buri et al. (2023). Advances implemented for this study include a 2-layer snowpack model, where the surface energy balance is solved at a skin layer, and a parameterization for glacier geometry changes as detailed in Supplementary Section 5. The sensitivity of the energy and mass fluxes involved in the computation of the glacier and snow mass balances to model parameters and meteorological forcing were presented in Fyffe et al. (2021) and Fugger et al. (2022). The model parameters were not calibrated in the traditional sense, e.g. through automatic calibration of multiple parameters against spatially integrated variables like runoff. Instead they were estimated from the literature and using expert knowledge (e.g. Fatichi et al., 2016). Parameters requiring optimization and manual adjustments from the T&C standard setup were related to the thermal properties of the supraglacial debris, the glacier geometry updates, bare-ice albedo, the vegetation phenology and to high-elevation precipitation at one of the sites (Supplementary Section 5).

Forcing data

The model was forced using downscaled hourly air temperature (Ta), relative humidity (RH), total precipitation (P), incoming shortwave radiation (S_{in}), incoming longwave radiation (L_{in}), wind speed (W_s) and air pressure (Pa) data from the ERA5-Land 9km reanalysis (Muñoz-Sabater, 2021). Statistical downscaling to 100 m spatial resolution was performed following the approach of Machguth et al (2009), which combines simple parameterisations with spatial interpolation (Supplementary Section 2, Figures S1-2). Bias correction of forcing variables was performed using Empirical Quantile Mapping (EQM) against local station data (Supplementary Section 3). Independent stations were used, where possible, to assess the efficacy of the bias-correction in space and time (Figures S4 - S21). Despite minor discrepancies, the forcing data are deemed acceptable for the representation of spatial and temporal variability in the catchment-wide meteorology, as indicated by low biases, RMSE values and high correlation coefficients against observations (Fig S4-S21, Table S3).

Model evaluation

Model performance was evaluated using a combination of in-situ and remote sensing data. Snowlines were derived from the MODIS Terra snow cover V6.1 product (Fugger, 2018; Hall et al., 2021) and compared to the modelled snowlines. Snow cover was additionally evaluated scene-by-scene against Sentinel-2/Landsat-8 and Dice coefficients (Dice, 1945) were calculated. The modelled surface mass balance of glaciers was evaluated against two references: the geodetic mass balance results of Hugonnet et al. (2021); and altitudinal values derived following the approach of Miles et al. (2021) that uses the thinning data of Hugonnet et al. (2021) and the surface velocities of Millan et al. (2022) at Langtang. At Kyzylsu and 24K the velocity and geodetic mass balance data quality prevented the second approach. Modelled snow depth (all sites) and ice melt (Kyzylsu, Langtang) were evaluated using automatic measurements of surface height. Catchment mean leaf area index (LAI) was compared against MODIS (MCD15A3H v.6, Myneni, Knyazkhin, 2015) and VIIRRS (VNP15A2H v.1; Myneni, Knyazkhin, 2018) LAI products. Modelled discharge was evaluated against data from gauging stations in proglacial streams of Kyzylsu, Langtang and 24K glaciers.

4. Results

Evaluation of model performance

Modelled snowlines correspond well with remote sensing observations are typically within the uncertainty ranges of the observed snowlines, with biases (R^2 values) of -52.2m (0.74), –16.6m (0.43), -194.4m (0.41) for Kyzylsu, Langtang and 24K, respectively (Figure S22).

Modelled snow cover agreed well with Landsat-8/Sentinel-2 scenes in a scene-by-scene comparison, and average Dice coefficients for each site were 0.66, 0.66, 0.76 (Figure S23), with higher performance during periods of more extensive snow cover and lower performance during patchy snow cover.

Compared to observations, the timing of local snow accumulation and glacier melt was very well reproduced, while some under- and overestimations of the snowpack height up to 45cm occurred at 24K and Kyzylsu (Figure S24). These local discrepancies are likely related to the absence of a wind-driven snow redistribution scheme in the model.

The model agrees very well with the remote-sensing-based glacier-wide and altitudinal mass balance values at Langtang (0.65 m w.e.yr^{-1} vs 0.62 +/- 0.13 w.e.yr^{-1}), to within observational uncertainty at 24K (-0.42 m w.e. yr^{-1} vs. 0.25 +/- 2.07 m w.e. yr^{-1}), and with a slight negative overestimation at the Kyzylsu glaciers (-0.46 m w.e. yr^{-1} vs. 0.18 +/- 0.22 m w.e. yr^{-1}) (Figure S25-S27).

Leaf area index (LAI) values show overall good agreement with observations in terms of magnitude (Figure S28), while there are mismatches in terms of timing at Kyzylsu (RMSE: 0.52) and Langtang (0.71) and peak LAI magnitudes at 24K (0.36).

Both the magnitude and timing of streamflow variations are well reproduced at the pro-glacial stream gauges, with NSE values of 0.5 at Kyzylsu, 0.55 at 24K, and a somewhat weaker agreement at Langtang with 0.27 (Figure S29).

Precipitation determines the relative importance of evaporative fluxes and glacier melt

The annual water throughput of the catchments, which is defined as the total water added to or removed from the water balance within a year in either liquid, solid or gaseous form, increases from west to east (Figure 2 & 5). The annual water throughput is highest in 24K, followed by Langtang and Kyzylsu: Langtang and 24K respectively receive around 1.8 times (1742 mm yr^{-1}) and 3.7 times (3523 mm yr^{-1}) more precipitation than Kyzylsu (961 mm yr^{-1}) (Figure 2 & 5). The partitioning of inputs into rain and snowfall is controlled by the precipitation seasonality: with a winter-accumulation regime, 70.6% of annual precipitation falls as snow at Kyzylsu, while those portions are smaller in Langtang (42.7%) and 24K (39.7%) (Figure 1f), where the bulk of the precipitation falls in the summer half-year.

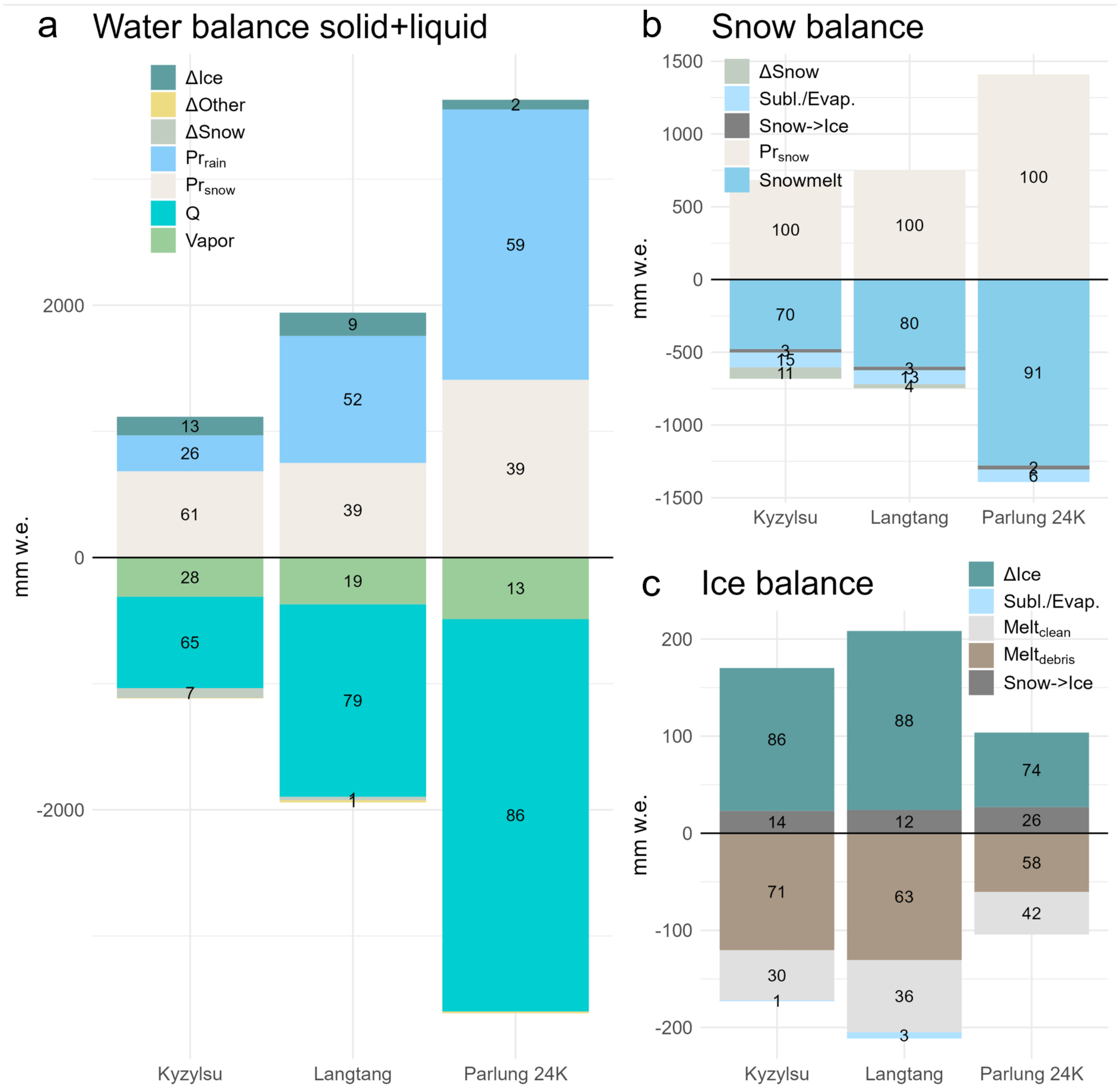

Figure 2: a) Annual catchment average water balances, b) catchment average snowpack balances, and c) catchment average ice mass balances for three catchments following a standard water balance formula (Precipitation = Runoff + Vapour fluxes + Storage Changes). Snow on glaciers is counted towards the catchment-wide snowpack rather than towards the ice pack. Numbers in segments show the percentage contribution to or withdrawal from the water balance. Once reaching the ground, precipitation in solid or liquid form passes through the snow- and/or ice-pack-, interception- or groundwater-storages, before being transferred out of the catchment in the form of runoff or vapour. An imbalance of those storages at the annual scale results in net addition or net removal of water to or from the water budget (Δ-components); ΔOther symbolises the summed differences of the interception storages of all surfaces including vegetation, the surface water and soil water storages.

Across the common elevation range of the three catchments (2500-5700 m asl), snowmelt contributes 67% of annual runoff in Kyzylsu, 35% in Langtang, and 41% in 24K (Figure 3a). Once most of the snow has melted out in Kyzylsu between the middle and end of August, ice melt becomes the dominant runoff contribution with 55% in September (annually 24%). In Langtang, which has a similar proportion of glacier area, the ice melt contribution peaks in post-monsoon with 21.7% in October, while later during summer, it is dwarfed by monsoonal rainfall so that the ice melt contribution is only 14% annually. At 24K, which hosts around half the proportion of glacier area compared to the other sites, but gets substantially higher liquid precipitation inputs, ice melt contributes only 8% to the runoff in August (3% annually) (Figure 3a). Note that snowmelt above glacier surfaces is counted towards the catchment-wide snowmelt rather than to the ice melt.

Rainfall runoff contributes the largest share (56%) to total runoff in 24K, followed by Langtang (51%), and Kyzylsu (9%) (Figure 3a). During the period March to August rainfall is transformed into runoff in Kyzylsu, while from September to October the majority of rainfall is evaporated (Figure 3a).

In all three catchments, catchment-wide, modelled glacier mass balances were negative over the study period with -0.46, -0.65 and -0.42 m w.e. yr^{-1} in Kyzylsu, Langtang and 24K respectively (Figure S25-S27). The imbalance melt, defined as the glacier melt not replenished by new ice formation, accounted for 13, 9 and 2% of the mass inputs to the water balance in Kyzylsu, Langtang and 24K, respectively (Figure 2). In all catchments, sub-debris ice melt is larger than bare-ice melt, with 66.8, 62.5, 57.9% for Kyzylsu, Langtang and 24K, respectively (Figure 2). The total E (combined ET and S) accounts for 28, 19 and 13 % of the catchment water output (Figure 2a) of Kyzylsu, Langtang and 24K, respectively. ET alone corresponds to 76% of the liquid precipitation falling in Kyzylsu, 28% in Langtang, and 19% in 24K. The relative importance of glacier melt and evaporative fluxes therefore decreases with an increasing water throughput from west to east. A spatial distribution of annual melt, evapotranspiration and sublimation is shown in Figure S30.

Net radiation is the main control on evaporative fluxes at all sites

Across the common elevation range, the evaporative fluxes follow the seasonality of net radiation (Rn) that is available for the turbulent heat transfer in the case of ET and additionally the snow covered area and temperature regime in the case of S (Figure 3b). Soil water limitations do not affect the ET rates in either of the catchments during average years, since the latent energy (LE) and ET follow the Rn regime throughout the season, and soil water limitations do not occur, as indicated by the soil moisture seasonality (Figure 3b). A high availability of intercepted water on leafs and rock surfaces however boosts evaporation rates in the wet climate of 24K (Figure 3b). Evaporation from supraglacial debris is a small flux for the catchment (not shown), but helps insulate the glacier ice by removing energy in the form of latent energy from entering the glacier (Fugger et al., 2022).

Sublimation is important, especially at the semi-arid site

In all three catchments, sublimation removes mass from the ground and canopy intercepted snowpack year-round (Figure 3b,c). Relative to the snowfall amounts, sublimation is largest in Kyzylsu, followed by Langtang and 24K (15, 13, 6 %, respectively) (Figure 2b). In absolute terms and for the common elevation range, sublimation is also largest in Kyzylsu (91 mm yr^{-1}), but it is second largest in 24K (71 mm yr^{-1}) and smallest in Langtang (57 mm yr^{-1}). In Langtang, however, where the snowline is generally higher, most sublimation happens above the elevation range of the other basins, amounting to 84 mm yr^{-1} over the whole elevation range of Langtang (Figure S32).

During the warmest months of the year, sublimation rates are low (e.g. Kyzylsu 0.2mm d^{-1}, Langtang <0.01 mm d^{-1}, Parlung24K 0.03 mm d^{-1}), since snow retreats to the highest elevations, and temperatures are often above the melting point during the periods of high radiation inputs, favouring snow and ice melt rather than sublimation (Figure 3c). Only in Kyzylsu there is notable snowpack sublimation also in the lower reaches of the catchment, owing to the lower temperatures and heavier snowfalls there during winter (Figure 3c).

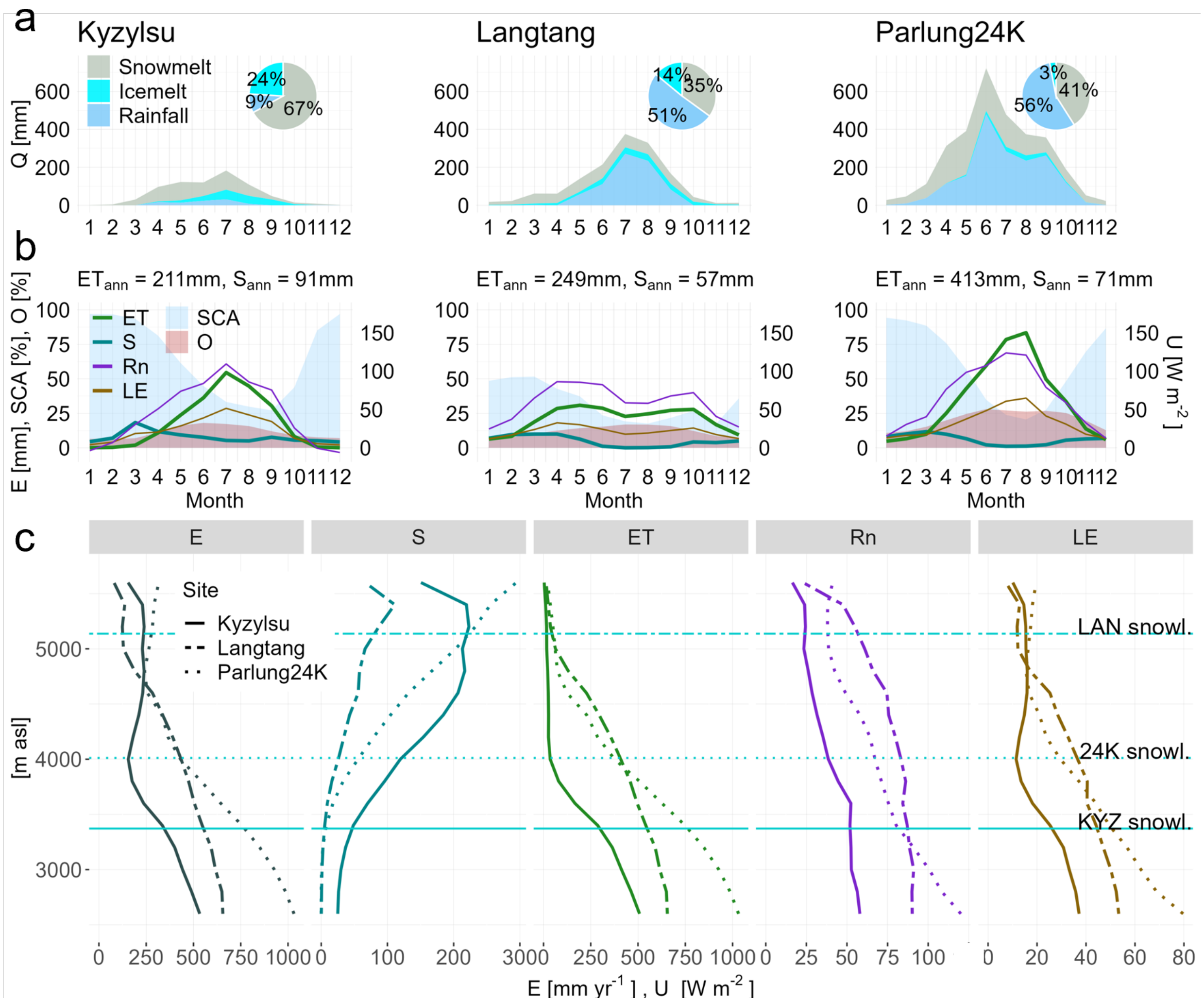

Figure 3: a) *Mean monthly runoff contributions of snowmelt, ice melt and rainfall (stacked bars), and shares of the total annual runoff (Q) (pie charts). Snowmelt from glacier surfaces is included in the snow share rather than in the ice share. b) Mean monthly evaporative fluxes ET and S together with energy fluxes (U) net radiation (Rn) and latent energy (LE); snow covered area (SCA) and soil moisture (O) as shaded areas in the figure background. c) Site comparison of evaporative and energy fluxes by altitude; turquoise horizontal lines indicate catchment annual mean snowline at each site. All values for the common elevation range (2500-5700 m asl).*

Melt partially compensates for supply deficits in warm-dry years

Under warmer- and drier-than-average conditions, such as during the hydrological years 2021/22 (Kyzylsu) and 2016/17 (Langtang) and 2017/18 (24K), additional ice melt of +35 mm, +33 mm and +10 mm partially compensates for the supply deficits. The supply deficit is here defined as the combination of precipitation deficits and ET losses, which amount to -225 mm, -153 mm and -368 mm compared to the multi-year average (2010/11-2021/22), at Kyzylsu, Langtang and 24K, respectively (Figure S31). Snowmelt under warm conditions has an even greater replenishing effect on the water yield, since old snow, e.g. from glacier accumulation zones, is being depleted: the snowmelt deficit (-32 mm, -22mm, -170mm) is considerably smaller than the snowfall deficit (-141 mm, -61 mm, -236 mm) (Figure S31), implying a net snowmelt increase of 109 mm, 39 mm and 66 mm. While ice melt alone offsets only around 16%, 22% and 3% of the supply deficits, the ice and snow melt enhancements together offset 64%, 47%, and 21% of the precipitation deficits. As a result of compensations due to enhanced glacier and snow melt, the driest and warmest hydrological years (such as 2021/22 at Kyzylsu, 2017/18 at Langtang and 24K) do not correspond to the greatest runoff deficits (Figure 4a).

Evapotranspiration anomalies can reach values similar to those of enhanced ice melt under warmer conditions (e.g. Kyzylsu: 2015, 2021; Langtang: 2021; 24K: 2017; Figure 4b), implying that evapotranspiration counterbalances the additional ice melt contribution to streamflow. Note however, that the level of this balancing is strongly related to the proportion of glacier cover versus the remaining land cover in a catchment.

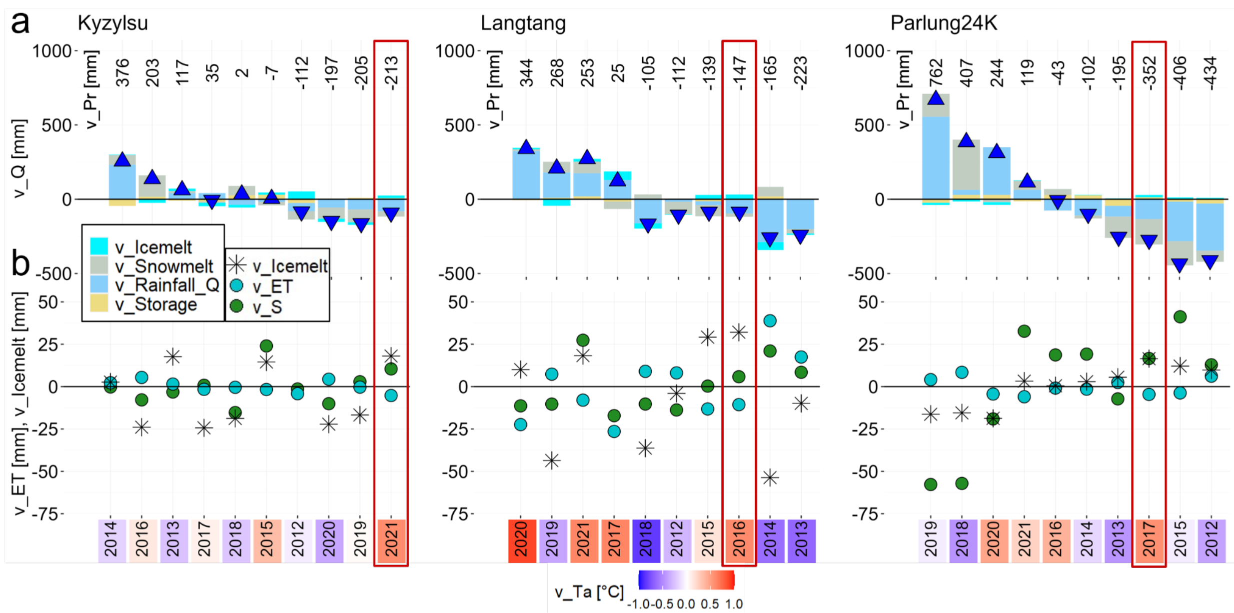

Figure 4: a) Annual runoff anomalies and their components (stacked bars), ranked by the precipitation anomaly (v_Pr) of each hydrological year from left to right (positive to negative v_Pr). Blue triangles show the runoff surplus (up) or deficit (down). Temperature anomalies (v_Ta) are shown in red to blue on the year labels; Precipitation anomalies (v_Pr) are given as numbers above the bars. b) Annual evapotranspiration (v_ET) and sublimation (v_S) anomalies along with ice melt anomalies (v_Icemelt). Red boxes indicate warm-dry focus years, which are detailed in Figure S31. All values are relative to the mean over the reference period (Oct-2012 to Sep-2022). Years on the x-axis indicate hydrological years (e.g. 2014 indicates the hydrological year 2014/15).

5. Discussion

Importance of evapotranspiration and sublimation

Sublimation is highest in both relative and absolute terms and across the common elevation range in Kyzylsu, supporting our first hypothesis (I) that sublimation is most important in semi-arid, high elevation catchments (Figure 2 & 3). Clear-sky conditions, with low winter temperatures and high snowfall rates create favourable conditions for sublimation. In contrast, cloudy, warm conditions during the accumulation period drastically reduce sublimation but favour melt (Mandal et al., 2021; Fugger et al., 2022). Snow sublimation has long been recognized as an important mass flux in snowy alpine environments, including in the Alps (Strasser et al., 2010), glacierized catchments in the Canadian Rockies (Pradhanga et al., 2022; Aubry-Wake et al., 2022), the Himalaya (Buri et al., 2023), and at the glacier scale in the Andes (Ayala et al., 2017). The share of snowfall removed by sublimation ranges between 5% and 90% in previous literature, depending on the study site's environment, elevation range and topography. Here, we estimate this share for the three catchments as 15% (Kyzylsu), 13% (Langtang) and 6% (24K). Modelling scenarios not including sublimation would overestimate the annual snowmelt runoff by this share, affecting especially summer season runoff and peak flows (Stigter et al., 2022).

Our second hypothesis (II), that ET is higher in monsoonal catchments, can also be confirmed, since Kyzylsu shows less overall ET than Langtang and 24K. This is mostly a result of the energy regimes and snow cover dynamics, rather than a result of soil water limitations (Figure 3). However, intense rainfalls over the greater part of the year provide additional water to evaporate from leaf-, rock- and other interception-storages, boosting ET at 24K.

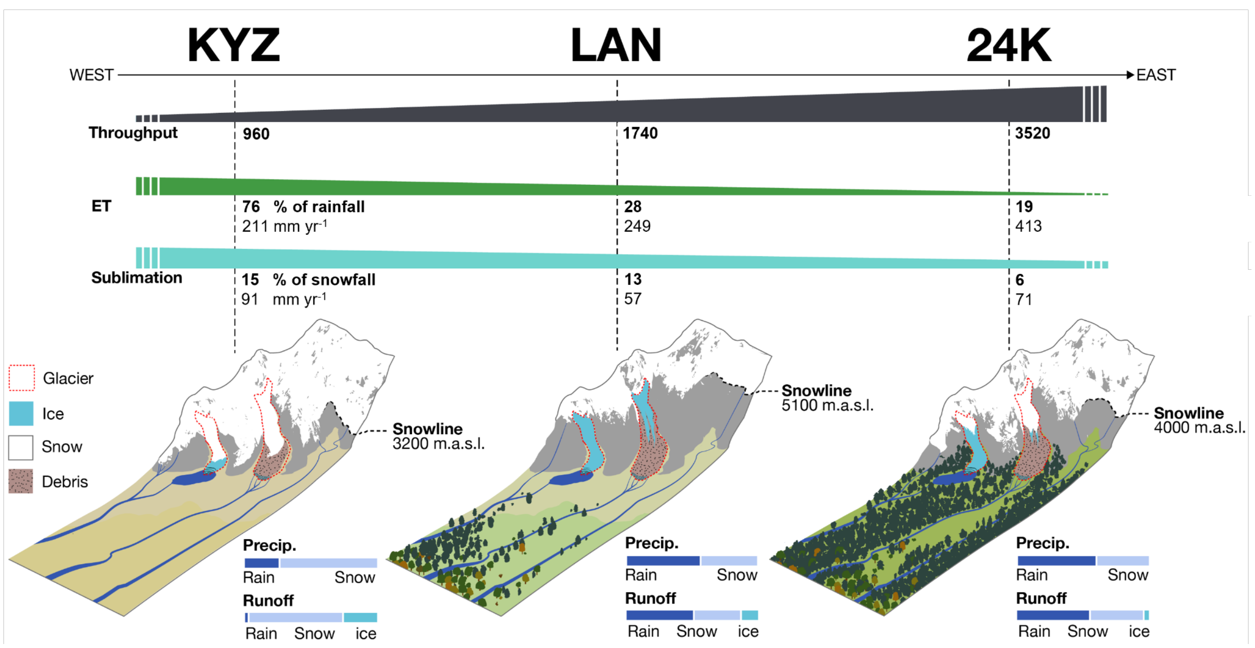

Figure 5: Conceptual summary of catchment features, hydro-climatic setting, land cover and study outcomes.

Trade-offs between ice melt and evaporative fluxes under warm-dry conditions

In none of the catchments and years did ice melt alone overcome the supply deficit during warm-dry years, although this may happen at the seasonal or event timescale (van Tiel et al., 2021). While ice melt enhancements reach similar magnitudes as the evaporative loss enhancements, the third hypothesis, that ice melt can compensate for the combination of both precipitation deficits and enhanced evaporative losses during warm-dry years, is not supported by our results. Ice melt combined with melt from old snow can however offset as much as 64% of the supply deficit in Kyzylsu. These results reveal important implications for the system behaviour under climate change and should contribute to the discussion around future water yield under a vanishing cryosphere (e.g. Ragettli et al., 2016; Huss & Hock, 2018, McCarthy et al. 2022).

Sensitivity to climate change

The interannual anomalies of sublimation and evapotranspiration can reach similar magnitudes as the ice melt anomalies (Figure 4b), depending on the catchment configuration. The interannual variability in evaporative fluxes is generally smaller than the interannual variability of rain- and snowfall inputs at all sites, in agreement with previous studies (Roberts 1983; Fatichi and Ivanov 2014). Under a warming climate, therefore, shifts in precipitation volume and phase (Jouberton et al., 2022; Shaw et al., 2022), as well as the decline in glacier cover will probably be more important to streamflow variability (e.g. Ragettli et al., 2016; Huss & Hock, 2018) than changes in the evaporative fluxes. The streamflow at the semi-arid site is likely the most sensitive to climate change, due to the important role of the cryosphere in runoff generation for two reasons: (i) glacier melt sustains summer runoff and glaciers are shrinking, even in the domains affected by the Pamir-Karakoram anomaly (Hugonnet et al., 2021). Where 'imbalance' ice melt at present compensates for runoff deficits under warm-dry conditions, this effect will initially increase, but eventually vanish, once ice masses have shrunken further (e.g. McCarthy et al. 2022); (ii) Our analysis shows that the melting of old snow can buffer streamflow deficits during warm-dry years to an even greater extent than the melting glacier ice, with the highest degree of compensation at Kyzylsu. These old snow reserves would however vanish quickly over a few consecutive warm-dry years. Additionally, seasonal snowpacks are thinning and global warming is bringing the bulk snowmelt events earlier in the season (Unger-Shayesteh et al., 2013). Modelling experiments based on future scenarios are needed, in order to fully understand the High Mountain Asian headwaters' sensitivity to climate change.

Limitations

Uncertainties in model outputs were not explicitly quantified due to the high computational demand of the model (Table S4) limiting our ability to perform a large number of simulations. Instead, the model results were compared against a large range of ground and remotely sensed data, confirming its ability to replicate the necessary physical processes. While sublimation from the ground- and canopy-intercepted snowpack is simulated, blowing snow sublimation is not, and so sublimation on wind-exposed mountain ridges is potentially underestimated in this study (Strasser et al., 2008). Similarly, due to the absence of a blowing snow transport scheme, the heterogeneity of snow depths between ridges and valleys is underrepresented (Aubry-Wake et al., 2022). The model does not have a separate firn layer representation. This might affect the mass balance of the accumulation zones, since the thermal and surface properties of firn differ from those of snow and ice (Pradhanga and Pomeroy, 2022). Supraglacial ice cliffs and ponds were not modelled, but these features are expected to enhance melt-rates of debris-covered glaciers (Miles et al., 2018; Buri et al., 2021; Miles et al., 2022; Kneib et al., 2023). Finally, measurements of the surface latent heat fluxes are needed to better evaluate these fluxes in high elevation catchments and should be a goal of future fieldwork.

6. Conclusion

Our mechanistic modelling approach, forced with downscaled reanalysis data at a spatial resolution suited to steep mountain topography, proved transferable across three glacierized catchments, which span the geographic and climatic spectrum of High Mountain Asia. Minimising the risk of equifinality issues, our approach requires minimal calibration, and addresses several key challenges for this domain (Azam et al., 2021): a detailed representation of supraglacial debris and an energy-balance based calculation of ice melt under debris cover, bias-corrected and spatially variable meteorological inputs, the computation of sublimation, as well as evapotranspiration and all-surface-evaporation. Our simulations show that water throughput determines the importance of the evaporative fluxes, and varies by a factor of 3.7 between the 'climatic ends' of HMA studied here (Kyzylsu vs. 24K, Figure 1). We find that over the 10 year study period, sublimation losses accounted for an average of 15, 13 and 6% of the snow falling in Kyzylsu, Langtang and 24K, respectively. They are highest at the site with the largest amount of winter and spring accumulation, Kyzylsu, also in absolute terms (Figure 5). Evapotranspiration removes 76, 28 and 19% of the liquid precipitation from the three catchments, respectively, and prevents almost any runoff generation from rainfall during the low-flow months in Kyzylsu. However, annual evapotranspiration is highest in absolute terms at 24K (Figure 5). Ice compensates for up to 17% of the supply deficit during a warm, dry year at the site with the highest glacier cover, Kyzylsu, but neither fully, nor over-compensates at the annual timescale and in either of the catchments. Old snow melt and ice melt combined, however, can offset as much as 64% of the supply deficit. Increased evapotranspiration during those years can reach similar magnitudes to the additional ice melt, intensifying the deficit in the runoff. In order to better anticipate future water yields, the sensitivity of HMA headwaters to global warming should be further tested with experiments using mechanistic models.

Acknowledgements
We would like to thank the team at the Center for the Research of Glaciers, Tajik National Academy of Sciences, Abduhamid Kayumov, Khusrav Kabutov, Ardamehr Halimov, among others, for their invaluable support over multiple field seasons in Kyzylsu. We thank Wei Yang, Zhao Xhuanxi and Zhen Cheng from the Institute of Tibetan Plateau Research, Chinese Academy of Sciences, for facilitating and supporting fieldwork and for sharing crucial data from the Parlung 24K catchment. We thank Reeju Shrestha and Himalayan Research Expeditions for their great support in Langtang. We extend our thanks to Jakob Steiner and the team at ICIMOD for their relentless efforts in data acquisition and curation in Langtang. Additionally, we are indebted to Masashi Niwano from the Meteorological Research Institute, Japan Meteorological Agency, for providing NHM atmospheric simulation outputs, which proved very valuable in the downscaling process.

Conflict of interest
The authors declare no conflicts of interest in relation to this research paper.

Funding

This project has received funding from the European Research Council (ERC) under the European Union's Horizon 2020 research and innovation program Grant Agreements No. 772751 (RAVEN, Rapid mass losses of debris-covered glaciers in High Mountain Asia). Further funding was provided by JSPS-SNSF (Japan Society for the Promotion of Science and Swiss National Science Foundation) Bilateral Programmes project (HOPE, High-elevation precipitation in High Mountain Asia; Grant 183633). Fieldwork support for Tajikistan was received from the Swiss Polar Institute Flagship Programme PAMIR, SPI-FLAG-2021-001. The project also received funding from the ESA and NRSCC Dragon 5 cooperation project "Cryosphere-hydrosphere interactions of the Asian water towers: using remote sensing to drive hyper-resolution ecohydrological modeling" (grant no. 59199)."

Data Access

The data that support the findings of this study will be openly available following a delay

References

Armstrong McKay, D. I., Staal, A., Abrams, J. F., Winkelmann, R., Sakschewski, B., Loriani, S., ... & Lenton, T. M. (2022). Exceeding 1.5 C global warming could trigger multiple climate tipping points. Science, 377(6611), eabn7950.

Azam, M. F., Kargel, J. S., Shea, J. M., Nepal, S., Haritashya, U. K., Srivastava, S., ... & Bahuguna, I. (2021). Glaciohydrology of the Himalaya-Karakoram. Science, 373(6557), eabf3668.

Beug, H. J., & Miehe, G. (1999). Vegetation history and human impact in the Eastern Central-Himalaya (Langtang and Helambu, Nepal). Dissertaciones Botanicae (318), 98 p.

Beven, K. (1995). Linking parameters across scales: subgrid parameterizations and scale dependent hydrological models. *Hydrological processes*, *9*(5-6), 507-525.

Botter, M., Zeeman, M., Burlando, P., & Fatichi, S. (2021). Impacts of fertilization on grassland productivity and water quality across the European Alps under current and warming climate: insights from a mechanistic model. Biogeosciences, 18(6), 1917-1939.

Buri, P., Miles, E. S., Steiner, J. F., Ragettli, S., & Pellicciotti, F. (2021). Supraglacial ice cliffs can substantially increase the mass loss of debris-covered glaciers. Geophysical Research Letters, 48(6), e2020GL092150.

Dice, Lee R. "Measures of the amount of ecologic association between species." *Ecology* 26.3 (1945): 297-302.

Pascal Buri, Simone Fatichi, Thomas E. Shaw, Evan S. Miles, Michael J. McCarthy, Catriona Fyffe, Stefan Fugger, Shaoting Ren, Marin Kneib, Achille Jouberton, Jakob Steiner, Koji Fujita, and Francesca

Pellicciotti, 2023. Land surface modeling in the Himalayas: on the importance of evaporative 2 fluxes for the water balance of a high elevation catchment

Farinotti, D., Huss, M., Fürst, J. J., Landmann, J., Machguth, H., Maussion, F., & Pandit, A. (2019). A consensus estimate for the ice thickness distribution of all glaciers on Earth. Nature Geoscience, 12(3), 168-173.

Fatichi, S., Ivanov, V. Y., & Caporali, E. (2012). A mechanistic ecohydrological model to investigate complex interactions in cold and warm water-controlled environments: 1. Theoretical framework and plot-scale analysis. Journal of Advances in Modeling Earth Systems, 4(2).

Fatichi, S., Ivanov, V. Y., and Caporali, E. (2012), A mechanistic ecohydrological model to investigate complex interactions in cold and warm water-controlled environments: 2. Spatiotemporal analyses, J. Adv. Model. Earth Syst., 4, M05003,doi:10.1029/2011MS000087.

Fatichi, S., & Ivanov, V. Y. (2014). Interannual variability of evapotranspiration and vegetation productivity. *Water Resources Research*, *50*(4), 3275-3294.

Fiddes, J., & Gruber, S. (2014). TopoSCALE v. 1.0: downscaling gridded climate data in complex terrain, Geosci. Model Dev., 7, 387–405, doi: 10.5194.

Fisher, J. B., Lee, B., Purdy, A. J., Halverson, G. H., Dohlen, M. B., Cawse-Nicholson, K., ... & Hook, S. (2020). ECOSTRESS: NASA's next generation mission to measure evapotranspiration from the international space station. Water Resources Research, 56(4), e2019WR026058.

Fugger, S., Fyffe, C. L., Fatichi, S., Miles, E., McCarthy, M., Shaw, T. E., ... & Pellicciotti, F. (2022). Understanding monsoon controls on the energy and mass balance of glaciers in the Central and Eastern Himalaya. The Cryosphere, 16(5), 1631-1652.

Fujita, K., Sakai, A., & Chhetri, T. B. (1997). Meteorological observation in Langtang Valley, Nepal Himalayas, 1996. Bulletin of Glacier Research, 15, 71-78.

Fujita, K., Takeuchi, N., & Seko, K. (1998). Glaciological observations of Yala Glacier in Langtang Valley, Nepal Himalayas, 1994 and, Bulletin of Glacier Research, 16, 75-8.

Fujita, K., & Sakai, A. (2014). Modelling runoff from a Himalayan debris-covered glacier. Hydrology and Earth System Sciences, 18(7), 2679-2694, doi:10.5194/hess-18-2679-2014

Fyffe, C. L., Potter, E., Fugger, S., Orr, A., Fatichi, S., Loarte, E., ... & Pellicciotti, F. (2021). The energy and mass balance of Peruvian glaciers. Journal of Geophysical Research: Atmospheres, 126(23), e2021JD034911.

Gascoin, S. (2021). Snowmelt and snow sublimation in the Indus Basin. Water, 13(19), 2621.

Hall, D. K. and G. A. Riggs. 2021. MODIS/Terra Snow Cover Daily L3 Global 500m SIN Grid, Version 61. [Indicate subset used]. Boulder, Colorado USA. NASA National Snow and Ice Data Center Distributed Active Archive Center. doi: https://doi.org/10.5067/MODIS/MOD10A1.061. [Date Accessed].

Higuchi, K. (Ed.). (1984). Glacial studies in Langtang Valley: Report of the glacier boring project 1981-82 in the Nepal Himalaya. Data Center for Glacier Research, Japanese Society of Snow and Ice.

Hugonnet, R., McNabb, R., Berthier, E., Menounos, B., Nuth, C., Girod, L., ... & Kääb, A. (2021). Accelerated global glacier mass loss in the early twenty-first century. Nature, 592(7856), 726-731.

ICIMOD & Utrecht University. (2020). Discharge: Langtang Khola [Data set]. ICIMOD. https://doi.org/10.26066/RDS.1972407

ICIMOD. (2021). Meteorological data from Kyanging automatic weather station [Data set]. ICIMOD. https://doi.org/10.26066/RDS.22464

Immerzeel, W. W., Van Beek, L. P. H., Konz, M., Shrestha, A. B., & Bierkens, M. F. P. (2012). Hydrological response to climate change in a glacierized catchment in the Himalayas. Climatic change, 110(3), 721-736.

Immerzeel, W. W., Pellicciotti, F., & Bierkens, M. F. P. (2013). Rising river flows throughout the twenty-first century in two Himalayan glacierized watersheds. Nature geoscience, 6(9), 742-745.

Immerzeel, W. W., Petersen, L., Ragettli, S., & Pellicciotti, F. (2014). The importance of observed gradients of air temperature and precipitation for modeling runoff from a glacierized watershed in the Nepalese Himalayas. Water Resources Research, 50(3), 2212-2226.

Immerzeel, W. W., Lutz, A. F., Andrade, M., Bahl, A., Biemans, H., Bolch, T., ... & Baillie, J. E. M. (2020). Importance and vulnerability of the world's water towers. Nature, 577(7790), 364-369.

Jobst, A. M., Kingston, D. G., Cullen, N. J., & Sirguey, P. (2016). Combining thin-plate spline interpolation with a lapse rate model to produce daily air temperature estimates in a data-sparse alpine catchment. International Journal of Climatology. https://doi.org/10.1002/joc.4699

Katul GG, Oren R, Manzoni S, Higgins C, Parlange MB. Evapotranspiration: a process driving mass transport and energy exchange in the soil-plantatmosphere-climate system. Rev Geophys 2012, 50: RG3002.

Khanal, S., Lutz, A. F., Kraaijenbrink, P. D., van den Hurk, B., Yao, T., & Immerzeel, W. W. (2021). Variable 21st century climate change response for rivers in High Mountain Asia at seasonal to decadal time scales. *Water Resources Research*, *57*(5), e2020WR029266.

Kneib, M., Miles, E. S., Buri, P., Fugger, S., McCarthy, M., Zhao, C., ... & Pellicciotti, F. (2022, May). Sub-seasonal evolution of ice cliffs captured with time-lapse photogrammetry. In *EGU General Assembly Conference Abstracts* (pp. EGU22-6163).

Kneib, M., Fyffe, C. L., Miles, E. S., Lindemann, S., Shaw, T. E., Buri, P., ... & Pellicciotti, F. (2023). Controls on Ice Cliff Distribution and Characteristics on Debris-Covered Glaciers. *Geophysical Research Letters*, *50*(6), e2022GL102444.

Lutz, A. F., Immerzeel, W. W., Shrestha, A. B., & Bierkens, M. F. P. (2014). Consistent increase in High Asia's runoff due to increasing glacier melt and precipitation. Nature Climate Change, 4(7), 587-592.

Manoli G., V. Y. Ivanov, and S. Fatichi (2018). Dry season greening and water stress in Amazonia: the role of modeling leaf phenology. Journal of Geophysical Research-Biogeosciences 123, 1909-1926, doi:10.1029/2017JG004282

Mastrotheodoros, T., Pappas, C., Molnar, P., Burlando, P., Hadjidoukas, P., & Fatichi, S. (2019). Ecohydrological dynamics in the Alps: Insights from a modelling analysis of the spatial variability. Ecohydrology, 12(1), e2054.

Mastrotheodoros, T., Pappas, C., Molnar, P., Burlando, P., Manoli, G., Parajka, J., ... & Fatichi, S. (2020). More green and less blue water in the Alps during warmer summers. Nature Climate Change, 10(2), 155-161.

McCarthy, M., Meier, F., Fatichi, S., Stocker, B. D., Shaw, T. E., Miles, E., Dussaillant, I., & Pellicciotti, F. (2022). Glacier contributions to river discharge during the current Chilean megadrought. Earth's Future, 10(10), e2022EF002852.

Miles, E. S., Willis, I., Buri, P., Steiner, J. F., Arnold, N. S., & Pellicciotti, F. (2018). Surface pond energy absorption across four Himalayan glaciers accounts for 1/8 of total catchment ice loss. Geophysical Research Letters, 45(19), 10-464.

Miles, E., McCarthy, M., Dehecq, A., Kneib, M., Fugger, S., & Pellicciotti, F. (2021). Health and sustainability of glaciers in High Mountain Asia. Nature communications, 12(1), 1-10.

Miles, E. S., Steiner, J. F., Buri, P., Immerzeel, W. W., & Pellicciotti, F. (2022). Controls on the relative melt rates of debris-covered glacier surfaces. *Environmental Research Letters*, *17*(6), 064004.

Millan, R., Mouginot, J., Rabatel, A., & Morlighem, M. (2022). Ice velocity and thickness of the world's glaciers. Nature Geoscience, 15(2), 124-129.

Mudryk, L., Santolaria-Otín, M., Krinner, G., Ménégoz, M., Derksen, C., Brutel-Vuilmet, C., ... & Essery, R. (2020). Historical Northern Hemisphere snow cover trends and projected changes in the CMIP6 multi-model ensemble. *The Cryosphere*, *14*(7), 2495-2514.

Muñoz Sabater, J., (2019): ERA5-Land hourly data from 1981 to present. Copernicus Climate Change Service (C3S) Climate Data Store (CDS). (Accessed on 6 June 2020), 10.24381/cds.e2161bac

Muñoz-Sabater, J., Dutra, E., Agustí-Panareda, A., Albergel, C., Arduini, G., Balsamo, G., ... & Thépaut, J. N. (2021). ERA5-Land: A state-of-the-art global reanalysis dataset for land applications. Earth System Science Data, 13(9), 4349-4383.

Myneni, R., Knyazkhin, Y. (2018). VIIRS/NPP Leaf Area Index/FPAR 8-Day L4 Global 500m SIN Grid V001 [Data set]. NASA EOSDIS Land Processes DAAC. doi: 10.5067/VIIRS/VNP15A2H.001. Accessed March 30, 2023

Myneni, R., Knyazikhin, Y., Park, T. (2015). MCD15A3H MODIS/Terra+Aqua Leaf Area Index/FPAR 4-day L4 Global 500m SIN Grid V006. NASA EOSDIS Land Processes DAAC. Accessed March 30, 2023 from https://doi.org/10.5067/MODIS/MCD15A3H.006. Accessed March 30, 2023.

Nie, Y., Pritchard, H. D., Liu, Q., Hennig, T., Wang, W., Wang, X., ... & Chen, X. (2021). Glacial change and hydrological implications in the Himalaya and Karakoram. Nature reviews earth & environment, 2(2), 91-106.

Parajka, J., Holko, L., Kostka, Z., & Blöschl, G. (2012). MODIS snow cover mapping accuracy in a small mountain catchment–comparison between open and forest sites. Hydrology and Earth System Sciences, 16(7), 2365-2377.

Paschalis A., S. Bonetti, Y. Guo, S. Fatichi (2022). On the Uncertainty Induced by Pedotransfer Functions in Terrestrial Biosphere Modeling. Water Resources Research, 58(9), e2021WR031871, doi:10.1029/2021WR031871

Poggio, L., de Sousa, L. M., Batjes, N. H., Heuvelink, G. B. M., Kempen, B., Ribeiro, E., and Rossiter, D.: SoilGrids 2.0: producing soil information for the globe with quantified spatial uncertainty, SOIL, 7, 217–240, https://doi.org/10.5194/soil-7-217-2021, 2021.

Poulin, A., Brissette, F., Leconte, R., Arsenault, R., & Malo, J. S. (2011). Uncertainty of hydrological modelling in climate change impact studies in a Canadian, snow-dominated river basin. Journal of Hydrology, 409(3-4), 626-636.

Pomeroy, J. W., Brown, T., Fang, X., Shook, K. R., Pradhananga, D., Armstrong, R., ... & Moreno, J. L. (2022). The Cold Regions Hydrological Modelling Platform for hydrological diagnosis and prediction based on process understanding. Journal of Hydrology, 615, 128711.

Pohl, E., Gloaguen, R., Andermann, C., & Knoche, M. (2017). Glacier melt buffers river runoff in the Pamir Mountains. Water Resources Research, 53(3), 2467-2489.

Pulliainen, J., Luojus, K., Derksen, C., Mudryk, L., Lemmetyinen, J., Salminen, M., ... & Norberg, J.

(2020). Patterns and trends of Northern Hemisphere snow mass from 1980 to 2018. *Nature*, *581*(7808), 294-298.

Ragettli, S., Pellicciotti, F., Immerzeel, W. W., Miles, E. S., Petersen, L., Heynen, M., ... & Shrestha, A. (2015). Unraveling the hydrology of a Himalayan catchment through integration of high resolution in situ data and remote sensing with an advanced simulation model. Advances in Water Resources, 78, 94-111.

Ragettli, S., Immerzeel, W. W., & Pellicciotti, F. (2016a). Contrasting climate change impact on river flows from high-altitude catchments in the Himalayan and Andes Mountains. Proceedings of the National Academy of Sciences, 113(33), 9222-9227.

Ragettli, S., Bolch, T., & Pellicciotti, F. (2016b). Heterogeneous glacier thinning patterns over the last 40 years in Langtang Himal, Nepal. The Cryosphere, 10(5), 2075-2097.

RGI Consortium, 2017. Randolph Glacier Inventory - A Dataset of Global Glacier Outlines, Version 6. [Indicate subset used]. Boulder, Colorado USA. NSIDC: National Snow and Ice Data Center. doi: https://doi.org/10.7265/4m1f-gd79

Roberts, J. (1983), Forest transpiration: A conservative hydrological process?, J. Hydrol., 66, 133–141.

Shaw, T. E., Miles, E. S., Chen, D., Jouberton, A., Kneib, M., Fugger, S., Ou, T., Lai, H. W., Fujita, K., Yang, W., Fatichi, S., & Pellicciotti, F. (2022). Multi-decadal monsoon characteristics and glacier response in High Mountain Asia. Environmental Research Letters, 17(10). https://doi.org/10.1088/1748-9326/ac9008

Sorg, A., Huss, M., Rohrer, M., & Stoffel, M. (2014). The days of plenty might soon be over in glacierized Central Asian catchments. Environmental Research Letters, 9(10), 104018.

Steiner, J. F., Gurung, T. R., Joshi, S. P., Koch, I., Saloranta, T., Shea, J., ... & Immerzeel, W. W. (2021). Multi-year observations of the high mountain water cycle in the Langtang catchment, Central Himalaya. Hydrological Processes, 35(5), e14189.

Stigter, E. E., Litt, M., Steiner, J. F., Bonekamp, P. N., Shea, J. M., Bierkens, M. F., & Immerzeel, W. W. (2018). The importance of snow sublimation on a Himalayan glacier. Frontiers in Earth Science, 6, 108.

Unger-Shayesteh, K., Vorogushyn, S., Farinotti, D., Gafurov, A., Duethmann, D., Mandychev, A., & Merz, B. (2013). What do we know about past changes in the water cycle of Central Asian headwaters? A review. Global and Planetary Change, 110, 4-25

Van Tiel, M., Stahl, K., Freudiger, D., & Seibert, J. (2020). Glacio-hydrological model calibration and evaluation. Wiley Interdisciplinary Reviews: Water, 7(6), e1483.7

Van Tiel, M., Van Loon, A. F., Seibert, J., & Stahl, K. (2021). Hydrological response to warm and dry weather: do glaciers compensate?. *Hydrology and Earth System Sciences*, *25*(6), 3245-3265

Yang, Y., Roderick, M. L., Guo, H., Miralles, D. G., Zhang, L., Fatichi, S., ... & Yang, D. (2023). Evapotranspiration on a greening Earth. Nature Reviews Earth & Environment, 1-16.

Zhao, M., Liu, Y., & Konings, A. G. (2022). Evapotranspiration frequently increases during droughts. Nature Climate Change, 12(11), 1024-1030.

Zhu, Z., Piao, S., Myneni, R. et al. Greening of the Earth and its drivers. Nature Clim Change 6, 791–795 (2016). https://doi.org/10.1038/nclimate3004

Hydrological regimes and evaporative flux partitioning at the climatic ends of High Mountain Asia

Supplementary Information

Content:
32 Figures
2 Tables

Note: Section numbering restarts

S1. Dataset details

A monitoring network was initially established around Kyzylsu glacier and across the headwater catchment it is contributing to, in June 2021. The network was expanded in 2022 and 2023 and is geared towards the observation and hydrological modelling of glacierized catchments. The network consists of on- and off-glacier weather stations measuring the full radiation balance in addition to standard meteorological variables, surface height/snow depth and total precipitation, three pro-glacial runoff gauges, automatic observations of snow depth, ablation stakes in the debris-covered portion of Kyzylsu glacier, and temperature measurements between 2100 and 3900 m asl. A list of the main stations as of September 2022 is provided in Table S1. More than 300 debris thickness measurements were made over the course of 3 years and used to construct the debris thickness product in this study (Supplementary Section 4). 13 ablation stakes, as well as a range of time-lapse cameras observing the glaciers and their fetch areas were installed and maintained over multiple seasons.

Table S1: Main meteorological and hydrological stations; Ta - air temperature, RH - relative humidity, SWin - incoming shortwave radiation, SWout - outgoing shortwave radiation, LWin - incoming longwave raditation, LWout - outgoing longwave radiation, Pr - Precipitation, WS - wind speed, WD - wind direction, SM - soil moisture, Tg - ground temperature, Tw - water temperature, SD - snow depth, IM - ice melt, Pa - air pressure.

Station Name	Lon	Lat	Elevation [m asl]	Variables	ID (Fig. 1)	In operation since/during
On-glacier AWS	39.09693	71.41767	3538	Ta, RH, SWin, SWout, LWin, LWout, WS, WD, TG, SD, IM, Pa	1	July 2021
Pluviometer station	39.11501	71.41185	3372	Ta, RH, SWin, SWout, Pr, WS, WD, SM, TG, SD, Pa	2	July 2021
Gauging station 1	39.1109	71.41408	3366	WL, Pa, Tg, Tw	3	July 2021-June 2023
Gauging station 2	39.13426	71.45053	3149	WL, Pa, Tg, Tw	4	July 2021
Gauging station 3	39.1578	71.54683	2106	WL, Pa, Tg, Tw	5	July 2021-June 2023
T-logger	39.1578	71.54683	2106	Ta	5	Sept 2022
T-logger	39.13514	71.4448	3186	Ta	4	July 2021
T-logger	39.1060	71.42113	3529	Ta	6	July 2021

	9					
T-logger	39.0827 3	71.42043	3695	Ta	7	July 2021

S2. Downscaling details

We provide hourly forcing to the model by statistically downscaling ERA5-Land grids (~9 km) to the final model resolution of 100 m. To do so, we follow the general method described in Machguth et al. (2009) who downscaled regional climate model simulations of air temperature, radiation and precipitation across Switzerland. The method involves a combination of interpolation methods and simplified sub-grid parameterisations that describe the elevation dependency of some variables. Specifically, the following steps are taken to downscale air temperature at every timestep (Fig. S1-S2):

1) All ERA5-Land grid cells that intersect the catchment outline are extracted and a regular grid is created (Fig. S1-1).
2) Using a vertical gradient of temperature (a 'lapse rate'), the values of each grid cell for a given timestep are adjusted to produce a new grid on a normalised 0 m a.s.l. reference plane, where only the horizontal gradients of temperature remain (Fig. S1-2).
3) The normalised air temperature grids for the timestep are spatially interpolated to the desired 100 m grid resolution, employing a thin-plate spline interpolation (Fig. S1-3).
4) The interpolated grid on the 0 m a.s.l. reference grid are re-mapped using the elevations of the provided DEM (Figure S1-4) and the same temperature gradients as in 2).

In the case of air temperature, the vertical gradients strongly outweigh the horizontal variability, especially for the smaller domains (Kyzylsu and 24K). For the larger Langtang domain, the horizontal variability preserved from the gridded input can reproduce the expected variability of different valley thermal regimes and potential differences in temperature due to precipitation seasonality affecting different parts of the catchment (e.g. Collier and Immerzeel, 2015). Temperature (and precipitation) gradients are derived on a site-by-site basis, based upon the author-evaluated representativeness of the available data. In the case of Langtang and 24K, long-term temperature records were available over a large elevation range of the total catchment, and as such the stations with the longest available records were used to generate a mean hourly-monthly temperature gradient following Shaw et al. (2022). In the case of Kyzylsu, the upper portions of the catchment are largely ungauged, and station-derived gradients risk over-fitting to the lower elevations. For that site, we derived mean hourly-monthly gradients of temperature from grids of a higher resolution non-hydrostatic atmospheric model (NHM, Niwano et al., 2018) recently developed over HMA (unpublished). 5km grids of NHM are deemed to represent a greater subgrid variability of temperature against elevation than is discernible from the raw ERA5-Land gridded data.

For the derivation of relative humidity, dew point temperature data from ERA5-Land grids are downscaled using the same steps and lapse rates as described above for temperature and subsequently converted into relative values using the already downscaled air temperature and air pressure information and following the calculation of saturated vapour pressure from Murphy and Koop (2005).

Precipitation is interpolated, with no vertical gradient prescribed in the case of Langtang and 24K. Again, for Kyzsylu, a substantial gradient of precipitation was witnessed from field visits and thus deemed to be more appropriately explained by an hourly-monthly mean vertical gradient, again derived from the NHM gridded data. Multiple pluviometers and tipping buckets in Langtang indicate the presence of a large spatial variability of precipitation related to strong horizontal gradients (Collier and Immerzeel, 2015), though with only weak and inconsistent vertical differences during most storm events. Low values from the interpolation process were set to zero if they were < 0.05 mm and the original discontinuities of ERA5-Land precipitation fields were preserved (i.e. that regions of the catchment with zero hourly precipitation are maintained after downscaling – Figure S2).

Short- and longwave radiation are equally treated as described above, though provided with small vertical gradients that decrease longwave (-2.9 W m^{-2} / 100 m) at higher elevations, based upon observations from monitoring across the Alps (Marty and Phillipona, 2000). Wind speeds are downscaled following the diagnostic WINDSmodel as described by Burlando et al. (2007) and Peleg et al. (2017), forced by the u- and v-component winds from the closest ERA5-Land grid cell. Air pressure is downscaled simply using its known relationship to elevation.

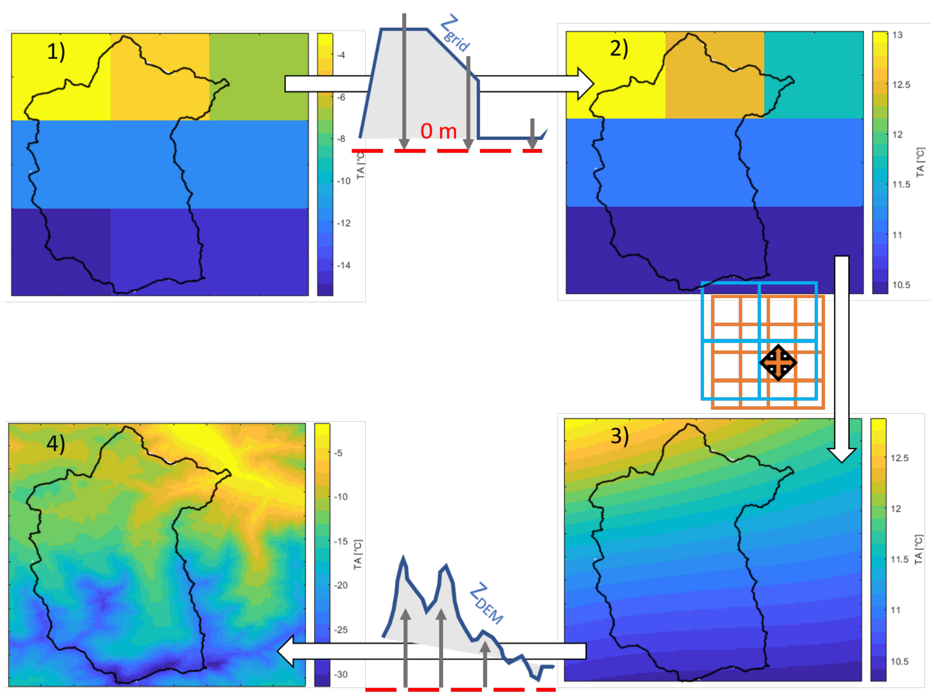

Figure S1: A schematic figure of the process used to downscale forcing grids following Machguth et al. (2009). The example is taken for the Kyzylsu catchment in Tajikistan using air temperature for the first hour (00:00) of April 2021. Steps 1-4 are described above. Note: Colour scales vary between plots.

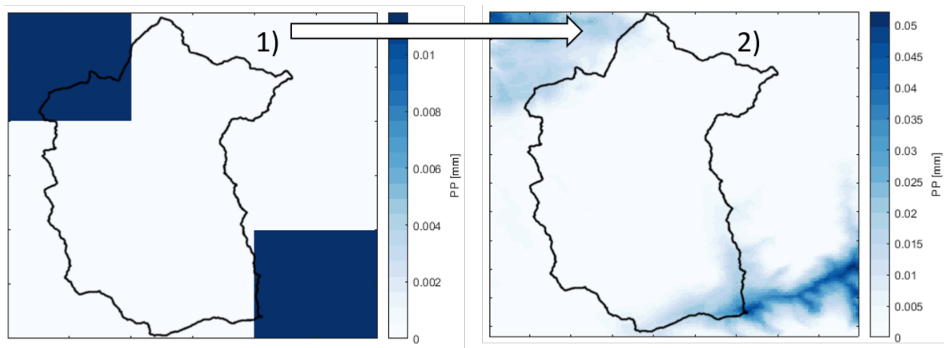

Figure S2: As Figure S1, but for the first and final step of precipitation downscaling, where the limits of the precipitation occurrence after-downscaling with a vertical gradient are preserved.

S3. Bias-correction details

Similarly to the choice of downscaling parameters (i.e. temperature/precipitation gradients), the choice of bias-correction observations were made based upon a manual interpretation of the most appropriate ground data available. With a few exceptions, downscaled forcing grids for each catchment were bias-corrected against the 'best' single station available. This 'best' station was determined by the total length and quality of its data for a given variable, thus ensuring the most robust bias-correction possible. Numerous station failures, data gaps and erroneous sensor recordings affect the overall time-series at any site, reflecting the challenging nature of monitoring meteorological conditions in remote, high elevation mountain regions. At each catchment, not one station could provide a reference dataset for all variables in question and therefore in the absence of a particular variable at the 'best' station, the nearest available and/or longest record was used. The variables and stations used for each catchment are indicated in Table S1.
Comparing the same total period over which observations are available, the pixels of the downscaled grids are extracted for each timestep and used to generate a monthly variable bias-correction coefficient series using an empirical quantile mapping approach (e.g. Rye et al., 2010). Therefore, for each month, all of the hourly data from observations and estimates (downscaled points) in all years were compared to define the additive or multiplicative (precipitation) correction factors based upon the cumulative distribution function of *n* quantiles. The value of *n* was chosen through optimization (300) and increasing this value further resulted in no additional improvement to performance. The quantile mapping made at the relevant station is used to bias-correct all grids of the catchment for the respective timestep and therefore assumed to be representative of the biases across the whole domain.

For precipitation, observations and estimates are aggregated into daily sums to create a multiplicative EQM correction (Themeßl et al., 2011; Wilcke et al., 2013). Observed precipitation data was undercatch-corrected beforehand following Masuda et al. (2019). The impacts of high frequency light precipitation ("drizzling effect" - e.g. Gutowski et al., 2003) known to be an issue in ERA5 products, are partly accounted for through a minimum threshold for precipitation set in the downscaling interpolation (see above). Nevertheless, monsoon-affected sites (Langtang and 24K) can still suffer from a near-continuous precipitation occurrence in certain months of the year, whereas pluviometer observations indicate a diurnal pattern of precipitation occurrence with greater intermittency. Accordingly, post bias-correction, we temporally disaggregate precipitation to hourly grids preserving the daily spatial patterns of ERA5-Land, while shifting the occurrence of individual hourly precipitation events to match the mean monthly diurnal patterns of the pluviometer sites.

Specifically, we identify the mean number of hours per day where observed precipitation occurs in each month (x). Next, we rank the magnitudes of mean precipitation for all hours and preserve only the x highest. The precipitation for the hours >x are summed and distributed evenly into the x hours where precipitation should occur. Hours <x in the given month no longer have precipitation. While the hourly precipitation grids now show a greater intermittency and more abrupt spatial patterns, we check that physical consistencies between variables are preserved (e.g. precipitation and radiation/RH). Temporal disaggregation of precipitation remains an ongoing challenge in the scientific community (e.g. Scher and Perßenteiner, 2021; Acharya et al., 2022) though a simplified treatment here is deemed to be appropriate for the representation of precipitation variability in our study catchments. In order to prevent melt-out of snow to unrealistically high elevations in Langtang, in addition to the bias-correction against lower-elevation stations, an elevation-dependent multiplicative precipitation adjustment (1 to 1.5) was applied along a linear gradient between 3000 and 6000 m asl. Above 6000 m asl, the precipitation was not increased further.

Table S2: Treatment of each ERA5-Land variable during downscaling and bias-correction for each site.

Site	**Kyzylsu**			**Langtang**			**24K**		
	Vert. distr.	Hor. distr.	Station for EQM (Figure 1)	Vert. distr.	Hor. distr.	Station ID for EQM (Figure 1)	Vert. distr.	Hor. distr.	Station ID for EQM (Figure 1)
Ta	NHM	ERA	1	Stat. 1-5, 10-24	ERA	4,11,12,16	NHM	ERA	1
RH	NHM	ERA	1	Stat 1-5, 10-17	ERA	4	NHM	ERA	1
P	NHM	ERA	2	ERA	ERA	4	ERA	ERA	2
Sin	ERA	ERA	1	ERA	ERA	4	ERA	ERA	1
Lin	Lit.	ERA	1	Lit.	ERA	4	Lit.	ERA	1
Ws	ERA/Peleg	ERA/ Peleg	1	ERA/ Peleg	ERA	4	ERA/ Peleg	ERA/ Peleg	1
Pa	env	none	3	env	none	4	env	none	1

S4. Spatial inputs details

Land cover was set up based on the PROBA-V (Sterckx et al., 2014) land cover and plant species (macro-types) were selected based on field observations and literature. The SOILGrids (Poggio et al., 2021) soil product was used for soil distribution and composition. Based on the RGI-6.0, glacier and debris outlines were manually updated where needed (Kneib et al., 2023). We used consensus ice thicknesses from Farinotti et al., (2019) which were bias-corrected with GPR measurements where available (24K, Kneib et al., 2022). At each site, the 'best available' debris product was used, custom-derived from in-situ-measurements and land-surface temperature (Kyzylsu) or from the HMA-wide product of McCarthy et al. (2022), which was then manually adjusted with in-situ observations (Supplementary Text). To represent supraglacial debris thickness in the model as best as possible, we took a pragmatic approach, using a combination of in-situ and remote sensing data. For the Langtang and 24K catchments, we used debris thickness data from the regional product by McCarthy et al. (2022), which we bias corrected multiplicatively using in-situ measurements. In the case of the Langtang catchment, these measurements came from Langtang and Lirung glaciers, and in the case of 24K they came from 24K Glacier (Wei et al. 2010). We filled gaps in the resulting debris thickness maps using a nearest neighbour interpolation. For Kyzylsu catchment, we used Google Earth Engine to generate a surface-temperature composite from Landsat 8 images, in which the temperature of each grid cell was the hottest for that location in the Landsat 8 archive, following Kraaijenbrink et al (2017). We then parameterised the relationship between surface temperature and debris thickness using in-situ debris thickness measurements from Kyzylsu Glacier, and used this parameterisation with the surface-temperature composite to calculate debris thickness for all the glacier areas with supraglacial debris in the catchment.

S5. Model details

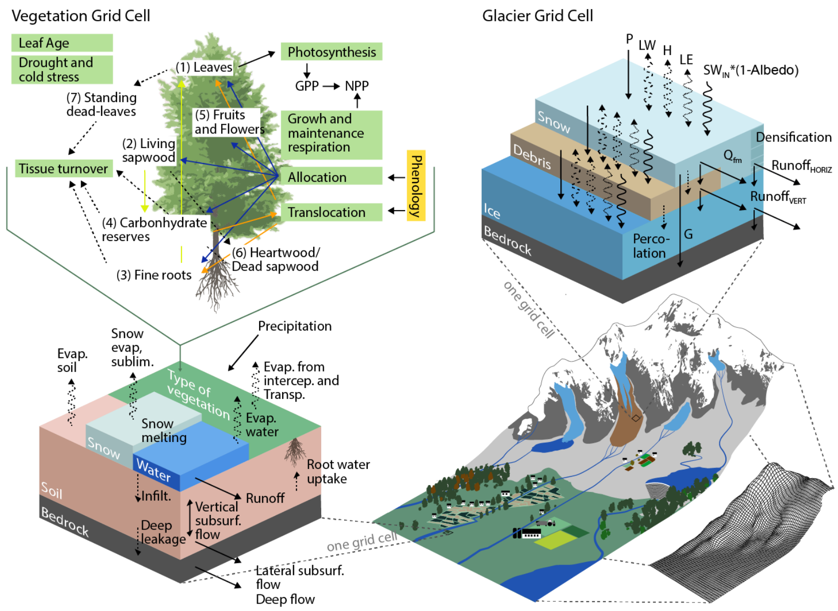

Figure S3: T&C model framework, hydrosphere, cryosphere and biosphere components, energy balance components.

Advances implemented for this study include the introduction of a 2 (multiple)-layer snowpack model, with a 3 mm thick surface skin-layer that interacts with the overlying atmosphere in the energy exchange and transfers heat inside the actual snowpack layer. Heat transfer is then computed over multiple snowpack layers, but single prognostic variables for snow density and snow water content are still used, reducing in this way complexity and computational time. Skin surface energy balance and eventual snowpack melting are solved to concurrently preserve energy and mass balance. Another addition was an adaptation of the parameterisation of Huss et al., (2010) to account for changes in glacier geometry, and adapted it to allow for advancing glaciers, with glacier-specific parameters derived from the elevation changes of Hugonnet et al. (2021) for each individual glacier in Kyzylsu and Langtang catchments. The standard parameters from Huss et al. (2010) were used in 24K. The model was run from October 2010 to September 2022, with October 2010 to September 2012 as a spin-up period.

Two parameters of the supraglacial debris layer (thermal conductivity k_d and surface roughness z_0) were found by optimising against energy balance simulations at automatic weather stations (AWS), where meteorological data and concurrent measurements of ablation were available. The two-step optimization used at each of the on-glacier AWS on the Kyzylsu, Langtang and 24K glaciers, is described in detail in Fugger et al. (2022). Phenological parameters were adjusted in order to account for grazing and the observed beginning and end of the growing season.

S6. Evaluation

S6.1. Forcing evaluation

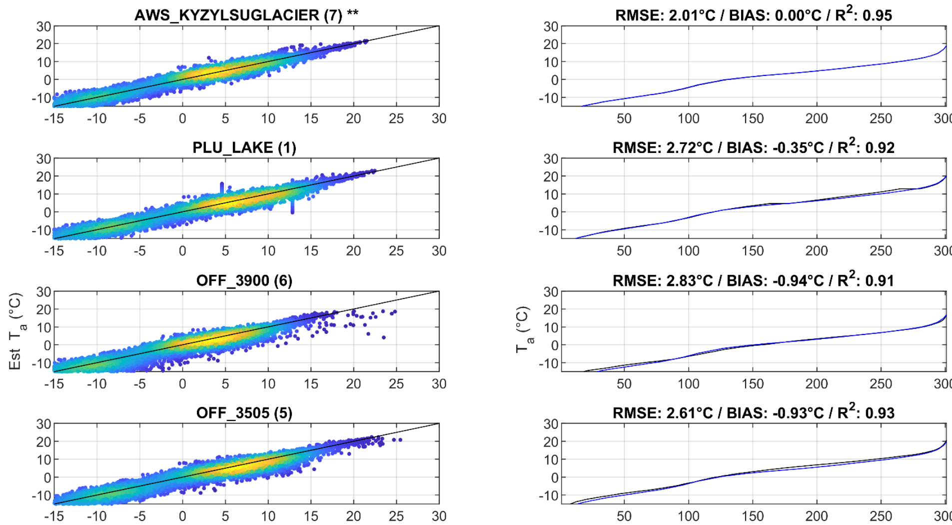

*Figure S4: Evaluation of air temperature (TA) against station data, Kyzylsu; Station identifier in brackets; ** indicates stations involved in the EQM bias correction (non-independent).*

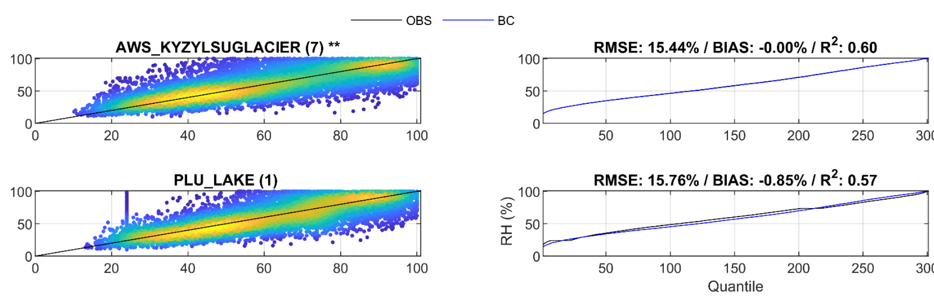

*Figure S5: Evaluation of relative humidity (RH) against station data, Kyzylsu; Station identifier in brackets; ** indicates stations involved in the EQM bias correction (non-independent).*

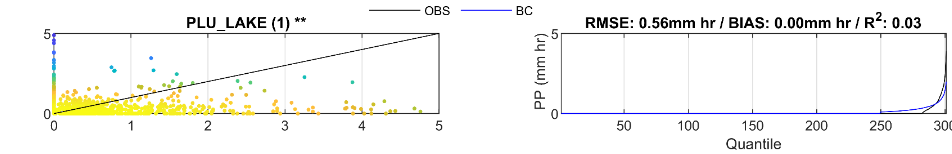

*Figure S6: Evaluation of total precipitation (PP) against station data, Kyzylsu; Station identifier in brackets; ** indicates stations involved in the EQM bias correction (non-independent).*

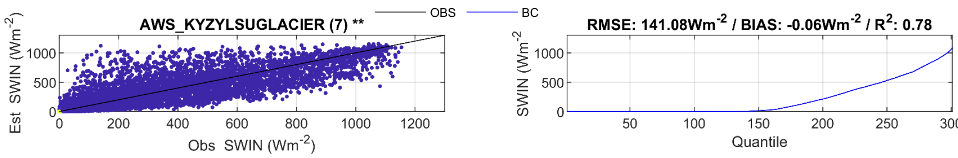

*Figure S7: Evaluation of incoming shortwave radiation (SWIN) against station data, Kyzylsu; Station identifier in brackets; ** indicates stations involved in the EQM bias correction (non-independent).*

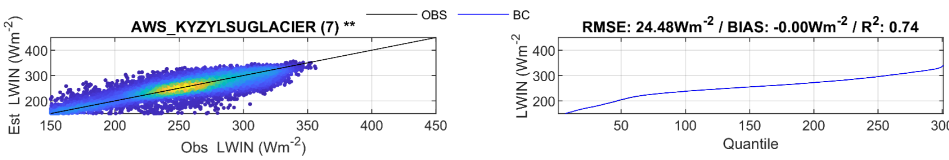

*Figure S8: Evaluation of incoming longwave radiation (LWIN) against station data, Kyzylsu; Station identifier in brackets; ** indicates stations involved in the EQM bias correction (non-independent).*

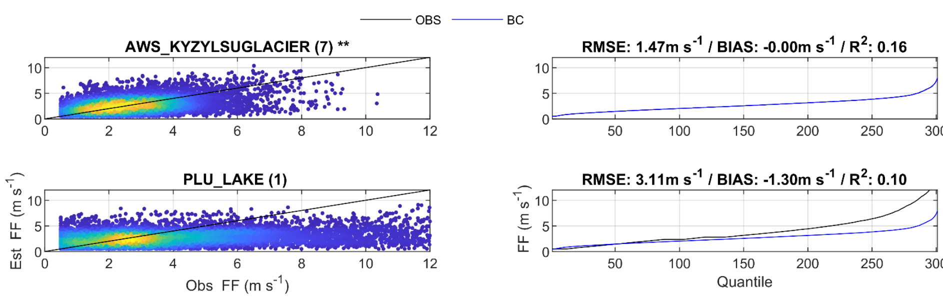

*Figure S9: Evaluation of wind speed (FF) against station data, Kyzylsu; Station identifier in brackets; ** indicates stations involved in the EQM bias correction (non-independent).*

LANGTANG

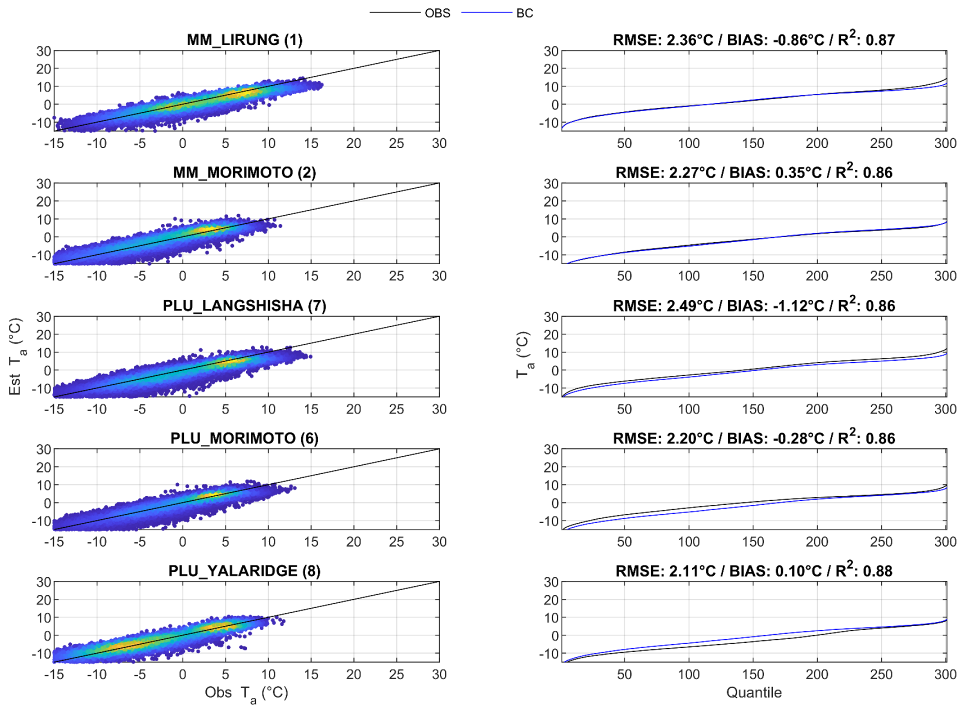

Figure S10-1: Evaluation of air temperature (TA) against station data, Langtang; Station identifier in brackets.

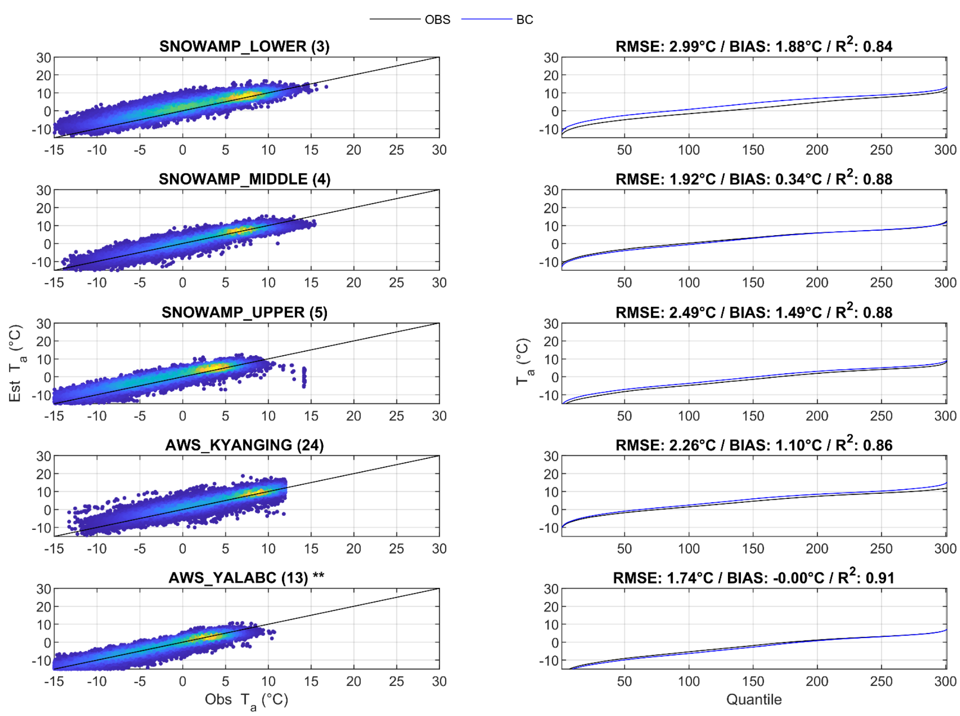

*Figure S10-2: Evaluation of air temperature (TA) against station data, Langtang; Station identifier in brackets; ** indicates stations involved in the EQM bias correction (non-independent).*

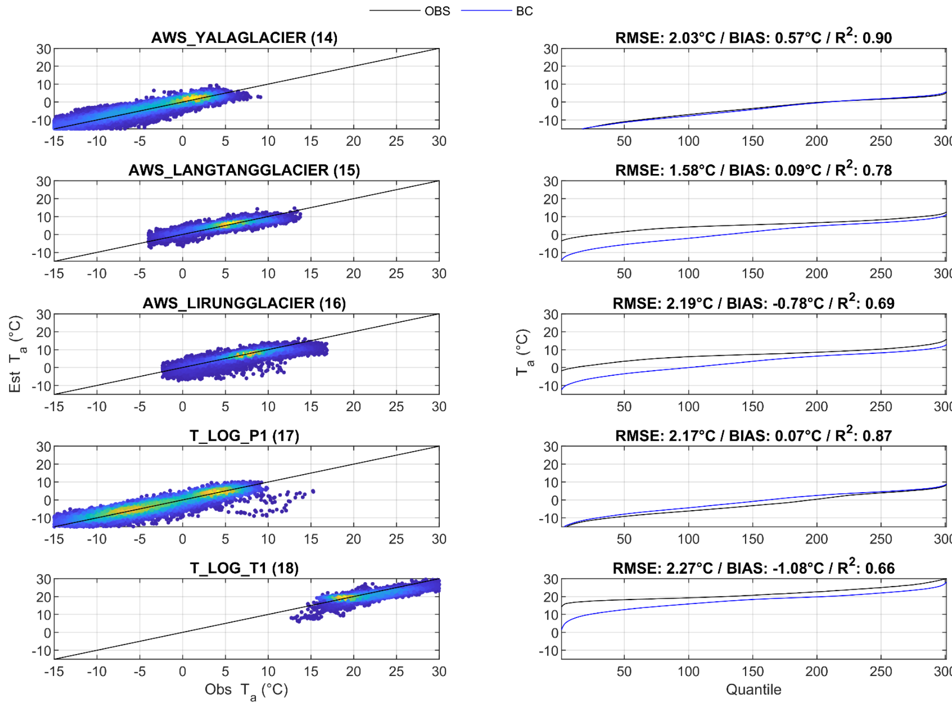

Figure S10-3: Evaluation of air temperature (TA) against station data, Langtang; Station identifier in brackets.

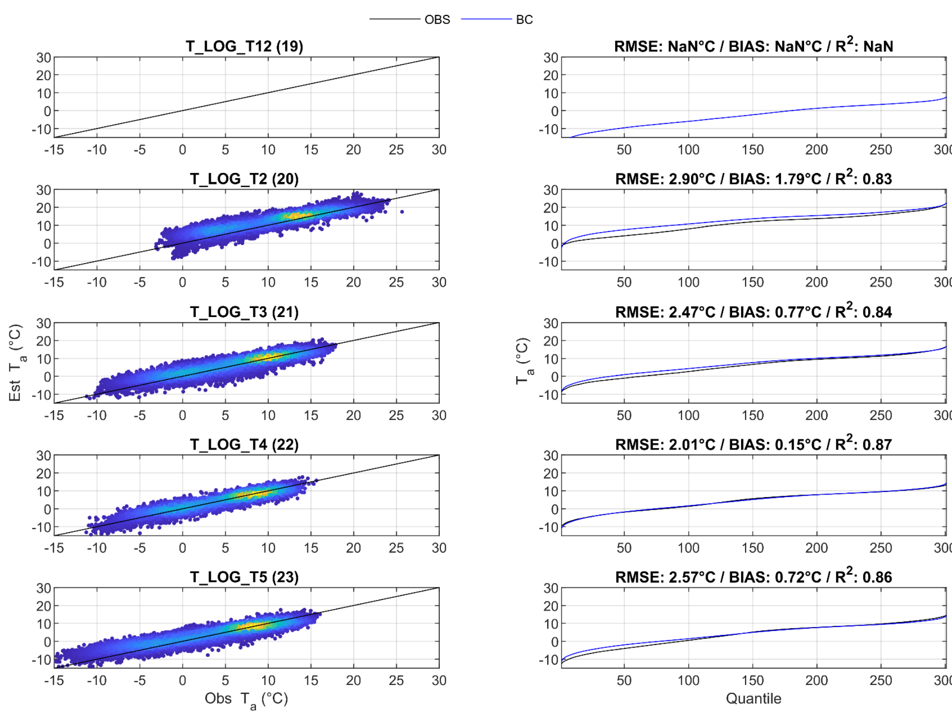

Figure S10-4: Evaluation of air temperature (TA) against station data, Langtang. Station identifier in brackets.

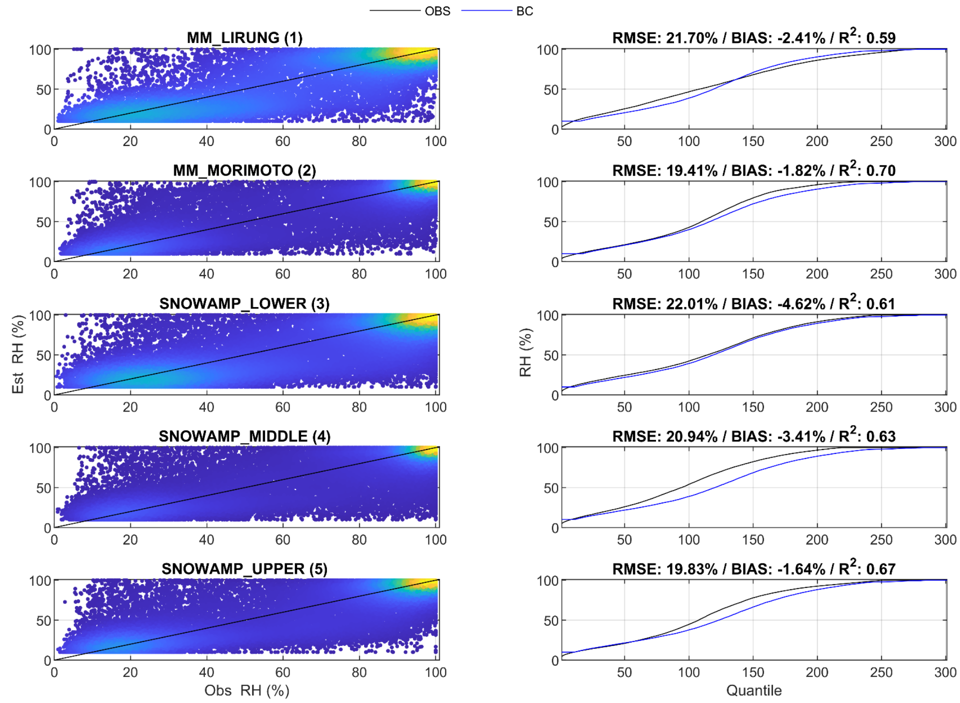

Figure S11-1: Evaluation of relative humidity (RH) against station data, Langtang; Station identifier in brackets.

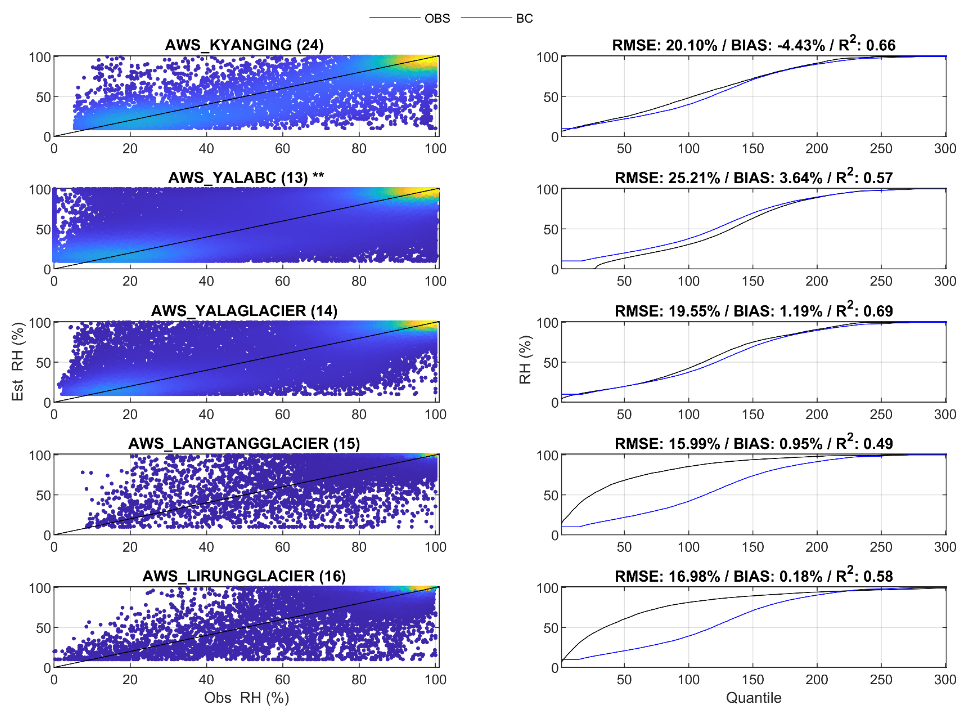

*Figure S11-2: Evaluation of relative humidity (RH) against station data, Langtang; Station identifier in brackets; ** indicates stations involved in the EQM bias correction (non-independent).*

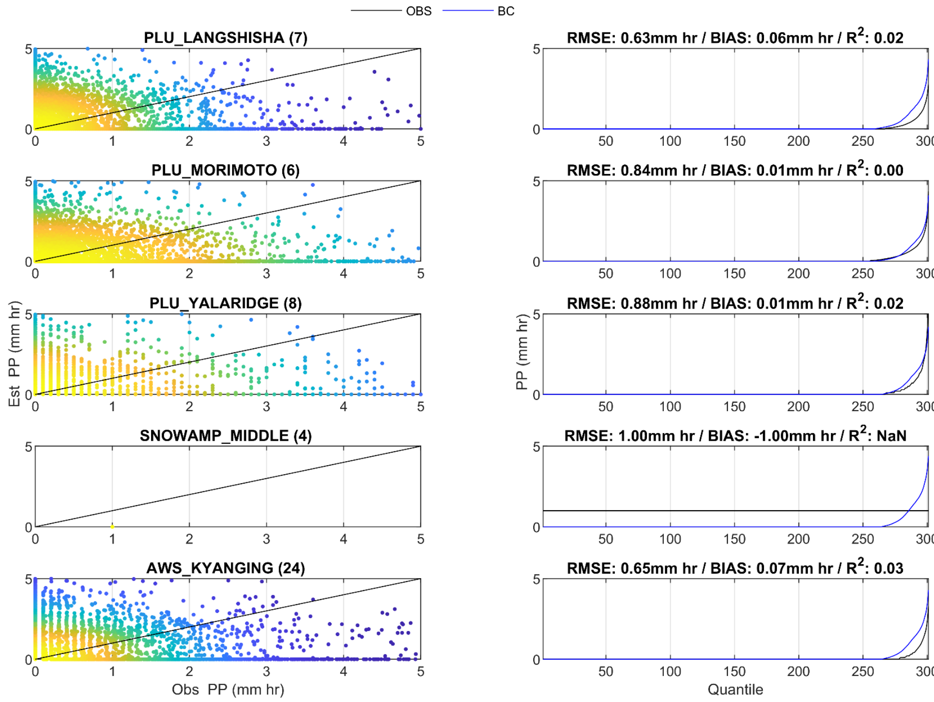

Figure S12-1: Evaluation of total precipitation (PP) against station data, Langtang; Station identifier in brackets.

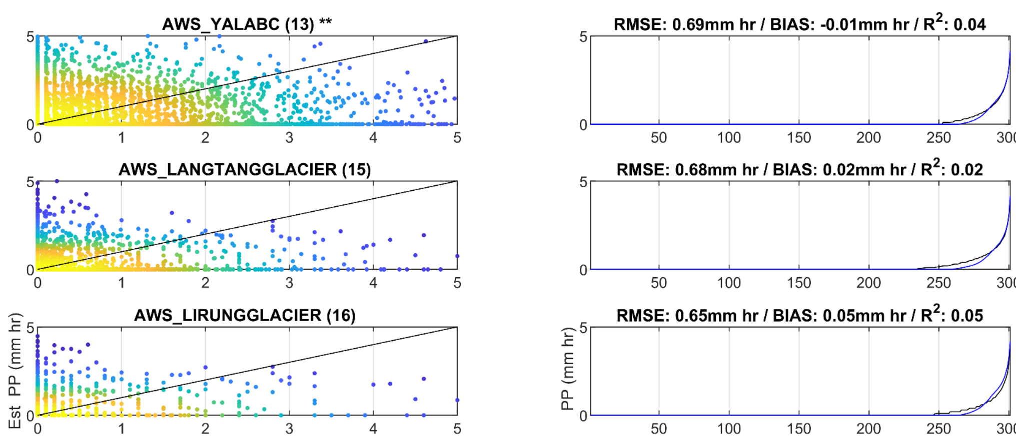

*Figure S12-2: Evaluation of total precipitation (PP) against station data, Langtang; Station identifier in brackets; ** indicates stations involved in the EQM bias correction (non-independent).*

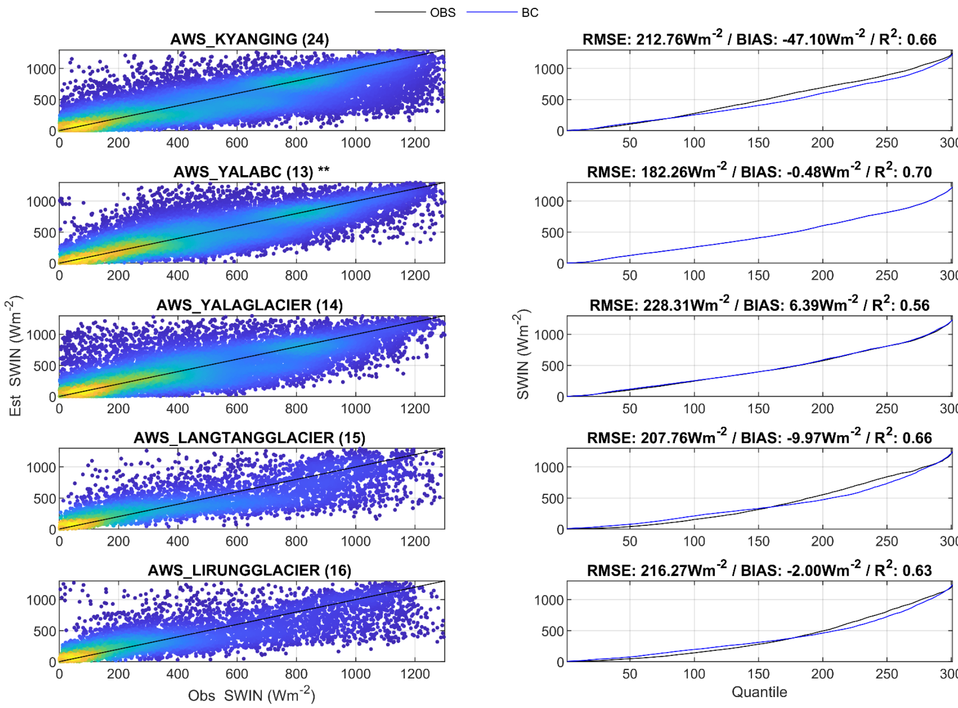

*Figure S13: Evaluation of incoming shortwave radiation (SWIN) against station data, Langtang. Station identifier in brackets; ** indicates stations involved in the EQM bias correction (non-independent).*

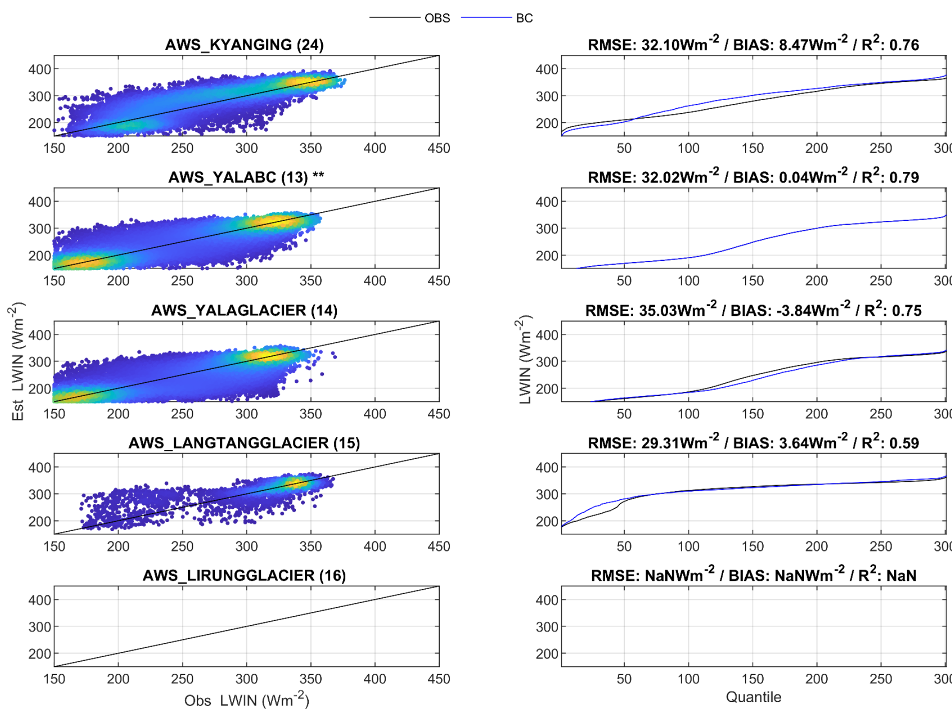

*Figure S14: Evaluation of incoming longwave radiation (LWIN) against station data, Langtang. Station identifier in brackets; ** indicates stations involved in the EQM bias correction (non-independent).*

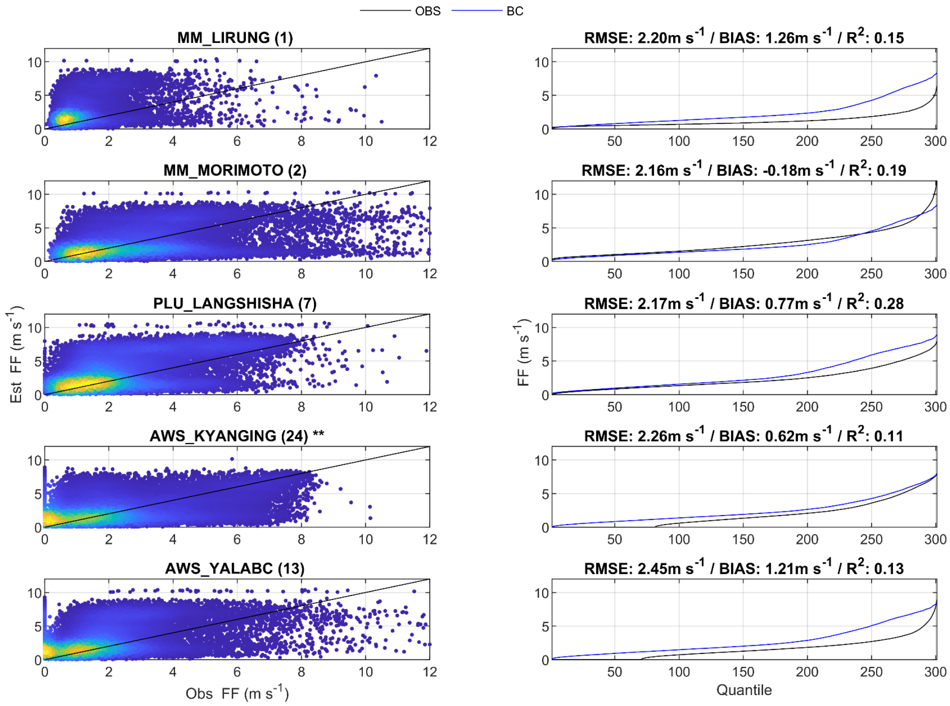

*Figure S15: Evaluation of wind speed (FF) against station data, Langtang. Station identifier in brackets; ** indicates stations involved in the EQM bias correction (non-independent).*

24K:

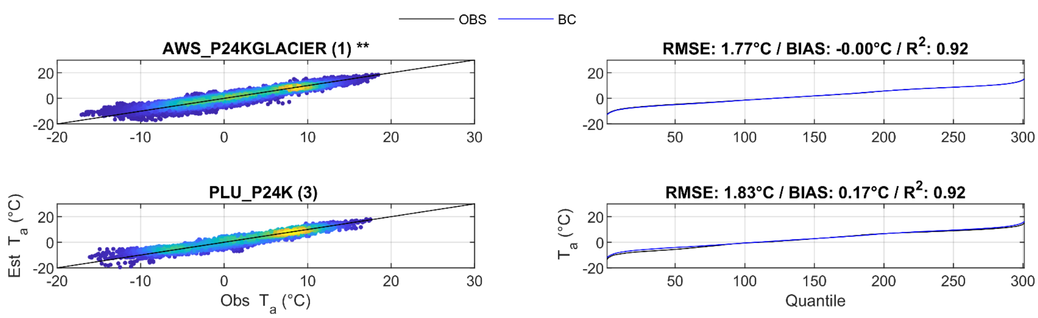

*Figure S16: Evaluation of air temperature (TA) against station data, 24K. Station identifier in brackets; ** indicates stations involved in the EQM bias correction (non-independent).*

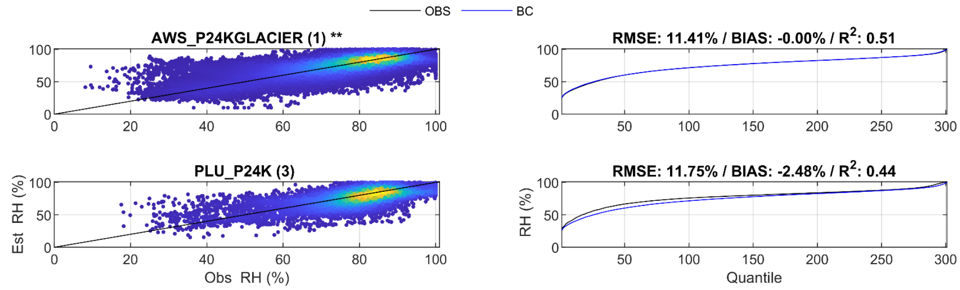

*Figure S17: Evaluation of relative humidity (RH) against station data, 24K. Station identifier in brackets; ** indicates stations involved in the EQM bias correction (non-independent).*

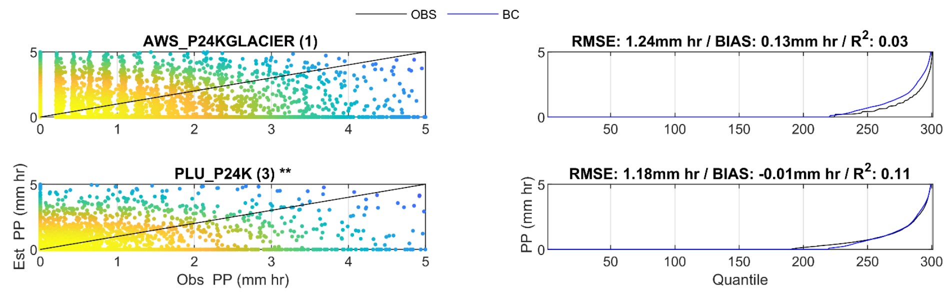

*Figure S18: Evaluation of total precipitation (PP) against station data, 24K. Station identifier in brackets; ** indicates stations involved in the EQM bias correction (non-independent).*

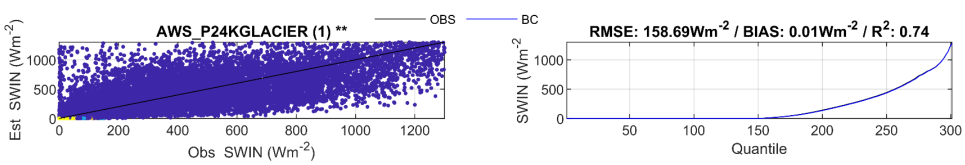

*Figure S19: Evaluation of incoming shortwave radiation (SWIN) against station data, 24K; Station identifier in brackets. ** indicates stations involved in the EQM bias correction (non-independent).*

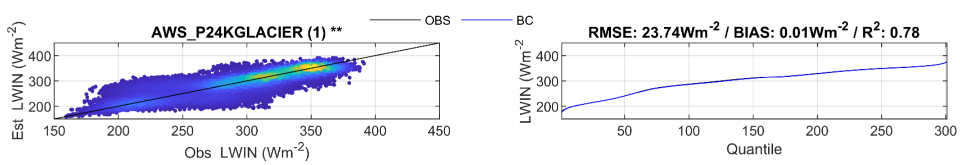

*Figure S20: Evaluation of incoming longwave radiation (LWIN) against station data, 24K. Station identifier in brackets; ** indicates stations involved in the EQM bias correction (non-independent).*

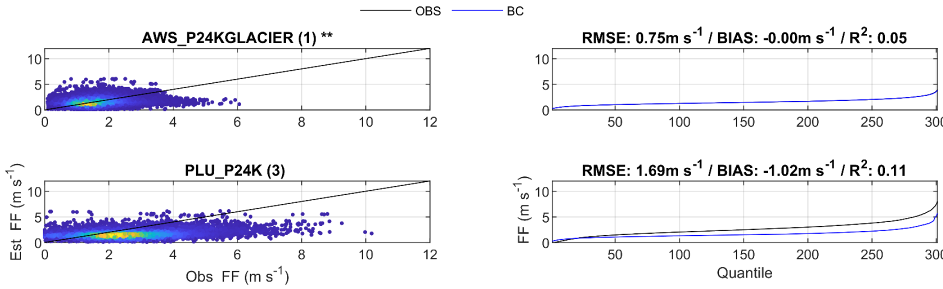

*Figure S21: Evaluation of wind speed (FF) against station data, 24K. Station identifier in brackets; ** indicates stations involved in the EQM bias correction (non-independent).*

Table S3: Aggregated performance metrics for the evaluation of the bias-corrected forcing dataset. Metrics are not shown where no additional and independent stations were available for the evaluation.

	Langtang			**Kyzylsu**			**24K**		
	BIAS	RMSE	R^2	BIAS	RMSE	R^2	BIAS	RMSE	R^2
TA [°C]	0.30	2.29	0.84	-0.74	2.72	0.92	0.17	1.83	0.92
RH [%]	-1.78	19.61	0.62	-0.85	15.76	0.57	-2.48	11.75	0.44
PP [mm]	0.31	0.23	0.05	-	-	-	0.13	1.18	0.11
SWIN [W m^2]	-4.18	153.99	0.79	-	-	-	-	-	-
LWIN [W m^2]	26.87	71.80	0.48	-	-	-	-	-	-
FF [m s^{-1}]	0.74	2.15	0.22	-1.30	3.11	0.10	-1.02	1.69	0.11

S6.2. Snow line

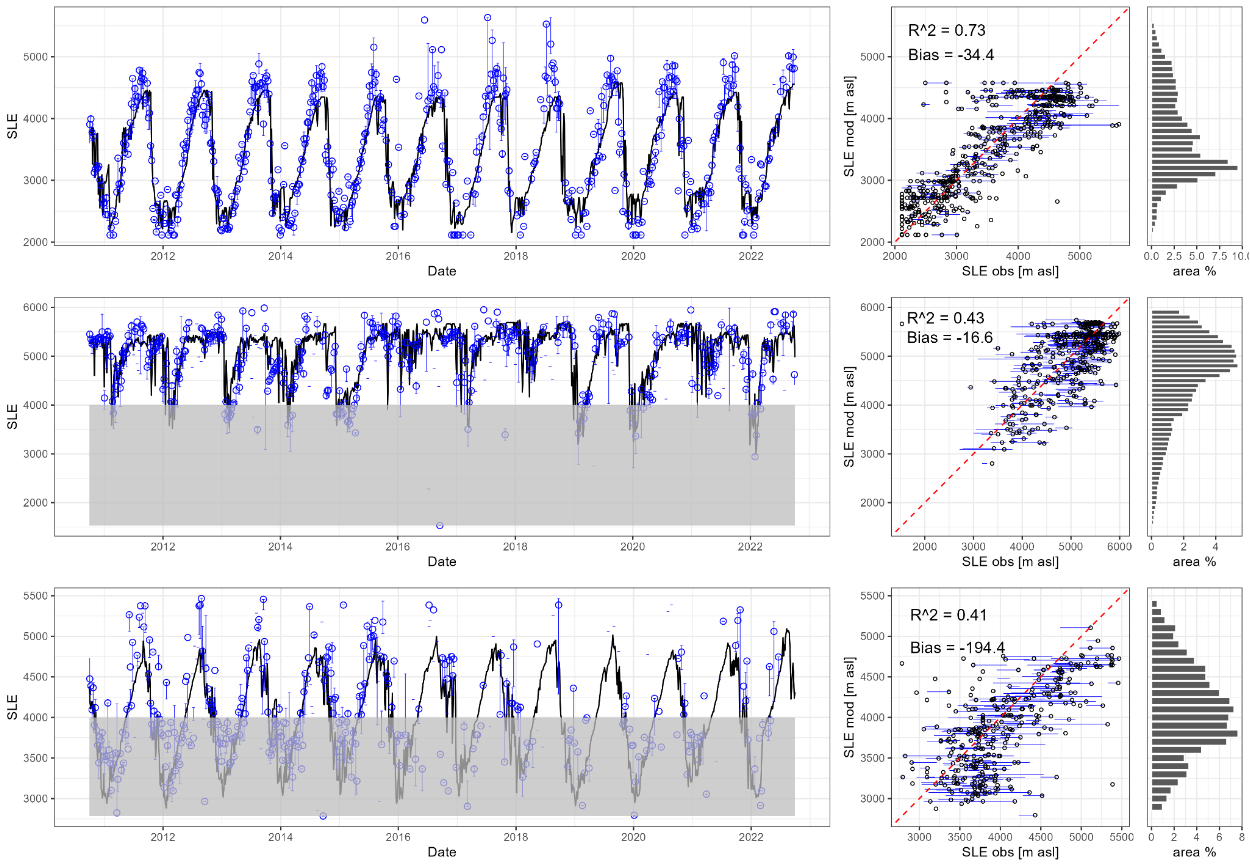

Figure S22: Snow cover evaluation against catchment-wide snowline elevation derived from MODIS Terra snow cover product (MOD10A1), together with scatter plots and catchment hypsometry, for a) Langtang, b) Kyzylsu, c) 24K; Forested elevations greyed-out for a) and c); Uncertainty bars indicate different NDSI thresholds (0.2, 0.4, 0.45) for the snow cover classification.

NDSI based snowcover products are useful above the treeline or over open pastures (e.g. Kyzylsu), but have difficulties representing the snowpack in forested areas (Parajka et al., 2012) which is the case below the forest line in 24K and Langtang at around 4050 m asl. Also, due to heavy cloud cover related to the monsoon conditions, fewer valid scenes were available and uncertainties increased.

S6.3 Snow cover

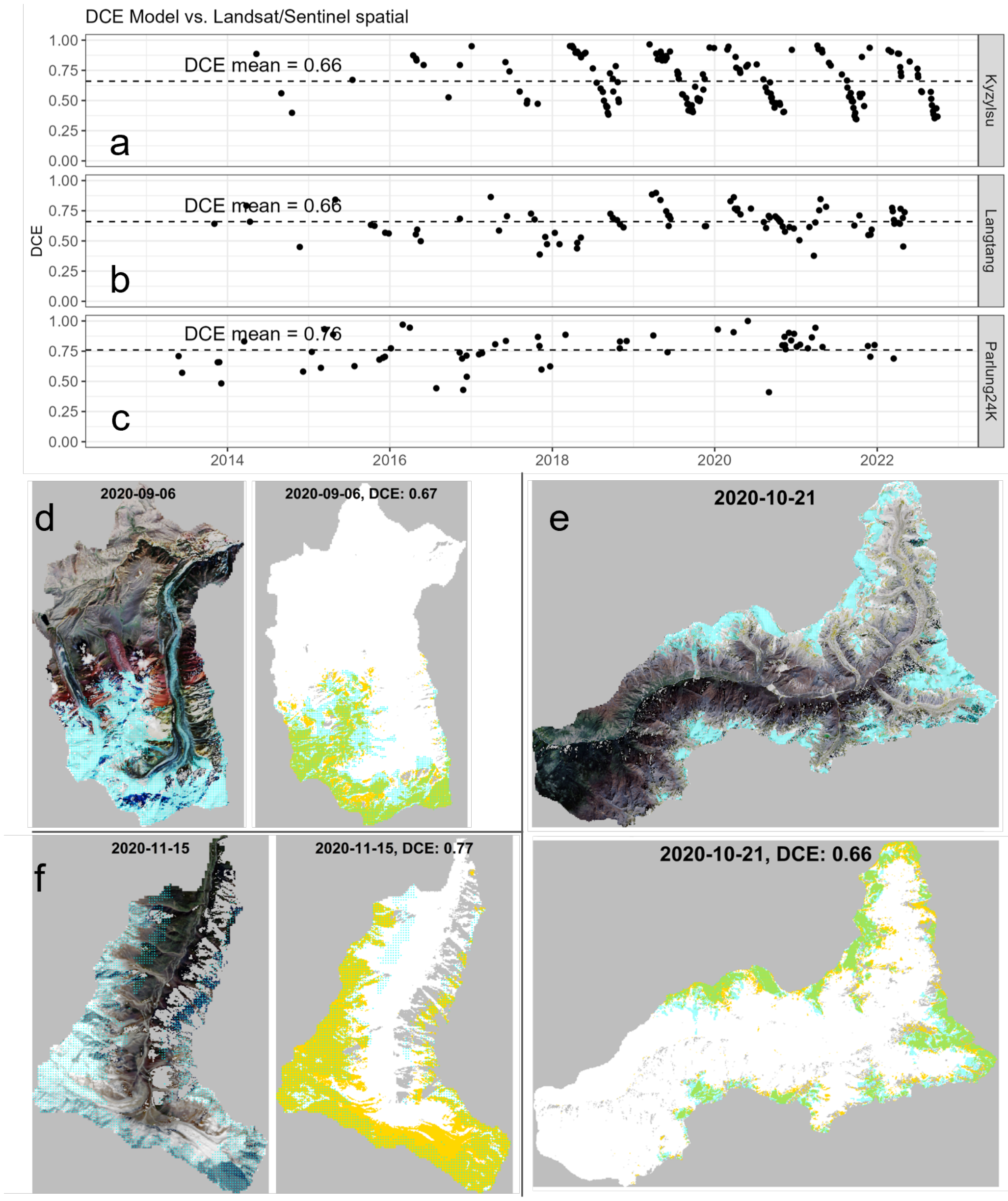

Figure S23 a-c) DCE coefficients for modelled snow cover scene-by-scene comparison against Landsat-8/Sentinel-2; d-e) Example scenes in true colour and binary snow cover information with observed snow cover in yellow and no snowcover in white, derived from NDSI and albedo, Modelled snow cover is overlaid in semi-transparent cyan coloured shading. At each site, one scene with an average DCE model performance was chosen.

S6.4 Snow depth and glacier melt

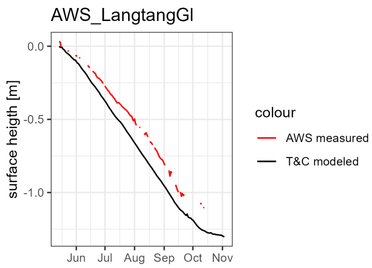

a)

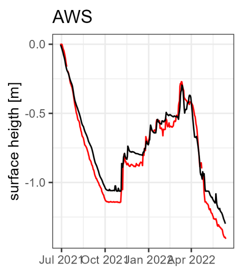

b)

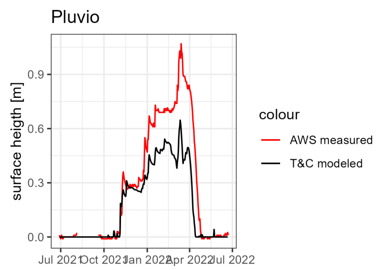

c)

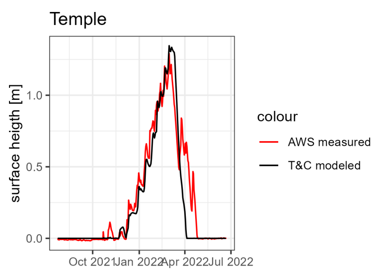

d)

Figure S24: Comparison of observed and modelled surface height at AWSs a) Langtang on-glacer/on-debris, b) Kyzylsu on-glacer/on-debris, c) Kyzylsu off-glacier, d) 24K off-glacier.

S6.5 Glacier mass balance

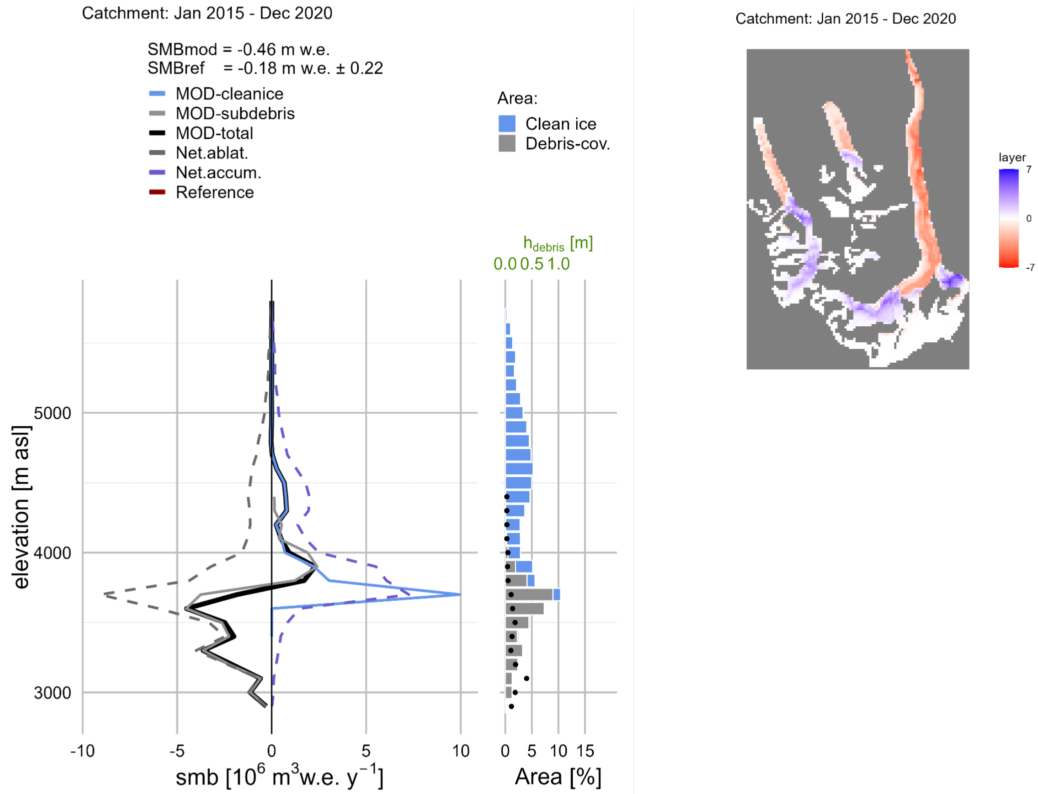

Figure S25: Glacier mass balance, Kyzylsu catchment.

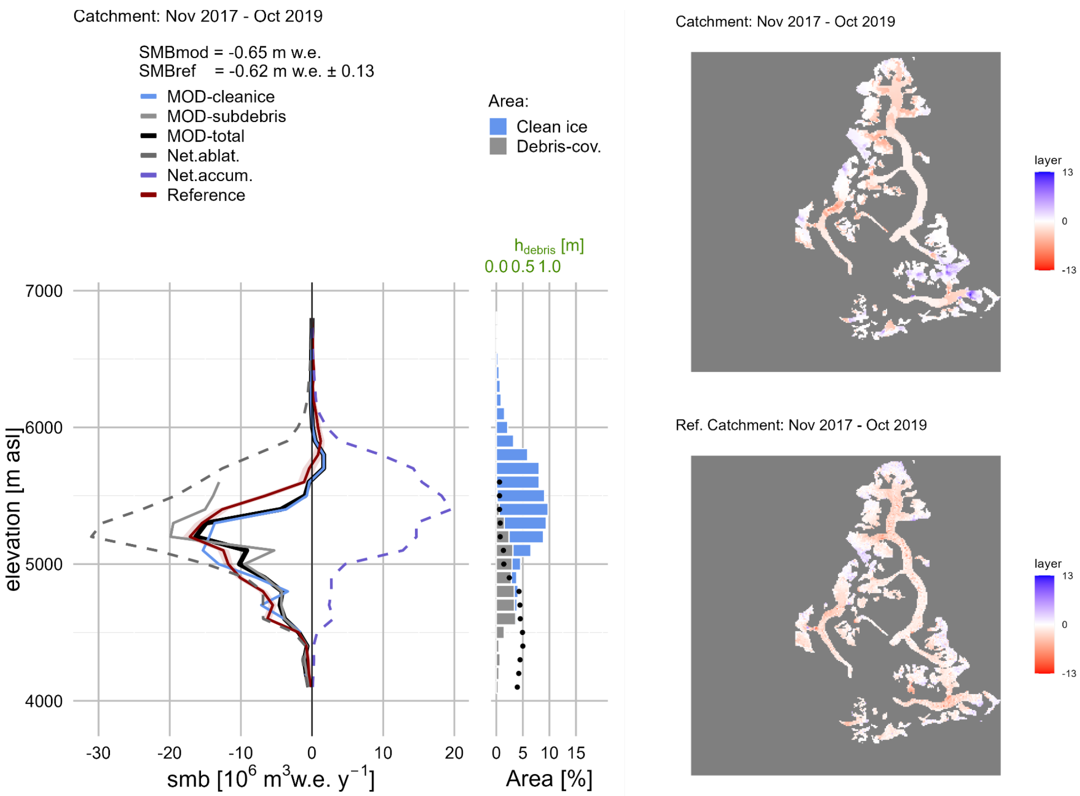

Figure S26: Glacier mass balance, Langtang catchment.

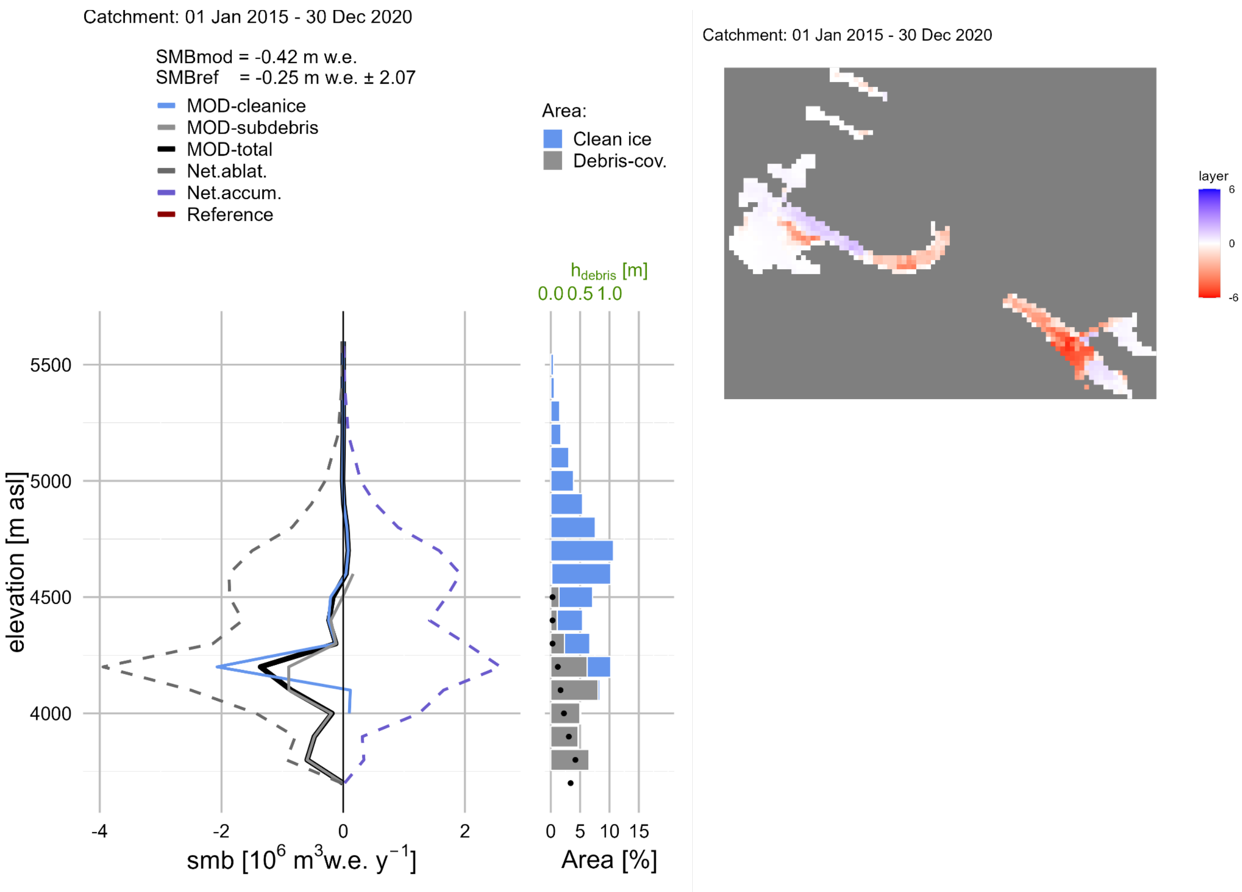

Figure S27: Glacier mass balance, 24K catchment.

S6.6 Leaf Area Index

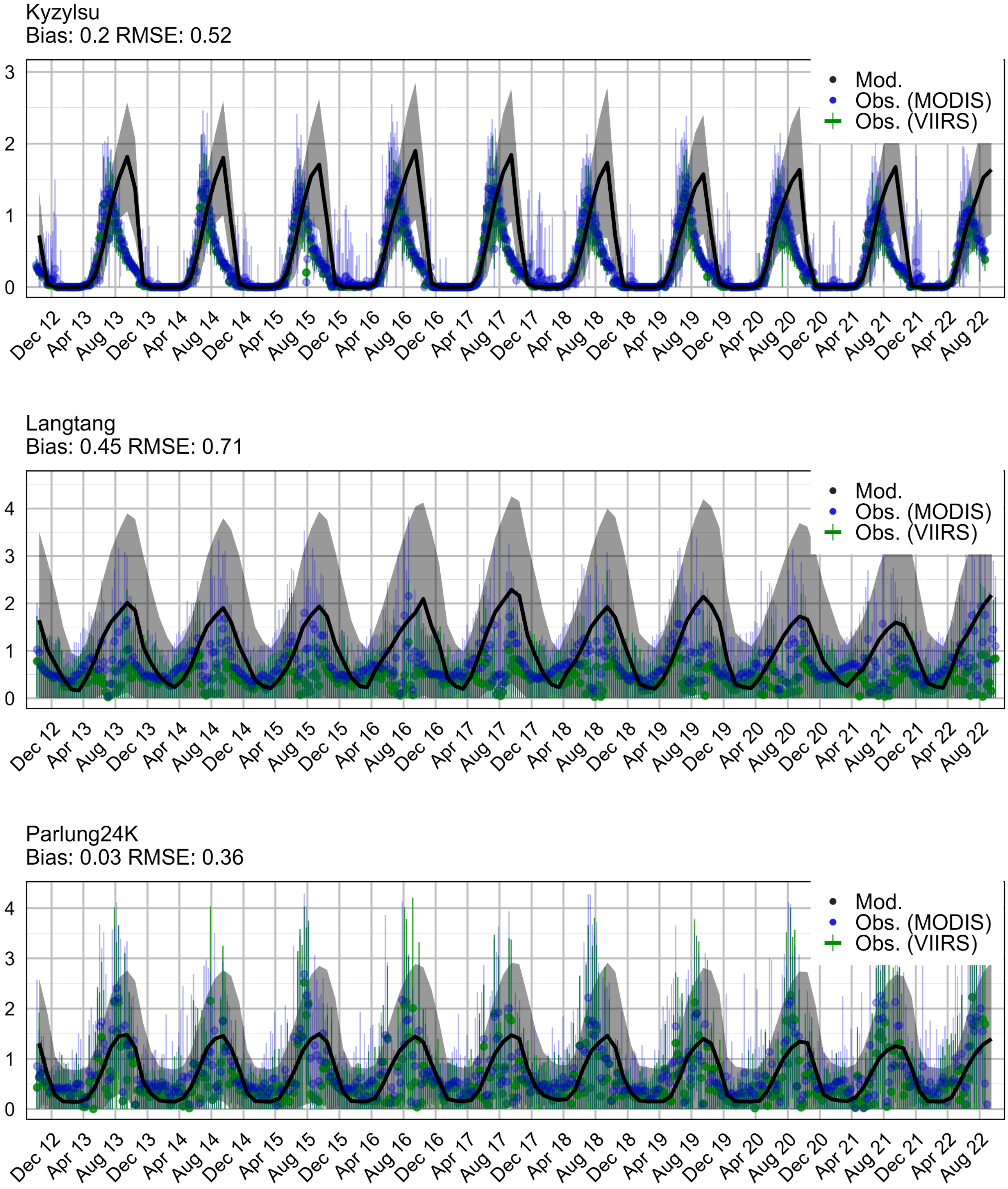

Figure S28: Modelled vs. observed (satellite derived) leaf area index (LAI), catchment average.

S6.7 Streamflow

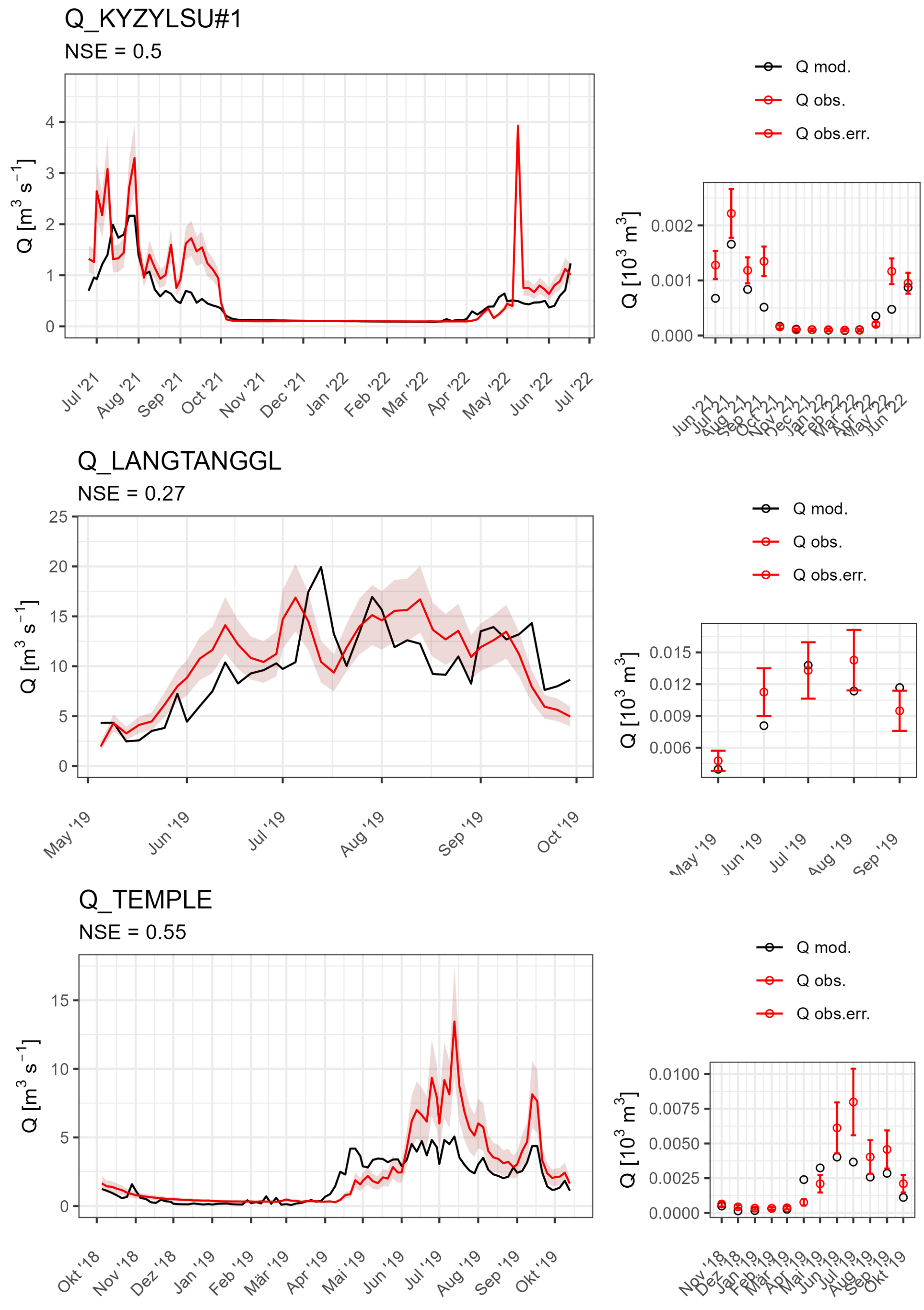

Figure S29: Runoff evaluation against measurements of pro-glacial stream discharge. a),b),c) Measured vs. modelled discharge series; To account for limitations in the model's ability to reproduce internal glacier drainage dynamics, stream discharge measurements were averaged over a 4-day moving window. d),e),f) monthly total discharge; shaded area in a) and error bars in b) indicate the measurement error.

Large uncertainties had to be associated with the rating curves of the stream gauges, due to a lack of observations during high-flow times, such as during the monsoon period in Langtang and 24K. Further uncertainties in the observations are introduced by instabilities of the cross-sections, where flooding occurred, e.g. due to supra-glacial-lake-drainages.

S7. Results

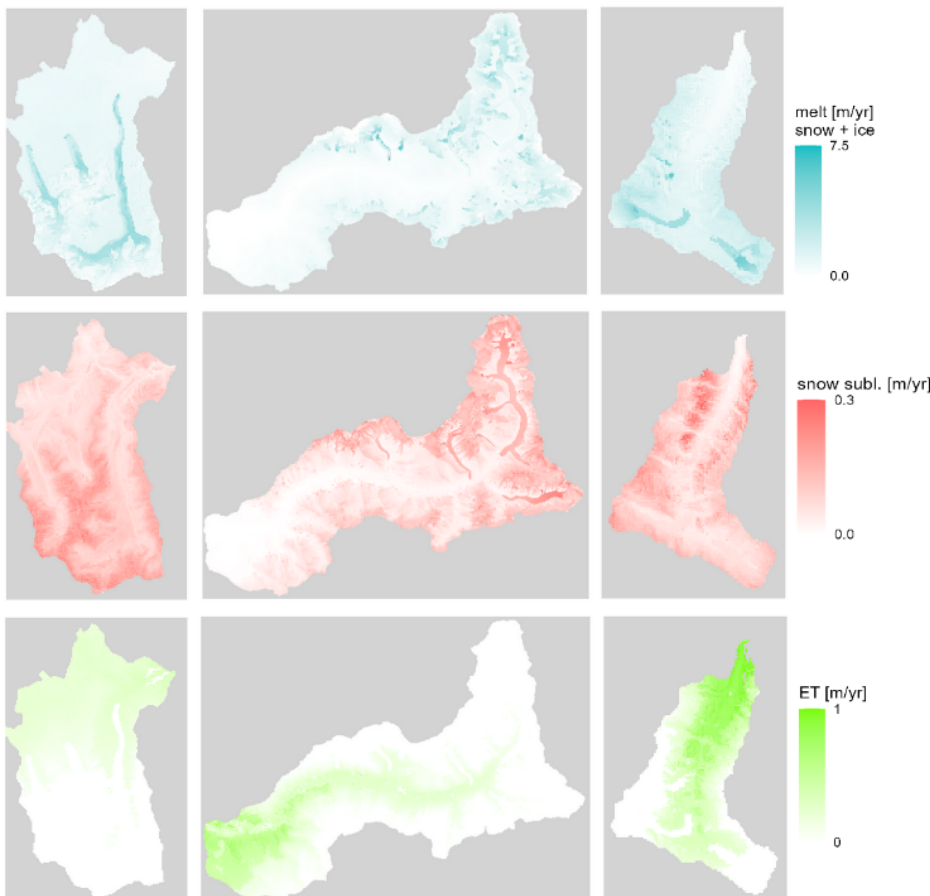

Figure S30: Spatial distribution of melt, sublimation and ET.

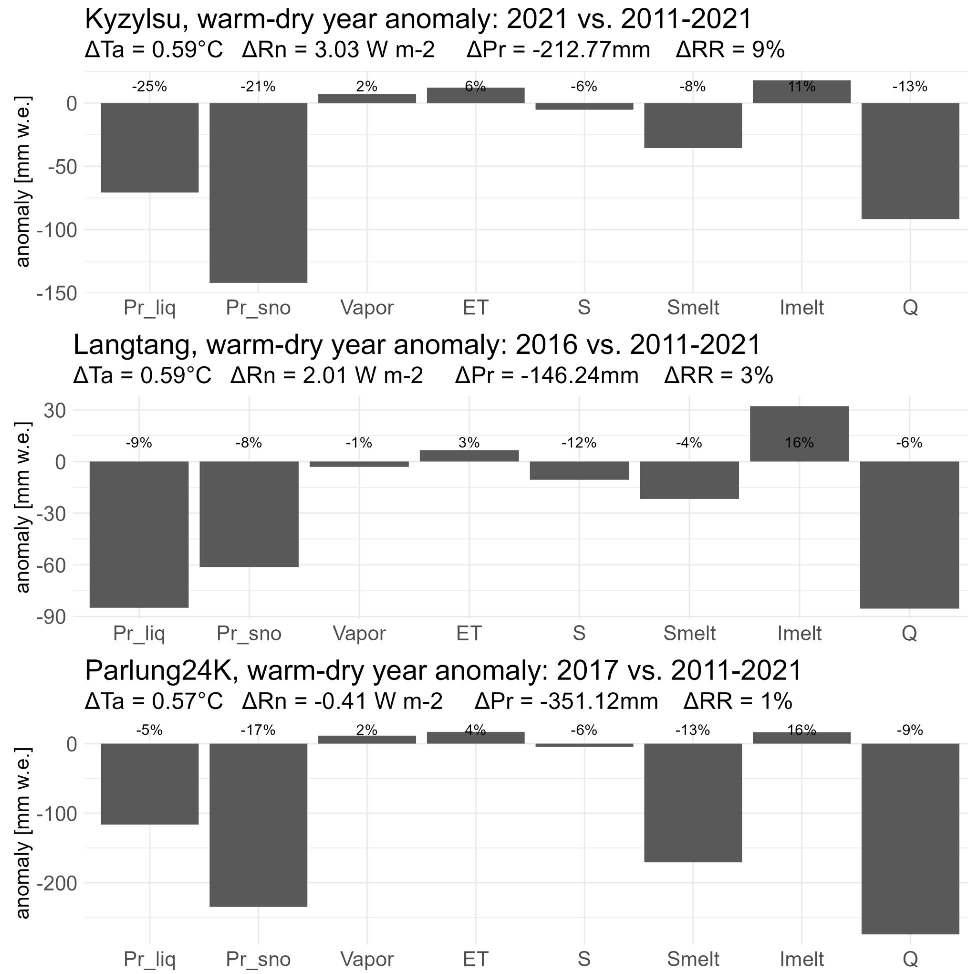

Figure S31: Analysis of mass fluxes of a warmer- and drier-than-average hydrological year.

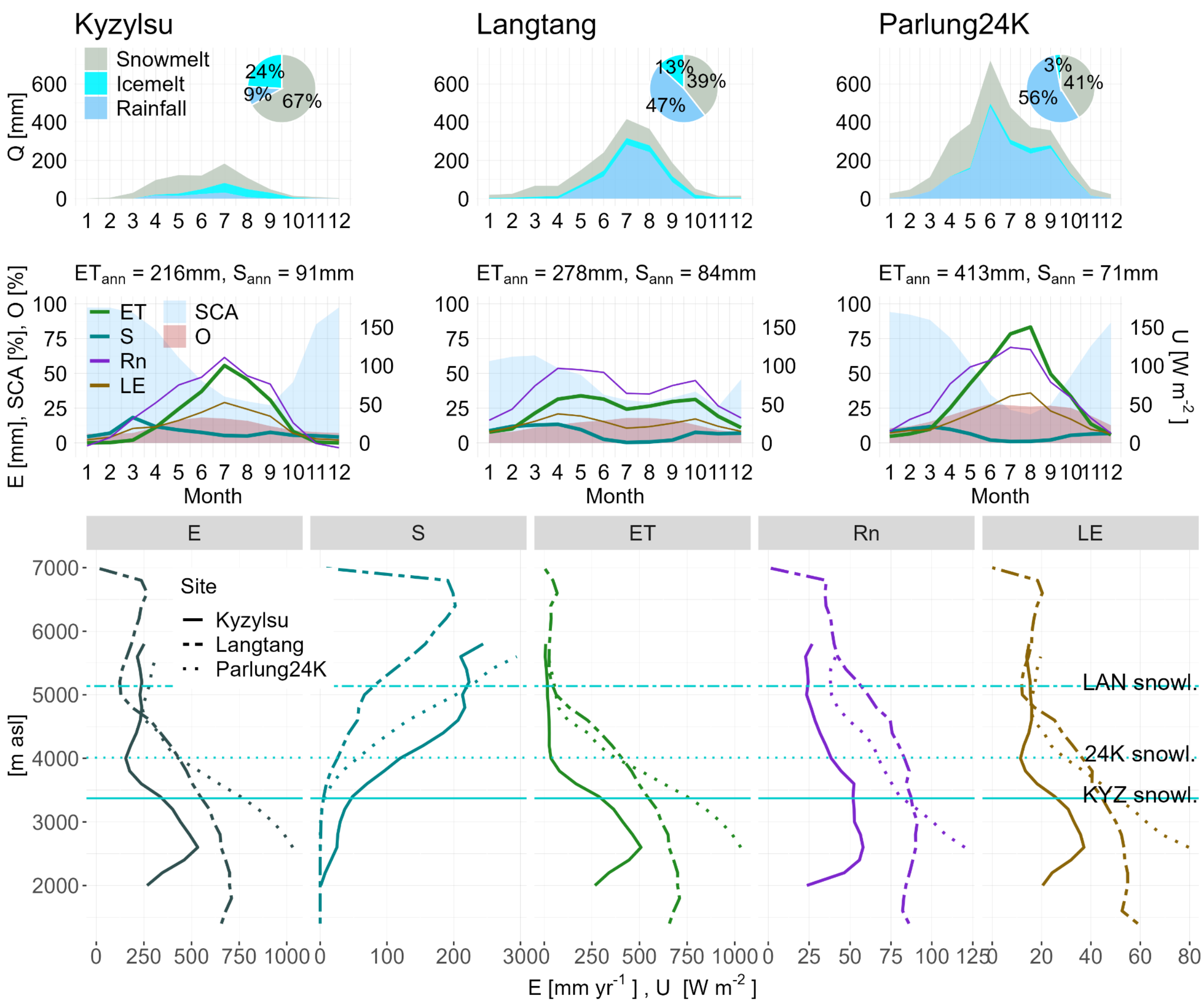

Figure S32: like Figure 3 (main text), but for the full elevation range; a) Mean monthly runoff contributions of snowmelt, ice melt and rainfall (stacked bars), and shares of the total annual runoff (Q) (pie charts); b) Mean monthly evaporative fluxes ET and S together with energy fluxes (U) net radiation (Rn) and latent energy (LE); snow covered area (SCA) and soil moisture (O) as shaded areas in the figure background; c) Site comparison of evaporative and energy fluxes by altitude; turquoise horizontal lines indicate catchment annual mean snowline at each site

Table S4: Computational details for model runs (excl. downscaling)

Site	CPU hours	@ cores	Software
Kyzylsu	13500	62	MATLAB 2022a
Langtang	72346	80	MATLAB 2022a
24K	9216	48	MATLAB 2022a

References

Burlando, M., Carassale, L., Georgieva, E., Ratto, C. F., & Solari, G. (2007). A simple and efficient procedure for the numerical simulation of wind fields in complex terrain. Boundary-Layer Meteorology, 125(3), 417–439. https://doi.org/10.1007/s10546-007-9196-3

Collier, E., & Immerzeel, W. W. (2015). High-resolution modeling of atmospheric dynamics in the Nepalese Himalaya. Journal of Geophysical Research: Atmospheres, 175(4449), 238. https://doi.org/10.1038/175238c0

Gutowski WJ Jr, Decker SG, Donavon RA, Pan Z, Arritt RW, Takle ES (2003) Temporal spatial scales of observed and simulated precipitation in central US climate. J Clim 16:3841–3847

Kraaijenbrink, P. D., Bierkens, M. F., Lutz, A. F., & Immerzeel, W. W. (2017). Impact of a global temperature rise of 1.5 degrees Celsius on Asia's glaciers. Nature, 549(7671), 257-260.

Niwano, M., Aoki, T., Hashimoto, A., Matoba, S., Yamaguchi, S., Tanikawa, T., Fujita, K., Tsushima, A., Iizuka, Y., Shimada, R., & Hori, M. (2018). NHM-SMAP: Spatially and temporally high-resolution nonhydrostatic atmospheric model coupled with detailed snow process model for Greenland Ice Sheet. Cryosphere, 12(2), 635–655. https://doi.org/10.5194/tc-12-635-2018

Marty, C., Philipona, R., Frøhlich, C., & Ohmura, a. (2002). Altitude dependence of surface radiation fluxes and cloud forcing in the alps: Results from the alpine surface radiation budget network. Theoretical and Applied Climatology, 72(3–4), 137–155. https://doi.org/10.1007/s007040200019

McCarthy, M., Miles, E., Kneib, M., Buri, P., Fugger, S., & Pellicciotti, F. (2022). Supraglacial debris thickness and supply rate in High-Mountain Asia. Communications Earth & Environment, 3(1), 269

Murphy and Koop; Review of the vapour pressures of ice and supercooled water for atmospheric applications. Q. J. R. Meteorol. Soc. (2005), 131, pp. 1539-1565. doi: 10.1256/qj.04.94 http://dx.doi.org/10.1256/qj.04.94

Peleg, N., Fatichi, S., Paschalis, A., Molnar, P., & Burlando, P. (2017). An advanced stochastic weather generator for simulating 2-D high-resolution climate variables. Journal of Advances in Modeling Earth Systems, 9, 1595–1627. https://doi.org/10.1002/2016MS000854.Received

Rye, C. J., Arnold, N. S., Willis, I. C., & Kohler, J. (2010). Modeling the surface mass balance of a high Arctic glacier using the ERA-40 reanalysis. Journal of Geophysical Research, 115(F2), F02014. https://doi.org/10.1029/2009JF001364

Scher, S. and Peßenteiner, S.: Technical Note: Temporal disaggregation of spatial rainfall fields with generative adversarial networks, Hydrol. Earth Syst. Sci., 25, 3207–3225, https://doi.org/10.5194/hess-25-3207-2021, 2021.

Shaw, T. E., Miles, E. S., Chen, D., Jouberton, A., Kneib, M., Fugger, S., Ou, T., Lai, H. W., Fujita, K., Yang, W., Fatichi, S., & Pellicciotti, F. (2022). Multi-decadal monsoon characteristics and glacier response in High Mountain Asia. Environmental Research Letters, 17(10). https://doi.org/10.1088/1748-9326/ac9008

Sterckx, S., Benhadj, I., Duhoux, G., Livens, S., Dierckx, W., Goor, E., ... & Zender, J. (2014). The PROBA-V mission: Image processing and calibration. International journal of remote sensing, 35(7), 2565-2588.

Suwash Chandra Acharya, Rory Nathan, Quan J. Wang, Chun-Hsu Su (2022) Temporal disaggregation of daily rainfall measurements using regional reanalysis for hydrological applications, Journal of Hydrology, 610, https://doi.org/10.1016/j.jhydrol.2022.127867.

Themeßl, M., Gobiet, A., & Leuprecht, A. (2011). Empirical-statistical downscaling and error correction of daily precipitation from regional climate models. International Journal of Climatology, 31(10), 1530–1544. https://doi.org/10.1002/joc.2168

Wei, Y., Tandong, Y., Baiqing, X., & Hang, Z. (2010). Influence of supraglacial debris on summer ablation and mass balance in the 24K Glacier, southeast Tibetan Plateau. Geografiska Annaler: Series A, Physical Geography, 92(3), 353-360.

Wilcke, R. A. I., Mendlik, T., & Gobiet, A. (2013). Multi-variable error correction of regional climate models. Climatic Change, 120(4), 871–887. https://doi.org/10.1007/s10584-013-0845-x

5. Research Article: *The sensitivity of High Mountain Asian headwater catchments to global warming*

submitted on March 5, 2024 to *Water Resources Research*, authored by

Stefan Fugger[1,2,3], Michael McCarthy[1], Evan S. Miles[1,4], Thomas E. Shaw[1,3], Achille Jouberton[1,2,3], Catriona Fyffe[3], Pascal Buri[1], Simone Fatichi[5], Khusrav Kabutov[6], Ardamehr Halimov[6], Abdulhamid Kayumov[6] & Francesca Pellicciotti[1,3]

[1]Swiss Federal Research Institute WSL, Birmensdorf, Switzerland
[2]Institute of Environmental Engineering, ETH Zurich, Zurich, Switzerland
[3]Institute of Science and Technology Austria, ISTA, Klosterneuburg, Austria
[4]Department of Geography, University of Zürich, Zürich, Switzerland
[5]Department of Civil and Environmental Engineering, National University of Singapore, Singapore
[6]Center for the Research of Glaciers, National Academy of Sciences, Dushanbe, Tajikistan

<u>Author contribution</u>

StF, MM, SiF, TES and FP designed the study. StF carried out the analysis with the help of MM, ESM, TES, AJ and CF. StF interpreted the results, created the figures and wrote the paper with the help of MM, ESM, TES, AJ and CF. MM, ESM, TES, AJ, CF, PB, SiF, KK, AH, AK and FP reviewed the paper. AJ, SF, ESM, KK, AH and AK organised and facilitated field campaigns and data collection.

<u>Key findings</u>

- Higher glacier mass balance sensitivity in monsoonal catchments driven by precipitation seasonality
- ET and ice melt responses oppose one another, while increasing the water transfer through catchments and keeping runoff almost unchanged
- Sublimation shows both increases and decreases under warming, depending on the site-specific temperature and vapour regime

Note: Separate section numbering in articles

The Sensitivity of High Mountain Asian Headwater Catchments to Climate Warming

Stefan Fugger[1,2,3], Michael McCarthy[1], Evan S. Miles[1,4], Thomas E. Shaw[1,3], Achille Jouberton[1,2,3], Catriona Fyffe[3], Pascal Buri[1], Simone Fatichi[5], Khusrav Kabutov[6], Ardamehr Halimov[6], Abdulhamid Kayumov[6] & Francesca Pellicciotti[1,3]

[1] *Swiss Federal Research Institute WSL, Birmensdorf, Switzerland*
[2] *Institute of Environmental Engineering, ETH Zurich, Zurich, Switzerland*
[3] *Institute of Science and Technology Austria, ISTA, Klosterneuburg, Austria*
[4] *Department of Geography, University of Zürich, Zürich, Switzerland*
[5] *Department of Civil and Environmental Engineering, National University of Singapore, Singapore*
[6] *Center for the Research of Glaciers, National Academy of Sciences, Dushanbe, Tajikistan*

Corresponding author: Stefan Fugger (stefan.fugger@ist.ac.at)

Abstract

Global warming impacts the water balance of high-elevation catchments, which are important source areas for river basins worldwide. Warming shifts precipitation from solid to liquid, reduces seasonal snow accumulation, impacts glacier mass balances and shifts runoff seasonality. It also affects the energy regimes of the non-glacierized areas, changing evaporative fluxes and vegetation productivity. Here, we conduct a modeling experiment in three glacierized headwater catchments in High Mountain Asia, each located in a distinct climate. We use a mechanistic model of snow-, glacier- and eco-hydrology to simulate runoff generation under current climate conditions, and with temperature perturbations from the CMIP6 SSP2-4.5 and SSP5-8.5 scenarios. Glacier mass balances are most sensitive to warming where monsoonal snowfalls play an important role in the accumulation regime. For the Southeast-Tibetan site, 24K, warming under SSP5-8.5 leads to up to 130% additional ice melt and 41% reduction in snowfall, the latter responsible for up to 76% of the additional ice melt. Evapotranspiration increases due to warming with higher increases at the wettest site. Controlled by the coupled temperature/vapor pressure response, winter sublimation increases at the Central Asian site, Kyzslsu and 24K, while summer sublimation decreases at all sites. Evapotranspiration enhancements (up to +50% in 24K) counteract glacier melt increases, resulting in only moderate or no changes in the catchment water yield. Ultimately, we find that magnitudes of climate warming likely to occur in the coming decades can modify runoff generation across headwater catchments in High Mountain Asia in complex and contrasting ways.

1. Introduction

The global climate has entered a trajectory of intense and committed change that has manifested in declines in snow and ice packs worldwide at accelerating rates (Notarnicola et al., 2020; Huggonet et al., 2021), including High Mountain Asia (HMA) (Kraaijenbrink et al., 2021; Miles et al. 2021). Recently, the summer heatwaves of 2022 and 2023 have led to unprecedented mass losses of glaciers in the northern hemisphere, due to both a lack of snow accumulation and temperature-driven melt (Berthier et al., 2023; Chen et al., 2023; Cremona et al., 2023; Xu et al., 2024).

Losses in cryospheric storage will continue to change the seasonal water cycle in mountain basins with both beneficial and adverse consequences downstream (Pritchard et al. 2019; Stahl et al., 2022), while the freshwater demand downstream of mountain ranges is increasing (Viviroli et al., 2020). The cumulative effects of climate and demographic stresses will be unequally distributed over the globe, depending on the hydro-geographic setting of each basin (Immerzeel et al., 2020).

Projected temperature increases are well established, statistically significant and more pronounced in HMA compared to the adjacent lower-elevation landmasses at similar latitudes, averaging at 1.8°C under SSP2-4.5 and 2.4°C under SSP5-8.5 for the medium-term future (2041-2060), compared to the recent past (1995-2014). The future changes to precipitation, snowfalls, relative humidity or wind speed, on the other hand, lack a robust projection across scenarios (Lee et al., 2021).

An increase in air temperatures and radiative forcing has manifold and interlinked consequences on the mountain cryosphere, hydrosphere and biosphere. This includes a decreasing ratio between snowfall and rainfall, a reduction of snowpack extents and thicknesses, a degradation of permafrost, a shrinkage of glaciers, changes in evaporation and sublimation, greening and vegetation succession, all of which result in changes in runoff magnitudes and timing (Berghuis et al., 2014; Huss et al., 2017; Thornton et al., 2021; Maina et al., 2022). Underlying these changes are the highly intricate relationships between surface albedo, the energy balance of the land surface, the moisture and turbulence conditions of the overlying atmosphere and underlying ground, plant physiology and the flux partitioning into water vapor and runoff. For thorough sensitivity testing of high mountain hydrology, it is important to consider all relevant elements of the hydrological system and their processes with a sufficient level of mechanistic description (Stigter et al., 2018; Aubry-Wake et al., 2022; Buri et al., 2023; Fugger et al., 2024).

Process-based hydrological models have high input data requirements, but allow for detailed, robust representations and diagnosis of all of the above-mentioned elements across different climatic conditions (Fatichi et al 2016; Pomeroy et al., 2022). They generate a wide array of outputs, many of which can be directly evaluated against in-situ and remotely sensed observations (Buri et al., 2023, 2024). They can serve as 'virtual laboratories' to gain new understanding about land surface or ecohydrological processes (Mastrotheodoros et al., 2019), or to study the sensitivity of runoff to land cover change and to projected future temperature and precipitation regimes (Meili et al 2024; Aubry-Wake et al., 2023). Tethys-Chloris (T&C) is one such process-based model, which has been applied to mountainous areas (Mastrotheodoros et al., 2019, 2020), such as the upper Langtang catchment, where Buri et al., (2023) showed that evaporative fluxes can remove as much moisture as ice melt contributes towards the runoff from high-elevation catchments. In a recent study applying T&C to three glacierized catchments in HMA, including Langtang, Fugger et al. (2024) found that, for the recent past, the response to warm-dry conditions is such that increases in evaporative fluxes can partially counterbalance additional ice melt, depending on the extent of glacier coverage. Evaporative fluxes, here defined as the sum of evapotranspiration (ET) and sublimation (S), played the greatest role in the water budget of the driest catchment they examined, Kyzylsu. The sublimation flux also demonstrated the highest magnitude at that site, while ET had the highest magnitude at the wettest site, Parlung 24K. The water throughput, defined as the total water added to or removed from the water balance within a year in either liquid, solid or gaseous form, thereby governed the relative importance of the evaporative fluxes (Fugger et al., 2024). Such process-based understanding is critical for a complete picture of catchment hydrology at high elevations, though little quantitative knowledge exists on how catchment-scale evapotranspiration and sublimation might respond to expected future warming, how important these changes will be compared to the changes in the cryospheric runoff contribution, and what the integrated effect on basin streamflow will be.

In this study, we simulate the hydrological responses three catchments in High Mountain Asia, Kyzylsu in the northeastern Pamir, Langtang in the Central Himalaya, and 24K on the Southeastern Tibetan Plateau, to monthly temperature increase for the medium-term future (2041-2060), which we derive as monthly increases compared to the recent past from CMIP6 projections (SSP2-4.5 and SSP5-8.5). Applying the same model, we then compare these simulations to those of Fugger et al (2024), which we consider as the baseline simulations for the recent past. This modeling approach allows us to then examine the response of the different components of the hydrological system (glacier and snow mass balances, evaporative regimes, storage and runoff dynamics), to changes in air temperature and temperature-coupled variables. Rather than attempting future projections, this study investigates the sensitivity of glacierized catchments to warming by isolating the temperature response alone. Since each of the catchments has a distinct hydroclimatic background, varying from seasonally dry conditions to high humidity year-round, we expect to observe a contrasting response between the three sites. We hypothesize that the catchments' sensitivities are such that,

I. Precipitation seasonality is a major control on how the water balances react to warming.
II. Warmer temperatures lead to an increase in ET and NPP due to an extension of the growing period.
III. There is a decrease in sublimation at all sites due to a decrease in precipitation falling as snow and a shortening of the sublimation-conducive period.

2. Study Sites and Methods

2.1. Study sites

The three study sites are distinct in their geographic location and along the climatic gradient of HMA. Each of the catchments features a glacio-hydrological observation network, including meteorological, hydrological and glaciological stations.

The *Kyzylsu* (168 km^2) catchment is located on the northwestern slopes of the Pamir mountain range (Figure 1a) with its outlet near the village Mok (elevation: 2100 m asl). It is a tributary to the Vaksh River which flows into the Amu Darya. Due to the low amounts of lowland-precipitation, the Amu Darya headwaters play a particularly important role in buffering river runoff (Pohl et al., 2017) placing them among the most important (and vulnerable) water towers globally (Immerzeel et al., 2020). Glaciers cover around 30% of the catchment's area, with three main, debris-covered valley glaciers, to which avalanching is an important mass input. The largest portion of the vegetated land consists of pastures, which is intensively grazed by the local livestock. Snowmelt (72%), followed by glacier melt (26%) are annually the most important runoff contributions while >92% of liquid precipitation inputs evaporate (Fugger et al., 2024). Details on the catchment and monitoring are presented in Fugger et al. (2024).

The *Langtang* catchment (586 km^2) is located in the Nepalese Himalaya and is a tributary to the Ganges-Brahmaputra river basin (Figure 1a). For this study, the outlet is considered upstream of the Syabru Besi village (1450 m asl). Out of the three study sites, it is the one with the largest elevation range, and the longest record of continuous monitoring (Steiner et al., 2021). The catchments' hydrology has been studied in several past contributions (e.g. Immerzeel et al., 2012, 2013; Pradhananga et al., 2014; Ragettli et al., 2015, 2016; Wijngaard et al., 2019; Buri et al., 2023). Monsoonal precipitation inputs dominate the runoff regime, with 51% of rainfall (36% snowmelt, 13% glacier melt) contributing to runoff (Fugger et al., 2024).

The *Parlung 24K* catchment (64km^2), the smallest and easternmost site in this study, is located on the Southeastern Tibetan Plateau. It contributes its water to the Yarlung-Zangbo/Brahmaputra river basin and has been a site of continuous monitoring since the mid 2010's (Yang et al., 2017, Zhao et al., 2023). Due to its exposure to Indian Summer and East Asian monsoons, it experiences very high precipitation inputs throughout the summer half-year, which is the reason why glaciers contribute only 3% to the annual water yield, while rainfall contributes the largest share to runoff (55%, versus 41% snowmelt) (Fugger et al., 2024).

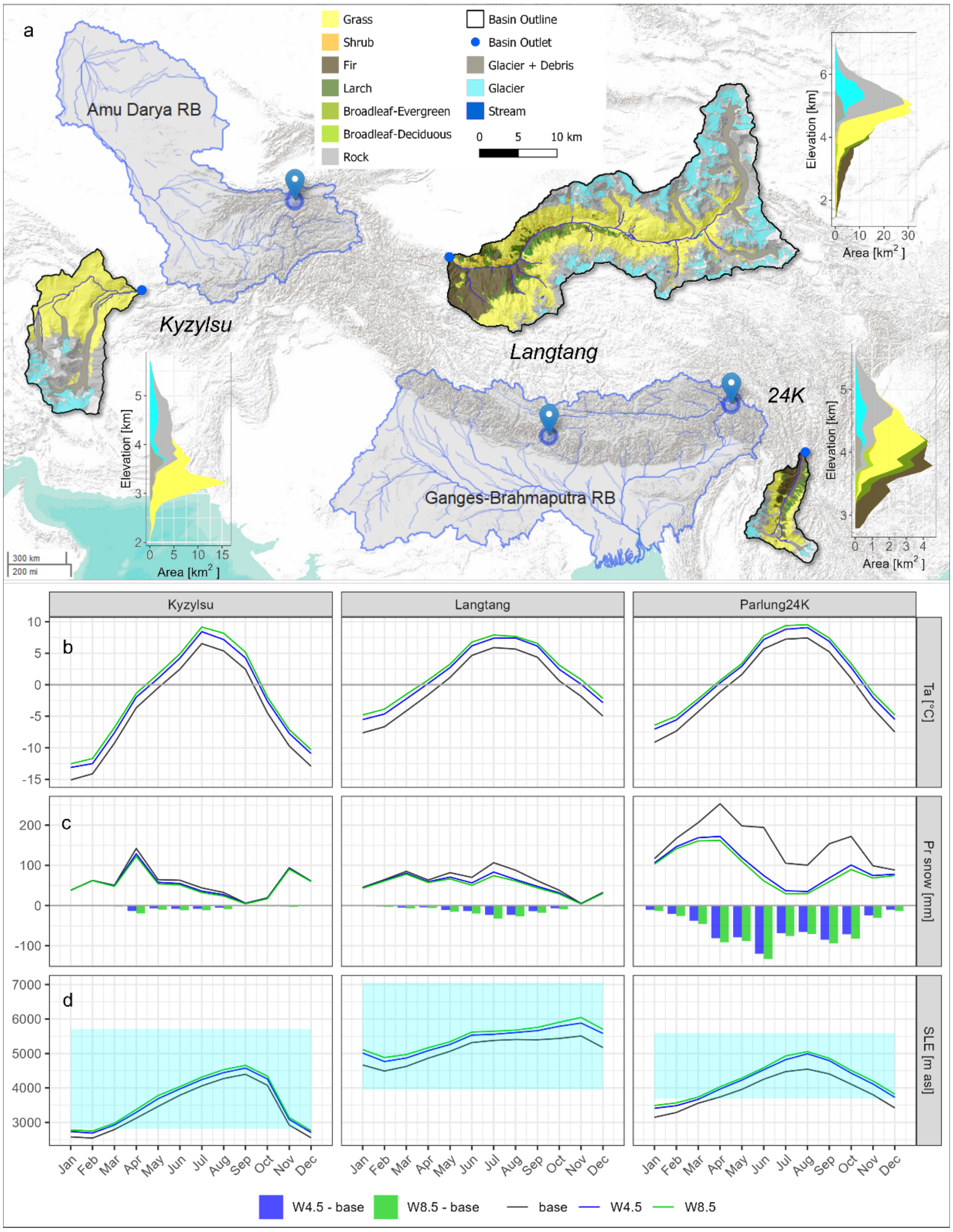

Figure 1. *a) Geographic location of study sites, detailed maps and landcover hypsometry; b) Air temperature (Ta) modification under the two alternative experiments. c) Model output of snowfall (Pr snow). Changes in the snowfall due to temperature changes under either experiment are shown in absolute values in the bars. d) Snow line elevation (SLE). Cyan shaded areas indicate the elevation range of glaciers in each catchment.*

2.2. Model description

The Tethys-Chloris model (T&C; Fatichi et al., 2012a,b; 2021; Manoli et al., 2018; Botter et al., 2021; Paschalis et al., 2022; 2024) is an ecohydrological model, which was updated to include energy-balance based representations of snow and glaciers (Figure S3).

The model represents a distributed, mechanistic approach to simulating the interplay between energy, water, and vegetation dynamics on the land surface. With a focus on a mechanistic representation, T&C integrates processes at hourly (for energy and water) and daily (for carbon and nutrient cycles) scales, encompassing a variety of surface types, including vegetated areas, bare soil, and snow or ice-covered regions. The model is used here at a 100-m spatial resolution. The model employs a single prognostic surface temperature for energy flux calculations, expanding to two in cases of snow-covered vegetation, to account for differences in radiative temperatures between snowpacks and vegetated areas.

T&C's methodology for transferring heat, moisture, and carbon involves resistance analogy schemes that calculate multiple forms of resistance, including aerodynamic and stomatal, based on established theories and semi-empirical parameterizations. Aerodynamic resistances for the estimation of turbulent heat- and vapor fluxes were determined using the Monin-Obukhov Similarity Theory (Monin and Obukhov, 1954).

Soil hydraulic parameters are estimated using the Saxton and Rawls pedotransfer function (Saxton and Rawls, 2006). The model solves the one-dimensional Richard's equation for vertical water movement and applies a heat diffusion model for soil temperature profiles. Lateral water transfer, surface runoff, and subsurface flow, incorporating the complexities of soil moisture dynamics and interactions with vegetation are also explicitly simulated.

Plant physiological processes are computed through detailed schemes of photosynthesis, respiration, and phenology, accounting for the effects of environmental conditions on vegetation growth and carbon allocation. This includes simulation of different phenological stages, leaf area index dynamics and carbon cycling.

The dynamics of snow and ice packs, including accumulation and melt processes, ice melting under debris-cover, are simulated using numerical solutions of heat transfer functions to track changes in snow, debris and ice layers. The partitioning of precipitation into rain, snow and sleet is based on the wet bulb temperature (Ding et al., 2014), the snow albedo dynamics are simulated using the parameterization of Ding et al. (2017) and the model also includes schemes for snow aging and settling and redistribution by gravity. More details are provided in Fatichi et al., (2012a,b, Mastrotheodoros et al 2020) and more recent developments for the cryospheric components are detailed in Fugger et al. (2022, 2024). The setup, including the evaluation of the model at the three study sites, is described in Fugger et al. (2024).

2.3. Forcing experiments

Baseline experiment

In the baseline experiment (base), generated by Fugger et al. (2024), the model was forced using downscaled ERA5-Land reanalysis data which was bias-corrected against in-situ weather station data using empirical quantile mapping. The model was run at a 100 m resolution with an hourly timestep for the hydrological years 2010-2022, including two years of spin-up at each site. The model performed well at simulating i) snow cover seasonality; ii) stake and remote sensing observations of glacier mass balance; iii) LAI and; iv) streamflow magnitudes and timing. The downscaling and evaluation of forcing data, as well as the model evaluation is detailed in Fugger et al. (2024).

Warming experiments

In the warming experiments (W4.5, W8.5), the air temperature (Ta) was perturbed with future projections of temperature change at each individual catchment. Temperature related variables, namely longwave radiation and dew point temperature, were adjusted in order to maintain physical and meteorological consistency, as described below. Two 'shared socio-economic pathways' were selected from the CMIP6 experiment: the 'Middle-of-the-Road' (SSP2-4.5) and 'Fossil-fueled Development' (SSP5-8.5). The ensemble-mean temperature changes of 34 climate model outputs were extracted for the catchments' center points, for the medium-term (2051-2060) future, compared to the past period 1995-2015 (Milinski and Marotzke, 2023). The temperature modification was applied per calendar month, and kept constant for all the days in a calendar month and over the diurnal cycle. Annual average increases under W4.5 (W8.5) are similar between Kyzylsu with +1.80 (+2.52) and Langtang with +1.81 (2.42), and slightly lower for 24K with +1.66 (+2.22).

In both warming experiments, the full model runs were repeated, including the 2-year spin-up period. In order to isolate the warming effect on the catchments' hydrology, all non-temperature-controlled variables were kept the same between the baseline and warming experiment. Total precipitation remained unchanged between the experiments, while the snowfall ratios are able to change in response to the temperature modifications, due to the model-internal precipitation partitioning. Similarly, land cover distribution and properties were kept constant, but vegetation responded to the different climatic conditions. Glacier area changes are sensitive to the precise SSP course (Rounce et al., 2023) but observations highlight that debris-covered glaciers, such as those at our study sites, respond to climate warming by thinning at first, rather than retreat (Scherler et al., 2011). Numerical models show that many of these glaciers will continue following this pattern, and are likely to experience limited area change before 2050 (e.g. Compagno et al, 2021). Importantly, this research design is not intended to make projections of future hydrology, but to test the hydrologic sensitivity of the catchments under investigation to realistic potential warming.

Air temperature Ta $[°C]$ was modified by adding a constant air temperature offset ΔTa $[°C]$ to all hourly air temperature values for each calendar month:

$$Ta_{mod} = Ta + \Delta Ta \tag{1}$$

Longwave radiation $L\downarrow$ $[W\,m^{-2}]$ was re-calculated using the Stefan Boltzman law with Ta_{mod} $[°C]$, while keeping the emissivity ε $[-]$ constant:

$$L\downarrow_{mod} = \varepsilon * \sigma * (Ta_{mod} + 273.15)^4, \tag{2}$$

$$\varepsilon = \frac{L\downarrow}{\sigma*(Ta+273.15)^4}, \quad (3)$$

where $\sigma = 5.67e^{-8}\left[W\,m^{-2}\,K^{-4}\right]$ is the Stefan Boltzmann constant. Finally, dew point temperature T_{dew} $[°C]$ was modified by recalculating the modified vapor pressure e_{mod} $[Pa]$ and saturation vapor pressure $e_{sat,mod}$ $[Pa]$ following Shuttleworth (2012) using Ta_{mod} and keeping the relative humidity U $[-]$ unchanged

$$T_{dew,mod} = -\frac{237.3}{1-17.27/ln(e_{mod}/611)}, \quad (5)$$

$$e_{mod} = U * e_{sat,mod}, \quad (6)$$

$$e_{sat,mod} = 611 * exp\left(\frac{17.27 * Ta_{mod}}{Ta_{mod}+273.15}\right), \quad (7)$$

2.4. Post-processing of results

Model outputs were spatially aggregated at each hourly time step across the whole catchment or the land cover of interest. Summing was used for mass fluxes, while means were used for energy fluxes and meteorological variables (except precipitation). Further aggregation of time series to multi-year daily, monthly or annual averages was performed for the hydrological years following the spin-up period, i.e. October 1, 2012 to September 30, 2022. The cumulative glacier mass balance (cGMB) values were calculated by cumulating the variations in the ice packs and on-glacier snow-packs starting with October 1 until September 30 of each hydrological year, before the yearly cumulative time series were averaged to multi-annual means.

The accumulation start date (ASD) was derived automatically by searching for the date in the multi-annual cGMB, on which the cGMB would first reach its minimum after the start of the hydrological year. The glacier loss day (GLD), which indicates the date when all mass gained during the accumulation period would be lost (Voordendag et al., 2023), was then identified as the date on which the cGMB would return to the value on the ASD.

To disentangle the effects of temperature increase and snow cover reductions on ice melt, the percentage of ice-melt enhancement due to snow cover reductions p_{es} $[\%]$ was calculated as

$$p_{es} = \frac{100}{n}\sum_{i=1}^{n}\left(\frac{t_{B,i} - t_{W,i}}{M_{W,i} - M_{B,i}}\,\frac{M_{B,i}}{t_{B,i}}\right), \quad (8)$$

where M_W is the monthly ice melt under either warming experiment in each computational element of the glacier surface i, M_B is the ice melt under the baseline experiment, t_w is the snow cover duration under either warming experiment, and t_B is the snow cover duration under the baseline experiment. It is assumed that the rest of the ice melt-enhancement happened directly due to temperature increases, acknowledging that exposure and temperature increases have a coupled effect on ice melt.

Since the initial glacier outlines were left unchanged between the warming experiments, but glaciers are expected to have retreated to some degree under warmer conditions, the effect of potential glacier shrinkage was post-computed after the simulations, by iteratively removing the spatial outputs of ice melt by 5, 10, 20 and 30%, starting from the lowest-elevation glacier cells according to the model's digital elevation model.

Growing season length (GSL) was derived from net primary productivity (NPP), by determining the day that NPP reaches (start date) and returns (end date) to 15% of its amplitude (maximum - minimum annual value) in the baseline scenario. Lengthening of the growing season (ΔGSL) was determined by differencing GSL between scenarios. Spring-/autumn lengthening was determined by differencing the start/end dates between scenarios.

3. Results

3.1. Impacts of warming on precipitation phase

The changes in snow- and rainfall partitioning in response to warming differ between the three sites and corresponds to the timing of the greatest snowfalls in the base experiment. The largest phase shifts occur at 24K, with -36 (-41)% reductions in annual total snowfall under W4.5 (W8.5) (Table 1). This reduction takes place mostly in the months before (April, June) and after the monsoon (September, October) (Figure 1c, Table 1). The reduction in snowfall is smaller in Langtang, where the strongest shifts happen during the core monsoon (July, August) (Figure 1c, Table 1), with -14 and -19% total snowfall reductions for W4.5 and W8.5, respectively. At Kyzylsu, the reductions in snowfall are smaller compared to the two monsoonal sites, with annual reductions in snowfall of -7 (-11)%, happening mainly during spring (April) and more moderate reductions from May through July. The mean annual snowline shifts upward in 24K by +289 (+365) m under W4.5 (W8.5), to a comparable degree in Langtang with +274 (+376) m and to a lesser degree in Kyzylsu with +170 (+239) m (Figure 1d, Table 1).

Table 1. *Differences in annual average model in- and outputs between W4.5/W8.5 and the baseline scenario. Differences are expressed in both their physical units, and as percentages where appropriate; Table S1 shows the original (non-differenced) values under each scenario. All values are averages across the entire catchment area. Ta - air temperature, Pr_liq - liquid precipitation, Pr_sno - solid precipitation, L↓ - incoming longwave radiation, Smelt - snowmelt, Imelt - ice melt, Tmelt - total melt (ice + snow melt), SLE - snow line elevation, SWE - snow water equivalent, ET - evapotranspiration, NPP - net primary productivity, S - sublimation, Q - runoff.*

Site		Kyzylsu				Langtang				24K			
Experiment		W4.5 - base		W8.5 - base		W4.5 - base		W8.5 - base		W4.5 - base		W8.5 - base	
Variable	*unit*	*units*	*%*	*units*	*%*	*units*	*%*	*units*	*%*	*units*	*%*	*units*	*%*
Ta	°C	1.8		2.5		1.8		2.4		1.7		2.2	
Pr_liq	mm	49	17	74	26	107	11	144	14	674	40	765	46
Pr_sno	mm	-49	-7	-74	-11	-107	-14	-144	-19	-674	-36	-765	-41
L↓	W m^{-2}	6	3	9	4	7	3	9	3	7	2	10	3
Smelt	mm	-24	-5	-36	-8	-68	-11	-96	-16	-642	-38	-722	-43
Imelt	mm	78	46	121	71	136	67	187	92	50	79	82	130
Tmelt	mm	54	8	85	13	68	9	92	11	-592	-34	-639	-36
SLE	m asl	170		239		274		376		289		365	
SWE	mm w.e.	-285	-28	-402	-39	-223	-39	-278	-48	-346	-44	-453	-57
ET	mm	48	22	67	31	73	26	96	34	128	38	167	50
NPP	gC m^{-2}	15	24	19	32	11	27	15	37	49	27	62	34
S	mm	8	8	9	10	-6	-7	-9	-11	-1	-1	-3	-4
Q	mm	60	8	98	14	108	7	149	10	-41	-1	-37	-1

3.2. Impacts on snow and glacier mass balances

As a result of the snowfall reductions and intensified melting, the catchment-average annual snow water equivalent decreases by -28 (-39)% in Kyzylsu under W4.5 (W8.5), by -39 (-48)% in Langtang and by -44 (-57)% in 24K (Table 1).

Changes are evident also in the glacier mass balance dynamics. The glacier mass balance changes from -0.43 to -0.93 (-1.2) m w.e. yr^{-1} in Kyzylsu, from -0.56 to -1.33 (-1.58) m w.e. yr^{-1} in Langtang and -0.2 to -0.85 (-1.21) m w.e. yr^{-1} in 24K (Figure 2 a,b). The accumulation start date (ASD) remains the same in Kyzylsu (1 day later under W8.5), shifts later by 15 (15) days at Langtang and 16 (17) days at 24K (Figure 2b, Table 2). The small change in Kyzylsu is determined by the later precipitation onset after the autumn dry spell, when temperatures are still cold enough for snowfall in the warming experiments. The larger changes at the two other sites are a result of phase changes under warming (Figure 1 c). The delayed start of the accumulation period under the warming experiments decreases mass balances in Langtang and 24K substantially even before the main ablation period starts (Figure 2 c). Finally, the glacier loss day (GLD) shifts by 22 (31) days earlier in Kyzylsu, 56 (74) earlier in Langtang and 28 (40) days earlier in 24K (Figure 2b, Table 2). An earlier exposure of ice surfaces in combination with higher temperatures and lower albedo accelerates ice melting, with overall increases in the ice melt contribution to runoff ranging between +46% (Kyzylsu, W4.5) and +130% (24K, W8.5) (Table 2, Figure 7). Of the additional ice melt, as much as 43 (48) % can be attributed to snow cover reductions (p_{es}) in Kyzylsu, 53 (55)% in

Langtang and 74 (76)% in 24K under W4.5 (W8.5) (Table 2), while the rest of the additional melt can directly be attributed to temperature increase.

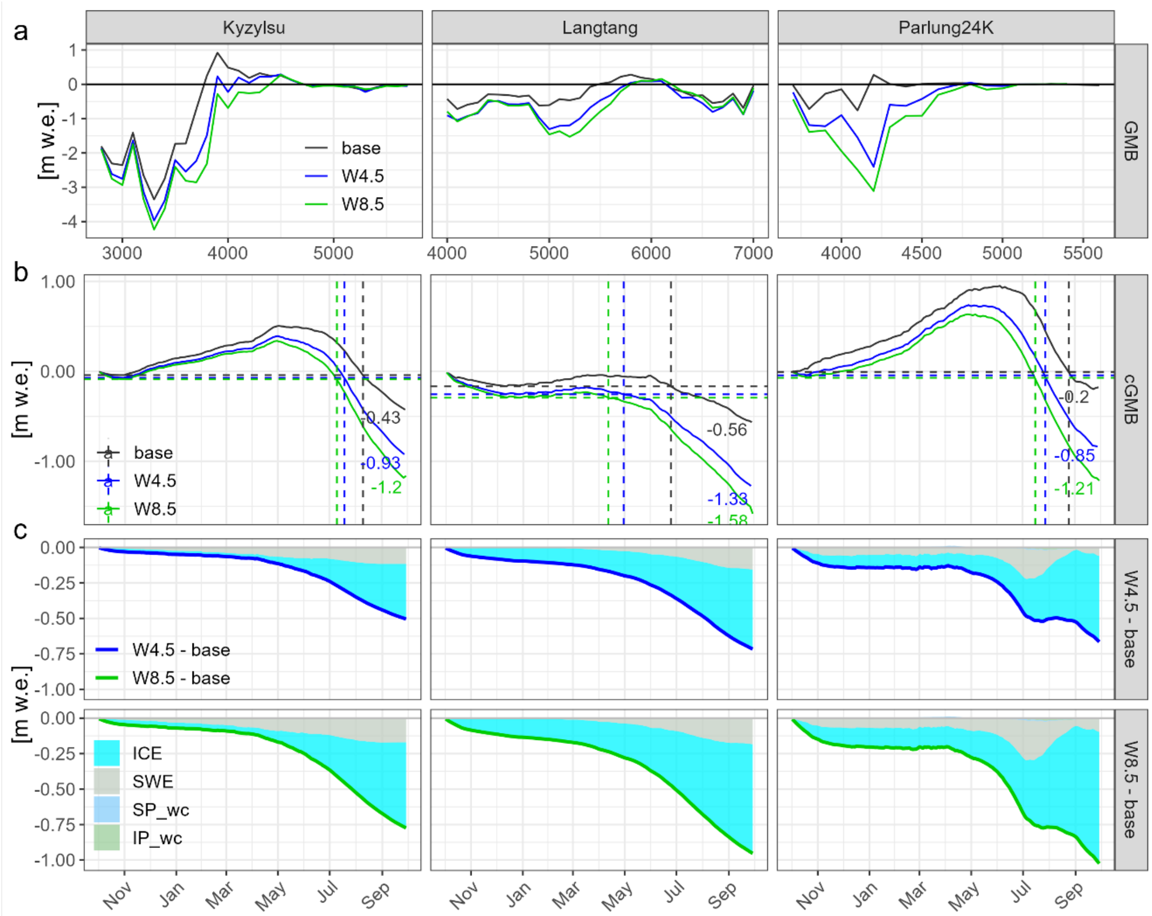

Figure 2. *a) Multi-annual (Oct.2012 - Sep.2022) mean glacier mass balance (GMB) hypsometry for three experiments. 100 m elevation bands' mean mass balance values across all glaciers in the catchment, including water equivalents stored in ice (ICE), snow (SWE), ice- and snowpack water contents (IP_wc, SP_wc) b) mean cumulative glacier mass balance (cGMB) given as inter-annual averages over all of the catchment-wide glacier mass. Vertical dashed lines indicate the glacier loss day (GLD). c) differences in cGMB between the experiments (lines) broken down by snow and ice components (color shading). The changes to SP_wc and IP_wc were included for completeness, but are small compared to the changes in the snow - and ice packs.*

Table 2. *Glacier mass balance (GMB), accumulation start day (ASD), glacier loss day (GLD) across sites and experiments, average percent-change-values for ice melt ($\Delta Icement$) and on-glacier snow water equivalent (ΔSWE), as well as the accumulation area ratio (aar) and the percentage of additional ice melt attributed to snow cover reductions (p_{es}). Values represent the entire glaciated area in each catchment.*

Site	Exp.	GMB [m w.e.]	ASD	GLD	ΔIcemelt [%]	ΔSWE [%]	aar [-]	p [%]
Kyzylsu	base	-0.43	30.10.	10.08.			0.3	
	W4.5	-0.93	30.10.	19.07.	+46	-28	0.26	43
	W8.5	-1.2	31.10.	10.07.	+71	-23	0.23	48
Langtang	base	-0.56	12.12.	25.06.			0.35	
	W4.5	-1.33	27.12.	30.04.	+67	-52	0.2	53
	W8.5	-1.58	27.12.	12.04.	+92	-68	0.19	55
24K	base	-0.2	03.10.	25.08.			0.33	
	W4.5	-0.85	19.10.	28.07.	+79	-14	0.29	74
	W8.5	-1.21	20.10.	16.07.	+130	-20	0.27	76

3.3. Impacts on evapotranspiration and plant productivity

At all three catchments, enhanced ET has the net effect of removing more water from the catchment under both warming experiments, with an increasing effect from west to east: annual ET increases under W4.5 (W8.5) by +22.0 (+31)% in Kyzylsu, +26.2 (+34.2)% in Langtang and +38.0 (49.8)% in 24K (Figure 3a, Table 1). ET increases throughout the year in the monsoonal catchments, with strongest increases during the rainy season. Pronounced increases in evapotranspiration also occur in Kyzylsu between spring and late summer, while from September onwards, when there is only little precipitation, ET does not further increase due to warming. Net primary productivity (NPP) does not increase linearly with ET, but surprisingly similarly across catchments with 24 (32)% in Kyzylsu, 27 (37)% in Langtang and 27 (34)% in 24K (Figure 3, Table 1). Similar to ET however, NPP does not increase during the late summer at Kyzylsu (under both W4.5 and W8.5) but drops below the baseline rates during September and early October (Figure 3b). An extension of the growing season ΔGSL is evident from the daily NPP catchment-averages at all sites (Figure 3), with the strongest extension at 24K with 25 (31) days, followed by Kyzylsu with 15 (17) days and with smallest extension 9 (10) days in Langtang (Table 3). The growing season primarily extends into spring in Kyzylsu, extends equally into spring and autumn in Langtang, and extends more into autumn than spring at 24K.

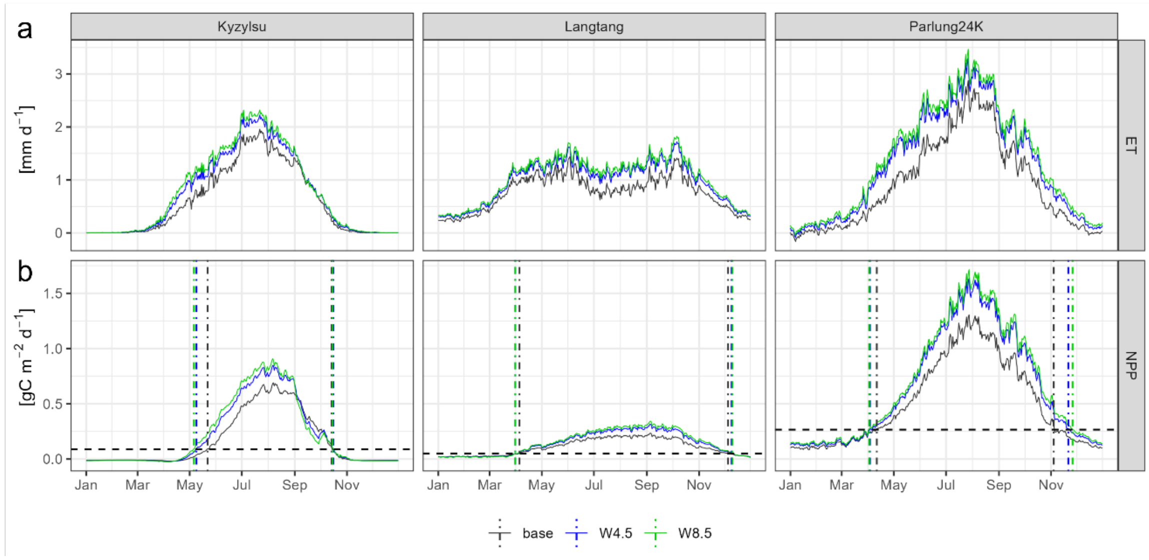

Figure 3. *Impacts of warming on (a) evapotranspiration and (b) net primary productivity. Annual average change values are given in Table 1, absolute values in Table S1. Horizontal dashed lines indicate the NPP level at which the growing season length was determined. Vertical dashed lines indicate the start and end dates of the growing season (Table 3).*

Table 3. *Growing season metrics derived from NPP as described in Section 2.4. GSL - Growing Season Length, ΔGSL - Lengthening of Growing Season, ΔSpring - Spring-lengthening of Growing Season, ΔAutumn - Autumn-lengthening of Growing Season*

Site	*Exp.*	*Start date*	*End date*	*GSL [d]*	*ΔGSL [d]*	*ΔSpring [d]*	*ΔAutumn [d]*
Kyzylsu	base	22.05	14.10	145			
	W4.5	09.05	16.10	160	+15	+13	+2
	W8.5	06.05	15.10	162	+17	+16	+1
Langtang	base	05.04	05.12	244			
	W4.5	31.03	09.12	253	+9	+5	+4
	W8.5	31.03	10.12	254	+10	+5	+5
24K	base	11.04	04.11	207			
	W4.5	03.04	21.11	232	+25	+8	+17
	W8.5	02.04	26.11	238	+31	+9	+22

The effect of Ta on ET is relatively uniform across the sites and all the hydrological years as indicated by the uniform and linear changes in ET with Ta (Figure S1a), with some deviations in Kyzylsu, where the available moisture can seasonally be a limiting factor on ET. Warming increases the vapor pressure deficit (vpd) due to an increase of the moisture holding capacity of the air, favoring ET (Figure S1 a,b), which results in a closely coupled response of ET to Ta and vpd changes. Snow line elevation (SLE) however, is less clearly controlling ET, although also closely coupled with Ta. The clearest linear response of ET to SLE is however observed in 24K, and the snow cover dynamics create a non-linear response of ET to Ta and vpd from the baseline to warming scenarios (Figure S1c). The response of NPP to Ta modifications is similar, while not as uniform and linear as the one of ET (Figure S1d,e). The interannual variability of NPP increases under warming in Kyzylsu, where water is expected to be a limiting factor on plant growth, especially during late summer, and to a lesser degree also in Langtang, (Figure S1d-f). Large interannual variabilities (and non-linearities) are found in Langtang and Kyzylsu for NPP as a response to changes in SLE (Figure S1f), suggesting that factors other than SLE exert an more important influence on NPP.

The Bowen ratio Bo (Schmidt, 1915; Bowen, 1926), defined as the ratio between the sensible H and latent LE heat fluxes, describes the relationship between the amount of heat transferred by convection and the amount transferred to the air by evaporation. Smaller values of Bo indicate a more temperate or humid environment, while a high ratio indicates a drier and or cold environment. Bo decreases under warming during the growing period at all sites across the snow- and ice-free land surface, indicating that energy is partitioned preferably toward evaporation compared to the baseline experiment (Figure 4). In 24K, for example, the September values of Bo decreased from an average of 0.42 under the baseline experiment to 0.36 (0.32) under W4.5 (W8.5), implying that available energy, rather than water, remains as the limiting factor to evapotranspiration. An exception is Kyzylsu during September, where Bo increases from 0.92 under the baseline experiment to 0.96 (1.05) under W4.5 (W8.5), indicating a shift towards more arid conditions (Figure 4). There, already depleted soil water does not allow for additional evapotranspiration, despite the warming-induced increase in net radiation.

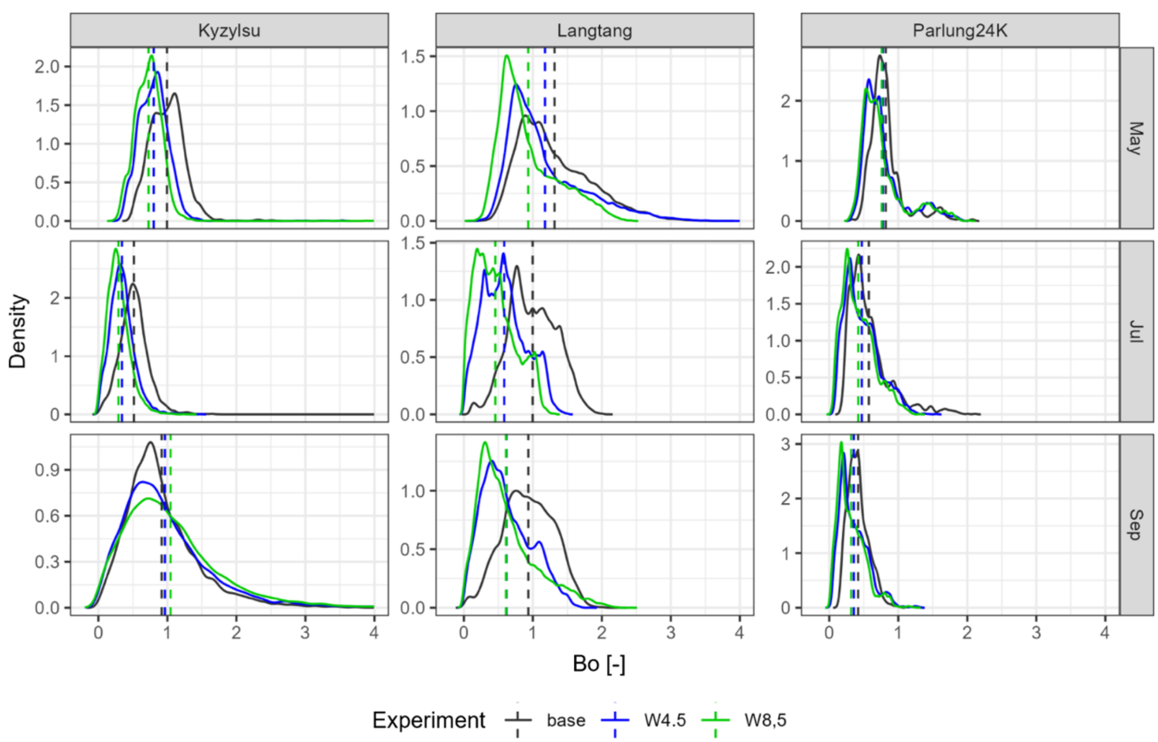

Figure 4. *Probability density functions (PDFs) of Bowen ratios ($Bo = H/LE$) across all snow– and glacier-free grid-cells; vertical dashed lines indicate the mean value of each distribution; Bowen ratios over natural landscapes can range from <0.1 over tropical oceans to > 10.0 over deserts (Stull et al., 2006). PDFs are provided for only for the months May, July and September as indicative of the seasonal changes and for neatness.*

3.4. Impacts on snowpack sublimation

Snowpack sublimation from the ground (including glaciers) and canopy (S) shows overall limited sensitivity to the warming (Figure 5), although annually, changes differ in sign between catchments. Net annual increases in S are found in Kyzylsu with +8.3 (+9.6)% under W4.5 (W8.5), small decreases in 24K with -1.4 (-3.7)%, and larger decreases in Langtang of -6.4 (-10.8)% (Table 1). At Kyzylsu and 24K the direction of changes varies by season, with sublimation increasing during the winter but decreasing during summer (Figure 5). The larger winter sublimation increase in Kyzylsu therefore leads to overall increased sublimation over the year, while in 24K, the seasonal changes are almost balanced out. In Langtang, on the other hand, sublimation rates decrease throughout the year.

Similar to ET, S is mainly controlled by Ta via the vapor pressure deficit (Figure S2). With catchment mean winter temperatures well below the freezing point, any temperature increase results in increases in S (e.g. Kyzylsu). However, the closer that the catchment mean winter Ta approaches the melting point, the more S is prone to decline (e.g. 24K) and the steeper the declines become (e.g. Langtang) (Figure S2a). The snow cover extent is a weaker control on sublimation than temperature and vpd, suggested by the decoupling of S from SLE (higher S under retreating SLE) in Kyzylsu in winter, but also in 24K between the baseline and W4.5 experiment (Figure S2a). Similarly S is decoupled from net radiation (Rn) in winter in Langtang (less sublimation under more net radiation) (Figure S2a) and at all sites in summer (Figure S2b), suggesting that it is also overpowered by the coupled Ta - vpd response. During summer, where mean catchment Ta is well above the freezing point at all sites and under all experiments, S follows Ta, as well as vpd and SLE, making a disentangling of controls more difficult (Figure S2b).

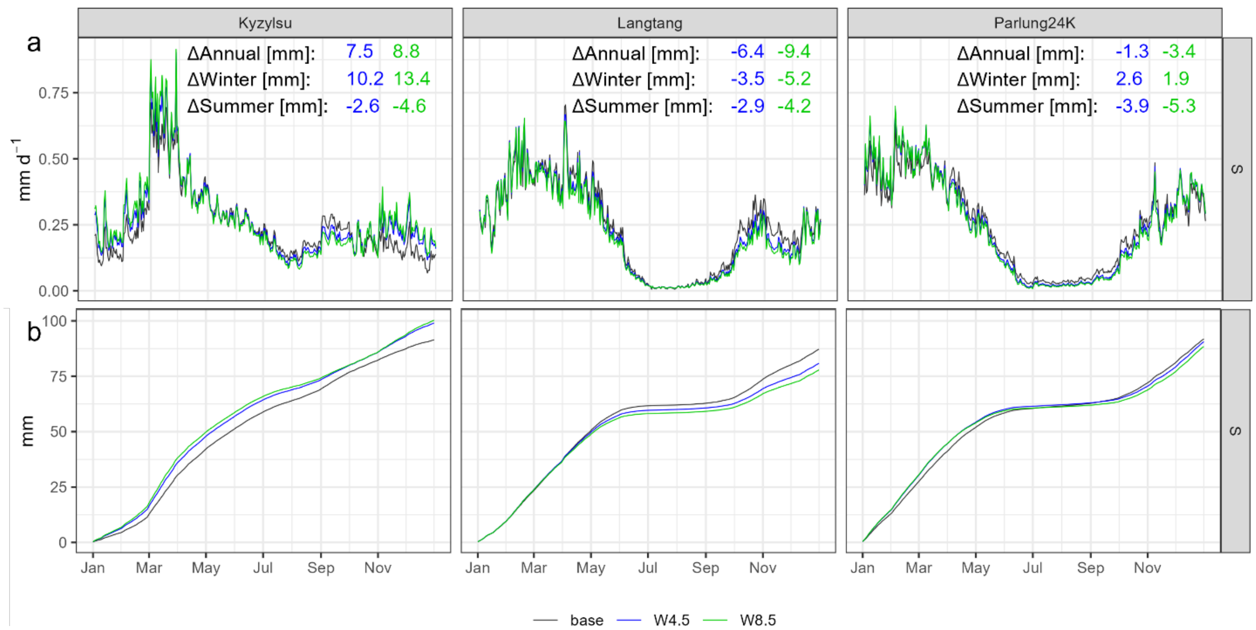

Figure 5. *a) Impacts of warming on sublimation (S), b) same as a, but cumulative. All annual average change values are given in Table 1, absolute values in Table S1.*

3.5. Impacts on runoff generation

In general, the runoff response of the three catchments is shaped by increases in ice melt and rainfall inputs (adding water), and decreases in snowmelt and increases in ET (removing water) (Figure 6a), while sublimation is implicit in the snowmelt inputs. On the supply-side, ice melt increases by +78 (+121) mm in Kyzylsu, +136 (+187) in Langtang and +50 (+82) mm in 24K under the warming experiments W4.5 (W8.5). On the withdrawal-side, ET increases by +48 (+67) mm, +73 (+96) mm and +128 (+167) mm, removing additional moisture from the catchments. As a result, runoff increases only moderately by +60 (+98) mm in Kyzylsu, +108 (+149) mm in Langtang (Figure 6a, Table 1). Runoff even decreases in 24K with -56 (-51) mm, where glacier area is small and ET overrides the increases on the supply side (Figure 6a and 9). In relative terms, changes in the 24K annual runoff do not exceed -1% compared to the baseline. Changes are highest in Kyzylsu with relative increases of 8 (14)%, and in Langtang, with relative increases of 7 (10)%.

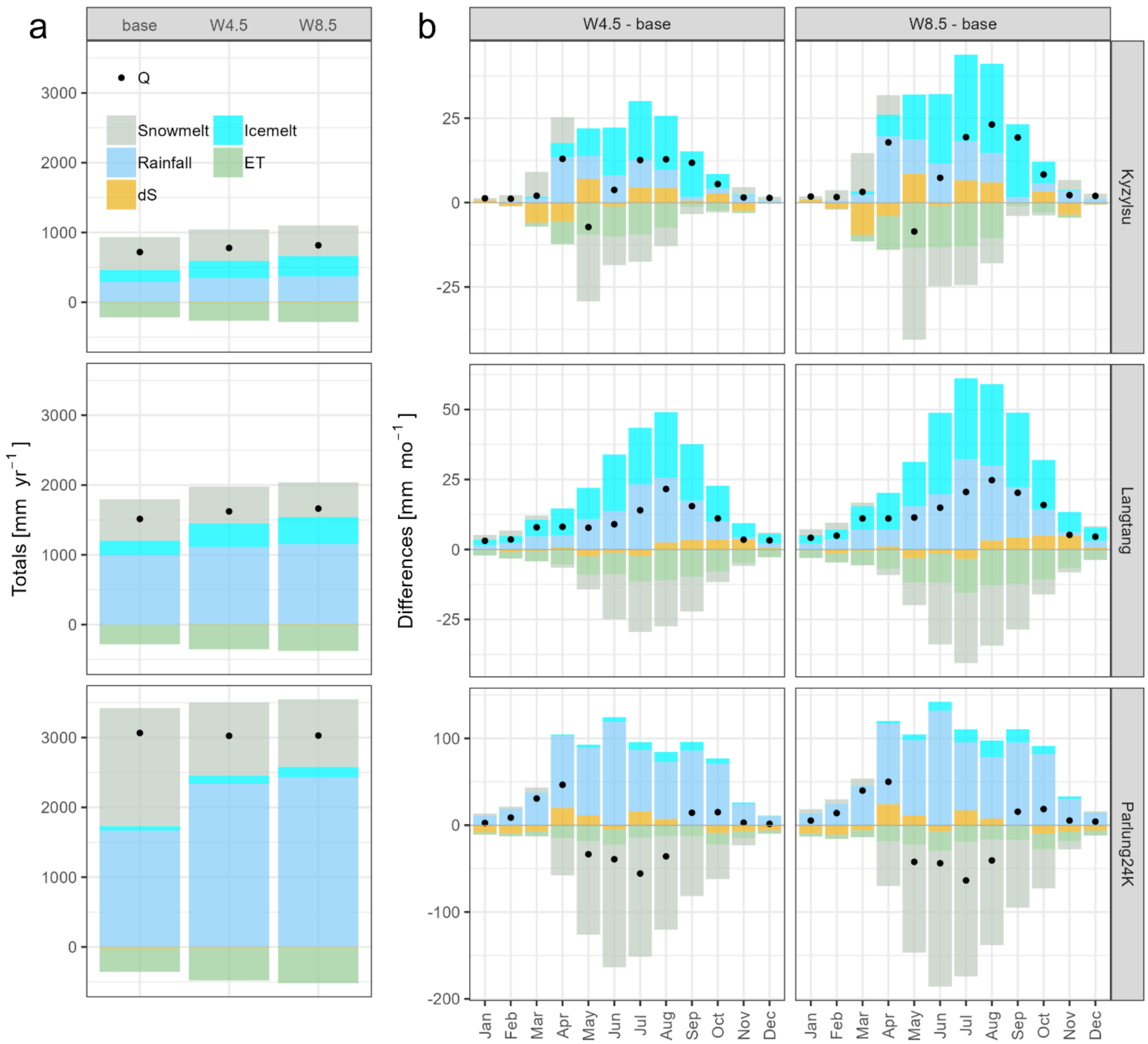

Figure 6. *Inputs to the streamflow where ET is removing water and the resulting runoff in streamflow: a) annually, and b) as differences between the two warming experiments and the baseline experiment; dS indicates the storage changes due to ground water and interception dynamics as well as snow and ice water storage. Note that the y-axis scales were left independent in b in order to allow for a better readability of the differences; Q = runoff, dS = Storage change;*

Modifications in the seasonality of runoff contributions are apparent (Figure 6b): Snowmelt events occur earlier in the hydrological year, evidenced by increased snowmelt contributions from January to March in Langtang and 24K, and from November to April in Kyzylsu. At the same time, contributions from snowmelt decrease at all sites during late spring and summer. Reductions in snowmelt are responsible for an overall lowering of runoff between April and October in 24K and in May in Kyzylsu. Icemelt increases dominate the late-season response in streamflow at Kyzylsu, most apparently so in September (Figure 6b).

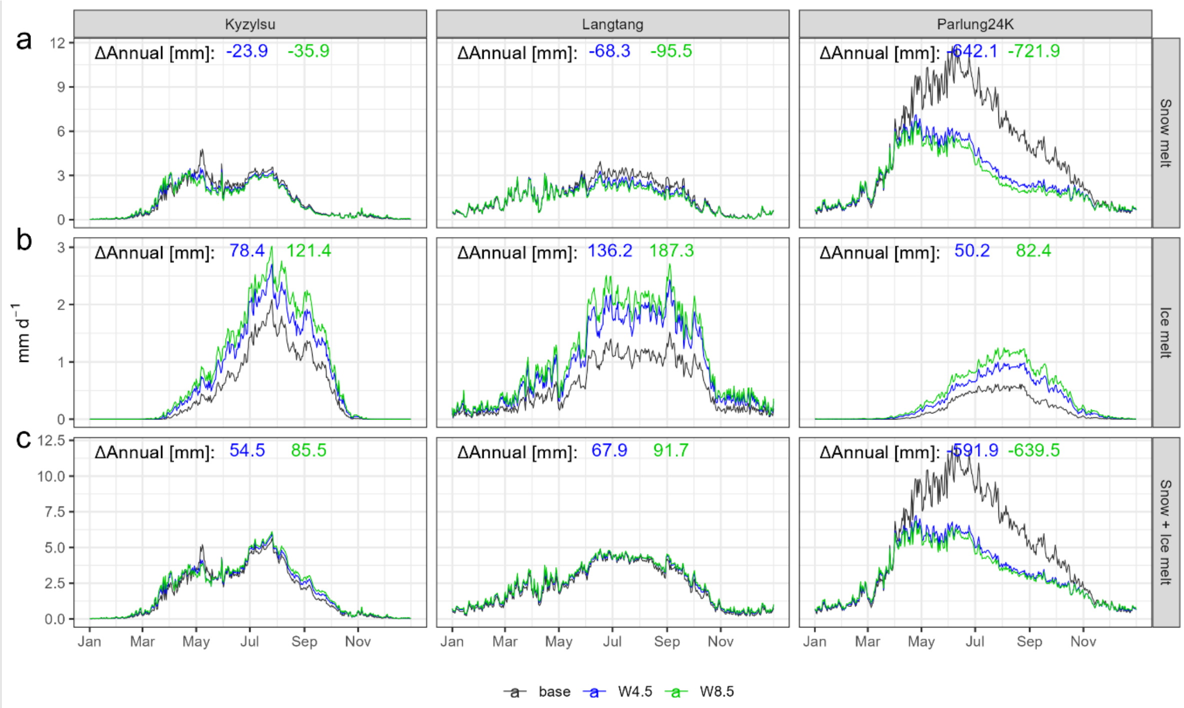

Figure 7. *Changes in snow and ice melt including the sum of snow and ice melt, daily resolution, catchment scale. Note the different scales of the y-axis in panel a, b and c.*

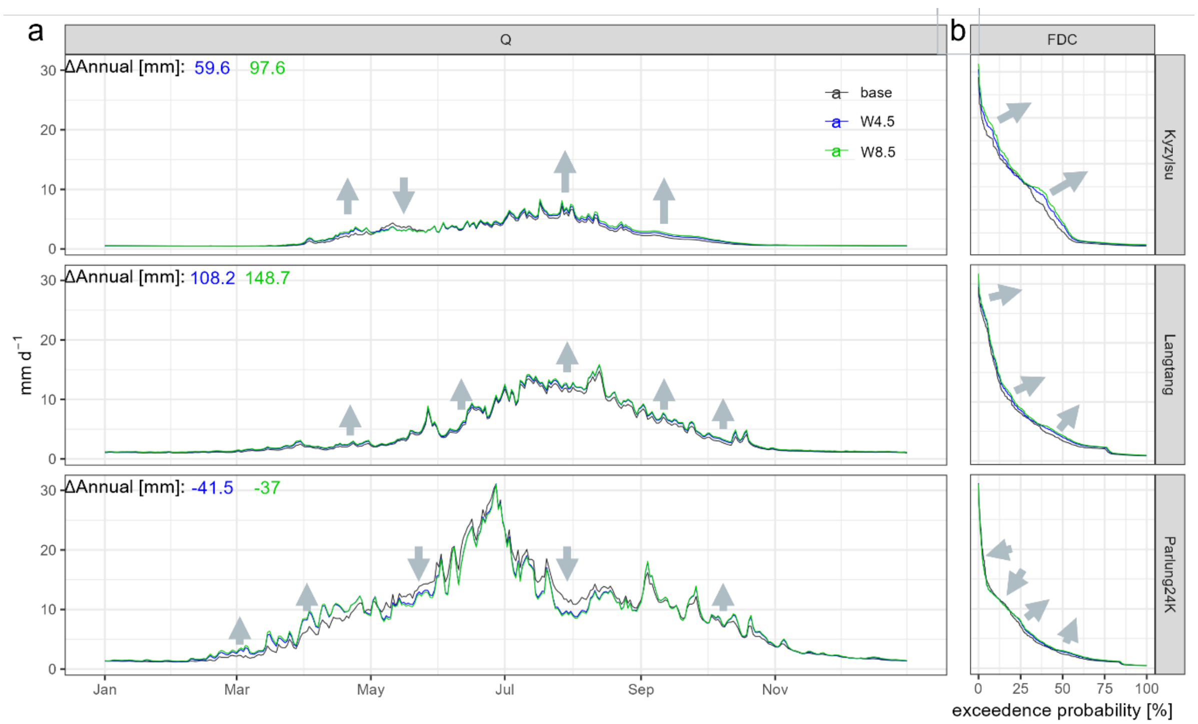

Figure 8. *a) Impacts of warming on streamflow, daily resolution; b) flow duration curves and changes for all three sites and experiments.*

In Langtang, the changes to ice melt are not constrained to the ablation season anymore in the warming experiments, but increase year-round, most strongly so during the monsoon months. Ice melt (over-)compensates for snowmelt decreases in Kyzylsu and Langtang remarkably during the summer, both in terms of magnitudes and timing (Figure 7 a,b), resulting in small increases in the combined ice- and snow melt from those two sites (Figure 7c). The glaciers in 24K, while ice melt is increasing also there, do not manage to compensate for snowmelt reductions in the same way (Figure 7a-c). At the same time, a distinctive increase in runoff happens during the driest month of the year, September, in Kyzylsu, which is the period during which the runoff production is maintained by glacier melting, while ET rates stay unchanged (Figure 8a). Increases in spring and autumn runoff are reflected in the pronounced changes to the lower tertile of the flow duration curve for Kyzylsu (Figure 8b). In Langtang, most parts of the hydrograph outside of the winter period are affected equally due to increased ice melt, while in 24K the moderate to low runoff magnitudes increase, which are related to the snowmelt period (Figure 8 a,b). The reasons for the difference between the two monsoonal sites are (1) a larger proportion of glacier cover in Langtang (30%) compared to 24K (9%), and (2) the greater amounts of precipitation (1.8 times more in 24K) and therefore the large impact of shifts between the liquid and solid phase precipitation.

4. Discussion

4.1. Water balance response mediated by precipitation seasonality

The sensitivities of the *snow and glacier mass balances to warming is found to be higher in the monsoonal catchments,* Langtang and 24K. The changes in the ratio between snow- and rainfall are strongly related to when precipitation arrives, and *the greatest changes occur when large amounts of precipitation fall during times when the temperatures are close to or above the phase partitioning threshold* (Figure 1 b-d). As a result, the change in the ratio between snow- and rainfall is stronger in the monsoonal catchments than in the westerly catchment. Even though the water yield and runoff timings of monsoon-dominated Himalayan catchments are not critically altered due to these phase shifts under climate change (Khanal et al., 2021, Kraajenbring et al., 2021), the *loss of glacier-protecting monsoonal snowfalls* and exposure of much darker glacier ice amplifies the temperature-driven melt-enhancement on the Langtang and 24K glaciers, with highest sensitivity of glaciers to warming in 24K, as shown here. Summer accumulation-type glaciers on the Tibetan Plateau and Himalaya were previously found to be highly sensitive to monsoonal snowfall variability (Fujita & Ageta, 2000, Shaw et al., 2022). A decrease in the proportion of solid precipitation, mainly during the monsoon, also caused the majority of the post-2000 mass loss on the nearby Parlung No.4 glacier, as shown by modeling (Jouberton et al., 2022). Snow and glacier mass balances are less sensitive in Kyzyslu, *but the sensitivity of the water yield is still greater there* since the glacier melt represents a greater component in the water balance. Shifts in the annual runoff peak are also expected to be stronger under continued climate change in catchments with a glacial-nival hydrological regime (Khanal et al., 2021), such as the one of Kyzylsu. The present study shows that precipitation seasonality does indeed play an important role in how the water balance reacts to warming, confirming *Hypothesis I.*

4.2. Greening in high-elevation catchments with water-limitations

Warming modifies all components of the land surface energy balance, as well as the land cover itself and the atmospheric conditions, such as the snow cover and soil moisture dynamics and the atmospheric vapor pressure. This, in turn, modifies evapotranspiration together with plant productivity. Warming under non-drought conditions *increases ET and NPP (greening)*, according to theory, observations and modeling studies (Yang et al., 2023), since the photosynthesis rate scales strongly with Ta in the temperature range experienced by three study sites (Sage et al., 2007). Here, we show that this is the case also in glacierized high elevation catchments of HMA, where vapor pressure deficit- or temperature-driven increases dominate the picture. An *extension of the growing season* (Maina et al., 2023), is evident from the catchment average NPP across sites and experiments. *Hypothesis II*, can therefore be fully confirmed. During the driest period of the year in Kyzylsu (September to early October), a decrease in NPP is simulated compared to the base experiment, indicating an earlier depletion of soil water due to warming-induced ET. An increase in the Bowen ratio also indicates a shift towards more arid conditions during this period in Kyzylsu, while during the rest of the year, as well as year-round at the other two sites, a shift towards warmer, but still not water-limited conditions is observed.

4.3. Response in sublimation follows temperature regime

As an evaporative flux, sublimation is positively coupled to air (surface) temperature via the vapor pressure deficit between the surface and the atmosphere: Saturation vapor pressure increases at warmer surfaces, increasing the near-surface vapor pressure gradient and therefore sublimation rates (Stigter et al., 2018). Sublimation however increases only until the air temperature reaches the melting point of water, above which the energy is invested into melting. In Langtang, where the mean winter air temperatures are not far below the freezing point, additional warming pushes them across the freezing threshold, such as under W4.5 and W8.5 with the result of reduced sublimation rates. A transition from increasing to decreasing winter sublimation is observed *between* the two warming experiments in 24K (Figure S2a). In Kyzylsu, where mean temperatures stay well below the freezing point during winter, sublimation increases, leading to a *mixed annual response* (Figure 5). *Hypothesis III*, that sublimation decreases unanimously at all sites is therefore not confirmed. In contrast, annual net snowpack sublimation increases in Kyzylsu and stays almost the same in 24K, mainly due to wintertime increases, while *summer sublimation decreases at all sites*. The net amounts involved however remain small in either direction (<10 mm). Greater reductions in sublimation (-92 mm), albeit representing blowing snow rather than snowpack sublimation, were found in a sensitivity study with a 5°C future temperature increase for the glacierized Canadian Peyto Research Basin, where the strong temperature modification shifted average air temperatures above 0°C (Aubry-Wake et al., 2023). Similar to the present study, a modeling study in the Colorado Rocky Mountains found that sublimation rates are relatively insensitive to climate warming and remain unchanged or slightly increase when the warming response is isolated (Sexstone et al., 2018). The sensitivity test presented here suggests that there exists a catchment-specific warming-threshold, at which net (summer+winter) sublimation does not further increase, but decline. Annual snowpack sublimation was shown to correspond to 75% of the ice melt generated in the upper Langtang catchment during 1 snow-rich hydrological year, while the figure increased to 154% when evapotranspiration was also included (Buri et al., 2024). For the extended Langtang catchment studied here, and on average over 10 years, the proportions are 43% (sublimation vs. ice melt) and 181% (evapotranspiration + sublimation vs. ice melt) under the baseline experiment. Under warming, proportions decrease to 24% and 128% (W4.5) and 20% and 116% (W8.5). These numbers underline the importance to include sublimation as a mass loss into hydrological studies, in order to avoid erroneous mass balance and runoff estimates (Stigter et al., 2018)

4.4. Low runoff sensitivity as a result of compensations

We show that *ice melt and evapotranspiration both increase in response* to warmer temperatures, with the net result of only slightly increasing runoff from the Kyzylsu and Langtang catchments, but minor decreases in runoff from 24K. Taking into account evapotranspiration losses, annual runoff from the Kyzylsu catchment would still increase until glacier areas have retreated by 20% under the stronger warming of W8.5, as shown with tentative estimates (Figure 9, Methods in Section 2.4). In Langtang, >30% of the glacier would have to retreat for evapotranspiration increases to overcome ice melt increases, and for the water yield to start decreasing (Figure 9).

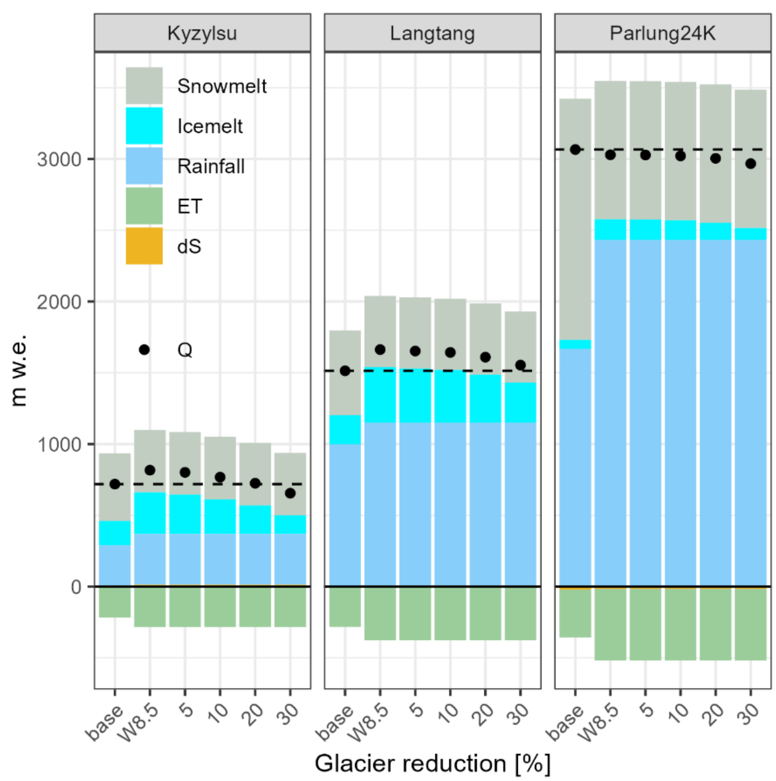

Figure 9. *Impact of reduced glacier area on ice melt and runoff. Methods for the post-computation of ice melt reductions due to glacier retreat are given in Section 2.4.*

In all catchments, the throughput of water is increasing under warming, with enhancements on both the supply- and withdrawal sites, indicating an *intensification of the water transfer through the catchment* (Figure 6a). While there are also considerable exchanges of mass among different water balance elements seasonally (Figure 6b), *changes in water yield are low and the runoff seasonality (hydrograph) remains relatively stable* at all sites (Figure 8). Strong shifts between the stream flow components are also projected in a 100-year simulation of Langtang based on future climate scenarios (Immerzeel et al., 2012). In their simulation, rainfall continues to increase the water yield until the end of the century and the runoff seasonality remains largely unchanged. In Ragettli et al. (2016), the main changes to the Langtang hydrograph until the mid-century are due to enhanced glacier melt and monsoonal increases in precipitation, while the runoff-seasonality remains almost unchanged, and larger shifts between the different terms of the water budget are only evident towards the end of the century. However, changes in evapotranspiration were not explicitly discussed in these two studies. The throughput, which is governed by the total precipitation and therefore 3.5 times higher in 24K compared to Kyzylsu (Fugger et al., 2024), also determines how much the changes in ice melt or evapotranspiration matter to the water yield and runoff seasonality, making the runoff response more sensitive in Kyzylsu than at the monsoonal sites. A somewhat paradoxical example of compensatory effects in high-altitude catchments is the observation that, during the dry period, streamflow at Kyzylsu catchment's outlet increases due to enhanced glacier-melt (less water in the landscape, more water in the river). This will likely be a prevailing pattern, even when accounting for glacier retreat, since glaciers of the Aral Sea basin are expected to reach their peak in ice melt runoff around the middle of the 21st under both RCP4.5 and RCP8.5 (Huss and Hock, 2018). After this peak however, further glacier loss, shifts in snowmelt timing and evapotranspiration increases will collectively act to reduce seasonal streamflow. As a result, semi-arid basins like the Amu-Darya might not be able to meet the increasing water demand downstream (Pohl et al., 2017), while this is not likely to be the case in monsoonal river basins (Immerzeel et al., 2013, 2020).

4.5. Limitations

Our results present a snapshot of the wealth and complexity of information that one can obtain from process-based simulations of high-elevation catchment hydrology. Our modeling approach allows us to assess the sensitivity of glacierized catchments to warming by isolating the detailed temperature response of all components of the hydrological system, though some limitations should nonetheless be stated. The initial glacier geometry was left unchanged between the warming experiments, while glacier area reductions due to melting were permitted during the simulation period. Glacier areas and volumes would in reality be already reduced in a warmer climate, so ice melt enhancements are likely somewhat overestimated. The hydrological impact of potential glacier shrinking was, however, estimated in a simple post-processing exercise and discussed above. Moreover, only temperature and temperature-controlled variables were modified, while maintaining physical consistency. Atmospheric CO_2 was left unmodified, although elevated CO_2 levels are expected to cause reduction in stomata aperture but also stimulate NPP. The effect of these counteracting processes on ET and NPP is however expected to be small. Running full future experiments is limited at present, since very few GCMs produce the whole set of forcing variables required for detailed energy balance model at these spatial and temporal resolutions. Moreover, the variability between model outputs and internal climate variability (stochastic uncertainty), especially for precipitation, is substantial (Fatichi et al., 2016b). For these reasons, the presented experiments should be understood as sensitivity tests to temperature, rather than future projections. Snow redistribution and blowing snow sublimation was not simulated, which is however not expected to affect the results around the direction and seasonality of sublimation changes, while the total rates of sublimation presented here might be underestimated (Strasser et al., 2008; Aubry-Wake et al., 2022). Finally, total precipitation amounts were chosen to be left unchanged so that the temperature effect could be isolated. It should be noted that the timing of precipitation and changes of phase can also be notably modified by the dynamics of the monsoon which are relevant to glaciers in the central Himalaya and southeast Tibetan Plateau (e.g., Mölg et al., 2012; Fugger et al., 2022; Shaw et al., 2022). These changes are not the focus here, but their inclusion into such sensitivity experiments and their interaction with the expected temperature projections would be an interesting avenue for future research.

5. Conclusion

The response to warming of the water balance components of three glacierized headwater catchments across distinct climatic regions of High Mountain Asia was studied using a mechanistic model of snow-, glacier- and eco-hydrology. This was done by applying the model in two warming experiments corresponding to SSP2-4.5 (W4.5) and SSP5-8.5 (W8.5), in addition to a baseline experiment representing the climate of the recent past. The study's aim was to understand the streamflow sensitivity to climate warming, while including the response of snow accumulation to precipitation phase shifts, as well as glacier mass balances and changes in vegetation growth and evaporative fluxes. The key findings are:

- Glacier mass balances and glacier meltwater generation in the monsoon-dominated catchments (Langtang and 24K) are more sensitive to warming than the ones of the westerly-dominated Kyzylsu catchment. This is indicated by more negative mass balances, the shifts in accumulation and melt-out-timing and the larger increases in melt rates. Due to the reduction of glacier-protecting snow cover during the ablation season, the period during which glacier ice is exposed directly to the atmosphere extends more at the monsoonal sites than at the westerly site, highlighting the important role of snowfall seasonality in determining glacier mass balance sensitivity to warming. This greater ice exposure causes the majority of additional melting under W8.5 at 24K (76%) and Langtang (55%), and almost half (48%) under W8.5 at Kyzylsu, while the rest of the ice melt increase can be directly attributed to temperature.

- Annual sublimation increases in response to warming at Kyzylsu, decreases in Langtang and is relatively insensitive to warming at 24K, whereby summer sublimation decreases and winter increases partly compensate for each other. Annual changes in either direction do not exceed 11% of the baseline values or 10 mm w.e. (Langtang, W8.5). Increases and decreases in sublimation are mainly controlled by the temperature regime of each individual catchment, rather than the snow cover extent: An increase of sublimation with temperature is observed under predominantly freezing conditions and a decrease under predominantly melting conditions.

- Evapotranspiration increases substantially, ranging annually between +22% in Kyzylsu under W4.5 and +50% in 24K under W8.5. Net primary productivity increases at all three sites with temperature-enhanced photosynthesis, when water is not a limiting factor. The growing season length increases between +9 days in Langtang (W4.5) and +31 days in 24K (W8.5).

- Enhanced evapotranspiration, comparable in magnitude to the ice melt, removes additional water from the catchments via the atmosphere. The balancing between ice melt and evapotranspiration implies an intensification of water transferred through all three catchments, but results in the overall runoff change being relatively insensitive to warming at 24K. Here, the change in water yield does not exceed 1% of the baseline under either W4.5 and W8.5, since a smaller glacier area combines with high precipitation inputs and large increases in evapotranspiration. Out of the three study sites, the annual water yield is most sensitive in Kyzylsu, with increases of up to 14% (W8.5), followed by Langtang with 10% (W8.5), mainly driven by increases in glacier melt which are over-compensating for increases in evapotranspiration.

- The dry-season response of ET and runoff at Kyzylsu however differs from the other seasons and sites: Water-limitations during the driest month prevent an increase in ET and cause a reduction of NPP under warming, while strong melting increases the total runoff during the dry period. This is highlighting the importance of the melt water component in the dry-season runoff from this catchment, which extends into the downstream Amu Darya basin, where precipitation inputs are overall small.

We have shown that simplified assumptions on the hydrological response of glacierized catchments to warming are likely incorrect as they are unable to represent the complex interactions and tradeoffs between the water balance terms. Assuming that ice melt increases will result in runoff increases, for instance, can be too simplistic given the complexity of the high mountain water cycle as we demonstrate here. At all three catchments, major changes in ice melt, snowmelt and evapotranspiration all result in only moderate or no change in total annual runoff. Indeed, we have shown that the role, quantities and timing of snowmelt and ice melting and evapotranspiration are crucial to quantify the trajectory of runoff changes, and more work should be devoted to understanding those elements and their future trajectories in combination with glacier changes. Modeling experiments using mechanistic models, allowing the isolation of the warming effect on the different water-balance components of glacierized headwaters, can deliver important insights into the internal functioning and integrated response of these complex catchment systems.

Acknowledgements
This project has received funding from the European Research Council (ERC) under the European Union's Horizon 2020 research and innovation program Grant Agreements No. 772751 (RAVEN, Rapid mass losses of debris-covered glaciers in High Mountain Asia).

Data availability
Data and analysis code will be made available following a delay. The T&C code is available here: doi.org/10.24433/CO.0905087.v3

References

Aubry-Wake, C. (2022). *From processes to predictions in hydrological modelling of glacierized basins* (Doctoral dissertation, University of Saskatchewan).

Aubry-Wake, C., & Pomeroy, J. W. (2023). Predicting hydrological change in an alpine glacierized basin and its sensitivity to landscape evolution and meteorological forcings. *Water Resources Research*, *59*(9), e2022WR033363.

Berthier, E., Vincent, C., & Six, D. (2023). Exceptional thinning through the entire altitudinal range of Mont-Blanc glaciers during the 2021/22 mass balance year. *Journal of Glaciology*, 1-6.

Berghuijs, W. R., Woods, R. A., & Hrachowitz, M. (2014). A precipitation shift from snow towards rain leads to a decrease in streamflow. *Nature climate change*, *4*(7), 583-586.

Bosson, J.B., Huss, M., Cauvy-Fraunié, S. *et al.* Future emergence of new ecosystems caused by glacial retreat. *Nature* **620**, 562–569 (2023). https://doi.org/10.1038/s41586-023-06302-2

Botter, M., Zeeman, M., Burlando, P., & Fatichi, S. (2021). Impacts of fertilization on grassland productivity and water quality across the European Alps under current and warming climate: insights from a mechanistic model. Biogeosciences, 18(6), 1917-1939.

Bowen, I. S. (1926). The ratio of heat losses by conduction and by evaporation from any water surface. *Physical review*, *27*(6), 779.

Buri, P., Fatichi, S., Shaw, T. E., Miles, E. S., McCarthy, M. J., Fyffe, C. L., ... & Pellicciotti, F. (2023). Land Surface Modeling in the Himalayas: On the Importance of Evaporative Fluxes for the Water Balance of a High-Elevation Catchment. *Water Resources Research*, *59*(10), e2022WR033841.

Chen, J., Xue, X., & Du, W. (2024). Extreme glacier mass loss triggered by high temperature and drought during hydrological year 2022/2023 in Qilian Mountains. *Research in Cold and Arid Regions*.

Compagno, L., Huss, M., Miles, E. S., McCarthy, M. J., Zekollari, H., Dehecq, A., ... & Farinotti, D. (2022). Modelling supraglacial debris-cover evolution from the single-glacier to the regional scale: an application to High Mountain Asia. *The Cryosphere*, *16*(5), 1697-1718.

Cremona, A., Huss, M., Landmann, J. M., Borner, J., & Farinotti, D. (2023). European heat waves 2022: contribution to extreme glacier melt in Switzerland inferred from automated ablation readings. *The Cryosphere*, *17*(5), 1895-1912.

Ding, B., Yang, K., Qin, J., Wang, L., Chen, Y., & He, X. (2014). The dependence of precipitation types on surface elevation and meteorological conditions and its parameterization. *Journal of hydrology*, *513*, 154-163.

Ding, B., Yang, K., Yang, W., He, X., Chen, Y., Lazhu, ... & Yao, T. (2017). Development of a Water and Enthalpy Budget-based Glacier mass balance Model (WEB-GM) and its preliminary validation. *Water Resources Research*, *53*(4), 3146-3178.

Fatichi, S., Ivanov, V. Y., & Caporali, E. (2012). A mechanistic ecohydrological model to investigate complex interactions in cold and warm water-controlled environments: 1. Theoretical framework and plot-scale analysis. *Journal of Advances in Modeling Earth Systems*, *4*(2).

Fatichi, S., Ivanov, V. Y., and Caporali, E. (2012), A mechanistic ecohydrological model to investigate complex interactions in cold and warm water-controlled environments: 2. Spatiotemporal analyses, J. Adv. Model. Earth Syst., 4, M05003,doi:10.1029/2011MS000087.

Fatichi, S., Vivoni, E. R., Ogden, F. L., Ivanov, V. Y., Mirus, B., Gochis, D., ... & Tarboton, D. (2016). An overview of current applications, challenges, and future trends in distributed process-based models in hydrology. *Journal of Hydrology*, *537*, 45-60.

Fatichi, S., Ivanov, V. Y., Paschalis, A., Peleg, N., Molnar, P., Rimkus, S., ... & Caporali, E. (2016). Uncertainty partition challenges the predictability of vital details of climate change. *Earth's Future*, *4*(5), 240-251.

Fatichi S., N. Peleg, T. Mastrotheodoros, C. Pappas, G. Manoli (2021). An ecohydrological journey of 4500 years reveals a stable but threatened precipitation-groundwater recharge relation around Jerusalem. Science Advances, 7 (37), eabe6303, doi:10.1126/sciadv.abe6303

Fugger, S., Fyffe, C. L., Fatichi, S., Miles, E., McCarthy, M., Shaw, T. E., ... & Pellicciotti, F. (2022). Understanding monsoon controls on the energy and mass balance of glaciers in the Central and Eastern Himalaya. *The Cryosphere*, *16*(5), 1631-1652.

Fugger, S., Shaw, T. E., Miles, ES., Jouberton, A., Buri, P., McCarthy, M., Fyffe, CL., Fatichi, S., Kneib, M., Molnar, P. & Pellicciotti, F. (2024). Hydrological regimes and evaporative flux partitioning at the climatic ends of High Mountain Asia. *Environ. Res. Lett.* https://doi.org/10.1088/1748-9326/ad25a0

Gascoin, S. (2023). A call for an accurate presentation of glaciers as water resources. WIREs Water, e1705. https://doi.org/10.1002/wat2.1705

Hugonnet, R., McNabb, R., Berthier, E., Menounos, B., Nuth, C., Girod, L., ... & Kääb, A. (2021). Accelerated global glacier mass loss in the early twenty-first century. *Nature*, 592(7856), 726-731.

Huss, M., Bookhagen, B., Huggel, C., Jacobsen, D., Bradley, R. S., Clague, J. J., ... & Winder, M. (2017). Toward mountains without permanent snow and ice. *Earth's Future*, *5*(5), 418-435.

Huss, M., & Hock, R. (2018). Global-scale hydrological response to future glacier mass loss. *Nature Climate Change*, *8*(2), 135-140.

Immerzeel, W. W., Van Beek, L. P. H., Konz, M., Shrestha, A. B., & Bierkens, M. F. P. (2012). Hydrological response to climate change in a glacierized catchment in the Himalayas. *Climatic change*, *110*, 721-736.

Immerzeel, W. W., Pellicciotti, F., & Bierkens, M. F. P. (2013). Rising river flows throughout the twenty-first century in two Himalayan glacierized watersheds. Nature geoscience, 6(9), 742-745.

Immerzeel, W. W., Lutz, A. F., Andrade, M., Bahl, A., Biemans, H., Bolch, T., ... & Baillie, J. E. M. (2020). Importance and vulnerability of the world's water towers. Nature, 577(7790), 364-369.

Jouberton, A., Shaw, T. E., Miles, E., McCarthy, M., Fugger, S., Ren, S., ... & Pellicciotti, F. (2022). Warming-induced monsoon precipitation phase change intensifies glacier mass loss in the southeastern Tibetan Plateau. *Proceedings of the National Academy of Sciences*, *119*(37), e2109796119.

Kraaijenbrink, P.D.A., Stigter, E.E., Yao, T. *et al.* Climate change decisive for Asia's snow meltwater supply. *Nat. Clim. Chang.* **11**, 591–597 (2021). https://doi.org/10.1038/s41558-021-01074-x

Lee, J.-Y., J. Marotzke, G. Bala, L. Cao, S. Corti, J.P. Dunne, F. Engelbrecht, E. Fischer, J.C. Fyfe, C. Jones, A. Maycock, J. Mutemi, O. Ndiaye, S. Panickal, and T. Zhou, 2021: Future Global Climate: Scenario-Based Projections and Near-Term Information. In Climate Change 2021: The Physical Science Basis. Contribution of Working Group I to the Sixth Assessment Report of the Intergovernmental Panel on Climate Change [Masson-Delmotte, V., P. Zhai, A. Pirani, S.L. Connors, C. Péan, S. Berger, N. Caud, Y. Chen, L. Goldfarb, M.I. Gomis, M. Huang, K. Leitzell, E. Lonnoy, J.B.R. Matthews, T.K. Maycock, T. Waterfield, O. Yelekçi, R. Yu, and B. Zhou (eds.)]. Cambridge University Press, Cambridge, United Kingdom and New York, NY, USA, pp. 553–672, doi:10.1017/9781009157896.006.

Maina, F. Z., Kumar, S. V., Albergel, C., & Mahanama, S. P. (2022). Warming, increase in precipitation, and irrigation enhance greening in High Mountain Asia. *Communications Earth & Environment*, *3*(1), 43.

Manoli G., V. Y. Ivanov, and S. Fatichi (2018). Dry season greening and water stress in Amazonia: the role of modeling leaf phenology. Journal of Geophysical Research-Biogeosciences 123, 1909-1926, doi:10.1029/2017JG004282

Mastrotheodoros, T., Pappas, C., Molnar, P., Burlando, P., Hadjidoukas, P., & Fatichi, S. (2019). Ecohydrological dynamics in the Alps: Insights from a modelling analysis of the spatial variability. *Ecohydrology*, *12*(1), e2054.

Mastrotheodoros, T., Pappas, C., Molnar, P., Burlando, P., Manoli, G., Parajka, J., ... & Fatichi, S. (2020). More green and less blue water in the Alps during warmer summers. *Nature Climate Change*, 10(2), 155-161.

Meili N., J. Beringer, J. Zhao, S. Fatichi (2024). Aerodynamic effects cause higher forest evapotranspiration and water yield reductions after wildfires in tall forests. Global Change Biology, 30, e16995. https://doi.org/10.1111/gcb.16995

Miles, E., McCarthy, M., Dehecq, A., Kneib, M., Fugger, S., & Pellicciotti, F. (2021). Health and sustainability of glaciers in High Mountain Asia. *Nature Communications*, 12(1), 1-10.

Milinski, Sebastian; Marotzke, Jochem (2023). *IPCC AR6 WGI assessed GSAT Projections*. World Data Center for Climate (WDCC) at DKRZ.; accessed on 30.11.2023 via https://interactive-atlas.ipcc.ch/ https://doi.org/10.26050/WDCC/AR6.IPCC-DDC_AR6_Sup_GSATPr

Muñoz-Sabater, J., Dutra, E., Agustí-Panareda, A., Albergel, C., Arduini, G., Balsamo, G., ... & Thépaut, J. N. (2021). ERA5-Land: A state-of-the-art global reanalysis dataset for land applications. Earth System Science Data, 13(9), 4349-4383.

Paschalis A., M. De Kauwe, M. Sabot, S. Fatichi (2024). When do plant hydraulics matter in terrestrial biosphere modelling? Global Change Biology, 30, e17022, https://doi.org/10.1111/gcb.17022

Paschalis A., S. Bonetti, Y. Guo, S. Fatichi (2022). On the Uncertainty Induced by Pedotransfer Functions in Terrestrial Biosphere Modeling. Water Resources Research, 58(9), e2021WR031871, doi:10.1029/2021WR031871

Pohl, E., Gloaguen, R., Andermann, C., & Knoche, M. (2017). Glacier melt buffers river runoff in the Pamir Mountains. Water Resources Research, 53(3), 2467-2489.

Pomeroy, J. W., Brown, T., Fang, X., Shook, K. R., Pradhananga, D., Armstrong, R., ... & Moreno, J. L. (2022). The Cold Regions Hydrological Modelling Platform for hydrological diagnosis and prediction based on process understanding. Journal of Hydrology, 615, 128711.

Pradhananga, N. S., Kayastha, R. B., Bhattarai, B. C., Adhikari, T. R., Pradhan, S. C., Devkota, L. P., ... & Mool, P. K. (2014). Estimation of discharge from Langtang River basin, Rasuwa, Nepal, using a glacio-hydrological model. *Annals of Glaciology*, *55*(66), 223-230.

Pritchard, H. D. (2019). Asia’s shrinking glaciers protect large populations from drought stress. *Nature*, 569(7758), 649-654.

Ragettli, S., Pellicciotti, F., Immerzeel, W. W., Miles, E. S., Petersen, L., Heynen, M., ... & Shrestha, A. (2015). Unraveling the hydrology of a Himalayan catchment through integration of high resolution in situ data and remote sensing with an advanced simulation model. Advances in Water Resources, 78, 94-111.

Ragettli, S., Immerzeel, W. W., & Pellicciotti, F. (2016). Contrasting climate change impact on river flows from high-altitude catchments in the Himalayan and Andes Mountains. *Proceedings of the National Academy of Sciences*, *113*(33), 9222-9227.

Rounce, D. R., Hock, R., Maussion, F., Hugonnet, R., Kochtitzky, W., Huss, M., ... & McNabb, R. W. (2023). Global glacier change in the 21st century: Every increase in temperature matters. *Science*, *379*(6627), 78-83.

Sage, R. F., & Kubien, D. S. (2007). The temperature response of C3 and C4 photosynthesis. *Plant, cell & environment*, *30*(9), 1086-1106.

Saxton, K. E., & Rawls, W. J. (2006). Soil water characteristic estimates by texture and organic matter for hydrologic solutions. *Soil Science Society of America Journal*, 70(5), 1569-1578.

Schmidt, W., 1915: Strahlung und Verdunstung an freien Wasserflachen, ein Beitrag zum Warmehaushalt des Weltmeers und zum Wasserhaushalt der Erde (Radiation and evaporation from an open water surface, a contribution to the heat budget of the world oceans and to the water budget of the earth). Ann.Hydrogr. Mar. Meteor., 43 , 111 - 124

Sexstone, G. A., Clow, D. W., Fassnacht, S. R., Liston, G. E., Hiemstra, C. A., Knowles, J. F., & Penn, C. A. (2018). Snow sublimation in mountain environments and its sensitivity to forest disturbance and climate warming. *Water Resources Research*, *54*(2), 1191-1211.

Stahl, K., Weiler, M., van Tiel, M., Kohn, I., Hänsler, A., Freudiger, D., Seibert, J., Gerlinger, K., Moretti, G. (2022): Impact of climate change on the rain, snow and glacier melt components of streamflow of the river Rhine and its tributaries. CHR report no. I 28. International Commission for the Hydrology of the Rhine basin (CHR), Lelystad.

Steiner, J. F., Gurung, T. R., Joshi, S. P., Koch, I., Saloranta, T., Shea, J., ... & Immerzeel, W. W. (2021). Multi-year observations of the high mountain water cycle in the Langtang catchment, Central Himalaya. Hydrological Processes, 35(5), e14189.

Stigter, E. E., Litt, M., Steiner, J. F., Bonekamp, P. N., Shea, J. M., Bierkens, M. F., & Immerzeel, W. W. (2018). The importance of snow sublimation on a Himalayan glacier. Frontiers in Earth Science, 6, 108.

Strasser, U., Bernhardt, M., Weber, M., Liston, G. E., & Mauser, W. (2008). Is snow sublimation important in the alpine water balance?. The Cryosphere, 2(1), 53-66.

Stull, R. (2006). The atmospheric boundary layer. *Atmospheric science: An introductory survey*, 375-417.

Thornton, J. M., Palazzi, E., Pepin, N. C., Cristofanelli, P., Essery, R., Kotlarski, S., ... & Adler, C. (2021). Toward a definition of essential mountain climate variables. *One Earth*, *4*(6), 805-827.

Viviroli, D., Archer, D. R., Buytaert, W., Fowler, H. J., Greenwood, G. B., Hamlet, A. F., ... & Woods, R. (2011). Climate change and mountain water resources: overview and recommendations for research, management and policy. *Hydrology and Earth System Sciences*, *15*(2), 471-504.

Voordendag, A., Prinz, R., Schuster, L., and Kaser, G.: Brief communication: The Glacier Loss Day as an indicator of a record-breaking negative glacier mass balance in 2022, The Cryosphere, 17, 3661–3665, https://doi.org/10.5194/tc-17-3661-2023, 2023.

Wijngaard, R. R., Steiner, J. F., Kraaijenbrink, P. D., Klug, C., Adhikari, S., Banerjee, A., ... & Immerzeel, W. W. (2019). Modeling the response of the langtang glacier and the hintereisferner to a changing climate since the little ice age. *Frontiers in Earth Science*, *7*, 143.

Yang, Y., Roderick, M. L., Guo, H., Miralles, D. G., Zhang, L., Fatichi, S., ... & Yang, D. (2023). Evapotranspiration on a greening Earth. *Nature Reviews Earth & Environment*, *4*(9), 626-641.

Zhao, C., Yang, W., Miles, E., Westoby, M., Kneib, M., Wang, Y., He, Z., and Pellicciotti, F.: Thinning and surface mass balance patterns of two neighboring debris-covered glaciers in the southeastern Tibetan Plateau, The Cryosphere, 17, 3895–3913, https://doi.org/10.5194/tc-17-3895-2023, 2023.

Xu C, Li H, Wang F, Li Z, Zhou P, Liu S. Heatwaves in summer 2022 forces substantial mass loss for Urumqi Glacier No. 1, China. Journal of Glaciology. Published online 2024:1-7. doi:10.1017/jog.2024.4

The Sensitivity of High Mountain Asian Headwater Catchments to Climate Warming

Supplementary Material

Content:

2 Figures

1 Table

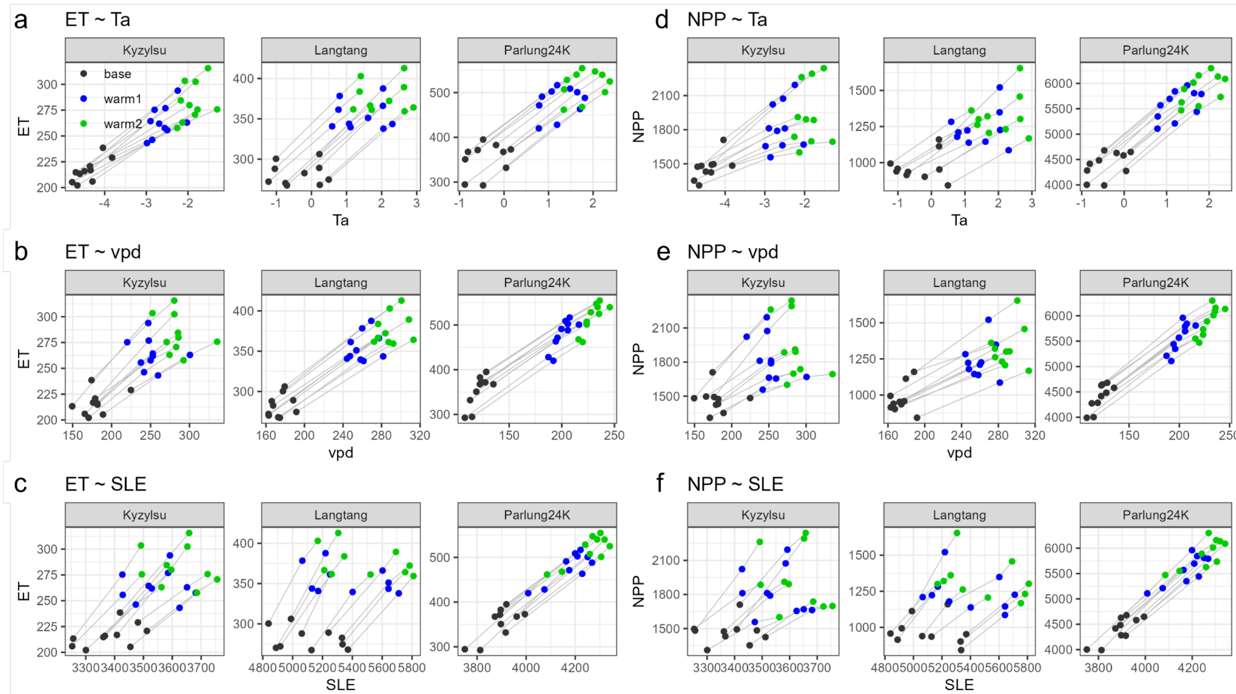

Figure S1. *Scatter plots illustrating the mechanisms behind ET and NPP dynamics; guides connect the same years between experiments; ET - evapotranspiration, Ta - air temperature, NPP - Net primary productivity, SLE - Snow line elevation, vpd - vapor pressure deficit*

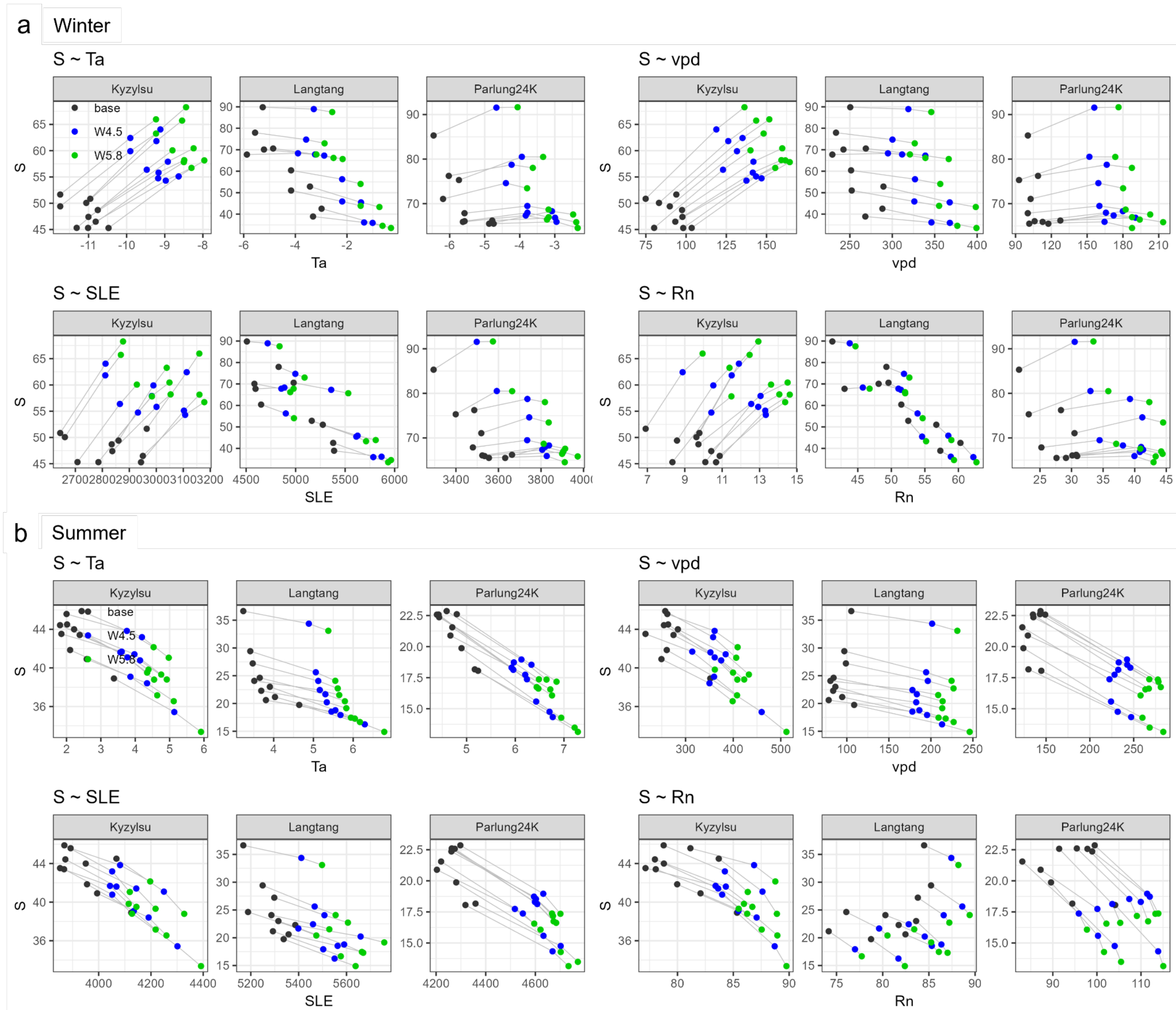

Figure S2. *a) Scatter plots illustrating the mechanisms behind sublimation dynamics in the* ***winter*** *half-year (October 16 - April 15) and b) in the* ***summer*** *half-year (April 16 - October 15); guides connect the same years between experiments; S - sublimation, Ta - air temperature, SLE - Snow line elevation, vpd - vapor pressure deficit, Rn - net radiation*

Table S1. *Average annual model in/outputs in absolute values across sites and experiments. Averages of the entire catchment area. Ta - air temperature, Pr_liq - liquid precipitation, Pr_sno - solid precipitation, L↓ - incoming longwave radiation, Smelt - snowmelt, Imelt - ice melt, Tmelt - total melt (ice + snow melt), SLE - snow line elevation, SWE - snow water equivalent, ET - evapotranspiration, NPP - net primary productivity, S - sublimation, Q - runoff.*

Site		Kyzylsu			Langtang			24K		
Experiment		base	W4.5	W8.5	base	W4.5	W8.5	base	W4.5	W8.5
Variable	*unit*									
Ta	°C	-4.4	-2.6	-1.9	-0.4	1.4	2.0	-0.4	1.3	1.8
Pr_liq	mm	282	332	356	999	1105	1142	1667	2341	2432
Pr_sno	mm	678	629	605	744	637	600	1857	1182	1092
L↓	W m^{-2}	240	246	249	248	255	257	292	300	302
Smelt	mm	474	451	439	594	526	499	1692	1050	970
Imelt	mm	171	249	292	203	339	391	63	114	146
Tmelt	mm	645	700	731	798	866	889	1756	1164	1116
SLE	m asl	3381	3551	3620	5110	5384	5486	3891	4180	4256
SWE	mm w.e.	1019	734	616	572	349	295	788	442	335
ET	mm	216	264	283	281	354	377	335	463	502
NPP	gC m^{-2}	61	76	80	40	51	55	183	232	246
S	mm	91	99	100	87	81	78	92	90	88
Q	mm	719	779	817	1514	1622	1663	3066	3025	3029

6. Synthesis and Conclusion

6.1. Summary of Results

The primary aim of this thesis was to quantify with a physically based model the current water balances of headwater catchments in High Mountain Asia. The investigations focused on the role of the cryosphere and evaporative fluxes in monsoonal and non-monsoonal catchments, and assessed the sensitivity of those elements to global warming with respect to their contributions to runoff.

For this purpose, the snow and glacier schemes of a fully distributed, ecohydrological model were improved in close collaboration with the model developer, including precipitation phase partitioning, ice-melt under debris and the representation of snowpacks.

The model was informed, driven and tested with in-situ observations and gridded data products, including remote sensing datasets. The efficacy of the model to correctly simulate a range of processes related to glaciers and snow packs, vegetation and the integrated runoff response, was demonstrated. For this purpose, primary field data were collected in all three catchments where the fully distributed version of the model was applied. Two of these catchments, Langtang (Nepal) and 24K (Tibet), were already established as reference catchments. The third, Kyzylsu (Tajikistan), was established and instrumented as a new reference catchment in a severely understudied and ungauged region.

The methodology included the application of the model over a period of one decade, at two different spatial scales: (1) at the point-scale location of weather stations installed in the ablation zone of glaciers, for the detailed study of energy and mass balances during the ablation period; (2) at the catchment scale, fully distributed and at the hillslope relevant spatial resolution of 100 m, in order to clarify the role of snow, glaciers and evaporative fluxes in the water balance and runoff generation. The following answers were found to the overarching research questions of the thesis:

RQ1: *How does the monsoon shape the glacier energy and mass balances, and their runoff contributing role in High Mountain Asian headwater catchments?*

This thesis investigated a number of components of the high-mountain water cycle which are strongly shaped by monsoonal conditions, providing a very detailed perspective on glacier energy- and mass balance regimes at the point scale, to a broader perspective on the runoff generation from glaciers and the importance of glacier melt runoff in the catchment-wide water balance.

In particular, it was found that:

- Firn-free clean-ice melt is almost entirely driven by variations in net shortwave radiation during the core monsoon, while increases in incoming longwave radiation due to cloud cover balance out almost entirely with outgoing longwave radiation, and turbulent heat fluxes tend to act melt-enhancing.
- Average melt-rates range from 6 mm d^{-1} at the site with thick debris cover to 43 mm d^{-1} at a site with thin debris cover. The turbulent heat fluxes over debris-covered ice, on the other hand, react to balance out changes in the radiative budget, with the result that there is little to no change in the under-debris ice melt between the pre-monsoon and core-monsoon seasons. The dark surface of thin debris cover together with increases in the turbulent fluxes enhance melting during the monsoon (Chapter 3).
- Sub-debris ice melt accounts for the majority of the total ice melt in the three catchments with distributed applications of T&C, with 66.8, 62.5, 57.9% for Kyzylsu, Langtang and 24K, respectively (Chapter 4), even though debris covers only 38.9, 23.6 and 31% of the glacier area in the three catchments.
- The runoff contribution of ice melt in the monsoonal catchments is smaller with 14% in Langtang and 3% and 24K, compared to 24% in the westerly-controlled Kyzylsu catchment. This is mainly due to the high (Langtang), very high (24K) and very low (Kyzylsu) share of rainfall inputs to the runoff, while relative glacier areas are comparable in Langtang and Kyzylsu with around 21% (smaller in 24K with around 11%) (Chapter 4).

RQ2: *How important are evaporative fluxes in monsoonal and westerly controlled catchments of High Mountain Asia?*

The thesis quantifies the role of evaporative fluxes, comprising all-surface evaporation, transpiration, snow- and ice pack sublimation, in the year-round water budget of headwater catchments in HMA over a period of 10 years.

It was found that:

- Evaporative fluxes together account for 28% (Kyzylsu), 19% (Langtang) and 13% (24K) of water throughput (all water transferred through the catchment), indicating that the relative importance of ET is highest in the driest catchment (Chapter 4).
- In relative terms, ET returns 76, 28 and 19% of rainfall to the atmosphere. Absolute ET fluxes however follow an opposite trend, with highest ET rates of 413 mm yr^{-1} in 24K, followed by 249 mm yr^{-1} in Langtang and 211 mm yr^{-1} in Kyzylsu (Chapter 4).
- Sublimation accounts for 15, 13 and 6 % of snowfalls in the Kyzylsu, Langtang and 24K catchments, respectively. Sublimation is also a greater flux at the driest site, with catchment-averages of 91 mm yr^{-1} in Kyzylsu, followed by 71 mm yr^{-1} in 24K and 57 mm mm yr^{-1} in Langtang (Chapter 4).
- The drying of water from the debris surface induces additional glacier cooling via the latent heat flux, contributing to the melt-reducing effect of debris-cover (Chapter 3).

RQ3: *How sensitive are the water balances of High Mountain Asian headwater catchments to warming in different climatic sub-regions?*

Experimental simulations were used to assess the sensitivity of the three main study sites' cryospheric and evaporative fluxes to climate warming, with respect to the runoff generation. For this purpose, the model was rerun twice for one decade, after adjusting air temperature and temperature related forcing variables, with perturbations representative of mid-century warming levels, which were derived from the SSP2-4.5 (W4.5) and SSP5-8.5 (W5.8) future climate scenarios.

It was found that:

- The changes to runoff overall remain small in the three catchments studied here, with +8% and +7% increases in water yield in Kyzylsu and Langtang, respectively, under W4.5. Runoff starts decreasing only after >30% and >20% has been lost at those two sites under the more extreme experiment (W8.5). Those increases are a result of increases in both ice melt and ET, whereby ET increases offset 60% and 63% of the ice melt increases in the two catchments. In 24K, where the relative glacier area is smaller, ET increases are even 2.6 times higher than the ice melt increases. In a context of very high precipitation inputs there (3500 mm yr^{-1}), the water yield stays almost unchanged (-1%) (Chapter 5).

- The growing season lengthens and ET increases due to warming everywhere, but most pronouncedly so in 24K, with +38% in annual ET, followed by Langtang with +26% (W4.5). Where a recurring dry-gap exists (i.e. very low precipitation, repeated in most years), on the other hand, which is the case during September in Kyzylsu, additional energy inputs do not result in ET increases, and NPP drops. This indicates that the catchment and its vegetation have partly been operating at the water limit, with annual increases in ET (+22%) being somewhat lower compared to the other sites (Chapter 5).
- According to our experiments, snowpack sublimation is relatively insensitive to mid-century warming and can both increase and decrease due to warming. Increases in winter sublimation (Kyzylsu and 24K) and decreases in summer sublimation (all three sites) are a result of the unique temperature regime at each site. Sublimation increases by 8% (or 8 mm yr^{-1}) in Kyzylsu, decreases in Langtang with -7% (or -6 mm yr^{-1}), and stays almost unchanged in 24K, with -4% (or -3 mm yr^{-1}) under W4.5. However, the reductions in snowfall due to shifts in the precipitation phase are around one to two orders of magnitude higher than the changes in sublimation (Chapter 5). Further experimentation and more detailed analysis with respect to the length of the snow-covered season, snow interception and blowing snow sublimation should be conducted in order to understand the sensitivity of sublimation in HMA headwater catchments.

6.2. Implications

The thesis presents a state-of-the art framework for investigative hydrological modelling in glacierized, high-elevation-catchments of High Mountain Asia. In the role of supplying water and energy to major economies like the Central Asian Countries, Nepal, India, Bangladesh and China, these water towers determine economic activity, food production, ecosystem services, and quality of life in major capitals. Enhanced knowledge on the hydrological functioning of upstream watersheds and future changes in water resources is fundamental to economic planning, hazard mitigation and the generation of climate change adaptation strategies (Wester et al., 2019). The thesis advances our knowledge about the functioning of High Mountain Asian headwater catchments in four key areas:

1. In this thesis, we show that *under-debris ice melt* is responsible for > 50% of the meltwater generation from glacier ice in all three study catchments (Chapter 4). This is the first time that the melting of debris-covered glaciers has been modelled with a spatially distributed

representation of debris thicknesses, using an energy-balance model at the catchment-scale over such a long period of time, and across different climates in High Mountain Asia. Moreover, we showed in a detailed energy-balance investigation that debris cover interacts with monsoonal conditions in a way that decouples the glacier's melting from air temperature, thereby attenuating melt rates (Chapter 3). With retreating glaciers, debris cover is also thickening and extending spatially (Bhambri et al., 2011, Stewart et al., 2021), with unknown consequences on runoff. These results imply that future modelling studies should include explicit representations of spatially and temporally varying debris extents and thickness, which account for the seasonally variable insulation effect of thick debris, the additional cooling effect of surface evaporation, as well as for the melt-enhancing effects of thin debris cover.

2. We presented concrete numbers around previously neglected energy and mass fluxes, *evapotranspiration and sublimation, latent and sensible energy* (Chapter 4)*,* including their sensitivity to climate warming (Chapter 5). These numbers highlight the importance of accounting for these fluxes and water sinks in high-mountain hydrology but especially so in dry catchments, where the total water budget is smaller. We showed that, with a higher isotherm in mountain areas, the catchments receive a higher amount of net radiation, which increases vegetation productivity (greening) and evapotranspiration (Chapter 5). However, once soils and interception storages are depleted in water, which is one effect of warming, ET is limited, and might be further limited under continued warming by limits to photosynthesis and assimilation, and possibly by a limit to the CO_2 fertilisation effect (Botter et al., 2023). Since ET and sublimation together account for up to 28% of the mass outputs of high-elevation catchments (Chapter 4), and since they respond in non-linear ways to temperature increases (Chapter 5), they should not be neglected or oversimplified in hydrological studies from catchment- to global scales.

3. We were able to *quantify compensatory effects of runoff generation*, by analysing all relevant mass balance terms of the high-mountain water cycle under warming, including evaporative fluxes. We showed, to our knowledge for the first time in HMA headwater catchments, that ET increases in particular can amount to similar magnitudes as the ice melt increases, while the two terms have opposite signs in the water balance, resulting in only small, or no changes in the catchment runoff response (Chapter 5). This insight invalidates future projections of catchment runoff maxima due to 'imbalance' glacier melt (e.g. Huss and Hock, 2018), which do not account for changes in evaporative fluxes, even in small, heavily glacierized catchments, and especially in dry places, where meltwater runoff is known to be the dominant runoff contribution (Chapter 5). Extending the catchments downstream, ET increases, given enough water available, could quickly overpower the meltwater increase, and, together with highly uncertain future changes in precipitation and moisture recycling, temporally shift or erase signals of "peak water" altogether. For updated predictions of future basin-scale water resources, the results of this thesis therefore imply that transient and large-scale simulations should include physically-based methods to account for all relevant water balance terms and processes in the runoff generation.

In addition to enabling these new insights, the presented simulations shall serve as benchmark simulations and stimulate further research. They provide the potential scientific basis for developing basin-scale models for future projections of water resources under climate change.
In the following outlook chapter, avenues for further research and model developments are outlined.

6.3. Outlook

While many research questions remain open related to the study of high-elevation and cold-region catchment science, some of them of fundamental nature, this outlook aims to address questions around where the modelling approach presented here, and similar approaches could deliver additional insights and answers. Guided by the question of which adaptations are needed in hydrological models to enable extrapolations to larger scales and changing climatic conditions (Question 19 of 23 unsolved problems in hydrology; Blöschl et al., 2019), further knowledge gaps and possible model developments for process-based models are outlined in the following.

6.3.1. Groundwater

Runoff production in mountain catchments is mediated by the recharge-, storage- and release-dynamics of *groundwater,* delaying e.g. the drainage of snowmelt by recharging aquifers that were depleted over winter (Chapter 4, Cochand et al., 2019). While the depth of hillslope soils and regoliths tend to be thinner than those of flatter areas, the alluvial deposits of wide, previously glacierized valley bottoms as well as moraines and talus can contain substantial aquifers (Somers et al., 2020). Bedrock can be highly permeable, draining ice-covered areas and hillslopes very efficiently. Karstic carbonates especially can be interspersed with fractures and faults, or almost impermeable such as unfractured crystallines, forcing water through the hillslope soil and regolith or to resurface. Topography-derived catchment outlines do not necessarily agree with the subsurface water-divides in natural landscapes and groundwater can bypass gauged outlets, resurfacing far away from the topography-derived catchment area (Wilson et al., 2004). In T&C, snowmelt is included in a realistic way due to the physically-based representation of snowpack accumulation and melt processes. Water released from the snowpack is allowed to infiltrate into the soil matrix and rock fractures at the grid cell level, being drained to the streams lower down in the catchment. Near-surface soil water can re-evaporate when the snow is gone and can be passed to the atmosphere via root water uptake and plant-transpiration. Similarly, glacier melt water is passed in a delayed way to the underlying bedrock via a liquid water storage of the ice pack. While glacier melt can also recharge groundwater instead of entirely contributing to surface water (Vincent et al., 2019, Lone et al., 2021), the extent to which snow and glaciers recharge groundwater in the three modelled catchments has not been analysed in this thesis, due to the poorly known properties of the subsurface. This choice was justified since the main focus of the chapters has not been on the downstream hydrograph, but on the overall water balances and role of cryospheric meltwater and evaporative fluxes. T&C or similar models could be extended to become fully coupled and internally consistent representations of cryosphere-, eco- and subsurface-hydrology. With the wide range of detailed and physically meaningful outputs, such models could quantify, for example, the role of groundwater dynamics in the runoff generation in high-mountain environments (Thornton et al., 2022), or how groundwater tables and low-flow will evolve with climate in (semi-) arid regions (Question 3 of 23 unsolved problems in hydrology; Blöschl et al., 2019), and how vegetation and evapotranspiration will respond to future soil moisture and groundwater regimes.

Improvements to the model could include layer-varying soil properties such as grain size distribution and hydraulic conductivity, parameterizations of preferential flow and spatially variable rock-fracturing based on geological maps. These improvements would however need to be informed and evaluated by additional (time-consuming and non-trivial) observations and expert surveys, such as geological characterization and geophysical observations, systematic streamflow gauging and groundwater table measurements, transit time measurements and hydrograph analysis.

6.3.2. Permafrost

New flow paths through previously frozen soils can open for groundwater recharge, due to permafrost thaw under climate warming. *Mountain permafrost and rock glaciers* are poorly constrained storage components in the high-mountain water budget and have to date been neglected in the vast majority of hydrological studies. The active layer above permafrost can act as a shallow, perched aquifer with the thawing front depth controlling water storage and drainage dynamics, while the underlying frozen layer prevents the deep percolation of water (Walvoord et al., 2016). The hydrological implications of widespread, observed permafrost degradation including an increasing depth of the active layer (Smith et al., 2022) remain speculative, especially in High Mountain Asia, where the distribution, volumes, water contents and hydraulic properties of permafrost are largely unknown, despite its areal extent being estimated at greater than that of glaciers in most HMA countries (Gruber et al., 2017; Barandun et al., 2020). The model applied in this thesis can technically be used to simulate the freezing and thawing of soil water. However, realistic simulations would require better constraints on soil thicknesses, hydraulic properties, a-priori assumptions of the three-dimensional permafrost distribution as initial condition or very long spin-up times (several decades to 100s of years) in order for permafrost layers to develop in realistic ways (Wheater et al., 2022). Informed by geophysical observation (Mathys et al., 2022), process-based hydrological models could provide highly sought-after answers to the combined role of permafrost and glacier melt in the runoff generation from cold regions at present and under continued climate warming (Blöschl et al., 2019; Krogh and Pomeroy, 2021; Gao et al., 2021).

6.3.3. Glacier cooling effect

The meteorological conditions above glacier surfaces differ from those of the surrounding, non-glacierized areas. Higher sensible heat flux towards the cold glacier surface cause the so-called *glacier cooling effect* (Greuell et al., 1998), with the associated air density changes causing a downward-advection of air masses, typically called katabatic winds (Ayala et al., 2015; Shaw et al., 2021). The colder katabatic boundary layer can reduce glacier ablation but also increase turbulence (Shaw et al., 2023, 2024). This effect has also been observed to extend beyond the glaciers and into large glacierized valley systems, potentially shifting convective precipitation patterns and has potentially stabilising effects on other temperature-sensitive elements of the periglacial environment, such as the conditions of permafrost and vegetation (Salerno et al., 2023). In T&C, feedbacks of the land surface on the atmospheric boundary layer are to date not included, so the cooling effect has not been implemented in a mechanistic way. In Chapter 2, the glacier cooling effect was however implicit in the forcing dataset which came from on-glacier

AWSs (Chapter 3). To account for the glacier cooling effect in a simplified way, when not implicit in the forcing (Chapter 4 and 5), a space-time-constant cooling offset of 1°C based on Shaw et al. (2022) was introduced above clean ice glacier areas and areas with very thin debris, while on sections with thick debris, where the katabatic glacier boundary layer does not develop in the same way (Shaw et al., 2016; Nicholson and Stiperski, 2020), the air temperature was left unmodified. In reality, there is space-time-variability in the temperature modifications across glaciers, as well as differences in the cooling effect due to the glacier's exposure to synoptic winds (Conway et al., 2021; Shaw et al., 2023, 2024).

A physically based and distributed inclusion of glacier-atmosphere interactions into a model like T&C could be used to investigate how important glacier cooling and katabatic winds are for future mass balances, and whether there will be non-linear responses in the valley thermal regimes to the shrinking of glaciers (Shaw et al., 2023).

Potential ways to account for the glacier cooling effect could include an adjustment of distributed forcing input using a parameterization based on dynamic glacier length and size, air temperature and humidity and glacier- or valley-exposure to synoptic winds. Extending the influence of katabatic winds to the periglacial environments, forcing data could be generated using dynamic atmospheric downscaling (e.g. WRF), allowing for surface-atmosphere feedbacks (Potter et al., 2018). This would however come at substantial computational costs, and would be limited both spatially and temporally. Accounting also for land cover changes such as glacier retreat and greening, a target to aim towards in model development would be a partial or full coupling of an atmospheric and an ecohydrological model, potentially involving statistical methods/deep learning to reduce computational costs (Section 6.3.8).

6.3.4. Blowing snow processes

Wind can substantially affect the spatial variability of the snowpack by either transporting snow grains from one location to another, or by sublimating the snow during its transport (Schmidt et al., 1982; Pomeroy, 1991). The importance of these blowing snow processes differ according to the spatial scale considered and climatic settings, and blowing snow sublimation estimates range from 0.1% of cumulative snowfall at an Alpine site (Zwaaftink et al. 2013) to as much as 19% in the Canadian Rockies (MacDonald et al., 2010). Recent efforts were reported in the literature where blowing snow processes were represented without dramatically increasing the computational costs (Marsh et al., 2020), allowing for an extension of the domain size in which these processes can be simulated (Vionnet al., 2021). Model developments in the framework of this thesis prioritised the improvement of the snowpack accumulation and vertical discretization, while the gravitational snow redistribution has been previously implemented following the widely used SnowSlide scheme (Bernhardt and Schulz, 2010). Including blowing snow processes would be another worthwhile addition. The meteorological forcing fields obtained from statistical-empirical downscaling were deemed of sufficient quality to reproduce the main components of the catchment water balance, but the quality of the generated wind fields, on which the estimates of blowing snow transport and sublimation strongly depend (Musselman et al., 2015; Vionnet et al., 2017), bias-corrected using one or few local station observations, might require further improvement. The generation of high-resolution wind fields, formerly generated by computationally costly atmospheric models, can now also be done using large-scale tools like Windmapper (Marsh et al., 2023), or even more efficient machine learning based approaches (e.g. Le Tourmelin et al. 2023, Reynolds et al. 2023). Starting from the newly implemented two-layer snowpack, blowing snow transport could be implemented based on the prairie blowing snow model (Pomeroy et al., 1993), or the computationally efficient finite volume blowing snow model (Marsh et al., 2020). Alternatively and to assess the importance of blowing snow processes in HMA catchments, for which to date no simulations exist, the scheme of Vionnet et. al (2018) could be used 'offline' in T&C.

6.3.5. Light-absorbing particles

Light-absorbing particles (LAPs) from anthropogenic and non-anthropogenic sources, deposited on snow and ice, alter the energy balance and result in faster snow- and glacier melt as shown by modelling and observations globally (Gabbi et al., 2015; Sarangi et al., 2020; Aubry-Wake et al., 2022; Réveiller et al., 2022; Cordero et al., 2022; Bonilla et al., 2023). In Kyzylsu, dust storms occur multiple times every year, depositing substantial amounts of dust on snow and glaciers, but the effect of these deposits on the surface energy balance could not be quantified here, due to a lack of dedicated measurements. The currently included albedo-parameterizations do not include a mechanism to account for the darkening quality of dust and other LAPs. For improved modelling of snow and glacier mass-balances, additional parameters representative of this darkening should be included and locally optimised, e.g. against remote sensing observations (Bertoncini et al., 2022), or local albedo measurements.

6.3.6. Observations

Model simulations involving the cryosphere are highly sensitive to the *precipitation input* and *phase*. However, precipitation remains the most challenging variable to measure in cold, high-elevation areas (Thornton et al., 2021; Pritchard et al., 2021). Pluviometers measuring total precipitation, including supplementary measurements for undercatch correction (e.g. Masuda et al., 2019) and automatic snow depth observations are valuable sources of information, as demonstrated here. These measurements should be maintained as long as possible and extended to other locations. Unfortunately, very few monitoring sites in High Mountain Asia feature even one such setup, and even fewer catchments feature several of them (e.g. Steiner et al., 2021a).

Most of our quantitative knowledge of *sublimation* in high mountain environments stems from modelling, but only very few observational studies exist (e.g. Reba et al., 2014; Stigter et al., 2018, Sextone et al., 2018). Sublimation from snow packs can be measured using eddy covariance systems, aerodynamic profile measurements, energy balance and Bowen ratio calculations and the bulk aerodynamic flux method (Sexstone et al., 2016). Eddy-covariance systems might be the most robust, but also most expensive, energy-consuming and data-intensive method. Aerodynamic profiles might be a more practicable option to derive sublimation via the turbulent heat fluxes in remote, high-elevation catchments, Since they only require automatic measurements of surface temperature, relative humidity, wind speed and air temperature at different heights above the ground (Box et al., 2001). Due to their relative simplicity, these measurements could be made in several different locations and across elevations within a catchment, to capture some degree of spatial variability. This approach was however shown to be associated with higher uncertainties in mountain terrain (Helgason and Pomeroy, 2005). Measurements should especially target semi-arid or arid regions and high elevations, where sublimation could be the main mass loss process (Ayala et al., 2017; Fyffe et al., 2021).

Measuring *discharge* operationally in highly dynamic streambeds typical for snow- and-glacier-fed streams is notoriously difficult using water-level logging, since rating curves break down with modifications to the stream's cross section. Level sensors installed inside or on the banks of streams are frequently destroyed or removed by flooding. The utility of remote sensors for inferring water surface velocities, such as radar flow sensors and ultrasonic flow metres or image-based methods should be tested towards this end (Tauro et al., 2018).

6.3.7. The challenge of upscaling in space and time

To address highly relevant water resources questions - such as whether the hydrological cycle is accelerating at large with climate and environmental change (Blöschl et al., 2019; Wang et al., 2023), or how large the mass loss of ice and snow due to sublimation from mountain ranges under a future climate will be (Gascoin et al., 2021), larger domains and longer timescales than modelled here need to be targeted. However, upscaling process-based models while maintaining physical consistency by avoiding extensive calibration is challenging for two reasons.

First, a major obstacle is reflected in the fact that demands on meteorological forcing availability and quality increase with model complexity, for the model to perform well (e.g. Grayson and Blöschl, 2001). While improving the input data quality comes with the advantage of (compensatory) error reduction in the modelling, it often involves substantial processing of diverse data sets for forcing and evaluation of the model. As an example, determining a representative spatial distribution of meteorological data, such as temperature and precipitation requires distributed local observations, proxy observations from space or dynamical downscaling with high-resolution atmospheric models, and ideally all of these sources of information combined, as done in this work. Due to limitations around site accessibility and visibility from space, and the high computational demand of dynamical downscaling, such an approach is currently limited to small spatial domains. Forcing such models with unadjusted reanalysis data will likely be biassed to an extent outside of the acceptable uncertainty range for studying hydrological processes. Assimilating remotely sensed information into the adjustment of forcing data, e.g. snow cover (Alonso-González et al., 2022) and inverse modelling, leveraging glacier mass balance and runoff observations (Immerzeel et al., 2015), might represent ways forward.

Second, many hydrological processes scale nonlinearly in space and time due to a variety of factors related to the physical characteristics of the Earth's surface and subsurface. These factors include spatial heterogeneity of landscapes and land cover types (Gao et al., 2018), complex feedbacks between multiple and simultaneously happening processes (Pimm, 1984), scale-dependent process dynamics (Vivoni et al., 2007) and threshold effects (Zehe and Sivapalan, 2009). Nonlinear responses are likely to be missed when applying simplified models at low resolutions over large spatial scales, which have not been built based on understanding of small-scale complexity (Clark et al., 2015), especially in mountain environments (Fan et al., 2019). In addition to the constraints on forcing data quality as summarised above, the application of process-based hydrological models is spatially and temporally limited due to computational constraints. T&C solves many equations numerically during each timestep, and timesteps have to be processed sequentially, due to the lateral routing of mass between cells (Fatichi et al., 2012). As an example, one full model run for a glacierized catchment with an area smaller than 580 km^2 (Langtang) for one decade plus spin-up time at 100m spatial resolution took around $7*10^4$ CPU hours (Chapter 3, Table S2), which is here considered the upper end of a manageable run. In this instance, when the model was run on a high-performance-computing cluster, the computational efficiency reached an optimum at about 80 CPUs. An application of the model at a similar spatiotemporal resolution to larger domains, without splitting into a high number of sub-catchments while sacrificing the integrated runoff response (Mastrotheodoros et al., 2020), therefore seems out of scope. A crucial challenge lies in scaling up the process understanding acquired through physically-based investigations at the local scale to river basin scales. Several avenues to accomplish this are emerging:

The *structures of model codes* could be improved in order to reduce processing overheads where parallel computing is used. Ideally, codes could be streamlined to such that they can be processed on graphical processing units (GPUs), which would potentially speed up processing time by orders of magnitude.

The introduction of *triangulated irregular networks* (TINs) instead of constant-resolution rasters, could reduce processing time by up to 90% in mountain areas (Ivanov et al., 2004; Vivoni et al., 2004; Marsh et al., 2020). These networks have a variable resolution and can be adapted to the model domain's complexity, such that the resolution is higher over mountain terrain than over flat areas, using topographic descriptors like the wetness index (Ivanov et al., 2004). Challenges however remain with the lateral routing of water through these networks (Marsh et al., 2020).

Upscaling in the conventional sense, which includes the *development of sub-grid parameterizations* for coarser-resolution, or variable-grid earth system models, has to start from process understanding, which is at the centre of this research. It needs to be understood at high spatial and temporal resolution, which processes matter most, are prone to nonlinear scaling, and require better representation across scales (Wijngaard et al., 2023). The sensitivity of large-scale outcomes to changes in small-scale processes can then be ingested into the development of new, or the refinement of existing, parameterizations for the larger-scale models. Some related challenges and potential ways in this direction are outlined in Wheater et al. (2022).

Deep-learning algorithms could aid mechanistic modelling at different levels of integration. As an example for a hybrid integration (Reichstein et al., 2019, Wei et al., 2023), a difficult-to-constrain physical parameter, such as aerodynamic roughness, could be learned by combining the ice melt output of the physical model with high resolution terrain-models of a glacier surface (Brock et al., 2006; Miles et al., 2017). A computationally expensive subroutine of a process-based model, such as the iterative solving of heat transfer through soil layers, could be learned by a neural network. This surrogate routine could replace the iterative solver of the physical module, with the latter ensuring physical consistency and closure of the energy balance. Since this is a routine repeated countless times under a wide range of conditions, preparing a training dataset encompassing the whole range of plausible states should not be a limitation.

The input-output response of a mechanistic model or parts of it, e.g. a certain set of output variables of interest, could be learned by 'model emulators'. However, it is unlikely that sufficient training data, being highly model-specific, will be available anytime soon. The main advantages of a mechanistic model, i.e. internal model consistency and transparency, as well as the closure of energy and mass balances would be lost with such a fully statistical approach. Such a model would also be unlikely to generate a robust response outside of the conditions it has been trained for and would therefore not serve as a virtual laboratory of the hydrological response of catchments to climate change and extreme events.

Curriculum Vitae

Personal Information

Date of Birth: October 10, 1988

Nationality: Austrian

Email: stefan.fugger@gmail.com

ORCID: 0000-0002-4659-4209

Github: mountainhydro

Education

March 2019 – May 2024:

Swiss Federal Institute of Technology (ETH), Zürich, Switzerland

Institute of Environmental Engineering

Doctorate in Alpine Hydrology

Title of thesis: *The Hydrology of High Mountain Asian Headwater Catchments via Mechanistic Modelling*

Oct 2014 – Sep 2018

University of Natural Resources and Life Sciences (BOKU), Vienna, Austria

Dipl.-Ing. Water Management and Environmental Engineering

Title of Thesis (at TU Delft): *Snow cover in the Greater Alpine Region (2000-2017): regional patterns, controls and change*

Passed with distinction

March 2010 – Oct 2014

University of Natural Resources and Life Sciences (BOKU), Vienna, Austria

BSc Water Management and Environmental Engineering

Thesis in collaboration with IRPI Perugia: *Geotechnical characterization of Soils in the Collazzone area*

Sep 2003 – Jun 2008

Higher Technical Education Institute (HTBLA2), Linz, Austria

Mechanical Engineering

Passed with distinction

Employment

Aug 2023 – May 2024

Institute of Science and Technology (ISTA), Klosterneuburg, Austria

Division: Cryosphere and Mountain Hydrosphere

Position: Visiting Pre-doctoral Scientist

Mar 2019 – Jul 2023

Swiss Federal Research Institute for Forest, Snow and Landscape Research

Division: Mountain Hydrology and Mass Movements

Position: Doctoral Candidate

Feb 2017 – Mar 2019

Self-employed Arborist in Vienna, Austria and Oslo, Norway

Oct 2015 – Jul 2016

University of Natural Resources and Life Sciences (BOKU), Vienna, Austria

Teaching Assistant Geology

Jun 2014 – Jun 2016

Kreitl e.U., Vienna, Austria

Training and Position as Arborist

Supervision

Feb 2023 – Mar 2024

Pascal Wyss, University of Zürich

Master Thesis: *Downscaling of future meteorology for land-surface modelling in the glacierized Amu Darya headwaters*

Mar 2022 – Dez 2022
Yuwei Lyu, ETH Zürich
Master Thesis: *Re-evaluating gradients of temperature and precipitation for hydrological modelling in a glacierized catchment of the Nepalese Himalaya*

Oct 2021 – Mar 2022
Gioele Piatti, ETH Zürich
Master Thesis: *Point scale modelling of evapotranspiration and latent heat fluxes in the Maipo basin during the Chilean megadrought*

Bibliography

Fugger, S., Shaw, T. E., Jouberton, A., Miles, E. S., Buri, P., McCarthy, M. J., ... & Pellicciotti, F. (2024). Hydrological regimes and evaporative flux partitioning at the climatic ends of High Mountain Asia. *Environmental Research Letters*.

Fugger, S., Fyffe, C. L., Fatichi, S., Miles, E., McCarthy, M., Shaw, T. E., ... & Pellicciotti, F. (2022). Understanding monsoon controls on the energy and mass balance of glaciers in the Central and Eastern Himalaya. *The Cryosphere*, *16*(5), 1631-1652.

Fugger, S. (2018). Snow cover in the Greater Alpine Region (2000-2017): Regional Patterns, Controls and Change. Master Thesis. BOKU University of Natural Resources and Life Sciences Vienna, TU Delft (available at: https://abstracts.boku.ac.at/download.php?dataset_id=18983&property_id=107)

Buri, P., Fatichi, S., Shaw, T. E., Miles, E. S., McCarthy, M. J., Fyffe, C. L., ... & Pellicciotti, F. (2023). Land Surface Modeling in the Himalayas: On the Importance of Evaporative Fluxes for the Water Balance of a High-Elevation Catchment. *Water Resources Research*, *59*(10), e2022WR033841.

Shaw, T. E., Miles, E. S., Chen, D., Jouberton, A., Kneib, M., Fugger, S., ... & Pellicciotti, F. (2022). Multi-decadal monsoon characteristics and glacier response in High Mountain Asia. *Environmental Research Letters*, *17*(10), 104001.

Jouberton, A., Shaw, T. E., Miles, E., McCarthy, M., Fugger, S., Ren, S., ... & Pellicciotti, F. (2022). Warming-induced monsoon precipitation phase change intensifies glacier mass loss in the southeastern Tibetan Plateau. *Proceedings of the National Academy of Sciences*, *119*(37), e2109796119.

Kneib, M., Miles, E. S., Buri, P., Fugger, S., McCarthy, M., Shaw, T. E., ... & Pellicciotti, F. (2022). Sub-seasonal variability of supraglacial ice cliff melt rates and associated processes from time-lapse photogrammetry. *The Cryosphere*, *16*(11), 4701-4725.

Fyffe, C. L., Potter, E., Fugger, S., Orr, A., Fatichi, S., Loarte, E., ... & Pellicciotti, F. (2021). The energy and mass balance of Peruvian glaciers. *Journal of Geophysical Research: Atmospheres*, *126*(23), e2021JD034911.

Miles, E., McCarthy, M., Dehecq, A., Kneib, M., Fugger, S., & Pellicciotti, F. (2021). Health and sustainability of glaciers in High Mountain Asia. *Nature Communications*, *12*(1), 2868.

Kneib, M., Miles, E. S., Buri, P., Molnar, P., McCarthy, M., Fugger, S., & Pellicciotti, F. (2021). Interannual dynamics of ice cliff populations on debris-covered glaciers from remote sensing observations and stochastic modeling. *Journal of Geophysical Research: Earth Surface*, *126*(10), e2021JF006179.

Menenti, M., Li, X., Jia, L., Yang, K., Pellicciotti, F., Mancini, M., ... & Paolini, G. (2021). Multi-Source Hydrological Data Products to Monitor High Asian River Basins and Regional Water Security. *Remote Sensing*, *13*(24), 5122.

References

Alonso-González, E., Aalstad, K., Baba, M. W., Revuelto, J., López-Moreno, J. I., Fiddes, J., ... & Gascoin, S. (2022). The Multiple Snow Data Assimilation System (MuSA v1. 0). *Geoscientific Model Development*, *15*(24), 9127-9155.

Andreadis, K. M., Storck, P., & Lettenmaier, D. P. (2009). Modeling snow accumulation and ablation processes in forested environments. *Water resources research*, *45*(5).

Aubry-Wake, C., & Pomeroy, J. W. (2023). Predicting hydrological change in an alpine glacierized basin and its sensitivity to landscape evolution and meteorological forcings. *Water Resources Research*, *59*(9), e2022WR033363.

Aubry-Wake, C., Bertoncini, A., & Pomeroy, J. W. (2022). Fire and ice: The impact of wildfire-affected albedo and irradiance on glacier melt. *Earth's Future*, *10*(4), e2022EF002685.

Aubry-Wake, C., Pradhananga, D., & Pomeroy, J. W. (2022). Hydrological process controls on streamflow variability in a glacierized headwater basin. *Hydrological Processes*, *36*(10), e14731.

Ayala, Á., Farías-Barahona, D., Huss, M., Pellicciotti, F., McPhee, J., & Farinotti, D. (2019). Glacier runoff variations since 1955 in the Maipo River Basin, semiarid Andes of central Chile.

Ayala, A., Pellicciotti, F., & Shea, J. M. (2015). Modeling 2 m air temperatures over mountain glaciers: Exploring the influence of katabatic cooling and external warming. *Journal of Geophysical Research: Atmospheres*, *120*(8), 3139-3157.

Ayala, A., Pellicciotti, F., Peleg, N., & Burlando, P. (2017). Melt and surface sublimation across a glacier in a dry environment: distributed energy-balance modelling of Juncal Norte Glacier, Chile. *Journal of Glaciology*, *63*(241), 803-822.

Azam, M. F., Kargel, J. S., Shea, J. M., Nepal, S., Haritashya, U. K., Srivastava, S., ... & Bahuguna, I. (2021). Glaciohydrology of the himalaya-karakoram. *Science*, *373*(6557), eabf3668.

Azam, M. F., Wagnon, P., Vincent, C., Ramanathan, A. L., Favier, V., Mandal, A., & Pottakkal, J. G. (2014). Processes governing the mass balance of Chhota Shigri Glacier (western Himalaya, India) assessed by point-scale surface energy balance measurements. *The Cryosphere*, *8*(6), 2195-2217.

Baker, D. G., D. L. Ruschy, and D. B. Wall (1990), The albedo decay of prairie snows, J. Appl. Meteorol., 29(2), 179–187.

Barandun, M., & Pohl, E. (2022). Central Asia's spatiotemporal glacier response ambiguity due to data inconsistencies and regional simplifications. *The Cryosphere Discussions*, *2022*, 1-34.

Barandun, M., Fiddes, J., Scherler, M., Mathys, T., Saks, T., Petrakov, D., & Hoelzle, M. (2020). The state and future of the cryosphere in Central Asia. *Water Security*, *11*, 100072.

Bernhardt, M., & Schulz, K. (2010). SnowSlide: A simple routine for calculating gravitational snow transport. *Geophysical Research Letters*, *37*(11).

Bertoncini, A., Aubry-Wake, C., & Pomeroy, J. W. (2022). Large-area high spatial resolution albedo retrievals from remote sensing for use in assessing the impact of wildfire soot deposition on high mountain snow and ice melt. Remote Sensing of Environment, 278, 113101.

Bhambri, R., Bolch, T., Chaujar, R. K., & Kulshreshtha, S. C. (2011). Glacier changes in the Garhwal Himalaya, India, from 1968 to 2006 based on remote sensing. *Journal of Glaciology*, *57*(203), 543-556.

Blöschl, G., Bierkens, M. F., Chambel, A., Cudennec, C., Destouni, G., Fiori, A., ... & Renner, M. (2019). Twenty-three unsolved problems in hydrology (UPH)–a community perspective. *Hydrological sciences journal*, *64*(10), 1141-1158.

Bolch, T., Kulkarni, A., Kääb, A., Huggel, C., Paul, F., Cogley, J. G., ... & Stoffel, M. (2012). The state and fate of Himalayan glaciers. *Science*, *336*(6079), 310-314.

Bonekamp, P. N., De Kok, R. J., Collier, E., & Immerzeel, W. W. (2019). Contrasting meteorological drivers of the glacier mass balance between the Karakoram and central Himalaya. *Frontiers in Earth Science*, *7*, 107.

Bonekamp, P. N. J., Collier, E., & Immerzeel, W. W. (2018). The impact of spatial resolution, land use, and spinup time on resolving spatial precipitation patterns in the Himalayas. *Journal of Hydrometeorology*, *19*(10), 1565-1581.

Bonilla, E. X., Mickley, L. J., Beaudon, E. G., Thompson, L. G., Rodriguez, W. E., Encarnación, R. C., ... & Ginot, P. (2023). Contribution of biomass burning to black carbon deposition on Andean glaciers: consequences for radiative forcing. *Environmental Research Letters*, *18*(2), 024031.

Bookhagen, B., & Burbank, D. W. (2006). Topography, relief, and TRMM-derived rainfall variations along the Himalaya. *Geophysical Research Letters*, *33*(8).

Bookhagen, B., & Burbank, D. W. (2010). Toward a complete Himalayan hydrological budget: Spatiotemporal distribution of snowmelt and rainfall and their impact on river discharge. *Journal of Geophysical Research: Earth Surface*, *115*(F3).

Boos, W. R., & Kuang, Z. (2010). Dominant control of the South Asian monsoon by orographic insulation versus plateau heating. *Nature*, *463*(7278), 218-222.

Bosson, J. B., Huss, M., Cauvy-Fraunié, S., Clément, J. C., Costes, G., Fischer, M., ... & Arthaud, F. (2023). Future emergence of new ecosystems caused by glacial retreat. *Nature*, *620*(7974), 562-569.

Botter, M., Zeeman, M., Burlando, P., & Fatichi, S. (2021). Impacts of fertilization on grassland productivity and water quality across the European Alps under current and warming climate: insights from a mechanistic model. Biogeosciences, 18(6), 1917-1939.

Box, J. E., & Steffen, K. (2001). Sublimation on the Greenland ice sheet from automated weather station observations. *Journal of Geophysical Research: Atmospheres*, *106*(D24), 33965-33981.

Brock, B. W., Mihalcea, C., Kirkbride, M. P., Diolaiuti, G., Cutler, M. E., & Smiraglia, C. (2010). Meteorology and surface energy fluxes in the 2005–2007 ablation seasons at the Miage debris-covered glacier, Mont Blanc Massif, Italian Alps. *Journal of geophysical research: atmospheres*, *115*(D9).

Brock, B. W., Willis, I. C., & Sharp, M. J. (2000b). Measurement and parameterization of albedo variations at Haut Glacier d'Arolla, Switzerland. *Journal of Glaciology*, *46*(155), 675-688.

Brock, B. W., Willis, I. C., & Sharp, M. J. (2006). Measurement and parameterization of aerodynamic roughness length variations at Haut Glacier d'Arolla, Switzerland. *Journal of Glaciology*, *52*(177), 281-297.

Brock, B. W., Willis, I. C., Sharp, M. J., & Arnold, N. S. (2000a). Modelling seasonal and spatial variations in the surface energy balance of Haut Glacier d'Arolla, Switzerland. *Annals of Glaciology*, *31*, 53-62.

Brun, F., Berthier, E., Wagnon, P., Kääb, A., & Treichler, D. (2017). A spatially resolved estimate of High Mountain Asia glacier mass balances from 2000 to 2016. *Nature geoscience*, *10*(9), 668-673.

Buchhorn, M., Smets, B., Bertels, L., De Roo, B., Lesiv, M., Tsendbazar, N. E., ... & Fritz, S. (2020). Copernicus global land service: land cover 100 m: collection 3: epoch 2019: Globe.https://doi.org/10.5281/zenodo.3939050

Burger, F., Ayala, A., Farias, D., Shaw, T. E., MacDonell, S., Brock, B., ... & Pellicciotti, F. (2019). Interannual variability in glacier contribution to runoff from a high-elevation Andean catchment: understanding the role of debris cover in glacier hydrology. *Hydrological Processes*, *33*(2), 214-229.

Buri, P., Fatichi, S., Shaw, T. E., Miles, E. S., McCarthy, M. J., Fyffe, C. L., ... & Pellicciotti, F. (2023). Land Surface Modeling in the Himalayas: On the Importance of Evaporative Fluxes for the Water Balance of a High-Elevation Catchment. *Water Resources Research*, *59*(10), e2022WR033841.

Burlando, M., Carassale, L., Georgieva, E., Ratto, C. F., & Solari, G. (2007). A simple and efficient procedure for the numerical simulation of wind fields in complex terrain. Boundary-layer meteorology, 125, 417-439.

Carenzo, M., Pellicciotti, F., Mabillard, J., Reid, T., & Brock, B. W. (2016). An enhanced temperature index model for debris-covered glaciers accounting for thickness effect. *Advances in Water Resources*, *94*, 457-469.

Cauvy-Fraunié, S., & Dangles, O. (2019). A global synthesis of biodiversity responses to glacier retreat. *Nature Ecology & Evolution*, *3*(12), 1675-1685.

Clark, M. P., Fan, Y., Lawrence, D. M., Adam, J. C., Bolster, D., Gochis, D. J., ... & Zeng, X. (2015). Improving the representation of hydrologic processes in Earth System Models. *Water Resources Research*, *51*(8), 5929-5956.

Cochand, M., Christe, P., Ornstein, P., & Hunkeler, D. (2019). Groundwater storage in high alpine catchments and its contribution to streamflow. *Water Resources Research*, *55*(4), 2613-2630.

Cogley, J. G., Kargel, J. S., Kaser, G., & van der Veen, C. J. (2010). Tracking the source of glacier misinformation. *Science*, *327*(5965), 522-522.

Collier, E., Maussion, F., Nicholson, L. I., Mölg, T., Immerzeel, W. W., & Bush, A. B. G. (2015). Impact of debris cover on glacier ablation and atmosphere–glacier feedbacks in the Karakoram. The Cryosphere, 9(4), 1617-1632.

Collier, E., Nicholson, L. I., Brock, B. W., Maussion, F., Essery, R., & Bush, A. B. G. (2014). Representing moisture fluxes and phase changes in glacier debris cover using a reservoir approach. *The Cryosphere*, *8*(4), 1429-1444.

Collins, D. N. (2008). Climatic warming, glacier recession and runoff from Alpine basins after the Little Ice Age maximum. *Annals of Glaciology*, *48*, 119-124.

Conway, J. P., Helgason, W. D., Pomeroy, J. W., & Sicart, J. E. (2021). Icefield breezes: mesoscale diurnal circulation in the atmospheric boundary layer over an outlet of the Columbia Icefield, Canadian Rockies. Journal of Geophysical Research: Atmospheres, 126(6), e2020JD034225.

Cordero, R. R., Sepúlveda, E., Feron, S., Wang, C., Damiani, A., Fernandoy, F., ... & Casassa, G. (2022). Black carbon in the Southern Andean snowpack. *Environmental Research Letters*, *17*(4), 044042.

Dehecq, A., Gourmelen, N., Gardner, A. S., Brun, F., Goldberg, D., Nienow, P. W., ... & Trouvé, E. (2019). Twenty-first century glacier slowdown driven by mass loss in High Mountain Asia. *Nature Geoscience*, *12*(1), 22-27.

Ding, B., Yang, K., Qin, J., Wang, L., Chen, Y., & He, X. (2014). The dependence of precipitation types on surface elevation and meteorological conditions and its parameterization. *Journal of hydrology*, *513*, 154-163.

Ding, B., Yang, K., Yang, W., He, X., Chen, Y., Lazhu, ... & Yao, T. (2017). Development of a Water and Enthalpy Budget-based Glacier mass balance Model (WEB-GM) and its preliminary validation. *Water Resources Research*, *53*(4), 3146-3178.

Dussaillant, I., Berthier, E., Brun, F., Masiokas, M., Hugonnet, R., Favier, V., ... & Ruiz, L. (2019). Two decades of glacier mass loss along the Andes. *Nature Geoscience*, *12*(10), 802-808.

Düthmann, D. (2015). *Hydrological modeling of mountain catchments in Central Asia: approaches for data sparse catchments* (Doctoral dissertation, Universität Potsdam).

Edwards, T. L., Nowicki, S., Marzeion, B., Hock, R., Goelzer, H., Seroussi, H., ... & Zwinger, T. (2021). Projected land ice contributions to twenty-first-century sea level rise. *Nature*, *593*(7857), 74-82.

Engelhardt, M., Ramanathan, A. L., Eidhammer, T., Kumar, P., Landgren, O., Mandal, A., & Rasmussen, R. O. Y. (2017). Modelling 60 years of glacier mass balance and runoff for Chhota Shigri Glacier, Western Himalaya, Northern India. *Journal of Glaciology*, *63*(240), 618-628.

Fan, Y., Clark, M., Lawrence, D. M., Swenson, S., Band, L. E., Brantley, S. L., ... & Yamazaki, D. (2019). Hillslope hydrology in global change research and earth system modeling. *Water Resources Research*, *55*(2), 1737-1772.

Farinotti, D., Huss, M., Fürst, J. J., Landmann, J., Machguth, H., Maussion, F., & Pandit, A. (2019). A consensus estimate for the ice thickness distribution of all glaciers on Earth. *Nature Geoscience*, *12*(3), 168-173.

Fatichi, S., Ivanov, V. Y., and Caporali, E. (2012), A mechanistic ecohydrological model to investigate complex interactions in cold and warm water-controlled environments: 2. Spatiotemporal analyses, J. Adv. Model. Earth Syst., 4, M05003,doi:10.1029/2011MS000087

Fatichi, S., Vivoni, E. R., Ogden, F. L., Ivanov, V. Y., Mirus, B., Gochis, D., ... & Tarboton, D. (2016). An overview of current applications, challenges, and future trends in distributed process-based models in hydrology. *Journal of Hydrology*, *537*, 45-60.

Fatichi S., N. Peleg, T. Mastrotheodoros, C. Pappas, G. Manoli (2021). An ecohydrological journey of 4500 years reveals a stable but threatened precipitation-groundwater recharge relation around Jerusalem. Science Advances, 7 (37), eabe6303, doi:10.1126/sciadv.abe6303

Fiddes, J., & Gruber, S. (2014). TopoSCALE v. 1.0: downscaling gridded climate data in complex terrain. *Geoscientific Model Development*, *7*(1), 387-405.

Fiddes, J., Aalstad, K., & Lehning, M. (2022). TopoCLIM: rapid topography-based downscaling of regional climate model output in complex terrain v1. 1. *Geoscientific Model Development*, *15*(4), 1753-1768.

Finger, D., Vis, M., Huss, M., & Seibert, J. (2015). The value of multiple data set calibration versus model complexity for improving the performance of hydrological models in mountain catchments. Water Resources Research, 51, 1939–1958. https://doi.org/10.1002/2015WR017200.A

Flanner, M. G. (2007). *Effects of Vertically-Resolved Solar Heating, Snow Aging, and Black Carbon on Snow-Albedo Feedback DISSERTATION* (Doctoral dissertation, University of California, Irvine).

Fujita, K., & Ageta, Y. (2000). Effect of summer accumulation on glacier mass balance on the Tibetan Plateau revealed by mass-balance model. *Journal of Glaciology*, *46*(153), 244-252.

Fyffe, C. L., Potter, E., Fugger, S., Orr, A., Fatichi, S., Loarte, E., ... & Pellicciotti, F. (2021). The energy and mass balance of Peruvian glaciers. *Journal of Geophysical Research: Atmospheres*, *126*(23), e2021JD034911.

Fyffe, C. L., Reid, T. D., Brock, B. W., Kirkbride, M. P., Diolaiuti, G., Smiraglia, C., & Diotri, F. (2014). A distributed energy-balance melt model of an alpine debris-covered glacier. *Journal of Glaciology*, *60*(221), 587-602.

Fyffe, C. L., Woodget, A. S., Kirkbride, M. P., Deline, P., Westoby, M. J., & Brock, B. W. (2020). Processes at the margins of supraglacial debris cover: Quantifying dirty ice ablation and debris redistribution. Earth Surface Processes and Landforms, 45(10), 2272-2290.

Gabbi, J., Huss, M., Bauder, A., Cao, F., and Schwikowski, M.: (2015). The impact of Saharan dust and black carbon on albedo and long-term mass balance of an Alpine glacier, The Cryosphere, 9, 1385–1400, https://doi.org/10.5194/tc-9-1385-2015

Gao, H., Sabo, J. L., Chen, X., Liu, Z., Yang, Z., Ren, Z., & Liu, M. (2018). Landscape heterogeneity and hydrological processes: a review of landscape-based hydrological models. *Landscape ecology*, *33*, 1461-1480.

Gao, H., Wang, J., Yang, Y., Pan, X., Ding, Y., & Duan, Z. (2021). Permafrost hydrology of the Qinghai-Tibet Plateau: A review of processes and modeling. *Frontiers in Earth Science*, *8*, 576838.

Gardelle, J., Berthier, E., Arnaud, Y., & Kääb, A. (2013). Region-wide glacier mass balances over the Pamir-Karakoram-Himalaya during 1999–2011. *The Cryosphere*, *7*(4), 1263-1286.

Gascoin, S. (2021). Snowmelt and snow sublimation in the Indus Basin. *Water*, *13*(19), 2621.

Girona-Mata, M., Miles, E. S., Ragettli, S., & Pellicciotti, F. (2019). High-resolution snowline delineation from Landsat imagery to infer snow cover controls in a Himalayan catchment. *Water Resources Research*, *55*(8), 6754-6772.

Grayson, R., & Blöschl, G. (2001). Spatial modelling of catchment dynamics. *Spatial patterns in catchment hydrology: observations and modelling*, 51-81.

Greuell, W., & Böhm, R. (1998). 2 m temperatures along melting mid-latitude glaciers, and implications for the sensitivity of the mass balance to variations in temperature. *Journal of Glaciology*, *44*(146), 9-20.

Groot Zwaaftink, C. D., Mott, R., & Lehning, M. (2013). Seasonal simulation of drifting snow sublimation in Alpine terrain. *Water Resources Research*, *49*(3), 1581-1590.

Gruber, S., Fleiner, R., Guegan, E., Panday, P., Schmid, M. O., Stumm, D., ... & Zhao, L. (2017). Inferring permafrost and permafrost thaw in the mountains of the Hindu Kush Himalaya region. *The Cryosphere*, *11*(1), 81-99.

Hanus, S., Schuster, L., Burek, P., Maussion, F., Wada, Y., & Viviroli, D. (2024). Coupling a large-scale glacier and hydrological model (OGGM v1. 5.3 and CWatM V1. 08)–Towards an improved representation of mountain water resources in global assessments. *EGUsphere*, *2024*, 1-31.

Herreid, S., & Pellicciotti, F. (2020). The state of rock debris covering Earth's glaciers. *Nature Geoscience*, *13*(9), 621-627.

Hewitt, K. (2005). The Karakoram anomaly? Glacier expansion and the elevation effect,'Karakoram Himalaya. *Mountain Research and Development*, 332-340.

Higuchi, K. E. I. J. I., Ageta, Y. U. T. A. K. A., Yasunari, T. E. T. S. U. Z. O., & Inoue, J. I. R. O. (1982). Characteristics of precipitation during the monsoon season in high-mountain areas of the Nepal Himalaya. *IAHS Publ*, *138*, 21-30.

Hock, R., G. Rasul, C. Adler, B. Cáceres, S. Gruber, Y. Hirabayashi, M. Jackson, A. Kääb, S. Kang, S. Kutuzov, Al. Milner, U. Molau, S. Morin, B. Orlove, and H. Steltzer, 2019: High Mountain Areas. In: IPCC Special Report on the Ocean and Cryosphere in Changing Climate [H.-O. Pörtner, D.C. Roberts, V. Masson-Delmotte, P. Zhai, M. Tignor, E. Poloczanska, K. Mintenbeck, A. Alegría, M. Nicolai, A. Okem, J. Petzold, B. Rama, N.M. Weyer (eds.)]. Cambridge University Press, Cambridge, UK and New York, NY, USA, pp. 131–202. https://doi.org/10.1017/9781009157964.004.

Hock, R. (2003). Temperature index melt modelling in mountain areas. Journal of Hydrology, 282(1–4), 104–115. https://doi.org/10.1016/S0022-1694(03)00257-9

Hoelzle, M., Azisov, E., Barandun, M., Huss, M., Farinotti, D., Gafurov, A., ... & Zemp, M. (2017). Re-establishing glacier monitoring in Kyrgyzstan and Uzbekistan, Central Asia. *Geoscientific Instrumentation, Methods and Data Systems*, *6*(2), 397-418.

Huang, L., Hock, R., Li, X., Bolch, T., Yang, K., Wang, N., ... & Li, Z. (2022). Winter accumulation drives the spatial variations in glacier mass balance in High Mountain Asia. *Science Bulletin*, *67*(19), 1967-1970.

Hugonnet, R., McNabb, R., Berthier, E., Menounos, B., Nuth, C., Girod, L., ... & Kääb, A. (2021). Accelerated global glacier mass loss in the early twenty-first century. *Nature*, *592*(7856), 726-731.

Huss, M., & Hock, R. (2018). Global-scale hydrological response to future glacier mass loss. *Nature Climate Change*, *8*(2), 135-140.

Huss, M., Bookhagen, B., Huggel, C., Jacobsen, D., Bradley, R. S., Clague, J. J., ... & Winder, M. (2017). Toward mountains without permanent snow and ice. *Earth's Future*, *5*(5), 418-435.

Immerzeel, W. W., Lutz, A. F., Andrade, M., Bahl, A., Biemans, H., Bolch, T., ... & Baillie, J. E. M. (2020). Importance and vulnerability of the world's water towers. *Nature*, *577*(7790), 364-369.

Immerzeel, W. W., Pellicciotti, F., & Bierkens, M. F. P. (2013). Rising river flows throughout the twenty-first century in two Himalayan glacierized watersheds. *Nature geoscience*, *6*(9), 742-745.

Immerzeel, W. W., Petersen, L., Ragettli, S., & Pellicciotti, F. (2014). The importance of observed gradients of air temperature and precipitation for modeling runoff from a glacierized watershed in the Nepalese Himalayas. *Water Resources Research*, *50*(3), 2212-2226.

Immerzeel, W. W., Van Beek, L. P. H., Konz, M., Shrestha, A. B., & Bierkens, M. F. P. (2012). Hydrological response to climate change in a glacierized catchment in the Himalayas. *Climatic change*, *110*, 721-736.

Immerzeel, W. W., Wanders, N., Lutz, A. F., Shea, J. M., & Bierkens, M. F. P. (2015). Reconciling high-altitude precipitation in the upper Indus basin with glacier mass balances and runoff. *Hydrology and Earth System Sciences*, *19*(11), 4673-4687.

Jakob Themeßl, M., Gobiet, A., & Leuprecht, A. (2011). Empirical-statistical downscaling and error correction of daily precipitation from regional climate models. *International Journal of Climatology*, *31*(10), 1530-1544.

Ji, H., Fang, G., Yang, J., & Chen, Y. (2019). Multi-objective calibration of a distributed hydrological model in a highly glacierized watershed in Central Asia. *Water*, *11*(3), 554.

Jouberton, A., Shaw, T. E., Miles, E., McCarthy, M., Fugger, S., Ren, S., ... & Pellicciotti, F. (2022). Warming-induced monsoon precipitation phase change intensifies glacier mass loss in the southeastern Tibetan Plateau. *Proceedings of the National Academy of Sciences*, *119*(37), e2109796119.

Kaser, G., Großhauser, M., & Marzeion, B. (2010). Contribution potential of glaciers to water availability in different climate regimes. *Proceedings of the National Academy of Sciences*, *107*(47), 20223-20227.

Khadka, D., Babel, M. S., Shrestha, S., & Tripathi, N. K. (2014). Climate change impact on glacier and snow melt and runoff in Tamakoshi basin in the Hindu Kush Himalayan (HKH) region. Journal of Hydrology, 511, 49–60. https://doi.org/10.1016/j.jhydrol.2014.01.005

Khanal, S., Lutz, A. F., Kraaijenbrink, P. D., van den Hurk, B., Yao, T., & Immerzeel, W. W. (2021). Variable 21st century climate change response for rivers in High Mountain Asia at seasonal to decadal time scales. *Water Resources Research*, *57*(5), e2020WR029266.

Kirschbaum, D., Kapnick, S. B., Stanley, T., & Pascale, S. (2020). Changes in extreme precipitation and landslides over High Mountain Asia. *Geophysical Research Letters*, *47*(4), e2019GL085347.

Klok, E. J., & Oerlemans, J. (2004). Modelled climate sensitivity of the mass balance of Morteratschgletscher and its dependence on albedo parameterization. *International Journal of Climatology: A Journal of the Royal Meteorological Society*, *24*(2), 231-245.

Kneib, M., Miles, E. S., Buri, P., Fugger, S., McCarthy, M., Shaw, T. E., ... & Pellicciotti, F. (2022). Sub-seasonal variability of supraglacial ice cliff melt rates and associated processes from time-lapse photogrammetry. *The Cryosphere*, *16*(11), 4701-4725.

Kraaijenbrink, P. D., Bierkens, M. F., Lutz, A. F., & Immerzeel, W. W. (2017). Impact of a global temperature rise of 1.5 degrees Celsius on Asia's glaciers. *Nature*, *549*(7671), 257-260.

Kraaijenbrink, P.D.A., Stigter, E.E., Yao, T. et al. Climate change decisive for Asia's snow meltwater supply. Nat. Clim. Chang. 11, 591–597 (2021).

Krogh, S. A., & Pomeroy, J. W. (2021). Simulating site-scale permafrost hydrology: Sensitivity to modelling decisions and air temperature. Journal of Hydrology, 602, 126771.

Lalande, M., Ménégoz, M., Krinner, G., Naegeli, K., & Wunderle, S. (2021). Climate change in the High Mountain Asia in CMIP6. Earth system dynamics, 12(4), 1061-1098.

Lee, J. Y., Marotzke, J., Bala, G., Cao, L., Corti, S., Dunne, J. P., ... & Zhou, T. (2021). Future global climate: scenario-based projections and near-term information. In *Climate change 2021: The physical science basis. Contribution of working group I to the sixth assessment report of the intergovernmental panel on climate change* (pp. 553-672). Cambridge University Press.

Le Toumelin, L., Gouttevin, I., Helbig, N., Galiez, C., Roux, M., & Karbou, F. (2023). Emulating the Adaptation of Wind Fields to Complex Terrain with Deep Learning. *Artificial Intelligence for the Earth Systems*, *2*(1), e220034.

Lone, S. A., Jeelani, G., Deshpande, R. D., Mukherjee, A., Jasechko, S., & Lone, A. (2021). Meltwaters dominate groundwater recharge in cold arid desert of Upper Indus River Basin (UIRB), western Himalayas. *Science of the Total Environment*, *786*, 147514.

Lutz, A. F., Immerzeel, W. W., Kraaijenbrink, P. D., Shrestha, A. B., & Bierkens, M. F. (2016). Climate change impacts on the upper Indus hydrology: sources, shifts and extremes. *PloS one*, *11*(11), e0165630.

Lutz, A. F., Immerzeel, W. W., Shrestha, A. B., & Bierkens, M. F. P. (2014). Consistent increase in High Asia's runoff due to increasing glacier melt and precipitation. *Nature Climate Change*, *4*(7), 587-592.

MacDonald, M. K., Pomeroy, J. W., & Pietroniro, A. (2010). On the importance of sublimation to an alpine snow mass balance in the Canadian Rocky Mountains. *Hydrology and Earth System Sciences*, *14*(7), 1401-1415.

Machguth, H., Paul, F., Kotlarski, S., & Hoelzle, M. (2009). Calculating distributed glacier mass balance for the Swiss Alps from regional climate model output: A methodical description and interpretation of the results. *Journal of Geophysical Research: Atmospheres*, *114*(D19).

Mandal, A., Angchuk, T., Azam, M. F., Ramanathan, A., Wagnon, P., Soheb, M., & Singh, C. (2022). An 11-year record of wintertime snow-surface energy balance and sublimation at 4863 m asl on the Chhota Shigri Glacier moraine (western Himalaya, India). *The Cryosphere*, *16*(9), 3775-3799.

Manoli G., V. Y. Ivanov, and S. Fatichi (2018). Dry season greening and water stress in Amazonia: the role of modeling leaf phenology. Journal of Geophysical Research-Biogeosciences 123, 1909-1926, doi:10.1029/2017JG004282

Marks, D., Kimball, J., Tingey, D., & Link, T. (1998). The sensitivity of snowmelt processes to climate conditions and forest cover during rain-on-snow: A case study of the 1996 Pacific Northwest flood. *Hydrological Processes*, *12*(10-11), 1569-1587.

Marks, D., & Winstral, A. (2001). Comparison of snow deposition, the snow cover energy balance, and snowmelt at two sites in a semiarid mountain basin. Journal of Hydrometeorology, 2(3), 213-227.

Marsh, C. B., Pomeroy, J. W., Spiteri, R. J., & Wheater, H. S. (2020). A finite volume blowing snow model for use with variable resolution meshes. *Water Resources Research*, *56*(2), e2019WR025307.

Marsh, C. B., Vionnet, V., & Pomeroy, J. W. (2023). Windmapper: An efficient wind downscaling method for hydrological models. Water Resources Research, 59(3), e2022WR032683.

Mastrotheodoros, T., Pappas, C., Molnar, P., Burlando, P., Manoli, G., Parajka, J., ... & Fatichi, S. (2020). More green and less blue water in the Alps during warmer summers. *Nature* Climate Change, 10(2), 155-161.

Masuda, M., Yatagai, A., Kamiguchi, K., & Tanaka, K. (2019). Daily adjustment for wind-induced precipitation undercatch of daily gridded precipitation in Japan. Earth and Space Science, 6(8), 1469-1479.

Mathys, T., Hilbich, C., Arenson, L. U., Wainstein, P. A., & Hauck, C. (2022). Towards accurate quantification of ice content in permafrost of the Central Andes–Part 2: An upscaling strategy of geophysical measurements to the catchment scale at two study sites. *The Cryosphere*, *16*(6), 2595-2615.

Matthews, T., Perry, L. B., Koch, I., Aryal, D., Khadka, A., Shrestha, D., ... & Mayewski, P. A. (2020). Going to extremes: installing the world’s highest weather stations on Mount Everest. *Bulletin of the American Meteorological Society*, *101*(11), E1870-E1890.

Maussion, F., Scherer, D., Mölg, T., Collier, E., Curio, J., & Finkelnburg, R. (2014). Precipitation seasonality and variability over the Tibetan Plateau as resolved by the High Asia Reanalysis. *Journal of Climate*, *27*(5), 1910-1927.

McCarthy, M., Miles, E., Kneib, M., Buri, P., Fugger, S., & Pellicciotti, F. (2022). Supraglacial debris thickness and supply rate in High-Mountain Asia. *Communications Earth & Environment*, *3*(1), 269.

Meili N., J. Beringer, J. Zhao, S. Fatichi (2024). Aerodynamic effects cause higher forest evapotranspiration and water yield reductions after wildfires in tall forests. Global Change Biology, 30, e16995. https://doi.org/10.1111/gcb.16995

Meyer, J., Kohn, I., Stahl, K., Hakala, K., Seibert, J., & Cannon, A. J. (2019). Effects of univariate and multivariate bias correction on hydrological impact projections in alpine catchments. *Hydrology and Earth System Sciences*, *23*(3), 1339-1354.

Miles, E., McCarthy, M., Dehecq, A., Kneib, M., Fugger, S., & Pellicciotti, F. (2021). Health and sustainability of glaciers in High Mountain Asia. *Nature Communications*, *12*(1), 2868.

Miles, E. S., Steiner, J. F., & Brun, F. (2017). Highly variable aerodynamic roughness length (z0) for a hummocky debris-covered glacier. *Journal of Geophysical Research: Atmospheres*, *122*(16), 8447-8466.

Miles, E. S., Steiner, J. F., Buri, P., Immerzeel, W. W., & Pellicciotti, F. (2022). Controls on the relative melt rates of debris-covered glacier surfaces. *Environmental Research Letters*, *17*(6), 064004.

Millan, R., Mouginot, J., Rabatel, A., & Morlighem, M. (2022). Ice velocity and thickness of the world's glaciers. *Nature Geoscience*, *15*(2), 124-129.

Mimeau, L., Esteves, M., Zin, I., Jacobi, H. W., Brun, F., Wagnon, P., ... & Arnaud, Y. (2019). Quantification of different flow components in a high-altitude glacierized catchment (Dudh Koshi, Himalaya): some cryospheric-related issues. *Hydrology and Earth System Sciences*, *23*(9), 3969-3996.

Mölg, T., Maussion, F., & Scherer, D. (2014). Mid-latitude westerlies as a driver of glacier variability in monsoonal High Asia. *Nature Climate Change*, *4*(1), 68-73.

Mölg, T., Maussion, F., Yang, W., & Scherer, D. (2012). The footprint of Asian monsoon dynamics in the mass and energy balance of a Tibetan glacier. *The Cryosphere*, *6*(6), 1445-1461.

Muñoz-Sabater, J., Dutra, E., Agustí-Panareda, A., Albergel, C., Arduini, G., Balsamo, G., ... & Thépaut, J. N. (2021). ERA5-Land: A state-of-the-art global reanalysis dataset for land applications. Earth System Science Data, 13(9), 4349-4383.

Musselman, K. N., Pomeroy, J. W., Essery, R. L., & Leroux, N. (2015). Impact of windflow calculations on simulations of alpine snow accumulation, redistribution and ablation. *Hydrological Processes*, *29*(18), 3983-3999.

Myneni, R., Knyazikhin, Y., Park, T. (2015). MCD15A3H MODIS/Terra+Aqua Leaf Area Index/FPAR 4-day L4 Global 500m SIN Grid V006. NASA EOSDIS Land Processes DAAC. Accessed March 30, 2023 from https://doi.org/10.5067/MODIS/MCD15A3H.006. Accessed March 30, 2023.

Myneni, R., Knyazkhin, Y. (2018). VIIRS/NPP Leaf Area Index/FPAR 8-Day L4 Global 500m SIN Grid V001 [Data set]. NASA EOSDIS Land Processes DAAC. doi: 10.5067/VIIRS/VNP15A2H.001. Accessed March 30, 2023

Naz, B. S., Frans, C. D., Clarke, G. K. C., Burns, P., and Lettenmaier,D. P.: Modeling the effect of glacier recession on streamflow response using a coupled glacio-hydrological model, Hydrol. Earth Syst. Sci., 18, 787–802, https://doi.org/10.5194/hess-18-787-2014, 2014.

Naegeli, K., & Huss, M. (2017). Sensitivity of mountain glacier mass balance to changes in bare-ice albedo. *Annals of Glaciology*, *58*(75pt2), 119-129.

Nicholson, L., & Benn, D. I. (2013). Properties of natural supraglacial debris in relation to modelling sub-debris ice ablation. *Earth Surface Processes and Landforms*, *38*(5), 490-501.

Nicholson, L., & Stiperski, I. (2020). Comparison of turbulent structures and energy fluxes over exposed and debris-covered glacier ice. *Journal of Glaciology*, *66*(258), 543-555.

Nie, Y., Pritchard, H. D., Liu, Q., Hennig, T., Wang, W., Wang, X., ... & Chen, X. (2021). Glacial change and hydrological implications in the Himalaya and Karakoram. *Nature reviews earth & environment*, *2*(2), 91-106.

Notarnicola, C. (2020). Hotspots of snow cover changes in global mountain regions over 2000–2018. *Remote Sensing of Environment*, *243*, 111781.

Oke, T. R. (2002). *Boundary layer climates*. Routledge.

Oreskes, N. (1998). Evaluation (not validation) of quantitative models. *Environmental health perspectives*, *106*(suppl 6), 1453-1460.

Orr, A., Listowski, C., Couttet, M., Collier, E., Immerzeel, W., Deb, P., & Bannister, D. (2017). Sensitivity of simulated summer monsoonal precipitation in Langtang Valley, Himalaya, to cloud microphysics schemes in WRF. *Journal of Geophysical Research: Atmospheres*, *122*(12), 6298-6318.

Östrem, G. (1959). Ice melting under a thin layer of moraine, and the existence of ice cores in moraine ridges. *Geografiska Annaler*, *41*(4), 228-230.

Paschalis A., M. De Kauwe, M. Sabot, S. Fatichi (2024). When do plant hydraulics matter in terrestrial biosphere modelling? Global Change Biology, 30, e17022, https://doi.org/10.1111/gcb.17022

Paschalis A., S. Bonetti, Y. Guo, S. Fatichi (2022). On the Uncertainty Induced by Pedotransfer Functions in Terrestrial Biosphere Modeling. Water Resources Research, 58(9), e2021WR031871, doi:10.1029/2021WR031871

Pellicciotti, F., Brock, B., Strasser, U., Burlando, P., Funk, M., & Corripio, J. (2005). An enhanced temperature-index glacier melt model including the shortwave radiation balance: development and testing for Haut Glacier d'Arolla, Switzerland. *Journal of Glaciology*, *51*(175), 573-587.

Pellicciotti, F., Buergi, C., Immerzeel, W. W., Konz, M., & Shrestha, A. B. (2012). Challenges and uncertainties in hydrological modeling of remote Hindu Kush–Karakoram–Himalayan (HKH) basins: suggestions for calibration strategies. *Mountain Research and Development*, *32*(1), 39-50.

Pellicciotti, F., Helbing, J., Rivera, A., Favier, V., Corripio, J., Araos, J., ... & Carenzo, M. (2008). A study of the energy balance and melt regime on Juncal Norte Glacier, semi-arid Andes of central Chile, using melt models of different complexity. *Hydrological Processes*, *22*(19), 3980-3997.

Pellicciotti, F., Stephan, C., Miles, E., Herreid, S., Immerzeel, W. W., & Bolch, T. (2015). Mass-balance changes of the debris-covered glaciers in the Langtang Himal, Nepal, from 1974 to 1999. *Journal of Glaciology*, *61*(226), 373-386.

Pepin, N. C., Arnone, E., Gobiet, A., Haslinger, K., Kotlarski, S., Notarnicola, C., ... & Adler, C. (2022). Climate changes and their elevational patterns in the mountains of the world. *Reviews of Geophysics*, *60*(1), e2020RG000730.

Petzold, D. E. (1977), An estimation technique for snow surface albedo, Climatol. Bull. McGill Univ., 21, 1–11.

Pfeffer, W. T., Arendt, A. A., Bliss, A., Bolch, T., Cogley, J. G., Gardner, A. S., ... & Randolph Consortium. (2014). The Randolph Glacier Inventory: a globally complete inventory of glaciers. *Journal of glaciology*, *60*(221), 537-552.

Pimm, S.L., 1984. The complexity and stability of ecosystems. Nature 307 (5949),

Poggio, L., de Sousa, L. M., Batjes, N. H., Heuvelink, G. B. M., Kempen, B., Ribeiro, E., and Rossiter, D.: SoilGrids 2.0: producing soil information for the globe with quantified spatial uncertainty, SOIL, 7, 217–240, https://doi.org/10.5194/soil-7-217-2021, 2021.

Pomeroy, J. W. (1991). Transport and sublimation of snow in wind-scoured alpine terrain. Snow, Hydrology and Forests in Alpine Areas, edited by: Bergman, H., Lang, H., Frey, W., Issler, D., and Salm, B., IAHS Press, 205, 131-140.

Pomeroy, J. W., Brown, T., Fang, X., Shook, K. R., Pradhananga, D., Armstrong, R., ... & Moreno, J. L. (2022). The cold regions hydrological modelling platform for hydrological diagnosis and prediction based on process understanding. *Journal of Hydrology*, *615*, 128711.

Potter, E. R., Orr, A., Willis, I. C., Bannister, D., & Salerno, F. (2018). Dynamical drivers of the local wind regime in a Himalayan valley. *Journal of Geophysical Research: Atmospheres*, *123*(23), 13-186.

Pradhananga, D., & Pomeroy, J. W. (2022). Diagnosing changes in glacier hydrology from physical principles using a hydrological model with snow redistribution, sublimation, firnification and energy balance ablation algorithms. Journal of Hydrology, 608, 127545.

Pritchard, H. D. (2019). Asia’s shrinking glaciers protect large populations from drought stress. *Nature*, *569*(7758), 649-654.

Pritchard, H. D. (2021). Global data gaps in our knowledge of the terrestrial cryosphere. *Frontiers in Climate*, *3*, 689823.

Ragettli, S., & Pellicciotti, F. (2012). Calibration of a physically based, spatially distributed hydrological model in a glacierized basin: On the use of knowledge from glaciometeorological processes to constrain model parameters. *Water Resources Research*, *48*(3).

Ragettli, S., Pellicciotti, F., Bordoy, R., & Immerzeel, W. W. (2013). Sources of uncertainty in modeling the glaciohydrological response of a Karakoram watershed to climate change. *Water Resources Research*, *49*(9), 6048-6066.

Ragettli, S., Pellicciotti, F., Immerzeel, W. W., Miles, E. S., Petersen, L., Heynen, M., ... & Shrestha, A. (2015). Unraveling the hydrology of a Himalayan catchment through integration of high resolution in situ data and remote sensing with an advanced simulation model. *Advances in Water Resources*, *78*, 94-111.

Reba, M. L., Marks, D., Link, T. E., Pomeroy, J., & Winstral, A. (2014). Sensitivity of model parameterizations for simulated latent heat flux at the snow surface for complex mountain sites. *Hydrological Processes*, *28*(3), 868-881.

Reichstein, M., Camps-Valls, G., Stevens, B., Jung, M., Denzler, J., Carvalhais, N., Prabhat, F. (2019). Deep learning and process understanding for data-driven Earth system science. *Nature*, *566*(7743), 195-204.

Reid, T. D., & Brock, B. W. (2010). An energy-balance model for debris-covered glaciers including heat conduction through the debris layer. *Journal of Glaciology*, *56*(199), 903-916.

Réveillet, M., Dumont, M., Gascoin, S., Lafaysse, M., Nabat, P., Ribes, A., ... & Ginoux, P. (2022). Black carbon and dust alter the response of mountain snow cover under climate change. *Nature communications*, *13*(1), 5279.

Reynolds, D. S., Gutmann, E., Kruyt, B., Haugeneder, M., Jonas, T., Gerber, F., ... & Mott, R. (2023). The high-resolution intermediate complexity atmospheric research (HICAR v1. 0) model enables fast dynamic downscaling to the hectometer scale. *Geoscientific Model Development Discussions*, *2023*, 1-30.

Rounce, D. R., Hock, R., Maussion, F., Hugonnet, R., Kochtitzky, W., Huss, M., ... & McNabb, R. W. (2023). Global glacier change in the 21st century: Every increase in temperature matters. *Science*, *379*(6627), 78-83.

Rounce, D. R., Quincey, D. J., & McKinney, D. C. (2015). Debris-covered glacier energy balance model for Imja–Lhotse Shar Glacier in the Everest region of Nepal. *The Cryosphere*, *9*(6), 2295-2310.

Sakai, A. (2019). Brief communication: Updated GAMDAM glacier inventory over high-mountain Asia. *The Cryosphere*, *13*(7), 2043-2049.

Salerno, F., Guyennon, N., Yang, K., Shaw, T. E., Lin, C., Colombo, N., ... & Pellicciotti, F. (2023). Local cooling and drying induced by Himalayan glaciers under global warming. *Nature Geoscience*, *16*(12), 1120-1127.

Sarangi, C., Qian, Y., Rittger, K., Ruby Leung, L., Chand, D., Bormann, K. J., & Painter, T. H. (2020). Dust dominates high-altitude snow darkening and melt over high-mountain Asia. *Nature Climate Change*, *10*(11), 1045-1051.

Scherler, D., Wulf, H., & Gorelick, N. (2018). Global assessment of supraglacial debris-cover extents. *Geophysical Research Letters*, *45*(21), 11-798.

Schmidt, R. A. (1982). Vertical profiles of wind speed, snow concentration, and humidity in blowing snow. Boundary-Layer Meteorology, 23(2), 223-246.

Sexstone, G. A., Clow, D. W., Fassnacht, S. R., Liston, G. E., Hiemstra, C. A., Knowles, J. F., & Penn, C. A. (2018). Snow sublimation in mountain environments and its sensitivity to forest disturbance and climate warming. Water Resources Research, 54(2), 1191-1211.

Sexstone, G. A., Clow, D. W., Stannard, D. I., & Fassnacht, S. R. (2016). Comparison of methods for quantifying surface sublimation over seasonally snow-covered terrain. *Hydrological Processes*, *30*(19), 3373-3389.

Shaw, T. E., Brock, B. W., Fyffe, C. L., Pellicciotti, F., Rutter, N., & Diotri, F. (2016). Air temperature distribution and energy-balance modelling of a debris-covered glacier. *Journal of Glaciology*, *62*(231), 185-198.

Shaw, T. E., Buri, P., McCarthy, M., Miles, E. S., & Pellicciotti, F. (2024). Local Controls on Near-Surface Glacier Cooling Under Warm Atmospheric Conditions. *Journal of Geophysical Research: Atmospheres*, *129*(2), e2023JD040214.

Shaw, T. E., Buri, P., McCarthy, M., Miles, E. S., Ayala, Á., & Pellicciotti, F. (2023). The Decaying Near-Surface Boundary Layer of a Retreating Alpine Glacier. *Geophysical Research Letters*, *50*(11), e2023GL103043.

Shaw, T. E., Yang, W., Ayala, Á., Bravo, C., Zhao, C., & Pellicciotti, F. (2021). Distributed summer air temperatures across mountain glaciers in the south-east Tibetan Plateau: Temperature sensitivity and comparison with existing glacier datasets. *The Cryosphere*, *15*(2), 595-614.

Shea, J. M., Wagnon, P., Immerzeel, W. W., Biron, R., Brun, F., & Pellicciotti, F. (2015). A comparative high-altitude meteorological analysis from three catchments in the Nepalese Himalaya. *International journal of water resources development*, *31*(2), 174-200.

Shean, D. E., Bhushan, S., Montesano, P., Rounce, D. R., Arendt, A., & Osmanoglu, B. (2020). A systematic, regional assessment of high mountain Asia glacier mass balance. *Frontiers in Earth Science*, *7*, 363.

Singh, P., & Bengtsson, L. (2005). Impact of warmer climate on melt and evaporation for the rainfed, snowfed and glacierfed basins in the Himalayan region. Journal of Hydrology, 300(1–4), 140–154. https://doi.org/10.1016/j.jhydrol.2004.06.005

Smith, S. L., O'Neill, H. B., Isaksen, K., Noetzli, J., & Romanovsky, V. E. (2022). The changing thermal state of permafrost. *Nature Reviews Earth & Environment*, *3*(1), 10-23.

Somers, L. D., & McKenzie, J. M. (2020). A review of groundwater in high mountain environments. *Wiley Interdisciplinary Reviews: Water*, *7*(6), e1475.

Steiger, R., Knowles, N., Pöll, K., & Rutty, M. (2022). Impacts of climate change on mountain tourism: A review. *Journal of Sustainable Tourism*, 1-34.

Steiner, J. F., Gurung, T. R., Joshi, S. P., Koch, I., Saloranta, T., Shea, J., ... & Immerzeel, W. W. (2021a). Multi-year observations of the high mountain water cycle in the Langtang catchment, Central Himalaya. *Hydrological Processes*, *35*(5), e14189.

Steiner, J. F., Kraaijenbrink, P. D., & Immerzeel, W. W. (2021b). Distributed melt on a debris-covered Glacier: field observations and melt modeling on the Lirung Glacier in the Himalaya. *Frontiers in Earth Science*, *9*, 678375.

Steiner, J. F., Litt, M., Stigter, E. E., Shea, J., Bierkens, M. F., & Immerzeel, W. W. (2018). The importance of turbulent fluxes in the surface energy balance of a debris-covered glacier in the Himalayas. *Frontiers in Earth Science*, *6*, 144.

Stewart, R. L., Westoby, M., Pellicciotti, F., Rowan, A., Swift, D., Brock, B., & Woodward, J. (2021). Using climate reanalysis data in conjunction with multi-temporal satellite thermal imagery to derive supraglacial debris thickness changes from energy-balance modelling. *Journal of Glaciology*, *67*(262), 366-384.

Stigter, E. E., Litt, M., Steiner, J. F., Bonekamp, P. N., Shea, J. M., Bierkens, M. F., & Immerzeel, W. W. (2018). The importance of snow sublimation on a Himalayan glacier. *Frontiers in Earth Science*, *6*, 108.

Stigter, E. E., Steiner, J. F., Koch, I., Saloranta, T. M., Kirkham, J. D., & Immerzeel, W. W. (2021). Energy and mass balance dynamics of the seasonal snowpack at two high-altitude sites in the Himalaya. *Cold Regions Science and Technology*, *183*, 103233.

Tang, Z., Deng, G., Hu, G., Zhang, H., Pan, H., & Sang, G. (2022). Satellite observed spatiotemporal variability of snow cover and snow phenology over high mountain Asia from 2002 to 2021. *Journal of Hydrology*, *613*, 128438.

Tauro, F., Petroselli, A., & Grimaldi, S. (2018). Optical sensing for stream flow observations: A review. *Journal of Agricultural Engineering*, *49*(4), 199-206.

Thornton, J. M., Palazzi, E., Pepin, N. C., Cristofanelli, P., Essery, R., Kotlarski, S., ... & Adler, C. (2021). Toward a definition of essential mountain climate variables. *One Earth*, *4*(6), 805-827.

Thornton, J. M., Therrien, R., Mariéthoz, G., Linde, N., & Brunner, P. (2022). Simulating fully-integrated hydrological dynamics in complex Alpine headwaters: potential and challenges. *Water Resources Research*, *58*(4), e2020WR029390.

Van Tiel, M., Stahl, K., Freudiger, D., & Seibert, J. (2020). Glacio-hydrological model calibration and evaluation. *Wiley Interdisciplinary Reviews: Water*, *7*(6), e1483.

Van Tiel, M., Van Loon, A. F., Seibert, J., & Stahl, K. (2021). Hydrological response to warm and dry weather: do glaciers compensate?. *Hydrology and Earth System Sciences*, *25*(6), 3245-3265.

Verseghy, D. L. (1991), CLASS-A Canadian land surface scheme for GCMs. I. Soil Model, Int. J. Climatol., 11(2), 111–133.

Vincent, A., Violette, S., & Aðalgeirsdóttir, G. (2019). Groundwater in catchments headed by temperate glaciers: A review. *Earth-Science Reviews*, *188*, 59-76.

Vionnet, V., Guyomarc'h, G., Lafaysse, M., Naaim-Bouvet, F., Giraud, G., & Deliot, Y. (2018). Operational implementation and evaluation of a blowing snow scheme for avalanche hazard forecasting. *Cold Regions Science and Technology*, *147*, 1-10.

Vionnet, V., Marsh, C. B., Menounos, B., Gascoin, S., Wayand, N. E., Shea, J., ... & Pomeroy, J. W. (2021). Multi-scale snowdrift-permitting modelling of mountain snowpack. *The Cryosphere*, *15*(2), 743-769.

Viviroli, D., Dürr, H. H., Messerli, B., Meybeck, M., & Weingartner, R. (2007). Mountains of the world, water towers for humanity: Typology, mapping, and global significance. *Water resources research*, *43*(7).

Viviroli, D., Kummu, M., Meybeck, M., Kallio, M., & Wada, Y. (2020). Increasing dependence of lowland populations on mountain water resources. *Nature Sustainability*, *3*(11), 917-928.

Viviroli, D., Weingartner, R., & Messerli, B. (2003). Assessing the hydrological significance of the world's mountains. *Mountain research and Development*, *23*(1), 32-40.

Vivoni, E. R., Entekhabi, D., Bras, R. L., & Ivanov, V. Y. (2007). Controls on runoff generation and scale-dependence in a distributed hydrologic model. *Hydrology and Earth System Sciences*, *11*(5), 1683-1701.

Vivoni, E. R., Ivanov, V. Y., Bras, R. L., & Entekhabi, D. (2004). Generation of triangulated irregular networks based on hydrological similarity. *Journal of hydrologic engineering*, *9*(4), 288-302.

Wagnon, P., Sicart, J. E., Berthier, E., and Chazarin, J. P. (2003).Wintertime high altitude surface energy balance of a Bolivian glacier, Illimani, 6340m above sea level. J. Geophys. Res. 108, 4177. doi: 10.1029/2002JD002088

Wagnon, P., Vincent, C., Arnaud, Y., Berthier, E., Vuillermoz, E., Gruber, S., ... & Pokhrel, B. K. (2013). Seasonal and annual mass balances of Mera and Pokalde glaciers (Nepal Himalaya) since 2007. *The Cryosphere*, *7*(6), 1769-1786.

Walvoord, M. A., & Kurylyk, B. L. (2016). Hydrologic impacts of thawing permafrost—A review. *Vadose Zone Journal*, *15*(6)

Wang, X., Tolksdorf, V., Otto, M., & Scherer, D. (2021). WRF-based dynamical downscaling of ERA5 reanalysis data for High Mountain Asia: Towards a new version of the High Asia Refined analysis. *International Journal of Climatology*, *41*(1), 743-762.

Wang, Y., Meili, N., & Fatichi, S. (2023). Evidence and controls of the acceleration of the hydrological cycle over land. *Water Resources Research*, *59*(8), e2022WR033970.

Wang, Y. H., Broxton, P., Fang, Y., Behrangi, A., Barlage, M., Zeng, X., & Niu, G. Y. (2019). A wet-bulb temperature-based rain-snow partitioning scheme improves snowpack prediction over the drier western United States. *Geophysical Research Letters*, *46*(23), 13825-13835.

Wheater, H. S., Pomeroy, J. W., Pietroniro, A., Davison, B., Elshamy, M., Yassin, F., ... & Bahrami, A. (2022). Advances in modelling large river basins in cold regions with Modélisation Environmentale Communautaire—Surface and Hydrology (MESH), the Canadian hydrological land surface scheme. Hydrological Processes, 36(4), e14557.

Wei, Y., Wang, R., & Feng, P. (2024). Improving Hydrological Modeling with Hybrid Models: A Comparative Study of Different Mechanisms for Coupling Deep Learning Models with Process-based Models. *Water Resources Management*, 1-18.

Wester, P., Mishra, A., Mukherji, A., & Shrestha, A. B. (2019). *The Hindu Kush Himalaya assessment: mountains, climate change, sustainability and people* (p. 627). Springer Nature.

Wiersma, P., Aerts, J., Zekollari, H., Hrachowitz, M., Drost, N., Huss, M., Sutanudjaja, E. H., and Hut, R.: Coupling a global glacier model to a global hydrological model prevents underestimation of glacier runoff, Hydrol. Earth Syst. Sci., 26, 5971–5986, https://doi.org/10.5194/hess-26-5971-2022, 2022.

Wijngaard, R. R., Herrington, A. R., Lipscomb, W. H., Leguy, G. R., & An, S. I. (2023). Exploring the ability of the variable-resolution Community Earth System Model to simulate cryospheric–hydrological variables in High Mountain Asia. *The Cryosphere*, *17*(9), 3803-3828.

Wilson, J. L., & Guan, H. (2004). Mountain-block hydrology and mountain-front recharge. *Groundwater recharge in a desert environment: The Southwestern United States*, *9*, 113-137.

Yang, W. E. I., Yao, T., Zhu, M., & Wang, Y. (2017). Comparison of the meteorology and surface energy fluxes of debris-free and debris-covered glaciers in the southeastern Tibetan Plateau. *Journal of Glaciology*, *63*(242), 1090-1104.

Yao, T., Bolch, T., Chen, D., Gao, J., Immerzeel, W., Piao, S., ... & Zhao, P. (2022). The imbalance of the Asian water tower. *Nature Reviews Earth & Environment*, *3*(10), 618-632.

Yao, T., Thompson, L., Yang, W., Yu, W., Gao, Y., Guo, X., ... & Joswiak, D. (2012). Different glacier status with atmospheric circulations in Tibetan Plateau and surroundings. *Nature climate change*, *2*(9), 663-667.

Yatagai, A., Kamiguchi, K., Arakawa, O., Hamada, A., Yasutomi, N., & Kitoh, A. (2012). APHRODITE: Constructing a long-term daily gridded precipitation dataset for Asia based on a dense network of rain gauges. *Bulletin of the American Meteorological Society*, *93*(9), 1401-1415.

You, Q. et al. Elevation dependent warming over the Tibetan Plateau: patterns, mechanisms and perspectives. Earth Sci. Rev. 210, 103349 (2020)

Zehe, E., & Sivapalan, M. (2009). Threshold behaviour in hydrological systems as (human) geo-ecosystems: manifestations, controls, implications. *Hydrology and Earth System Sciences*, *13*(7), 1273-1297.

Zemp, M., Huss, M., Thibert, E., Eckert, N., McNabb, R., Huber, J., ... & Cogley, J. G. (2019). Global glacier mass changes and their contributions to sea-level rise from 1961 to 2016. *Nature*, *568*(7752), 382-386.

Zhao, C., Yang, W., Miles, E., Westoby, M., Kneib, M., Wang, Y., ... & Pellicciotti, F. (2022). Thinning and surface mass balance patterns of two neighboring debris-covered glaciers in southeastern Tibetan Plateau. *The Cryosphere Discussions*, *2022*, 1-28